Rapid Post-Earthquake Damage Detection of Buildings based on Machine Learning

(機械学習に基づく地震直後の建物損傷検出法)

July 2023

Doctor of Philosophy (Engineering)

Moscoso Alcantara Edisson Alberto

モスコソ アルカンタラ エデイソン アルベルト

Toyohashi University of Technology

Abstract

Currently, the decision-making response to an earthquake is limited by the time it takes to identify the extent of damage to buildings. This limitation and accuracy rely on various factors, including on-site inspections by professionals, structural analysis from engineering offices, and limited information due to logistical resources. It has been observed in past earthquakes that structural engineering professionals are insufficient to cover the needs of all the affected buildings. Therefore, new technologies such as structural health monitoring and machine learning (ML) can be employed to decrease response time. This research proposes several methodologies to use ML methods and ground and roof sensors to predict damage conditions represented by the maximum ductility ratio, inter-story drift ratio, and absolute acceleration on each floor under earthquake conditions.

Moreover, Incremental Dynamic Analyses of the structures for each case study are carried out to cover elastic and inelastic behavior. Initially, a Lumped Mass Model was used to represent the buildings, and their damage condition was obtained using wavelet spectra as images in the Convolutional Neural Network method. Subsequently, the methodology was improved using Wavelet Power Spectra and a proposed selection of records to increase accuracy. The procedure was applied to three-dimensional frame models of two actual instrumented buildings in Japan and an artificial RC building in order to consider distinct materials, lateral force-resisting systems, and structural configurations. Even though the high accuracy of the previous methodology, it was updated to predict new earthquakes of different characteristics (without a selection methodology), obtain information on the main predicting features, and reduce the bias from splitting training and validation records by using seven ML methods and 27 Intensity Measures (IM) and applied to the two buildings in Japan. Later, a new methodology based on the previous ML and IMs is proposed to predict new buildings and earthquakes. It was applied to 600 buildings of a moment-resisting frame system archetype. The archetype is designed using the virtual work method. For all the methodologies, high accuracy with low splitting dispersion of the predictions is obtained, and the building's post-earthquake condition is possible to detect immediately since the ML is trained and validated beforehand.

The results will be helpful for countermeasures after an earthquake, such as evacuating buildings, resuming economic and social activities, and mitigating future damage by aftershocks.

Table of contents

List of figures

List of tables

List of abbreviations

SHM	Structural Health Monitoring
ML	Machine Learning
CNN	Convolutional Neural Network
JSCA	Japan Structural Consultants Association
RC	Reinforced Concrete
LMM	Lumped Mass Model
DL	Deep Learning
SVM	Support Vector Machine
ANN	Artificial Neural Networks
CapsNet	Capsule Network
FCN	Fully Convolutional Network
STFT	Short-Time Fourier Transform
CWT	Continuous Wavelet Transform
PhyCNN	Physics-guided Convolutional Neural Network
WS	Wavelet Spectrum
WPS	Wavelet Power Spectrum
ReLU	Rectified Linear Unit
MSE	Mean Squared Error
PGA	Peak Ground Acceleration
USGS	United States Geological Survey
3D-FM	three-dimensional frame model
IDA	Incremental Dynamic Analysis
SRC	Steel-Reinforced Concrete
Sa	Acceleration Response Spectrum
IM	Intensity Measure
DM	Damage Measure
UHS	Uniform Hazard Spectrum

Dedication

To my wife, Jenny Gonzalez, who has stood by my side with unwavering support for the past 16 years,

To my two children, Leonardo and Vania, who are always in my thoughts and inspire me to strive for the best version of myself,

"Una familia unida te da las raices para crecer alto y fuerte"

Acknowledgments

Completing a Ph.D. is a challenging feat. Yet, with the aid of support from various sources, it becomes more feasible. Thus, I am immensely grateful to the individuals listed below:

- Parents, Augusto and Maria, as well as my siblings, Augusto (in heaven), Dessire, Norma, Andersson, Karla, Joaquin, and Nikolaz, who accompanied me all the way from Peru during this tough challenge.
- Late grandfather, Celestino Alcantara (lovingly known as “papá Tino”), who provided guidance and support until the end of his days.
- Supervisor, Taiki Saito sensei. His guidance, patience, and support were instrumental in enabling me to complete this dissertation.
- Close laboratory friends, Majima and Zafira, who always provided me with valuable academic and personal advice from the beginning.
- Two research kohais, Michelle and Enku, who accompanied me during the process.
- Saito’s laboratory members, Taufiq, Ataie, Sharafi, Muhammed, Husaini, Khalid, our late friend Aung and everyone else with whom I have spent meaningful moments.
- Latin-American friends from TUT, I always cherished our gatherings on Wednesdays for the renowned pizza nights.
- UNI’s Professors Carlos Zavala, Jorge Gallardo, Miguel Diaz, and Roy Reyna, who generously provided me with invaluable advice and knowledge.
- Peruvian friends, Zafiros, for their heartfelt and supportive companionship.
- Friends and family not mentioned, who stood by me throughout my academic journey.
- JICA for providing me with the SDGs Global Leader scholarship and the necessary resources for pursuing my Ph.D. without any financial constraints.

Chapter 1. Introduction

1.1 Research background

Earthquakes in the proximity of structurally vulnerable buildings could cause damage of varying intensities. Making decisions, such as evacuating buildings, resuming economic and social activities, and mitigating future damage by aftershocks, is one of the most critical necessities for government, owners, and stakeholders after an earthquake. If damage to a building caused by an earthquake is not detected immediately, the opportunity to decide on quick action is lost. However, damage of different risk levels (see Figure 1.1) is often difficult to classify rapidly, making it difficult to determine the structural safety of a building accurately. For instance, the current conventional post-earthquake actions report the usability of the buildings related to protecting their occupants in days or even weeks after the event, depending on the post-earthquake evaluation methods and the technicians' expertise [1]. Also, if a deep behavioral understanding of the structure is requested, it is obtained after months [2]. According to the National Institute of Civil Defense of Peru, during the Pisco earthquake on 15 August 2007, in the five central regions of Peru (Lima included, which is the capital of Peru), 136,149 dwellings, 1,278 educational buildings, and 126 health buildings collapsed or were damaged, where their use was classified as restricted or unsafe [3]. However, this report was released almost two months after the earthquake, during which time, all activities in the affected areas of the main regions had to be suspended, including the construction of temporary dwellings (see Figure 1.1 and Figure 1.2). For this reason, it is necessary to develop new technologies that can rapidly obtain buildings' post-earthquake structural safety conditions.

Resilient cities are goals that countries are building towards to increase the capacity for learning from past disasters for better future protection and to improve risk reduction measures[1]. In particular, as part of this concept, modern structures need to be developed to quickly obtain structural safety information after an earthquake to minimize social and economic disruption and mitigate future earthquake effects [4]. For example, in order to promote and disseminate knowledge to increase social resilience and reduce earthquake risk, experts from academia and industry gathered in 2019 for a workshop focused on state-of-the-art risk-reduction strategies. It identified a need for structural health monitoring (SHM) research to assess the integrity and performance of engineering structures to detect post-earthquake damage and quick decision-making [5]. The general process of SHM is shown in Figure 1.3.

SHM is a field where it is possible to obtain real-time structural responses and successful post-earthquake damage detection of monitored buildings, bridges, cultural heritage structures, dams, base-isolated buildings, and others. [6,7]. Acceleration or displacement recordings from instrumented buildings during earthquakes offer valuable information to identify and monitor their damage extent. Thus, structural health monitoring is an expanding field that allows for establishing procedures to screen the structural status of buildings. Moreover, various methods for estimating the lateral strength of buildings using the sensors' information have been proposed. For example, Quispe et al. [8] obtained the capacity curve and the inter-story drift ratios of the Edgardo Rebagliati Martins hospital in Peru using a sparse number of sensors, the wavelet transform method, and the spline shape function. Also, Schanze et al. [9] compared the effect of different underground story modeling approaches on Chile's instrumented Alcazar building office. For this reason, the implementation of instrumented buildings has been increasing recently [10-12].

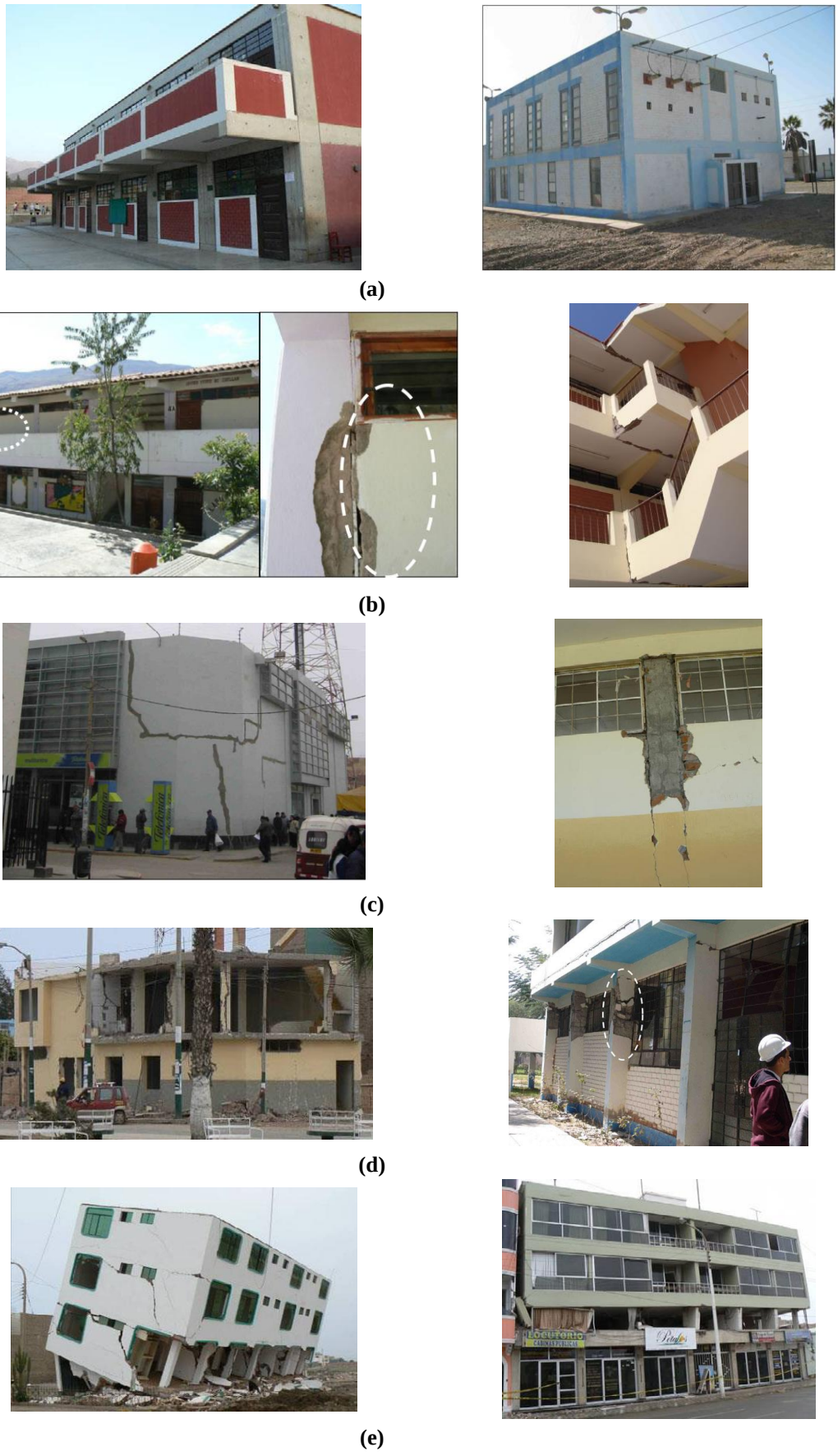

Figure 1.1. Pisco, Peru, earthquake of August 15, 2007: Damage of different risk levels. (a) No damage; (b) Minor damage; (c) Significant damage; (d) Severe damage; (e) Collapse [13].

Figure 1.2. Pisco, Peru, earthquake of August 15, 2007: Temporary dwellings [13].

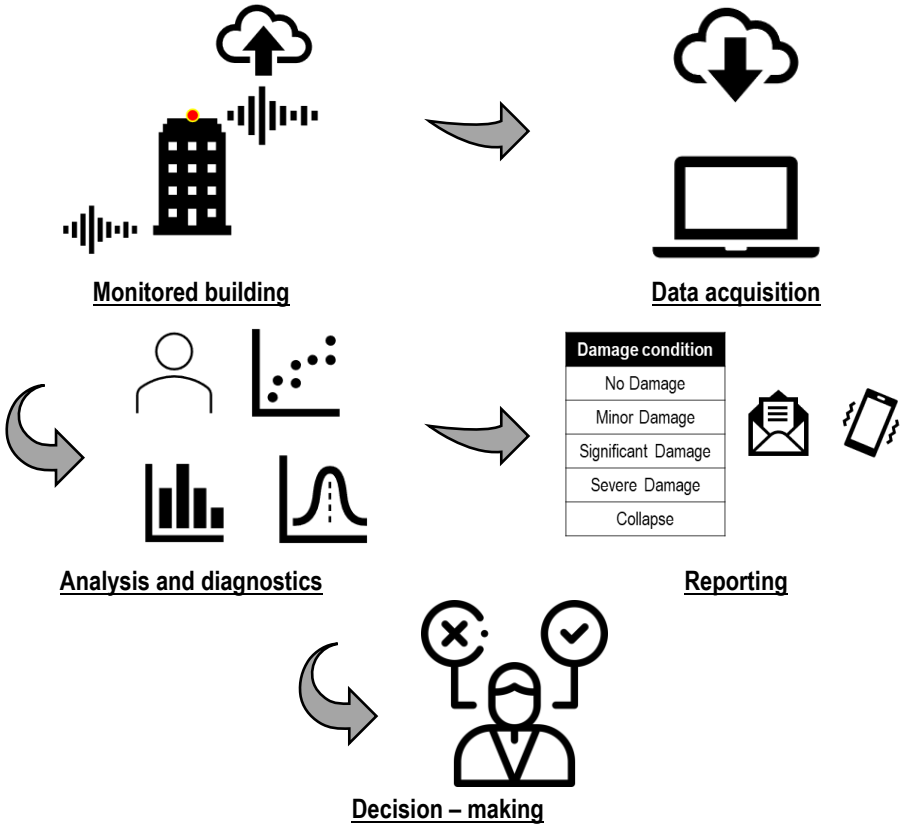

Figure 1.3. General SHM process.

In the field of SHM, there are several types of sensors to measure and diagnose the static and dynamic properties of the monitored buildings. Antunez et al. demonstrated that optical fiber sensors could be helpful in the static and dynamic monitoring of large raw earth masonry structures common in cultural, historical, and architecturally recognized buildings worldwide [14]. Piezoelectric sensors are another type of monitoring device, and Roghaei et al. proposed a method to identify stress and deformation using an array of sensors mounted in certain locations [15]. They verified the proposed method using a three-story steel building and confirmed that continuous monitoring and analysis of sensor signals could help the building

manager to apply warning alarms and call for evacuation. However, the most common monitoring control sensor is the accelerometer which will be used herein.

Structural responses such as ductility, maximum inter-story drift, and acceleration can be used in order to determine structural integrity. Hazus is a geographic information system-based natural hazard analysis tool used by the Federal Emergency Management Agency of the USA, and the Hazus earthquake model evaluates the damage probability of buildings and infrastructures considering inter-story drift and acceleration limits to establish the structural and nonstructural damage states [16]. The Japan Structural Consultants Association (JSCA), an organization of building structural engineers in Japan, uses three parameters of safety criteria used to assess a building in its performance-based guidelines: absolute acceleration, maximum ductility ratio, and maximum inter-story drift ratio [17]. Acceleration is related to damage in nonstructural components, and ductility and story drift ratio to damage in structural components. This study uses this criterion in order to classify the damage condition of buildings.

The maximum ductility ratio (ductility ratio from now on) indicates the amount of inelastic deformation over the yielding threshold, as defined in Figure 1.4. Damage identification is based on JSCA [17] as follows: a ductility ratio <1.0 means no damage, a ductility ratio ≥1.0 but <2.0 means minor damage, a ductility ratio ≥2.0 but <3.0 means significant damage, a ductility ratio ≥3.0 but <4.0 means severe damage, and a ductility ratio ≥4.0 means collapse. These values are defined in Table 1.1. Even though the ductility ratio is greater than 1, in this study, lower ratios are obtained to differentiate between elastic and inelastic behavior.

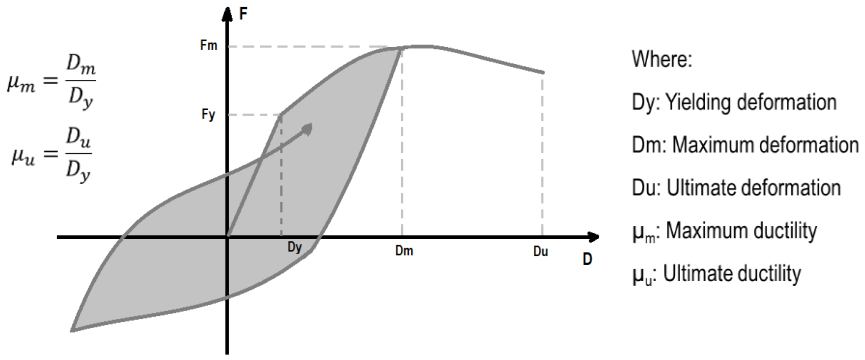

Figure 1.4. Definition of ductility ratio.

The maximum inter-story drift ratio (story drift ratio from now on) represents the maximum relative displacement that a particular story reaches, as defined in Figure 1.5. A larger story drift ratio after the yielding stage corresponds to a larger extent of the damage. Damage identification is based on JSCA [17], as follows: a story drift ratio <1/300 means no damage, a story drift ratio ≥1/300 but <1/150 means minor damage, a story drift ratio ≥1/150 but <1/100 means significant damage, a story drift ratio ≥1/100 but <1/75 is severe damage, and a story drift ratio ≥1/75 means collapse. These values are defined in Table 1.1.

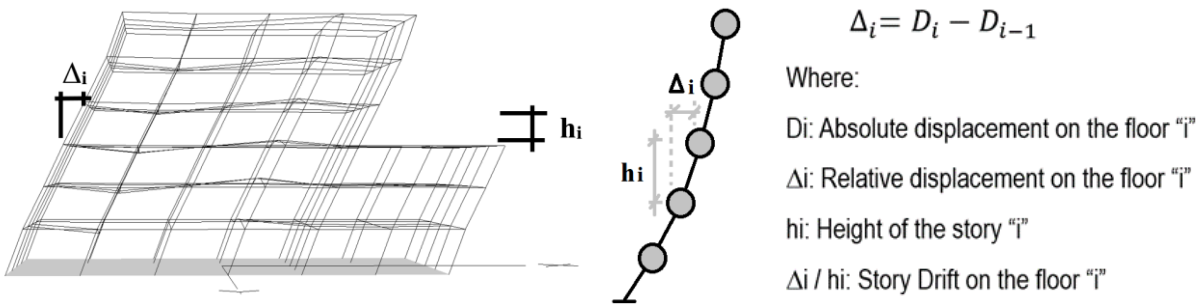

Figure 1.5. Definition of story drift ratio.

The maximum absolute acceleration (acceleration from now on) indicates the intensity that a particular story is subjected to. Damage identification is based on JSCA [17], as follows: an acceleration <250 gal means no damage, acceleration ≥250 gal but <500 gal means minor damage, acceleration ≥500 gal but <1000 gal means significant damage, an acceleration ≥1000 gal but <1500 gal means severe damage, and an acceleration ≥1500 gal means collapse. These values are defined in Table 1.1.

Table 1.1. Damage condition and usability according to the structural response for damage identification.

Usability of building	**Safe Use**		**Restricted Use**	**Unsafe Use**	
Damage Condition	**No Damage**	**Minor Damage**	**Significant Damage**	**Severe Damage**	**Collapse**
Ductility ratio	<1	≥1.0 but <2.0	≥2.0 but <3.0	≥3.0 but <4.0	≥4.0
Inter-story drift ratio	<1/300	≥1/300 but <1/150	≥1/150 but <1/100	≥1/100 but < 1/75	≥1/75
Acceleration (gal)	<250	≥250 but <500	≥500 but <1000	≥1000 but < 1500	≥1500

In all cases, the damage condition after severe damage is considered a collapse condition. Besides, no damage and minor damage represent a building that is safe for use, significant damage represents a building that can have restricted use, and severe damage represents a building that is unsafe for use, that is, a value greater than minor damage is a restricted or unsafe condition, which is a parameter used for evacuating the building. Even though these parameters and their values are considered in this study, it is known that the damage condition depends on each building. For this reason, it is recommended to obtain it for future studies.

Even though SHM helps detect buildings' damaged state, the reporting time depends on the analysis detail. For this reason, it is necessary to use modern techniques to prepare a model beforehand to predict the post-earthquake damage immediately. According to study [18], there are two approaches for damage identification: model-driven methods and data-driven methods. In a model-driven approach, usually, a high-fidelity physical model of the structure is used to establish a comparison metric between the model and the measured data from the real structure to distinguish the damage condition from the normal condition. In a data-driven approach, a structural model is used as a statistical representation of the system, and the main algorithms developed for this purpose are those in the field of pattern recognition or, more broadly, machine learning (ML). ML is the part of artificial intelligence that uses statistical methods to obtain experience (learning process) from main features to predict future actions or responses. Recently, ML has been studied to assess damage without response analysis of structures. The ML methods may provide higher accuracy by updating the model after each earthquake or if the number of features increases [19]. ML methods are currently used to predict structures' damage states [20,21]. For example, Cardellicchio et al. proposed a methodology to interpret defect detection results using Class Activation Maps and eXplainable Artificial Intelligence techniques applied to Reinforced Concrete (RC) bridges in Southern Italy [22]. It is, likewise, detecting the damage condition of buildings after an earthquake is obtained for instrumented buildings [23-25]. For instance, Yongjia et al. used IMs to train ML models to classify the damage state of buildings [26]. Also, Sajedi et al. proposed a framework for building damage diagnosis using the Support Vector Machines method for damage classification and the Bayesian method for the input features and hyperparameters optimization.

In this study, the ML methods use the building's structural features as input data and the structural responses as output data. As shown in Figure 1.6, the ML methods have a training and testing process. The input and output data are used to train the ML model in the training process. The trained ML model is used to get new predictions in the testing process, and its accuracy is evaluated using reference results.

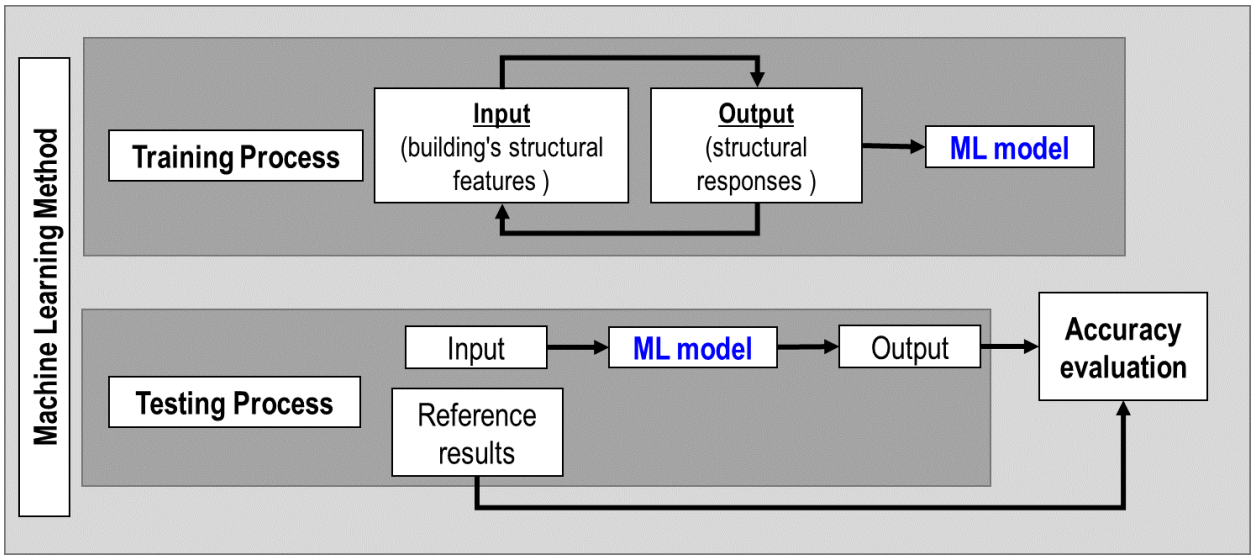

Figure 1.6. Machine learning method.

Finally, ML methods are used in the SHM field to rapidly detect the post-earthquake damage state of buildings. The general process of SHM is shown in Figure 1.7.

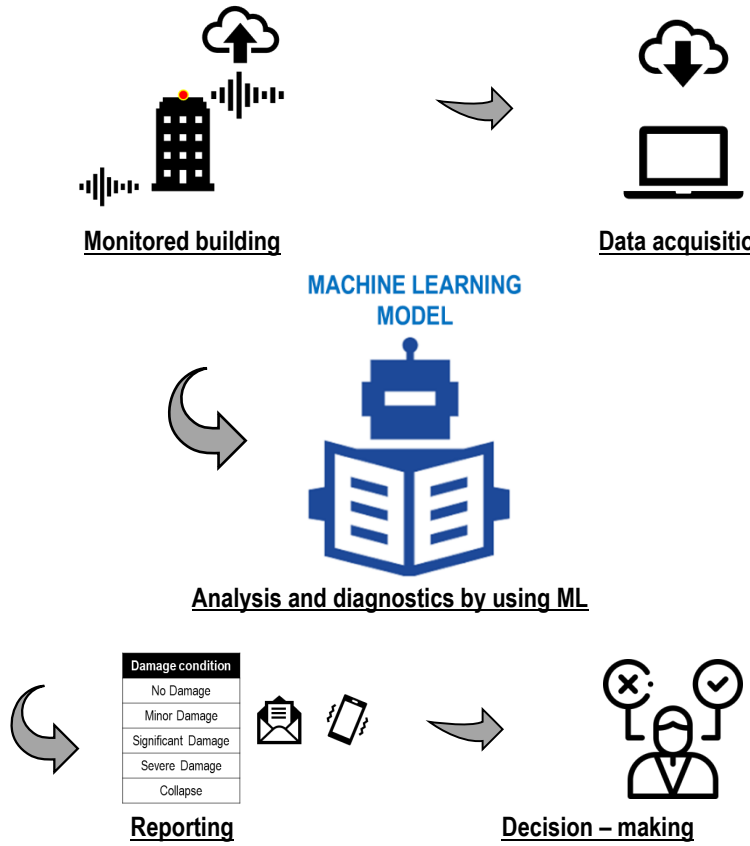

Figure 1.7. General SHM process using ML methods.

1.2 Problem statement

Nowadays, the action response after an earthquake is limited by the time taken to detect the damaged state of buildings. It depends on the post-inspection of buildings carried out by professionals in-situ, structural analysis developed in engineering offices, or the minimum information not allowed by the logistic resources. The experience of past earthquakes shows there are not enough structural engineering experts to cover the demand for all affected buildings. For this reason, new technologies such as structural health monitoring combined with machine learning methods are feasible options to reduce the response time.

1.3 Research objectives

The research aim is to propose methodologies based on machine learning applied to SHM for rapid post-earthquake damage detection of buildings which derives from the following objectives:

- Propose a methodology based on convolutional neural networks (CNN) for detecting lumped mass model building damage using structural feature images of roof sensors.
- Propose a methodology based on CNN for detecting three-dimensional frame model building damage by proposing a selection of ground motion records and using structural feature images of roof sensors.
- Propose a methodology based on ML methods for detecting three-dimensional frame model building damage using intensity measures of ground and roof sensors.
- Propose a methodology based on ML methods for detecting new three-dimensional frame model buildings damage by proposing a selection of ground motion records and using intensity measures of ground and roof sensors.

1.4 Research outline

0 presents an overview of the current situation of the damage state detection of buildings after an earthquake occurs and describes the SHM and ML fields as alternatives to improve the time response for immediate actions.

Chapter 2 presents a methodologic proposal based on CNN using wavelet spectra as structural feature images applied to lumped mass model buildings to detect their post-earthquake damage condition.

Chapter 3 presents a methodologic proposal based on CNN using power wavelet spectra as structural feature images applied to three-dimensional frame model buildings to detect their post-earthquake damage condition. A selection of ground motion records is proposed in order to increase prediction accuracy.

Chapter 4 presents a methodologic proposal based on ML methods using IMs as structural features applied to three-dimensional frame model buildings to detect their post-earthquake damage condition. A prediction accuracy comparison with the methodology presented in Chapter 3 is carried out.

Chapter 5 presents a methodologic proposal based on ML methods using IMs as structural features applied to a proposed archetype moment-resisting three-dimensional frame model buildings to detect their post-earthquake damage condition. A structural design methodology of the archetype members based on the virtual work method is proposed. The bias of the selection of buildings and ground motion records is evaluated.

Chapter 6 presents conclusions and recommendations based on the proposed methodologies for future research.

Chapter 2. CNN–Based Damage Detection using Wavelet Spectra for LMM Buildings

2.1 Introduction

This study proposes a methodology to use machine learning methods and roof sensors to predict damage conditions (represented by ductility ratio, story drift ratio, and acceleration, as defined in section 1.1) on each building floor (represented by a lumped mass model) under earthquake conditions. In the beginning, the earthquake responses of a model building are calculated under the scaled earthquake records with several intensities (scale factors). The level of intensity is established to obtain a range of elastic and inelastic behavior of the building. Then, wavelet spectra are developed from the structural response accelerations on the upper floor of the building. The wavelet spectra are the input data of a CNN model to predict the absolute acceleration, ductility ratio, and story drift ratio on each floor, which correspond to the damage to the nonstructural and structural components of the building. This study was published by the author in [27].

This chapter contains sections as follows: In Section 2.2, a review of relevant literature is presented. Section 2.3 and 2.4 discusses the research methodology, which defines the structural model and responses, wavelet spectrum, and Convolutional Neural Network used in this study. Section 2.5 presents the case study, input ground motion, and scale factor of records. The Machine learning methodology is described in section 2.6. The results and the comparison of the prediction and reference values of the case study are shown in Section 2.7. Section 2.8 presents a summary and discussion of the research results.

2.2 Literature review

Goulet et al. proposed a methodology that updates the prediction of the damage state of uninspected monitored buildings as the model learns from collected data of the damage state of inspected buildings [25]. This proposal was validated in a city with 1000 buildings. Furthermore, Sivasuriyan et al. reviewed a large number of studies on the practical implementation and operations of SHM in multi-story buildings, as well as damage evaluation of monitored buildings, and discussed the structural response by considering static and dynamic analysis using numerical simulations such as finite element analysis [10]. Wang et al. developed a method to evaluate the story damage index based on the modal frequency and mode shape obtained from the records of the earthquake response of a building [28]. Furthermore, an approximate story damage index was developed without considering the information on the floor mass to identify the extent of damage to the story. Although it was possible to verify the damage index by some numerical simulations and the experimental data analysis established previously, it was necessary to calculate the modal frequency and mode shapes from the post-earthquake structural responses of each story and to compare with the values of the building before the earthquake. It is worth pointing out that a large number of sensors will require a high investment. For this reason, Xu et al. estimated the maximum drift and time histories of relative displacement in all stories of multi-degree-of-freedom structures considering only one accelerometer, verifying the method's effectiveness by considering the robustness, installation location, and truncation error [29].

Deep Learning (DL) is a subset of ML inspired by the work of neurons in a brain. DL makes a multi-layer neural network computation to perform this task [30]. CNN is a part of DL that works by analyzing visual imagery. CNN is the ML method used in this study. CNN is a tool for solving the problem of pattern recognition related to image and video recognition, classification, natural language processing, and others. An overview of CNN as a subset of AI, ML, and DL is shown in Figure 2.1.

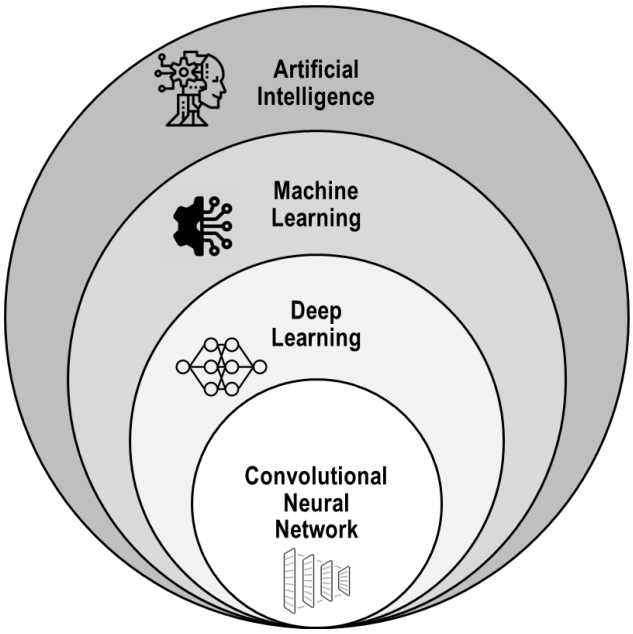

Figure 2.1. Overview of CNN as a subset of AI, ML and DL.

Oh et al. studied a method of predicting the time histories of displacement of building structures from the measured acceleration responses on each floor based on a CNN, considering that the time series of structural acceleration response is similar to pixel-based image data (every acceleration value corresponds to one pixel), which is the basic input data in CNN [31]. Their proposed method was validated from a numerical process using the ASCE benchmark model and an experimental test on a reinforced concrete frame structure. However, the structural model and dynamic responses used in the studies exhibited linear behavior. Tsuchimoto et al. proposed a rapid safety evaluation of multi-story buildings using sparse acceleration measurements [23]. Their proposed method predicts the maximum story drift ratio. It ultimately classifies the damage into three classes, namely "Safe", "Restricted Use", and "Unsafe" from a damage-sensitive feature (comparison between linear and nonlinear acceleration measurement responses) and ground acceleration as input data. Subsequently, Tsuchimoto et al. modified the previous method for high-rise buildings and validated considering an experimental test of a large-scale structure (1/3-scale 18-story steel building tested on the shaking table at E-Defense in Japan) [32]. Since CNN can manage a large amount of data through the pixels of the images, its accuracy is commonly higher than that of other ML methods. For example, Hasan et al. developed a comparative analysis to classify vegetation species using three ML methods: the support vector machine (SVM), artificial neural network (ANN), and CNN, and the accuracy obtained was 91%, 94%, and 99%, respectively [33]. Keeling et al. compared CNN with ML methods for text classification, including Logistic Regression, SVM, and Random Forest. The precision rate of 75% showed that CNN performs slightly better than others on average [34]. Jiang et al. compared the performance in image classification of capsule network (CapsNet), CNN, and fully convolutional network (FCN) methods, concluding in general that the CNN and FCN models obtained a better performance than CapsNet [35].

There are two main characteristics observed on the ground motion records due to earthquakes. The first is the non-stationary characteristics in which the intensity of the ground motion varies with time; they are represented by the acceleration, velocity, and displacement. The second is the non-stationary characteristics in which the frequency content of the ground motion varies with time; they depend on several parameters such as magnitude, source and path effects, local site conditions, etc. [36]. Time–frequency distribution analysis is a method of obtaining a two-dimensional spectral function (there are several types of functions according to resources and needs) from a one-dimensional signal (ground motion or time–history structural response) that reflects the time and frequency of the original signal and is suitable to analyze the changes in the linear and non-linear structural responses with only one function. For instance, Tao et al. used the

matching pursuit decomposition algorithm to analyze the time–frequency distribution of the ground motion and verify the effect on the dynamic response of a nonlinear structure, and finally, this method reveals the effect of the ground motion on the nonlinear structural response [37]. Moreover, Cao et al. demonstrated the effect of energy concentration on the structural nonlinear response by using the wavelet transform to obtain a local spectrum and change the energy distribution over time for several earthquake records [38]. Spanos et al. analyzed the undamaged and damaged condition of a 20-story steel frame building using the harmonic wavelet transform applied to structural responses to obtain the variation of the effective natural frequencies due to the influence of the nonlinearity developed during the seismic event [39]. Balafas and Kiremidjian used the continuous wavelet transform of the input and output acceleration measurements to extract damage sensitive features for seismic damage estimation in civil structures [40]. Noh et al. proposed an ex-traction method of three damage-sensitive features using wavelet transform spectrum for structural damage diagnosis and applied them to experimental data of a reinforced concrete bridge column and a four-story steel moment-resisting frame structure [41]. In general, time–frequency distributions are two-dimensional spectral functions that can be used as input data for a CNN to predict dynamic issues related to structural engineering. For example, Xu et al. proposed a methodology to recognize and classify different types of vibrational events (digging, walking, vehicles passing, and damaging) [42]. First, they de-noise the unknown signal and use the short-time Fourier transform (STFT) to obtain the time–frequency spectra and input them to the CNN for automatic feature extraction and classification. The proposed method used the support vector machine method to compare the obtained recognition rates of vibration events over 90% with the previous soft-max classifier. Dokht et al. used a CNN and STFT to consider a dataset of over 4900 earthquakes recorded over 3 years in Canada to classify between earthquake and noise signals. They also used another CNN and wavelet spectrum to classify and separate P from S waves and estimate their approximate arrival times [43]. Their results achieved an average accuracy of nearly 99% for both networks. Mousavi et al. proposed a detector based on a deep neural network (CNN belongs to this field) called CNN-RNN Earthquake Detector, which is a network that combines a CNN and a recurrent neural network, specifically the bidirectional long-short-term-memory method, to learn the time-frequency characteristics of the dominant phases in an earthquake signal from three-component data recorded at a single station, having an accuracy of 99.95% [44].

Recently, studies have been conducted in the field of structural engineering to develop CNN models that use the time domain responses as input data. For instance, Ghahremani B. et al. used the fast S-transform from the structural acceleration response as an input map of a CNN model [45]. Similarly, Wang X. et al. applied the Hilbert–Huang time–frequency spectrum in a 2D CNN model to identify damage conditions of a benchmark structure [45]. Furthermore, Lu X. et al. developed a CNN-based rapid post-event seismic damage evaluation methodology using the continuous wavelet transform (CWT) to extract the time and frequency features of the ground motion acceleration [24]. Zhang et al. developed a physics-guided convolutional neural network (PhyCNN) for data-driven structural seismic response modeling. The proposed PhyCNN considers the ground motion as input and the structural responses as output data to learn the feature mapping between them [46]. Moreover, Teng S. et al. used the acceleration response in a one-dimensional (1D) CNN followed by a decision-level fusion strategy to improve the accuracy of structural damage detection [47]. Other studies considered more than one structural parameter to increase the features of the input data. Park H. et al. established a CNN-based strain prediction technique that enables structural safety evaluations in cases of the absence or defect of strain sensors. The CNN model used dynamic acceleration and displacement responses as input data to predict the strains of structural members [48]. Xu Y. et al. used 48 intensity measures to represent ground motion characteristics as input data to indicate the damage state of structures [26].

On the other hand, studies have been conducted using frequency domain responses to improve the accuracy of CNN prediction. For example, Oh B.K. et al. built a CNN model using the displacement response, displacement frequency, and the wind speed frequency of tall buildings as input maps to estimate the safety of instrumented columns from their maximum and minimum strains [49]. Additionally, Liu T. et al. used the transmissibility function (ratio of the cross-spectral density and the auto-spectral density of the

response) as input data for a 1D CNN to identify structural damage [50]. In addition, Liao et al. proposed an identification method for a structural seismic response using a wavelet spectrum as input data in a CNN to distinguish the responses during an earthquake event under serviceability conditions [51]. Linear and nonlinear behaviors are considered in the research.

According to previous studies, the CNN method in the SHM field has advantages over other methods in terms of higher accuracy by updating the model after each earthquake, flexibility to combine different methodologies, wide application areas, etc., however, it requires a large database of known data to train the model.

2.3 Research methodology

Figure 2.2 shows two processes for obtaining the trained and validated ML (CNN) model in this methodology. They are called the training process (TP) and the validation process (VP). The records are divided into two parts for each process. 80% of the records are used for the TP and 20% for the VP.

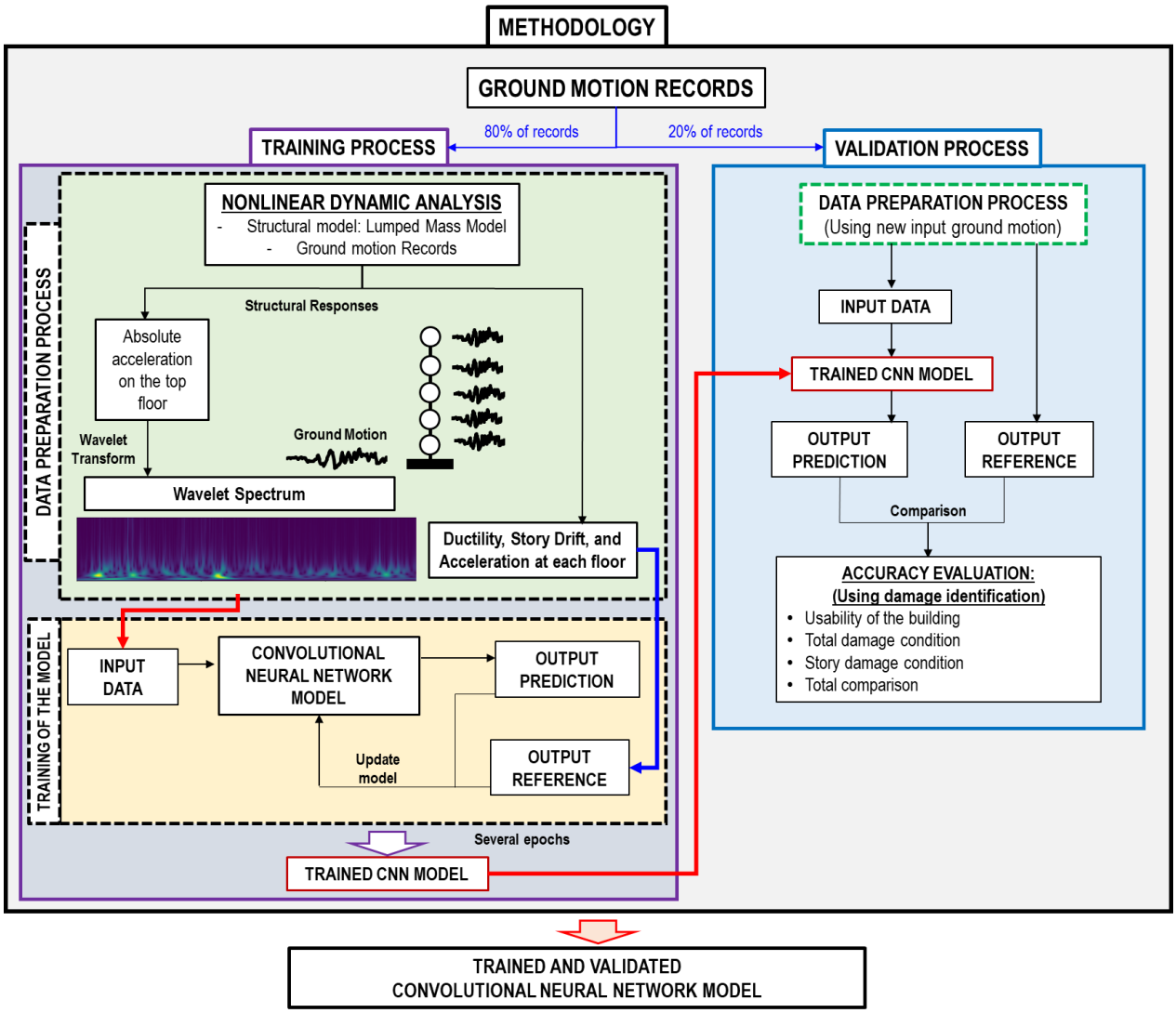

Figure 2.2. Methodology flowchart to obtain the trained and validated CNN model using WS.

The TP has two subprocesses: the data preparation process and the training of the model process. The input data (WS) and the output reference (ductility ratio, story drift ratio, or acceleration on each floor) are obtained from the IDA in the data preparation process. The trained CNN model is obtained in TP and used in the VP.

In the VP, the data preparation process is used in order to predict new input data and output references. Subsequently, the trained CNN model (from the TP) is validated when the highest accuracy is found by comparing it to structural damage identification.

2.4 Structural model, wavelet spectrum, and CNN

2.4.1 Structural model and responses for damage identification

In this study, a lumped mass model (LMM) is considered as the structural model of the building, which takes into account the concentrated mass and the hysteresis model in each story of a low- to mid-rise building as shown in Figure 2.3(a). The structural responses (displacement and acceleration) of each story of the LMM under the ground motion acceleration are obtained by a time history response analysis using the STERA_3D software [52]. The process is shown in Figure 2.3(b).

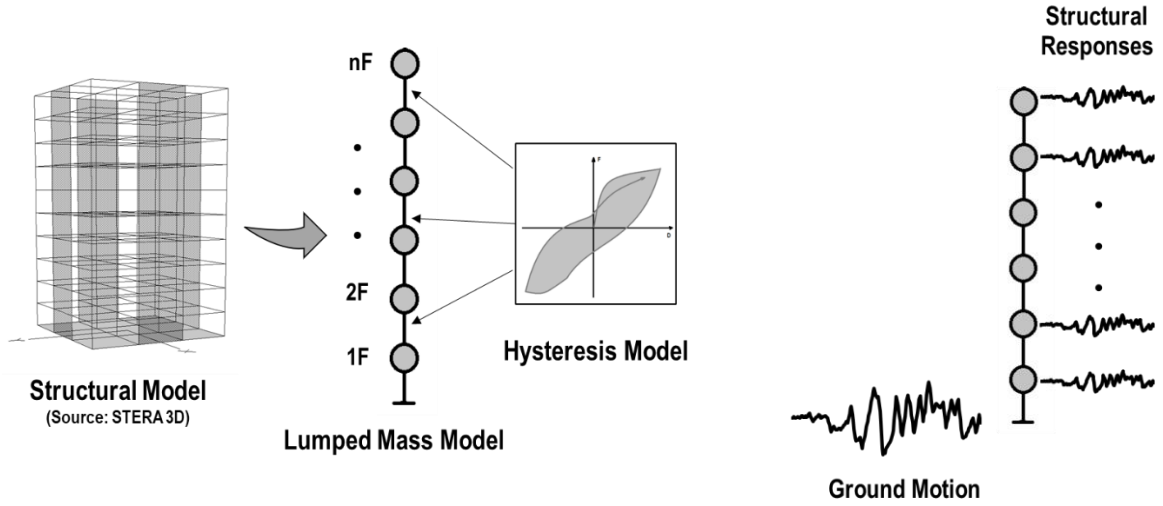

Figure 2.3. Structural model. (a) Lumped mass model; (b) Structural responses from and inelastic time-history structural analysis.

This study identifies the damage condition from each story's ductility, inter-story drift ratio, and acceleration, as shown in Table 1.1.

2.4.2 Wavelet spectrum

Various transformation functions are used to extract the characteristics of a signal. For example, the Fourier transform can be used to obtain the frequency components of a signal, but it cannot capture the changes over time. On the other hand, if the frequency component varies with time, there are methods such as using the instantaneous frequency or the short-time Fourier transform, both of which have the property that the resolution of time and frequency is constant. However, in actual analysis, it is often the case that low frequency components change slowly over time, while high frequency components change rapidly over time. In the wavelet transform, the optimal time and frequency resolution for each component can be obtained by changing the time resolution according to the frequency of the signal component (see Figure 2.4 and Figure 2.5, respectively).

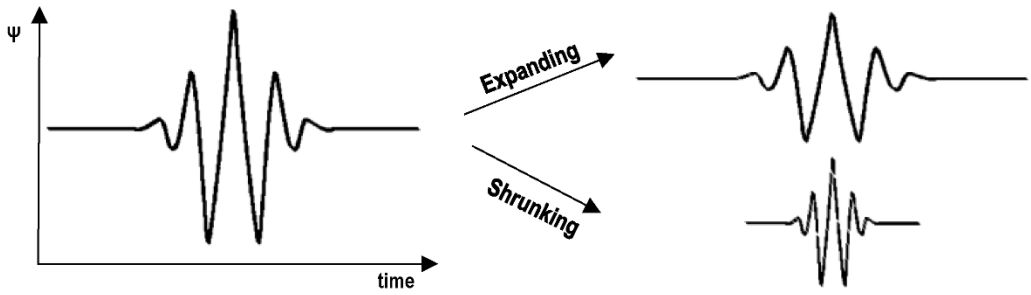

Figure 2.4. Types of dilation of the mother wavelet function.

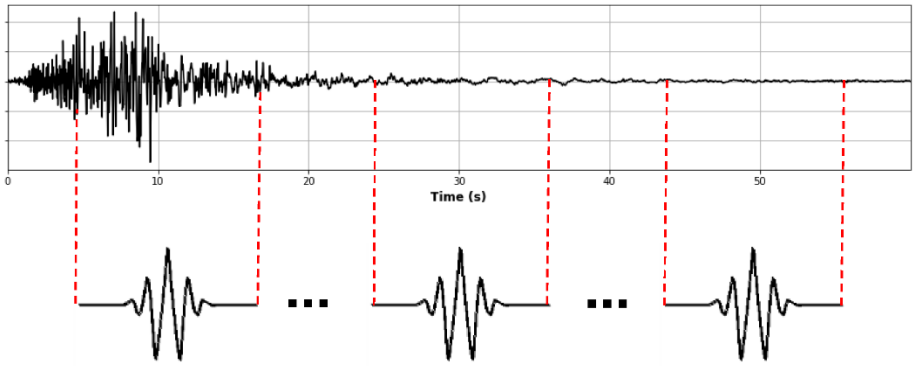

Figure 2.5. Translation of wavelets over time.

Wavelet functions convolute the original signal into a space and scale field. The scale decomposition (related to the frequency domain) is obtained by dilating and shortening the wavelet. On the other hand, space decomposition comes from their variability in time (position) [53,54].

The wavelet signal is called the mother wavelet. The wavelet used in this study is the Morlet wavelet (complex-valued wavelet), which is the product of a sine (complex exponential) wave and a Gaussian envelope, as defined by Equation 2-1[54]:

$$\psi_0(x) = \pi^{-\frac{1}{4}} \cdot e^{-\frac{x^2}{2}} \cdot e^{-i\omega_0 x} \qquad \textit{Equation 2-1}$$

where ω_0 is the nondimensional frequency. In this study, ω_0 is taken to be 6 in order to accomplish the admissibility property, according to [53]. Subsequently, ψ_0 will be normalized to keep constant the total energy when it is scaled. Furthermore, the parameters "a" and "b" are included in the Morlet wavelet in order to modify the scale and space (translation), respectively. The normalized Morlet wavelet is defined by Equation 2-2.

$$\psi\left[\frac{(t-b)\delta t}{a}\right] = \left(\frac{\delta t}{a}\right)^{1/2} \cdot \psi_0\left[\frac{(t-b)\delta t}{a}\right] \qquad \textit{Equation 2-2}$$

The continuous wavelet transform (CWT) of a discrete signal s(t) is defined by Equation 2-3:

$$W(a,b) = \sum_{t=0}^{N-1} s_{(t)} \psi^*\left[\frac{(t-b)\delta t}{a}\right] \qquad \textit{Equation 2-3}$$

where "N" is the number of samples of the signal and the asterisk symbol (*) indicates the complex conjugate of the wavelet.

The continuous wavelet transform (CWT) of a signal s(t) is given by Equation 2-4:

$$W(a,b) = \frac{1}{\sqrt{a}} \int_{-\infty}^{\infty} s(t)\psi^* \left(\frac{t-b}{a}\right) dt \qquad \textit{Equation 2-4}$$

CWT is a complex function because of the Morlet wavelet. Therefore, the module of CWT is the wavelet spectrum (WS), defined by Equation 2-5:

$$WS(t,f) = |W(a,b)| = \sqrt{W_{real}^2 + W_{imaginary}^2} \qquad \textit{Equation 2-5}$$

Therefore, the wavelet transformation permits transformation from a signal to a spectrum (wavelet spectrum) in two dimensions (time and frequency) with coefficients (scales) that represent the intensity of the signal, in the time-domain and frequency-domain. The wavelet spectrum shows the highest intensity of the wave on the time-domain and frequency-domain only in one graph (Figure 2.6b). As a reference, Figure 2.6a shows the acceleration wave, and Figure 2.6c shows a 3D graph of the wavelet spectrum.

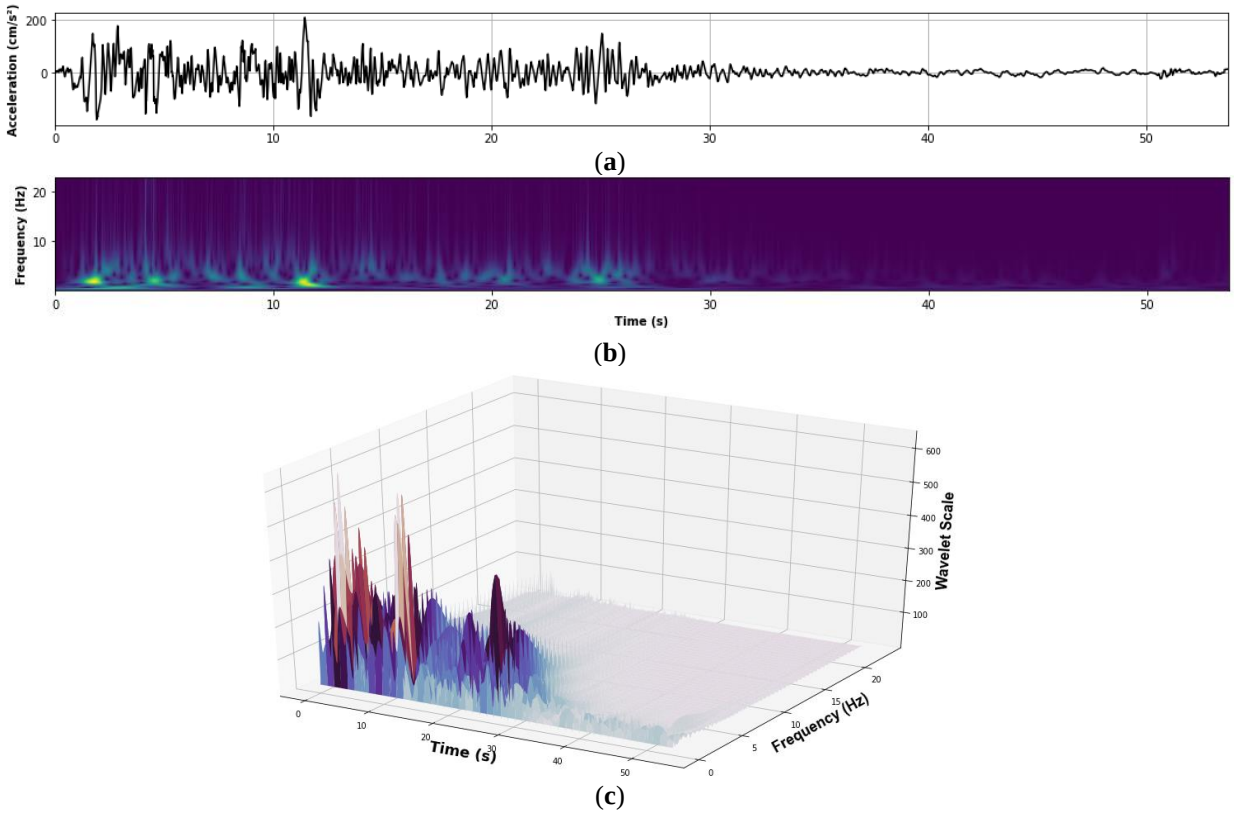

Figure 2.6. Wavelet spectrum (a) Acceleration wave; (b) 2D spectrum; (c) 3D spectrum.

This is a powerful tool for extracting the characteristics of the waveform signals such as response acceleration, velocity, and displacement. Thus, the wavelet spectrum of the acceleration response waveform obtained from the accelerometer installed in the building is computed in this study and used as an input to the CNN model.

2.4.3 Convolutional neural network

An image is processed by a computer as a grayscale image (image from now on) represented by an arrangement of numbers. For example, in Figure 2.7, the right matrix contains numbers between 0 and 255, each of which corresponds to the pixel brightness in the left image [55].

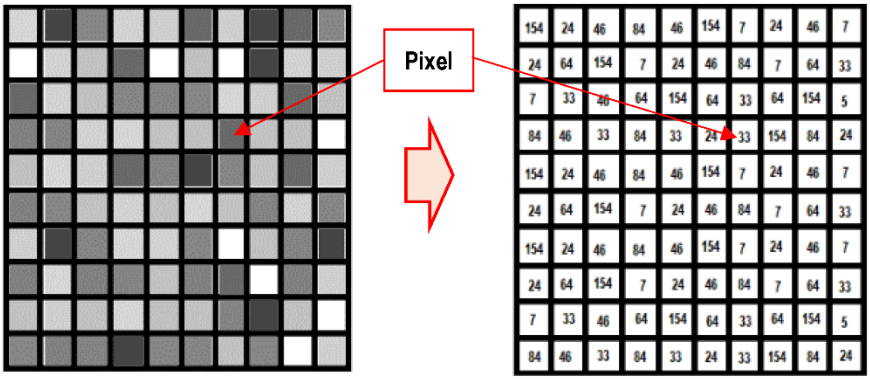

Figure 2.7. Digital image by an arrangement of pixels represented as numbers.

The convolution of the input image is performed by applying a set of weights, also known as a kernel or filter, as shown in Figure 2.8 [56].

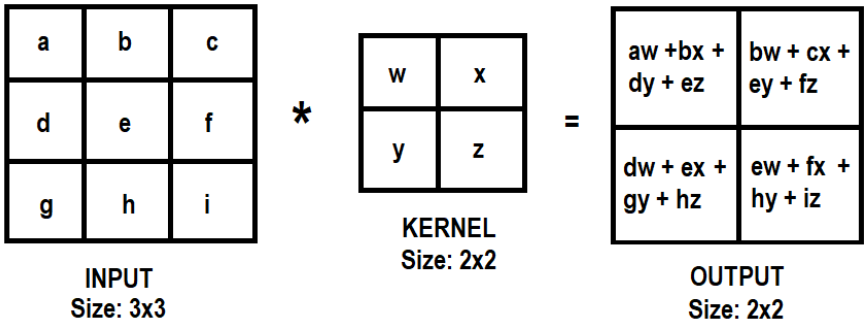

Figure 2.8. Convolution process of a part of an image by matrix multiplication (the symbol (*) means the convolution operator.)

A convolutional process is a mathematical operation of two functions. The functions used in CNN are arrays of data. The set of images is the first array, and the second is a set of filters used to extract and learn the main features of the first one. They are called kernels (K) or feature detectors. Since CNN is part of the ANN, a kernel is a set of updatable weights for the training process of the CNN model.

According to the prediction project, CNN uses one-, two-, or three-dimensional space. This study used a two-dimensional space. Equation 2-6 defines the convolutional operation in CNN [57]:

$$FM_{(a,b)} = (Img * K)_{(a,b)} = \sum_{c}\sum_{d} K_{(c,d)} \cdot Img_{(a-c,b-d)} \qquad \textit{Equation 2-6}$$

where FM is the feature map, Img is the image used as input data, and K is the kernel array. In this study, CNN uses the images obtained from the WS.

In the CNN method, images are used as input data, and for every input data set, the features of the input data are extracted by the convolution of the kernels. However, this convolution step loses information that might exist on the border of the image because they are only captured when the kernel slides (the kernel must start and finish its process on the image borders) [58]. For this reason, the size of the input image is reduced as shown in Figure 2.8 (from input size: 3 × 3 to output size: 2 × 2). In order to obtain the same size as the original input, it is possible to apply the “same padding”, also called “zero-padding”, method (used in this study), which means the input is filled with zeros along its border as shown in Figure 2.9.

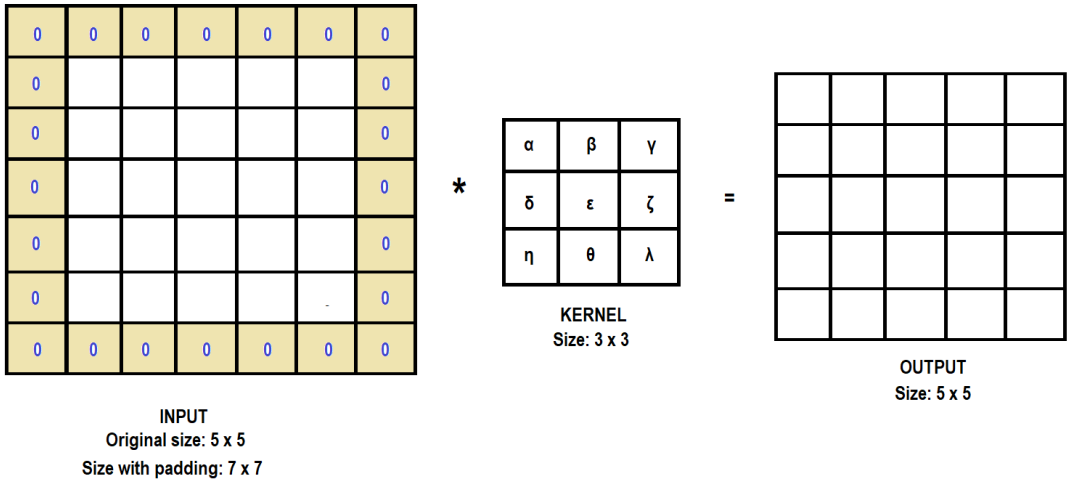

Figure 2.9. Same padding method.

Then, every resultant matrix is evaluated by a nonlinear activation function to allow for the learning of more complex models. The nonlinear activation function (activation function from now on) used in this study is the rectified linear unit (ReLU), defined as the function Y = max(X, 0) [57], defined by Equation 2-7 and shown in Figure 2.10:

$$y = \begin{cases} 0, & if\ x < 0 \\ x, & if\ x \geq 0 \end{cases} \qquad \textit{Equation 2-7}$$

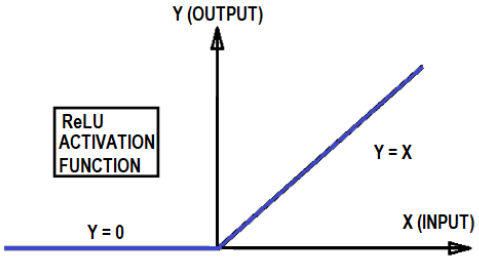

Figure 2.10. ReLU activation function.

Finally, the new input data, the feature maps, are obtained. The process from the input data to the feature maps using the previous definitions is called the typical convolutional layer and is formed from the convolutional process, padding, and activation function methods, as shown in Figure 2.11. and Figure 2.12.

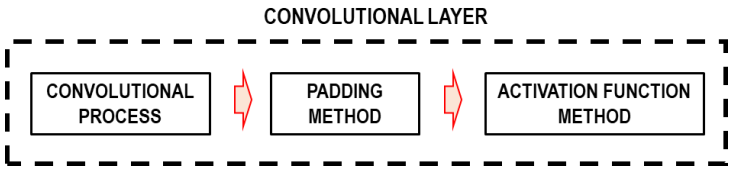

Figure 2.11. Typical convolutional layer.

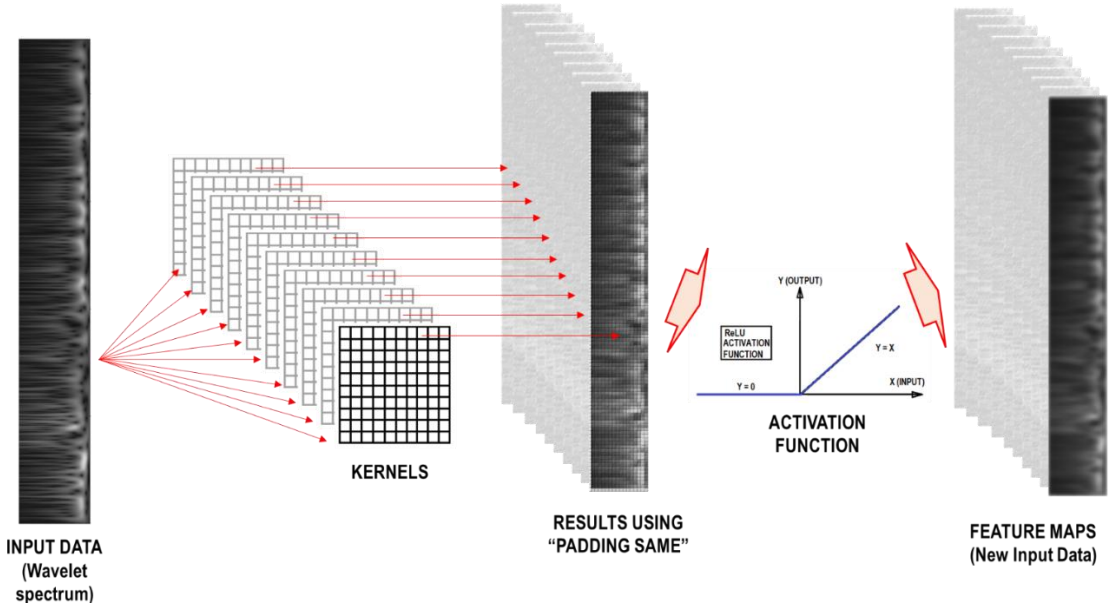

Figure 2.12. Typical convolutional layer.

The typical convolutional layer is followed by a pooling layer to reduce the number of operations since the number of parameters increases as the network processes more kernels. A type of pooling layer is the "maximum pooling" or "max pooling" process, which takes the maximum value sliding along the feature map [55], as shown in Figure 2.13 .

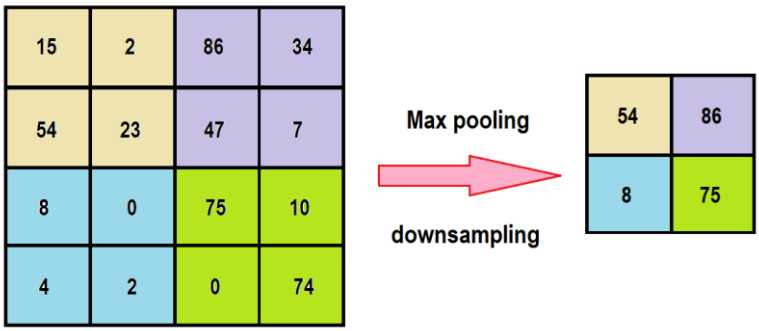

Figure 2.13. Maximum pooling process.

The pooling layer is required for image classification. It adjusts the features' robust-ness to noise and disorder by reducing the resolution of the previous feature maps [57]. Since the pooling layer reduces the resolution and sizes of the feature maps, it results in a lower computational cost. Moreover, a hierarchical architecture is used in advance to propose the number of convolutional layers for the CNN architecture model [59].

Subsequently, the last convolutional layer is fully connected to the 1D layer or the flattening layer [57] (matrix of one column) as shown in Figure 2.15. This layer is connected to the dense layer, which provides the predicting results. In order to optimize the convergence and measure the error between the predicted and reference output, "Adam" [60] and mean squared error (MSE) are used as the optimizer function and the loss function. Equation 2-8 defines MSE, where y_{pred} is the prediction output, y_{ref} is the reference output, and N is the number of samples, in an iterative process.

$$MSE = \frac{1}{N} \cdot \sum_{i=1}^{N} (y_{pred} - y_{ref})^2, \qquad \textit{Equation 2-8}$$

The criteria of the error measure could be modified in order to improve the forecasting accuracy [61]. The predicted results are the structural responses of each story of the target building. As mentioned, the structural responses are used as damage indicators.

Figure 2.14 shows a general CNN model. The input, convolutional, pooling, and fully connected layers compose the architecture of the CNN model. Each target building has a particular CNN model architecture, which depends on its accuracy after evaluation.

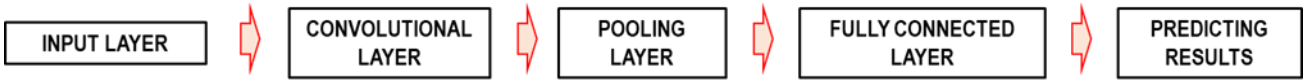

Figure 2.14. A general CNN model.

In this study, after several trainings, 17 convolutional layers are finally used in the proposed CNN model. Moreover, the models with and without the maximum pooling layer were trained, and the model without the maximum pooling layer converged on the output prediction more effectively. Therefore, the pooling layer is not used in the proposed CNN model. Also, the flattening matrix contains structural responses for the damage identification, which can be the ductility ratio, story drift ratio, and acceleration. Figure 2.15 shows the CNN scheme used in this research.

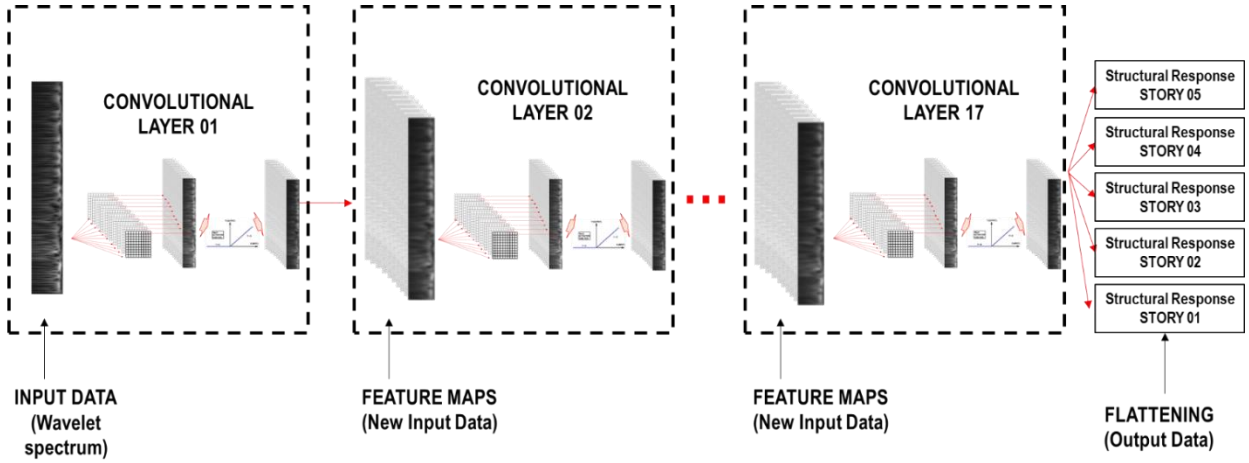

Figure 2.15. Convolutional neural network scheme. Structural response: ductility ratio, story drift ratio, or acceleration.

Table 2.1 shows the architecture of the CNN for the structural response prediction method. This was finalized by extensive analysis of trained CNNs in advance. In Table 2.1, "N° kernels" is the number of filters or kernels assigned in each layer. Ten different kernels are used for the first layer and eight kernels are used for the other layers. Two types of kernel initializer are used in this study. "He_Normal" is used for the first four convolutional layers and "glorot_uniform" is used for the rest of the others. The kernel size is 10 x 10 for the first convolutional layer and 3 × 3 for the rest. The "same padding" and ReLU activation function are used in all convolutional layers.

Table 2.1. CNN architecture for the structural response prediction method.

N° of Layer	N° Kernels	Kernel Size	Padding	Kernel Initializer	Activation Function
Convolutional Layer 01	10	10 × 10	Same	He Normal	ReLU
Convolutional Layer 02	8	3 × 3	Same	He Normal	ReLU
Convolutional Layer 03	8	3 × 3	Same	He Normal	ReLU
Convolutional Layer 04	8	3 × 3	Same	He Normal	ReLU
Convolutional Layer 05	8	3 × 3	Same	glorot_uniform	ReLU
Convolutional Layer 06	8	3 × 3	Same	glorot_uniform	ReLU
Convolutional Layer 07	8	3 × 3	Same	glorot_uniform	ReLU
Convolutional Layer 08	8	3 × 3	Same	glorot_uniform	ReLU
Convolutional Layer 09	8	3 × 3	Same	glorot_uniform	ReLU
Convolutional Layer 10	8	3 × 3	Same	glorot_uniform	ReLU
Convolutional Layer 11	8	3 × 3	Same	glorot_uniform	ReLU
Convolutional Layer 12	8	3 × 3	Same	glorot_uniform	ReLU
Convolutional Layer 13	8	3 × 3	Same	glorot_uniform	ReLU
Convolutional Layer 14	8	3 × 3	Same	glorot_uniform	ReLU
Convolutional Layer 15	8	3 × 3	Same	glorot_uniform	ReLU
Convolutional Layer 16	8	3 × 3	Same	glorot_uniform	ReLU
Convolutional Layer 17	8	3 × 3	Same	glorot_uniform	ReLU

Figure 2.16 shows the convergence curve of the CNN model using the CNN architecture shown in Table 2.1, where "Loss" is the value of the loss function, and "Number of epochs" is the number of training iterations over the input data [56].

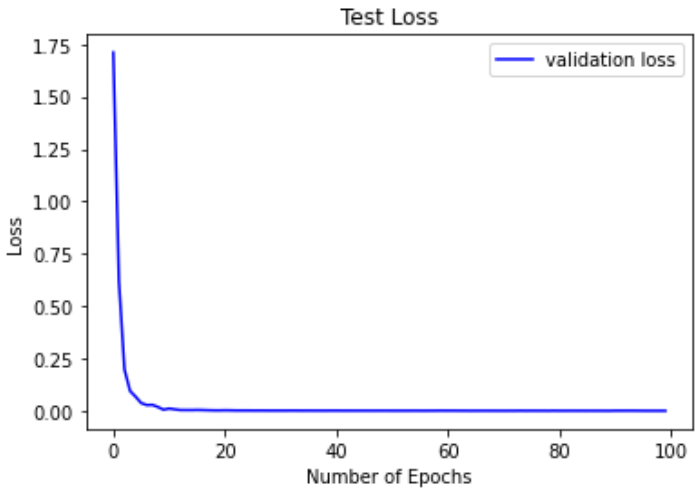

Figure 2.16. Converge curve of the trained CNN.

Firstly, the CNN model is trained with known input and output data. This is called the "training process". Subsequently, new unknown input data are used to validate the trained CNN model by comparing the output data (structural responses for damage identification) with the reference structural responses. This process is called the "validation process" and the MSE function is used to evaluate the error.

2.5 Case study and input ground motion

2.5.1 Case study

The case study is a building of five stories with the following considerations (see Table 2.2 for more details):

- The fundamental period is considered the following: T1 = 0.025 H (H: total height of the building). The height of each story (h) is 4.0 m, then, H is 20 m and T1 is 0.5 s.

- LMM is used for the model of the building, and the bilinear hysteresis model (see Figure 2.17) is used to represent the nonlinear relationship between shear force and story drift for each story.
- The structural responses for damage identification (ductility ratio, story drift ratio, and acceleration) under earthquake ground motions are calculated by STERA 3D software [52].

Table 2.2. Structural configuration of the case study.

Description	Nomenclature (Units)	Value
Number of stories	N	5
Story height	h (m)	4
Building height	H (m) = h × N	20
Width	B (m)	30
Area of floor	$A = B^2$ (m^2)	900
Weight per floor area	w (kN/m^2)	12
Weight of floor	W (kN)	1080
Fundamental Period	T_1 (s)	0.5

In order to build the bilinear hysteresis model, the yielding shear force (Qi) is calculated to be equal to the design shear force under the horizontal seismic load according to Japanese code. Moreover, the story stiffness (ki) is calculated so that the first mode shape becomes a triangular shape. Table 2.3 shows the parameters used in this study to define the bilinear hysteresis model in each story. The post-yield stiffness ratio (k2/k1, see Figure 2.17) is 0.1 for each story.

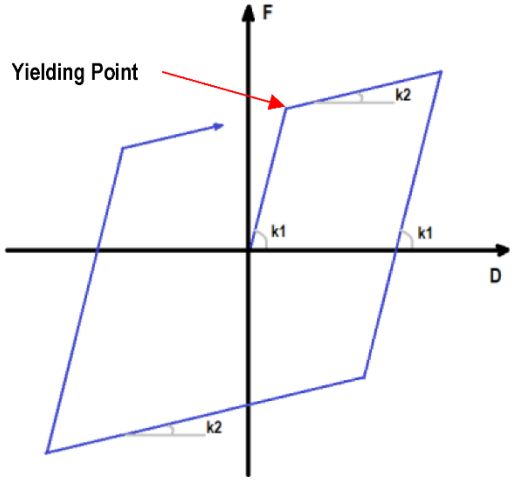

Figure 2.17. Bilinear hysteresis model for each story.

Table 2.3. Parameters of the bilinear hysteresis model used in the case study.

Story	ki (kN/mm)	Qi (kN)
5	87	587.87
4	157	954.15
3	209	1240.66
2	244	1460.87
1	261	1620.00

2.5.2 Input ground motion

Table 2.4 shows the 25 earthquake ground motions considered in this study. Every earthquake contains two directions (E–W and N–S). Consequently, the total number of records used is 50. As mentioned, there are two processes in the CNN method—the training and the validation processes. For this reason, the records are subdivided into two groups. The number of records for the training is 40 (20 earthquakes) and the number of records for the validation is 10 (5 earthquakes). This obeys the split ratio recommended for typical CNN procedures (80% training records and 20% validation records). The earthquakes are selected

randomly to avoid extracting the same characteristics between different records. Figure 2.18 shows the acceleration response spectrum of the 50 records scaled to have the same values at the fundamental period of the structure (T1 = 0.5 s) as Sa (T1) = 100 gal.

Table 2.4. Earthquake ground motions.

N°	Name	Location	Station Reference	Magnitude	Date
	Training Process *				
01	Anza_01	USA	33.706N, 116.235W/Ground Floor: South Wing	Mw = 5.2	12/06/2005
02	Anza_02	USA	33.706N, 116.235W/Roof: Center Hallway of S. Wing	Mw = 5.2	12/06/2005
03	El Centro 1940	USA	Imperial Valley Earthquake	Mw = 6.9	18/05/1940
04	Kobe 1995	Japan	Great Hanshin Earthquake/Kobe Marine Observatory	Mw = 6.9	17/01/1995
05	Loma Prieta_01	USA	36.974N, 121.952W/Capitola—Fire Station	Ms = 7.1	18/10/1989
06	Loma Prieta_02	USA	36.973N, 121.572W/Gilroy #1—Gavilan College	Ms = 7.1	18/10/1989
07	Loma Prieta_03	USA	36.987N, 121.536W/Gilroy #3—Gilroy Sewage Plant	Ms = 7.1	18/10/1989
08	Loma Prieta_04	USA	37.046N, 121.803W/Corralitos—Eureka Canyon Rd.	Ms = 7.1	18/10/1989
09	Loma Prieta_05	USA	37.118N, 121.550W/Coyote Lake Dam	Ms = 7.1	18/10/1989
10	Loma Prieta_06	USA	37.255N, 122.031W/Saratoga—Aloha Ave.	Ms = 7.1	18/10/1989
11	Northridge_01	USA	34.068N, 118.439W/Los Angeles—UCLA Grounds	Mw = 6.7	17/01/1994
12	Northridge_02	USA	34.236N, 118.439W/Arleta—NordHoff Ave. Fire Station	Mw = 6.7	17/01/1994
13	Northridge_03	USA	34.387N, 118.530W/Newhall—LA County Fire Station	Mw = 6.7	17/01/1994
14	Petrolia_01	USA	40.325N, 124.287W/Petrolia	Mw = 7.0	25/04/1992
15	Petrolia_02	USA	40.503N, 124.100W/Rio Dell—101/Painter St. Overpass	Mw = 7.0	25/04/1992
16	Petrolia Aftershock_01	USA	40.325N, 124.287W/Petrolia/04/26/92, 07:41:40 UTC	Ms = 6.6	26/04/1992
17	Petrolia Aftershock_02	USA	40.325N, 124.287W/Petrolia/04/26/92, 11:18:25 UTC	Ms = 6.6	26/04/1992
18	Petrolia Aftershock_03	USA	40.026N, 124.069W/Shelter Cove—Airport	Ms = 6.6	26/04/1992
19	Whittier_01	USA	34.037N, 118.178W/Los Angeles—Obregon Park	Ml = 6.1	01/10/1987
20	Whittier_02	USA	34.160N, 118.534W/Tarzana—Cedar Hill Nursery	Ml = 6.1	01/10/1987
	Validation Process *				
21	Palm Springs	USA	33.962N, 116.509W/Desert Hot Springs	Ml = 6.1	08/07/1986
22	Petrolia California	USA	40.325N, 124.287W/Petrolia	Ml = 5.9	17/08/1991
23	Taft 1952	USA	Kern County, California Earthquake	Mw = 7.3	21/07/1952
24	Tohoku 1978	Japan	Miyagi Earthquake/Recorded at Tohoku University	Ms = 7.7	12/06/1978
25	Westmorland	USA	33.037N, 115.623W/Westmorland	Ml = 6.0	26/04/1981

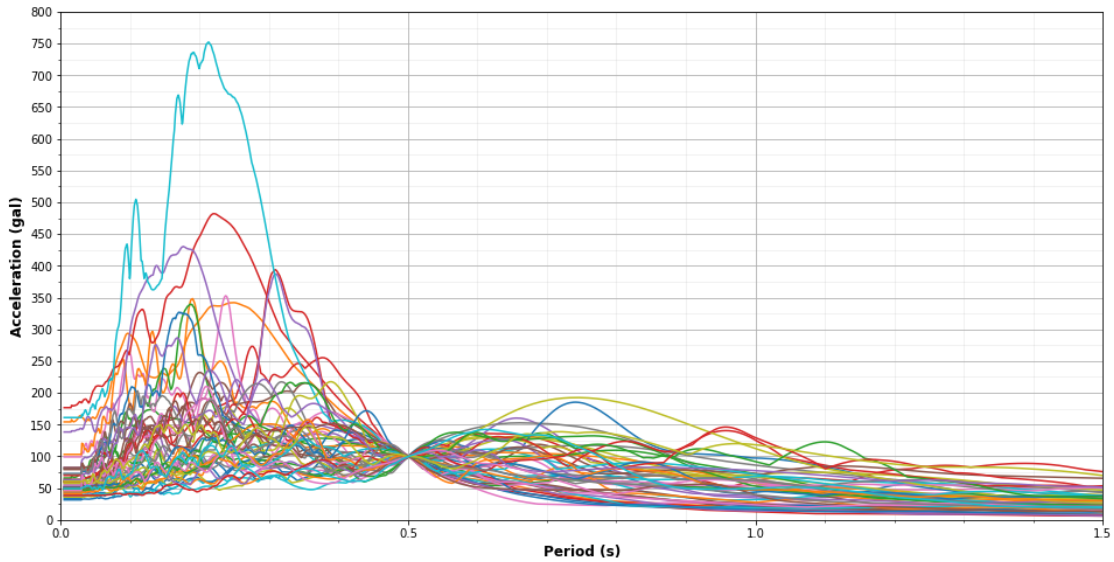

Figure 2.18. Acceleration response spectrum of 50 records scaled to have the same values at the fundamental period T1 = 0.5 s.

2.5.2.1 Scale factor of records

The linear and nonlinear behavior of the structure is obtained by using different in-tensities of earthquake ground motions. Thus, the records are scaled to include a wide range of earthquake intensity. In order to evaluate the range of the scale factors, an incremental dynamic analysis with the structural responses for damage identification is conducted by taking into account the variation of the Peak Ground Acceleration (PGA), and the ordinate of the response acceleration spectrum evaluated on the fundamental period of the structure (Sa(T1)).

Figure 2.19 presents the incremental structural responses for damage identification (ductility ratio, story drift ratio, and acceleration) in each story for the input ground motion “El Centro 1940” (Figure 2.19a) and “Northridge” (Figure 2.19b) using the same scale factor applied to Sa(T1) such that the minimum scale factor produces Sa(T1) = 100 gals and the maximum scale factor produces Sa(T1) = 1500 gals. Figure 2.19a shows the structural response under the maximum PGA of El Centro up to 500 gals. As shown in Figure 2.19b, the maximum PGA of Northridge must be around 1000 gals to achieve the same degree of response. Furthermore, the PGA of the threshold of the nonlinear behavior is around 150 gals in Figure 2.19a (El Centro) and 250 gals in Figure 2.19b (Northridge). On the other hand, the relationship between the responses and Sa(T1) is roughly the same in Figure 2.19a (El Centro 1940) and Figure 2.19b (Northridge). Therefore, the Sa(T1) is more stable for characterizing the structural response of the structure. For this reason, the scale factor is based on Sa(T1) such that the minimum scale factor produces Sa(T1) = 100 gals, and the maximum scale factor produces Sa(T1) = 1500 gals and Sa(T1) = 1000 gals to train and validate the CNN model, respectively. Figure 2.20 shows the Acceleration Response Spectra of the “Loma Prieta” input ground motion considering the minimum and maximum scale factor and the original value.

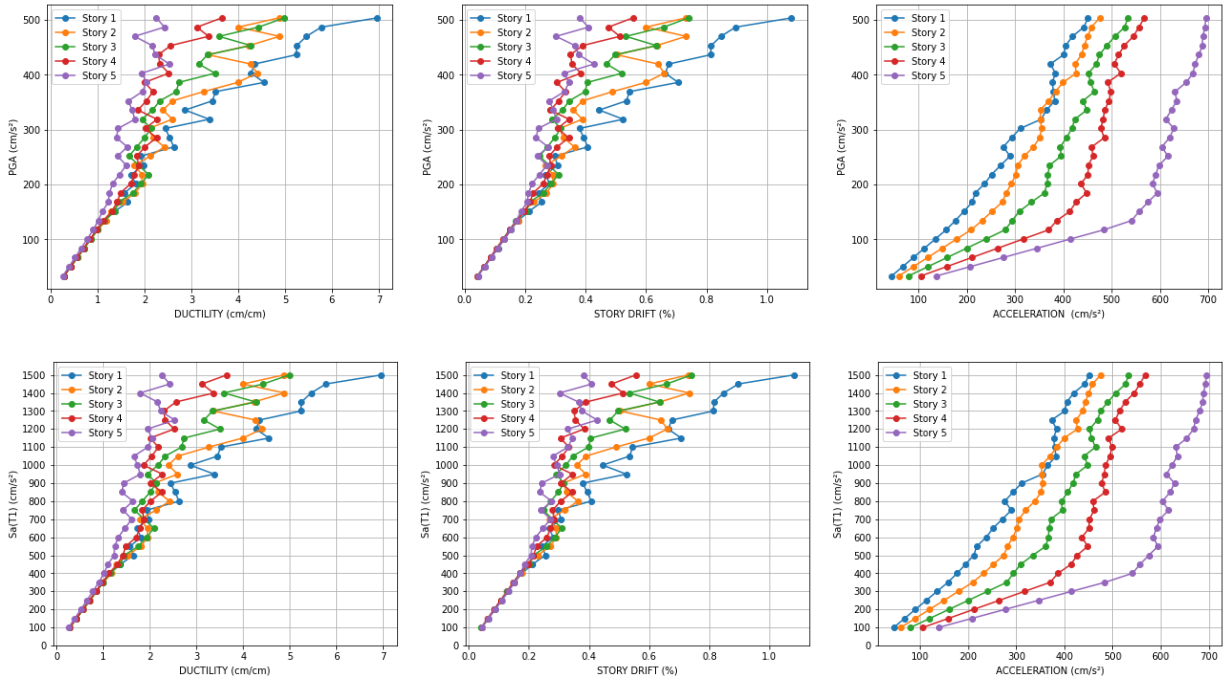

(a)

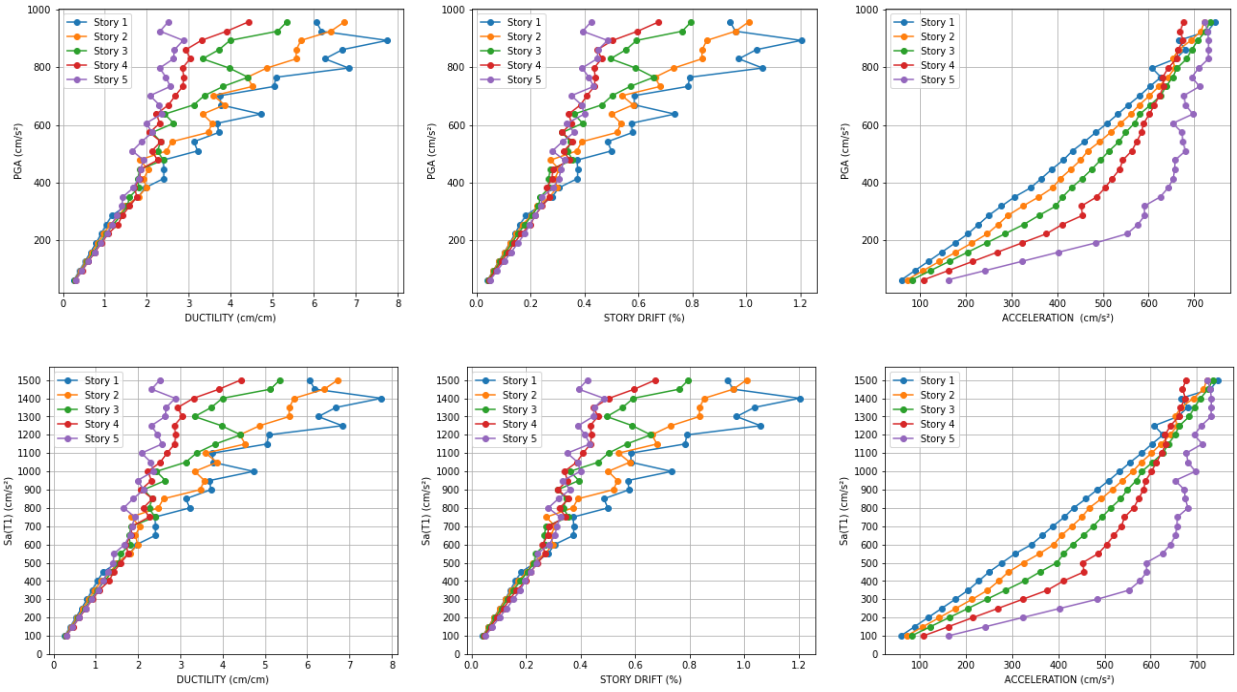

(b)

Figure 2.19. Incremental structural responses for damage identification in each story (a) "El Centro 1940" input ground motion; (b) "Northridge" input ground motion.

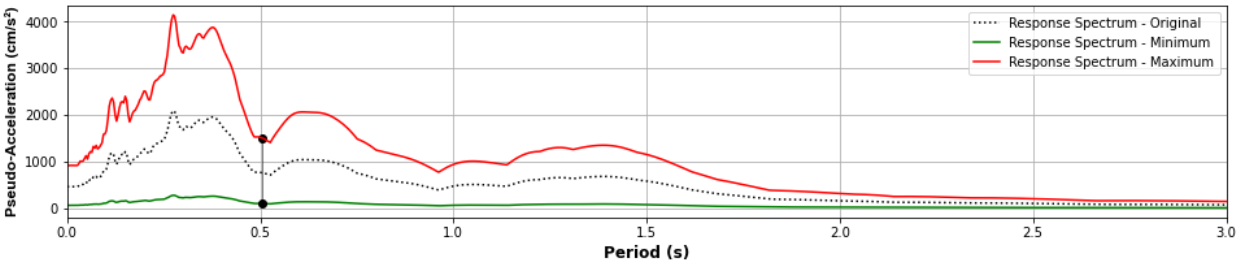

Figure 2.20. Acceleration response spectra of the "Loma Prieta" input ground motion (the red line is with the maximum scale factor such that it produces Sa(T1) = 1500 gal, the green line is with the minimum scale factor such that it produces Sa(T1) = 100 gal, and the black dashed line considers the original input ground motion.)

2.6 Machine learning methodology

The methodology for predicting the structural responses for damage identification was as follows:

- The wavelet spectrum was obtained from the time–history acceleration response on the upper floor of the building. The frequency range was from 0.1/T1 to 5/T1, where T1 is the fundamental period of the case study structure (T1 = 0.5s), which is from 0.2 Hz to 10 Hz. This covered the high and low frequencies produced during high mode vibrations and nonlinear frequencies.
- There were two sets of scale factors for the training and validation of CNN processes.
- The training scale factor set was the minimum scale factor, which produces Sa(T1) = 100 gal, to the maximum, which produces Sa(T1) = 1500 gal, at increments of 50 gal.
- The validation scale factor set was the minimum scale factor, which produces Sa(T1) = 100 gal, to the maximum, which produces Sa(T1) = 1000 gal, at increments of 25 gal.
- There were 1160 structural analyses conducted for the training process by considering 40 records with 29 scale factors, while there were 370 structural analyses conducted for the validation process by considering 10 new records with 37 scale factors. Therefore, 1530 structural analyses carried out were used in this study.

The application of the methodology to predict the structural responses for damage identification was conducted as follows:

TRAINING PROCESS

- STEP 01: 40 training records are scaled with 29 scale factors per record. As a result, 1160 scaled records are generated.
- STEP 02: 1160 structural analyses are carried out for the structural model of the case study. As a result, 1160 absolute acceleration data on the upper floor are obtained. Additionally, the responses for damage identification (ductility ratio, story drift, and acceleration) are computed from the structural analyses for validating and calibrating the CNN model.
- STEP 03: 1160 wavelet spectra are obtained from the absolute acceleration of the previous step. The wavelet spectra are the input data for training the CNN model.
- STEP 04: The CNN model is trained for each structural response for damage identification (ductility ratio, story drift ratio, and acceleration).

VALIDATION PROCESS

- STEP 01: 10 validation records are scaled with 37 scale factors per record. As a result, 570 scaled records are generated.
- STEP 02: 370 structural analyses are carried out for the structural model of the case study. As a result, 370 absolute acceleration data on the upper floor are obtained. Additionally, the responses for damage identification (ductility ratio, story drift, and acceleration) are computed as reference outputs to validate the prediction.
- STEP 03: 370 wavelet spectra are obtained from the absolute acceleration of the previous step. The wavelet spectra are the input data for predicting the structural response for the damage identification using the trained CNN model.
- STEP 04: Prediction outputs are calculated using the CNN model for each structural response for damage identification (ductility ratio, story drift ratio, and acceleration).
- STEP 05: The reference and prediction outputs are compared.

2.7 Prediction and validation of the case study

An example of the analysis results is shown in Figure 2.21. Figure 2.21a shows the ductility ratio results under the scaled Petrolia California E–W records, comparing the prediction (horizontal axis) and the reference (vertical axis). In the figure, the straight line represents the perfect prediction. The points represent the results of each story and scale factor defined in Sections 2.1 and 2.4. Additionally, Figure 2.21a shows the regions that define the damage condition. The green, yellow, orange, and red regions represent the no damage, minor damage, significant damage, and severe damage conditions, respectively. The collapse condition is considered for any value greater than the severe damage condition. The dashed red rectangle encloses the region for any value that is greater than the minor damage condition and means that the use of the building is restricted or unsafe (condition for evacuating the building). Figure 2.21b shows an example of the prediction and reference values of each story for a scale factor that produces Sa(T1) = 900 gal.

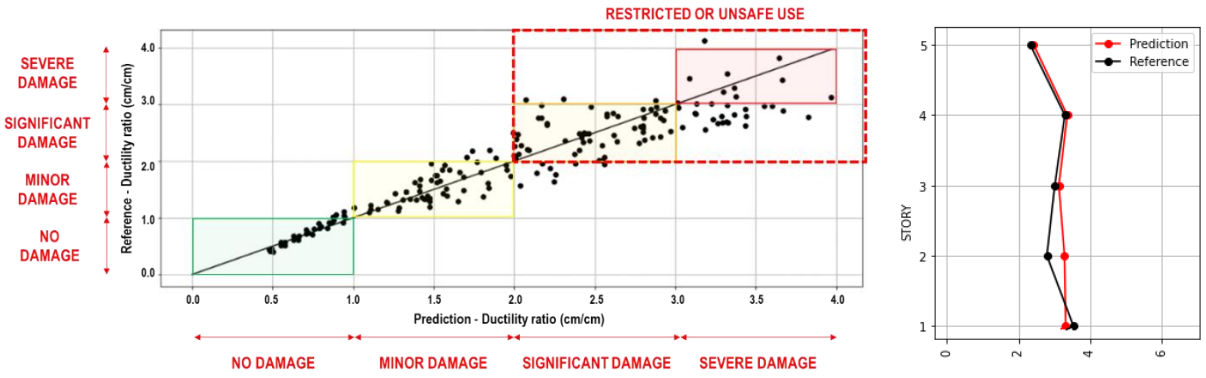

(**a**) (**b**)

Figure 2.21. Example of the ductility ratio results (Petrolia California E–W record); (a) Comparison between prediction and reference values (points) and damage condition regions; (b) Prediction and reference ductility ratio of each story for a scale factor that produces Sa(T1) = 900 gal.

Figure 2.22 shows the results of the ductility ratio, story drift ratio, and acceleration for the validation process under the scaled Petrolia California N–S records. The regions that define the damage condition are also shown in the figure. As seen in Figure 2.22b, the story drift ratios do not reach the significant damage, severe damage, and collapse condition. Likewise, the restricted or unsafe use condition is not reached.

Figure 2.23 shows the prediction and reference values of the ductility ratio, story drift ratio, and acceleration on each floor considered under the same record for a scale factor that produces Sa(T1) = 875 gal.

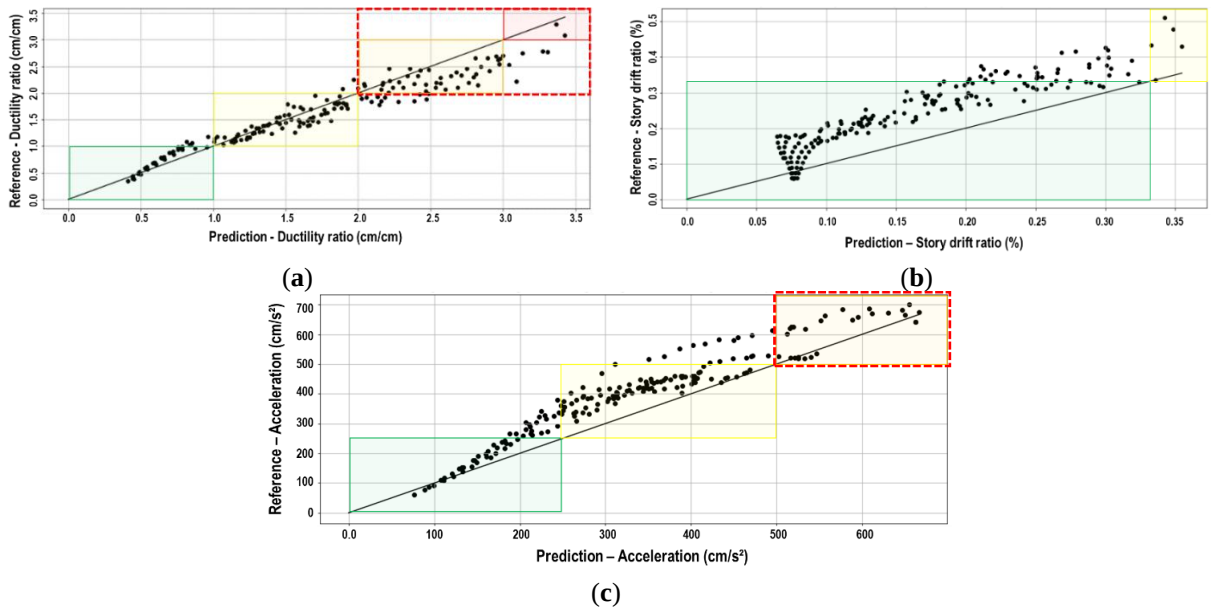

Figure 2.22. Comparison between reference and prediction of the Petrolia California N–S record for the validation process of (a) Ductility ratio; (b) Story drift ratio, and (c) Acceleration.

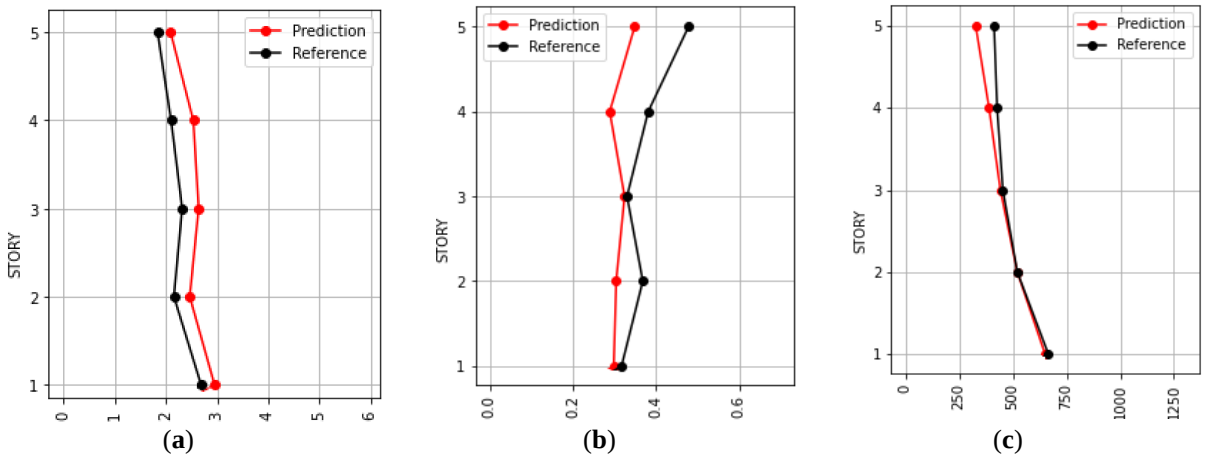

Figure 2.23. Prediction and reference values on each floor of the Petrolia California N–S record and scale factor that produces Sa(T1) = 875 gal for the validation process of (a) Ductility ratio; (b) Story drift ratio, and (c) Acceleration.

The coefficient of correlation (r) is used to measure the accuracy of the CNN model in this study, and it is defined as shown in Equation 2-9:

$$r = \frac{\frac{1}{N} \cdot \sum_i^N (y_{pred,i} - \overline{y_{pred}})(y_{ref,i} - \overline{y_{ref}})}{\sqrt{\frac{1}{N} \cdot \sum_i^N (y_{pred,i} - \overline{y_{pred}})^2} \cdot \sqrt{\frac{1}{N} \cdot \sum_i^N (y_{ref,i} - \overline{y_{ref}})^2}} \qquad \textit{Equation 2-9}$$

where y_{pred} is the prediction output by the CNN model, y_{ref} is the reference output by the structural analysis, ($\overline{y_{pred}}$) and ($\overline{y_{ref}}$) are the mean of y_{pred} and y_{ref}, respectively, and N is the number of samples. Table 2.5 shows the r-values for the validation process. The average values of the r-values of the ductility ratio, story drift ratio, and acceleration are 0.905, 0.846, and 0.829, respectively. In particular, the accuracy of the estimation of the ductility ratio is the highest.

Table 2.5. Coefficient of correlation for the validation process.

N°	Record	Ductility Ratio	Story Drift Ratio	Acceleration
01	Palm Springs E–W	0.953	0.947	0.928
02	Palm Springs N–S	0.895	0.917	0.951
03	Petrolia California E–W	0.933	0.845	0.873
04	Petrolia California N–S	0.972	0.926	0.956
05	Taft 1952 E–W	0.872	0.771	0.417
06	Taft 1952 N–S	0.806	0.848	0.870
07	Tohoku 1978 E–W	0.833	0.466	0.562
08	Tohoku 1978 N–S	0.943	0.890	0.797
09	Westmorland E–W	0.925	0.969	0.985
10	Westmorland N–S	0.916	0.883	0.950
	Average	0.905	0.846	0.829

2.8 Conclusions and discussion

In this study, a methodology is proposed to estimate the damage of a building by applying a machine learning method from the acceleration response on the upper floor of the building. The results of this research are summarized as follows:

- The maximum ductility factor, inter-story drift ratio, and maximum response acceleration of each floor were predicted via a CNN model using the acceleration record at the upper floor of the building.
- The wavelet spectrum of the acceleration record of the upper floor of the building was used as the input of the CNN model to account for the non-stationarity of both the amplitude and frequency of the building response.
- A CNN model was trained for the linear to the nonlinear response of a building by in-putting two horizontal components of 20 different earthquake ground motions with varying scales. The trained CNN model was then validated by inputting the two-directional horizontal components of five different earthquake motions to the building with different scales.
- The correlation coefficients between the predicted values and the reference values by the CNN model exceeded 0.8 for all response values, confirming the high accuracy of the model.

The methodology using only the time– and frequency–domain of the sensor response represented by the wavelet spectrum obtains high accuracy for predicting damage conditions. Moreover, the damage condition of the building is possible to detect immediately after the earthquake occurs because the ML is trained and validated beforehand. However, nonlinear structural analysis of Lumped Mass Models does not consume high computation time. Then, evaluating the methodology on three-dimensional frame models where irregularity configurations effects are present is recommended, which will be studied in the next chapter.

Chapter 3. CNN–Based Damage Detection using Wavelet Power Spectra for Three-Dimensional Buildings

3.1 Introduction

Damage condition of buildings immediately after an earthquake is one of the most critical indicators for future government, owners, and stakeholders' decision-making. For example, in order to tackle federal buildings, Mehmet Çelebi from the United States Geological Survey (USGS) reported guidelines for the seismic instrumentation of structures as part of a USA project in 2002 [62]. However, the accuracy of the structural responses depends mainly on the adopted structural model and the type of structural analysis. For example, an LMM is less accurate than a three-dimensional frame model (3D-FM) of high-rise or irregular structural configuration buildings. Nevertheless, the computation time with an LMM is much shorter. To improve the convergence and computational speed of building structural analyses, Koh et al. proposed an improved condensation-based method for 3D-FM. Besides this, Yoon et al. proposed a methodology to determine the LMM parameters via non-linear analyses of 3D-FM and applied it to an irregular structural configuration and high-rise building [63].

Chapter 2 developed a framework in which a 2D CNN model predicts the ductility ratio, story drift, and the acceleration of each story of the LMM using the acceleration record of a single sensor located on the top floor of the building, where the wavelet spectra were obtained from the absolute acceleration of this sensor and used as images for the input maps. In this study, the damage identification method proposed is updated and improved as follows:

- The structural models are 3D-FM. This allows all buildings to have different lateral force-resisting systems, structural configurations, material types, and elastic and inelastic behavior of their members;
- The structural responses used as damage identifiers are the maximum inter-story drift (SD) and the maximum absolute acceleration (AA) of each story of the target buildings;
- A methodology to select records for each damage identifier is introduced using the Incremental Dynamic Analysis (IDA) responses of each target building, where the ground motions are scaled in order to cover the elastic and inelastic behavior of the target building;
- The input map data for the training CNN model uses the Wavelet Power Spectrum (WPS) computed from the absolute acceleration response measured by the sensor located on the top floor of each target building.
- The validation of the CNN model is applied to two instrumented buildings in Japan. Additionally, an artificial building is validated in both orthogonal directions in order to consider distinct lateral force-resisting systems;

The accuracy of the results is evaluated by comparing the damage condition of the building with the reference values. Although training and validating the CNN model is computationally intensive, once the CNN model is developed, the CNN algorithm trained for the target building can automatically predict the elastic and inelastic structural responses and detect the damage condition immediately after the earthquake. This study was published by the author in [64].

This chapter contains sections as follows: Section 3.2 presents the methodology, including an overview of the proposed research procedure. Section 3.3 shows the general information about the target buildings, the nonlinear structural models used for the target buildings, damage levels based on the story drift ratio and acceleration as damage identifiers, and the methodology used to select records from the database to reduce the variability of structural responses. Section 3.4 specifies the wavelet power spectrum used as input data for the CNN model, and its procedure and characteristics are described. Additionally, it defines the training

and validation process used to obtain a trained CNN model. It is applied to the target buildings, and their prediction results are shown in Section 3.5. Finally, Section 3.6 presents a summary of conclusions and a discussion of the research results.

3.2 Research methodology

Figure 3.1 shows the methodology flowchart to obtain the trained CNN model. As mentioned, this study uses 3D-FM to cover the most complex buildings and increases the accuracy by selecting spectrum-matched records and using WPS.

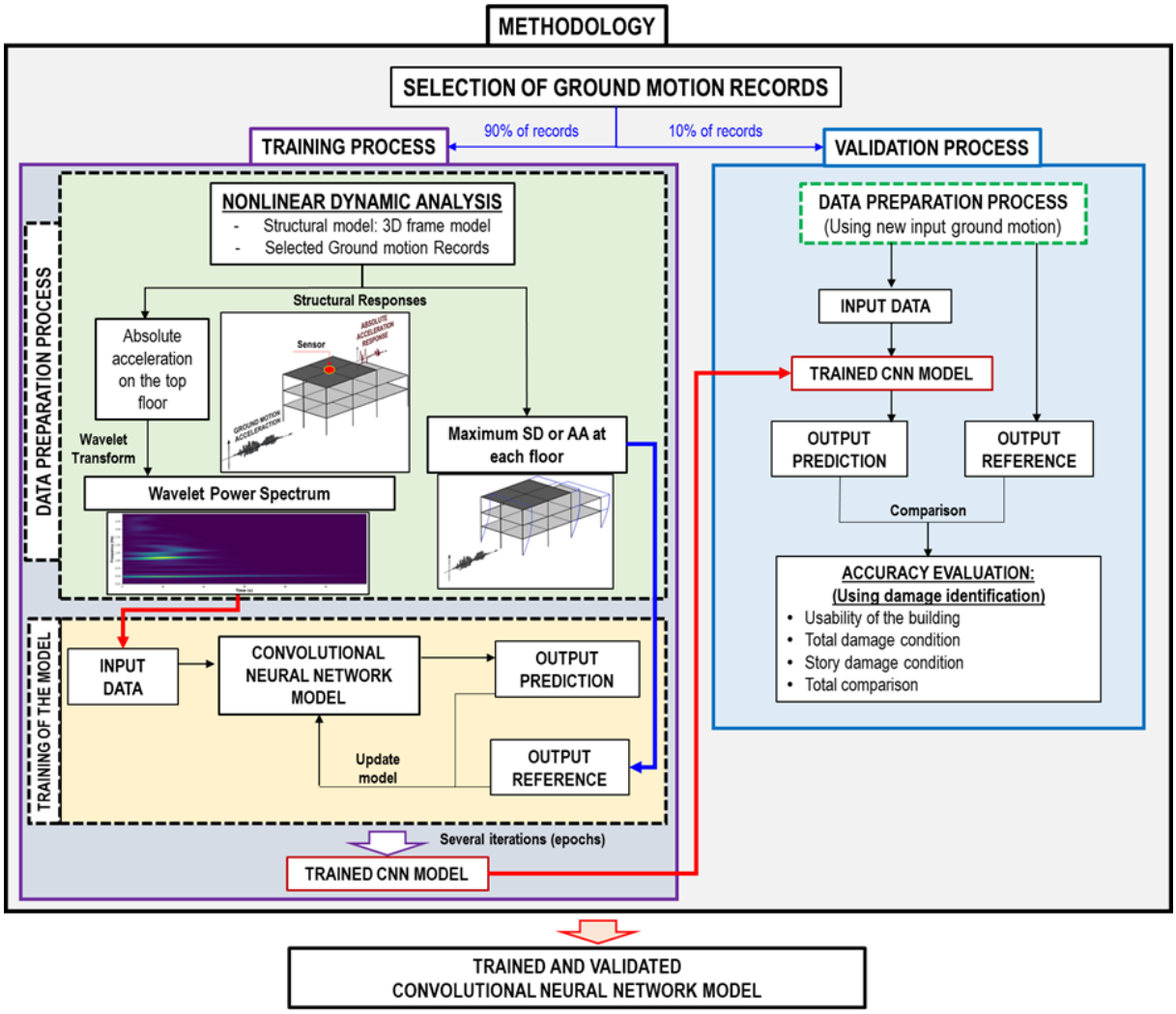

Figure 3.1. Methodology flowchart to obtain the trained CNN model using WPS.

3.3 Case study and input ground motion

3.3.1 Target buildings

Three target buildings are considered to validate a CNN model. Two instrumented buildings in Japan are Tahara City Hall (steel structural system) and Toyohashi Fire Station (steel-reinforced concrete structural system). In addition, one artificial building is considered in order to validate two different RC structural systems (both orthogonal directions).

3.3.1.1 Tahara City Hall building

The Tahara City Hall is a local government office building located in Toyohashi city of Aichi prefecture in Japan (see Figure 3.2). This building is an instrumented building, and the location of the sensor is shown in Figure 3.3. The main structural characteristics are as follows:

- The structural system of the building is a moment-resisting frame in steel;
- The number of floors is six, and the story heights are 1st story = 4.45 m, 2nd to 4th story = 4.10 m, 5th story = 4.40 m, and 6th story = 4.35 m;
- The story weights are 1st story = 15,068 kN, 2nd story = 13,422 kN, 3rd story = 15,290 kN, 4th story = 9899 kN, 5th story = 10,387 kN, and 6th story = 11,853 kN;
- I cross-section and box cross-section for beams and columns, respectively;
- The X-direction presents an irregular configuration in its elevation (see Figure 3). On-ly the X-direction is analyzed in this study;
- The natural period (T1) of the building in the X-direction is 0.681 s (1.468 Hz) with an effective modal mass ratio of 0.77. The second mode period (T2) is 0.264 s (3.788 Hz) with an effective modal mass ratio of 0.145. The values are obtained from numerical simulations of the structural model according to Section 4.

Figure 3.2. Tahara City Hall building.

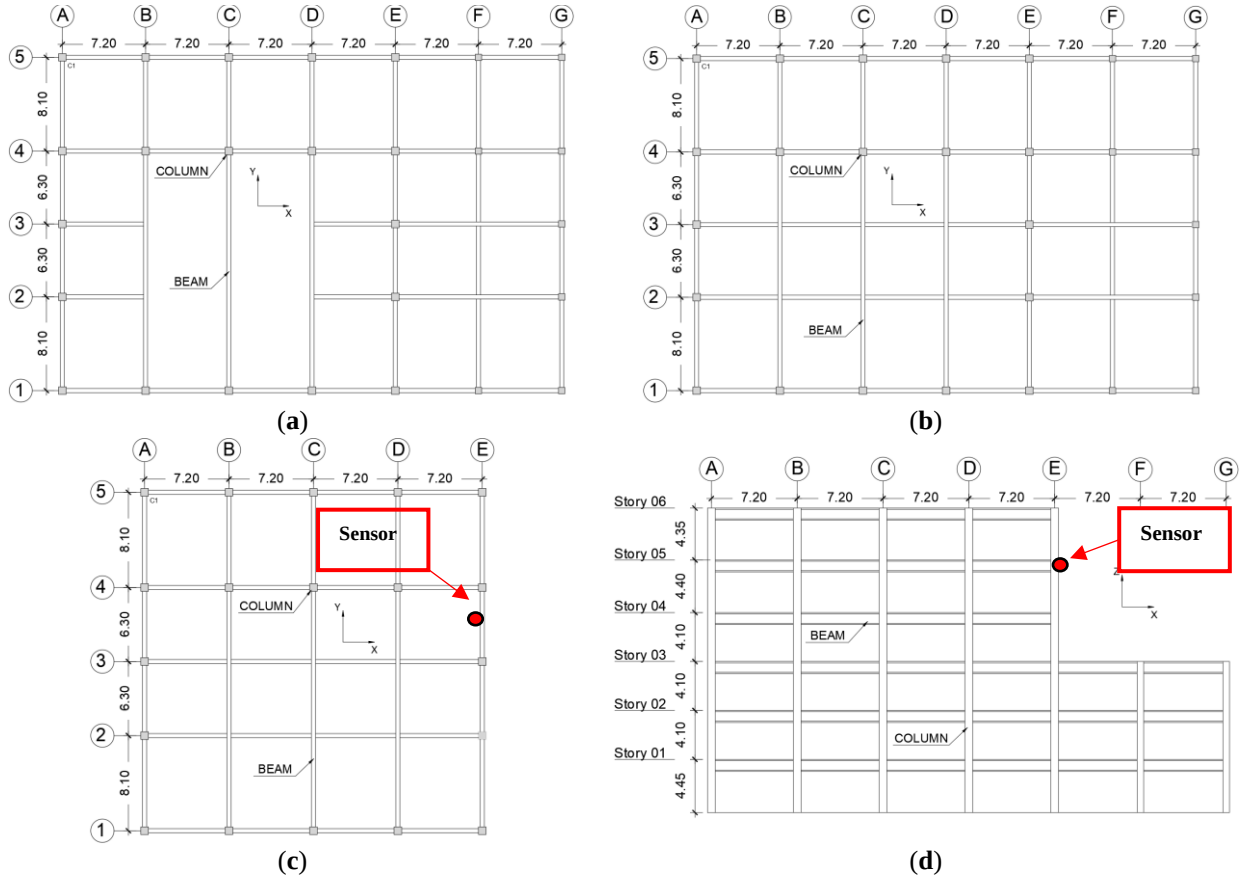

Figure 3.3. General drawings of Tahara City Hall building. (a) Plan of 1st story view. (b) Plan of 2nd and 3rd stories' views. (c) Plan from 4th to 6th story view. (d) Elevation of X-direction view.

3.3.1.2 Toyohashi Fire Station building

The Toyohashi Fire Station is a fire station located in Toyohashi city of Aichi prefecture in Japan (see Figure 3.4). This building is an instrumented building, and the location of the sensor is shown in Figure 5. The main structural characteristics are as follows:

- The structural system of the building is a moment-resisting frame in steel-reinforced concrete (SRC);
- The number of floors is six with a basement, and the typical story height is 4.00 m;
- The story weights are basement = 18,019 kN, 1st story = 14,570 kN, 2nd story = 12,483 kN, 3rd story = 12,470 kN, 4th story = 13,043 kN, 5th story = 12,412 kN, 6th story = 11,834 kN, and 7th story = 10,588 kN;
- The steel I cross-sections are embedded in RC rectangular beams and columns;
- Both the X- and Y-directions are regular configurations, as shown in Figure 3.5. Only the X-direction is analyzed in this study;
- The natural period (T1) of the building in the X-direction is 0.748 s (1.337 Hz), with an effective modal mass ratio of 0.62. The second mode period (T2) is 0.277 s (3.610 Hz) with an effective modal mass ratio of 0.12.

Figure 3.4. Toyohashi Fire Station building.

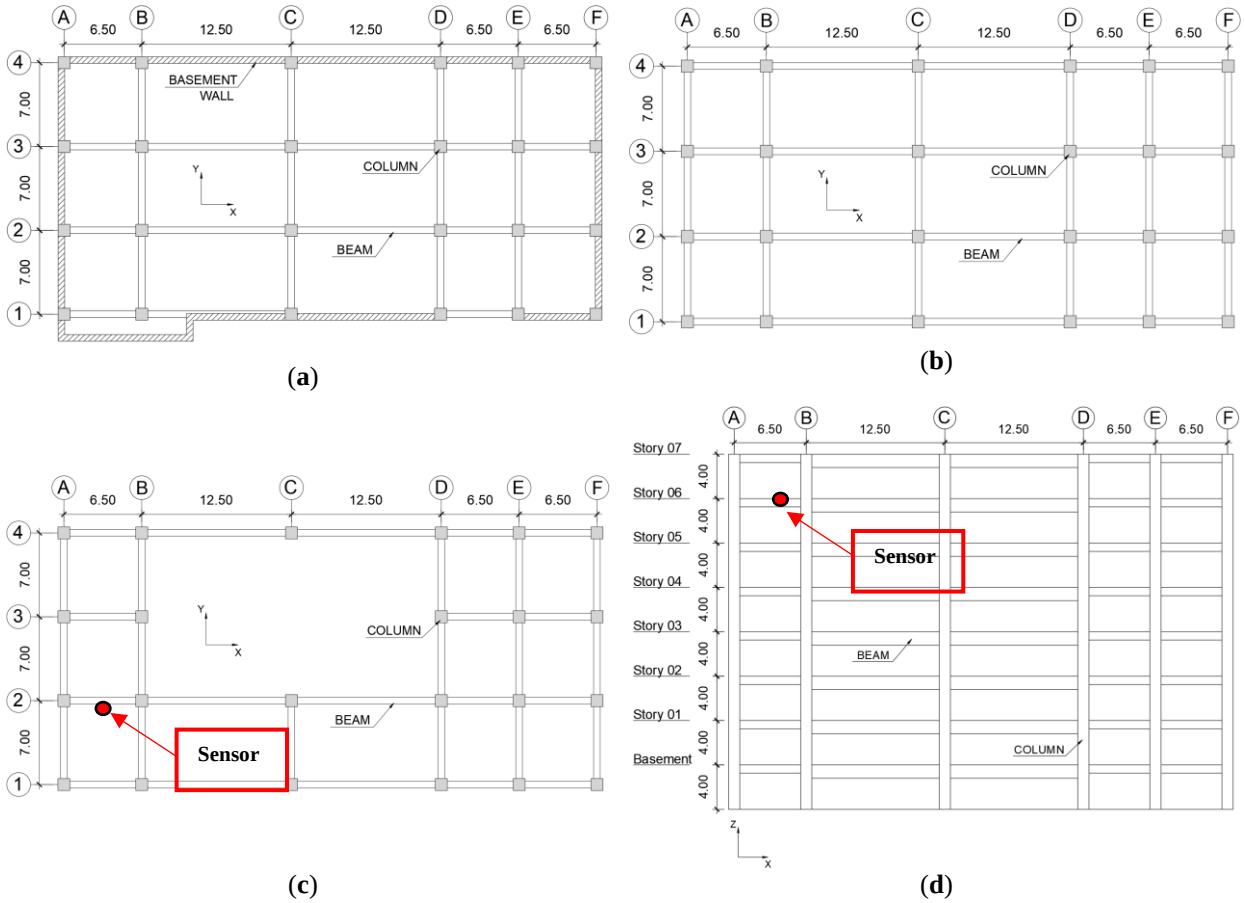

Figure 3.5. General drawings of Toyohashi Fire Station building. (a) Plan of basement view. (b) Plan from 1st to 6th story view. (c) Plan of 7th story view. (d) Elevation of X-direction view.

3.3.1.3 RC building

The RC building is an artificial structure in order to evaluate the accuracy of the methodology with different lateral force-resisting systems. This building is assumed as an instrumented building, and the location of the sensor is shown in Figure 3.6. The main structural characteristics are as follows:

- The structural system of the building is a moment-resisting frame in RC;
- The number of floors is seven, and the typical story height is 4.00 m;
- The typical story weight is 7,200 kN;
- RC rectangle and square cross-section for beams and columns, respectively;
- Both the X- and Y-directions are regular configurations, as shown in Figure 3.6. Both directions are analyzed in this study;
- The natural X-direction (T_1) period is 0.46 s (2.174 Hz) with an effective modal mass ratio of 0.705. The second mode period (T_2) is 0.121 s (8.264 Hz) with an effective modal mass ratio of 0.18.
- The natural Y-direction (T_1) period is 0.751 s (1.332 Hz) with an effective modal mass ratio of 0.788. The second mode period (T_2) is 0.254 s (3.937 Hz) with an effective modal mass ratio of 0.104.

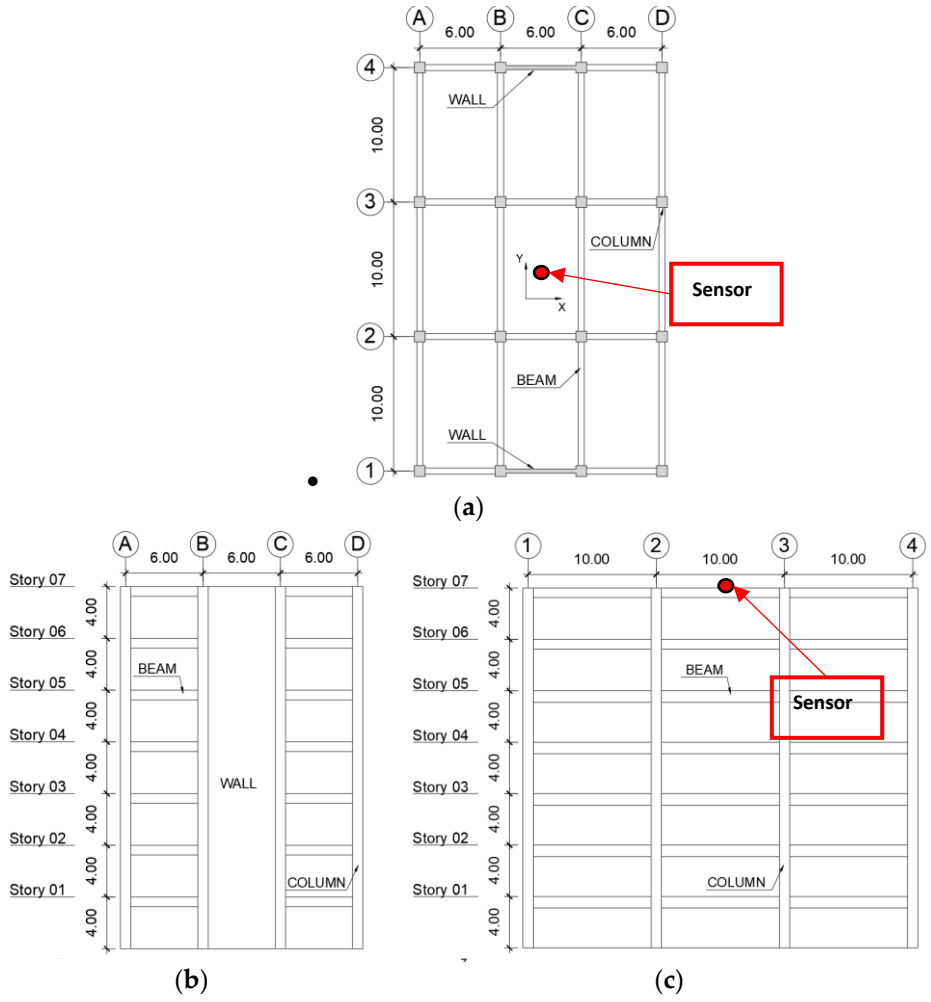

Figure 3.6. General drawings view of RC building. (a) Typical plan view; (a) Elevation of X-direction; (b) Elevation of Y-direction.

In this study, the signals of the sensors have been simulated from the 3D structural models, which were constructed element by element based on the structural drawings. After the earthquake, the sensors will be activated and read the acceleration when a threshold is reached. Subsequently, all data are automatically stored on the network cloud and can be used to assess the damage. However, for future research, it is recommended to use other methods in order to reconstruct the missing data due to anomalies and other factors [65,66].

3.3.2 Nonlinear structural models for the target buildings

The structural models for the target buildings consist of three-dimensional elements with elastic and inelastic behavior. The software STERA_3D [52] was used, wherein the frame beam elements were modeled using nonlinear flexural springs at their ends and a nonlinear shear spring in the middle, as shown in Figure 3.7. The structural analysis computation time was optimized by running 16 models in parallel.

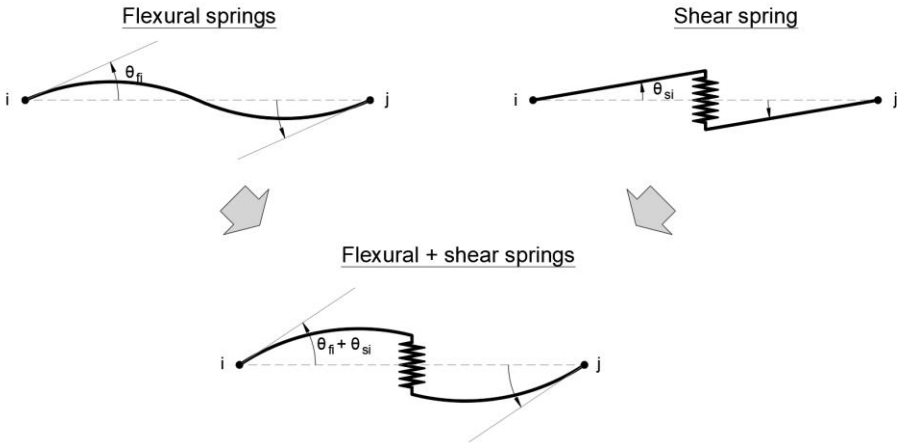

Figure 3.7. Beam model with nonlinear flexural and shear springs [52].

Figure 3.8 shows the hysteresis models of flexural springs. Figure 3.8a shows the degrading trilinear slip model for the RC sections. Figure 3.8b shows the bilinear model for steel sections.

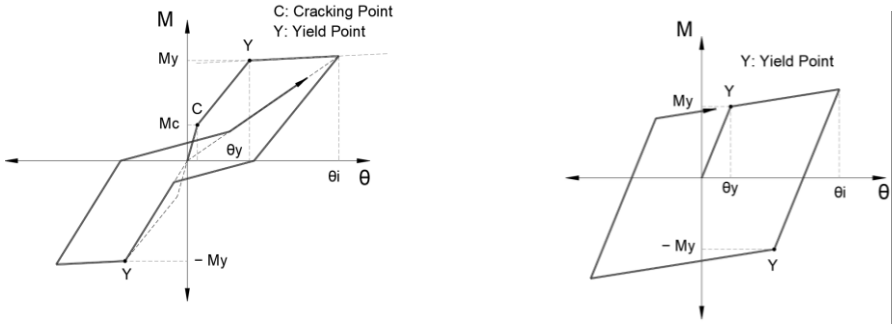

(**a**) (**b**)

Figure 3.8. Hysteresis model. (a) Degrading trilinear slip model for RC sections; (b) Bilinear model for steel sections [52].

Likewise, the frame column elements are modeled as multi-spring models considering a nonlinear interaction between the bidirectional–flexural and axial effects (Mx-My-Nz, as shown in Figure 3.9a). The springs are distributed in the RC and steel cross-sections, as shown in Figure 3.9b. Moreover, Figure 3.9c shows the hysteresis model for steel and concrete springs. The nonlinear shear springs in the X- and Y-directions are de-fined independently.

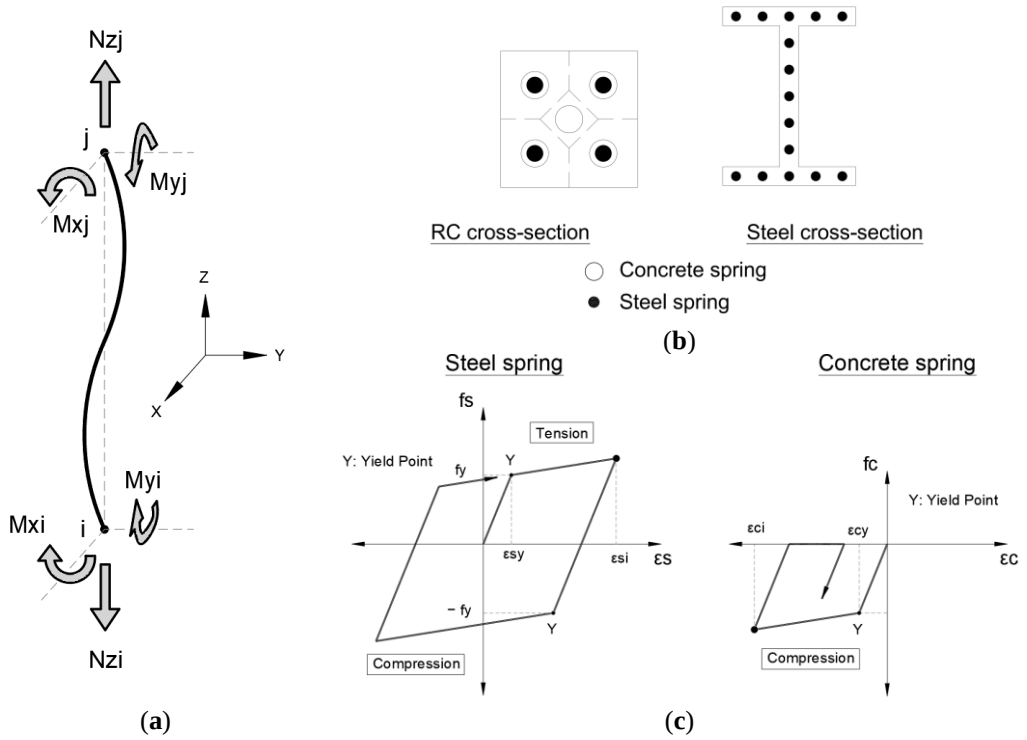

Figure 3.9. Column structural model. (a) Multi-springs to consider Nz-Mx-My nonlinear interaction; (b) Concrete and steel springs; (c) Hysteresis model for steel and concrete springs [52].

For wall elements (wall panel + end components), the nonlinear interaction between the bidirectional-flexural and axial effects is considered (M_{ip} - M_{op} - N, as shown in Figure 3.10). The wall cross-section assumes a plane section, representing a linear strain distribution. The in-plane wall moment (M_{ip}) is from the end components and wall panel. On the other hand, the out-plane wall moment (M_{op}) is only from the end components. Besides, the wall element is divided into different parts among steel and concrete areas in order to use the multi-spring method, as shown in Figure 3.10b. Figure 3.9c shows the hysteresis model for each subdivided part, either concrete or steel area, to obtain the nonlinear behavior of the wall element.

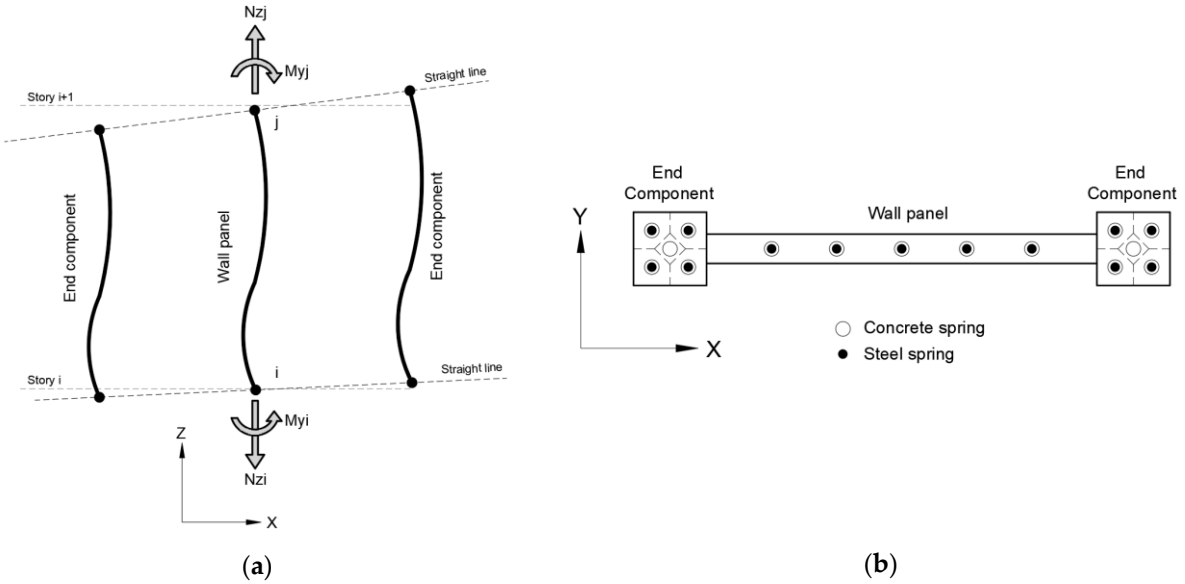

Figure 3.10. RC wall structural model. (a) M_{ip} - M_{op} - N; (b) Wall (concrete and steel) subdivision; (c) Hysteresis models. [52]

3.3.3 Damage identification of the target buildings

The inelastic 3D-FMs for the target buildings are made to obtain detailed structural responses. This study identifies the damage condition from the maximum structural responses SD and AA on each story.

The usability of the building is defined in order to evaluate the habitability of the building. It is represented by safe use, restricted use, and unsafe use, as shown in Table 1.1.

3.3.4 Selection of ground motion records

A record database was generated from the records obtained in the Center for Engineering Strong Motion Data by USGS and the California Geological Survey. This center receives worldwide records from the cooperation of international strong-motion seismic networks [67].

In order to consider the ground motion records with high intensity and reduce the number of samples (less than 3000), the records with a PGA greater than 400 gal and a time range from 5% to 95% of the Arias intensity have been selected [64,68,69]. Finally, 183 ground motion records have been selected in this study for the database.

3.3.4.1 Incremental dynamic analyses

In the structural analysis, the variability of the structural responses of the building depends mainly on the ground motion used. On the other hand, the prediction accuracy of ML is improved when the output variability is reduced. Therefore, a methodology to select the records from structural responses has been developed using the IDA of each target building. Figure 3.11 shows the procedure for determining the ground motion records from the database.

For the IDA, the demand measure is either the SD or AA (on the vertical axis) and the intensity measure is the 5% damped spectral acceleration matched at the fundamental period (Sa(T1, 5%) on the horizontal axis). Sa(T1, 5%) is selected to represent the seismic intensity, where the main modal mass contribution is obtained. Besides this, a normal distribution is considered to represent the variability of the structural responses along Sa(T1, 5%). Thus, 68% of the structural responses are represented within $\pm 1\sigma$ (one standard deviation) of the mean, resulting in a confidence interval from 16% to 84% fractile.

Therefore, in order to cover elastic and inelastic behavior ranges, the IDA curves use a confidence interval from 0% to 84% fractile of the structural responses. Besides this, 1/50 has been established as the story drift ratio limit. The selected records and Sa(T1, 5%) have been derived from accomplishing both previous conditions for SD. The IDA scale factors are such that the resultant spectral acceleration (ΔSa) is 25 gal if Sa(T1, 5%) max is less than 1000 gal, and 50 gal if Sa(T1, 5%) max is greater than 1000 gal. The IDA curves for AA, the same confidence interval, scale factors, and maximum Sa(T1, 5%) have been used to find their selected ground motion records. These criteria were developed after several structural analyses in this research.

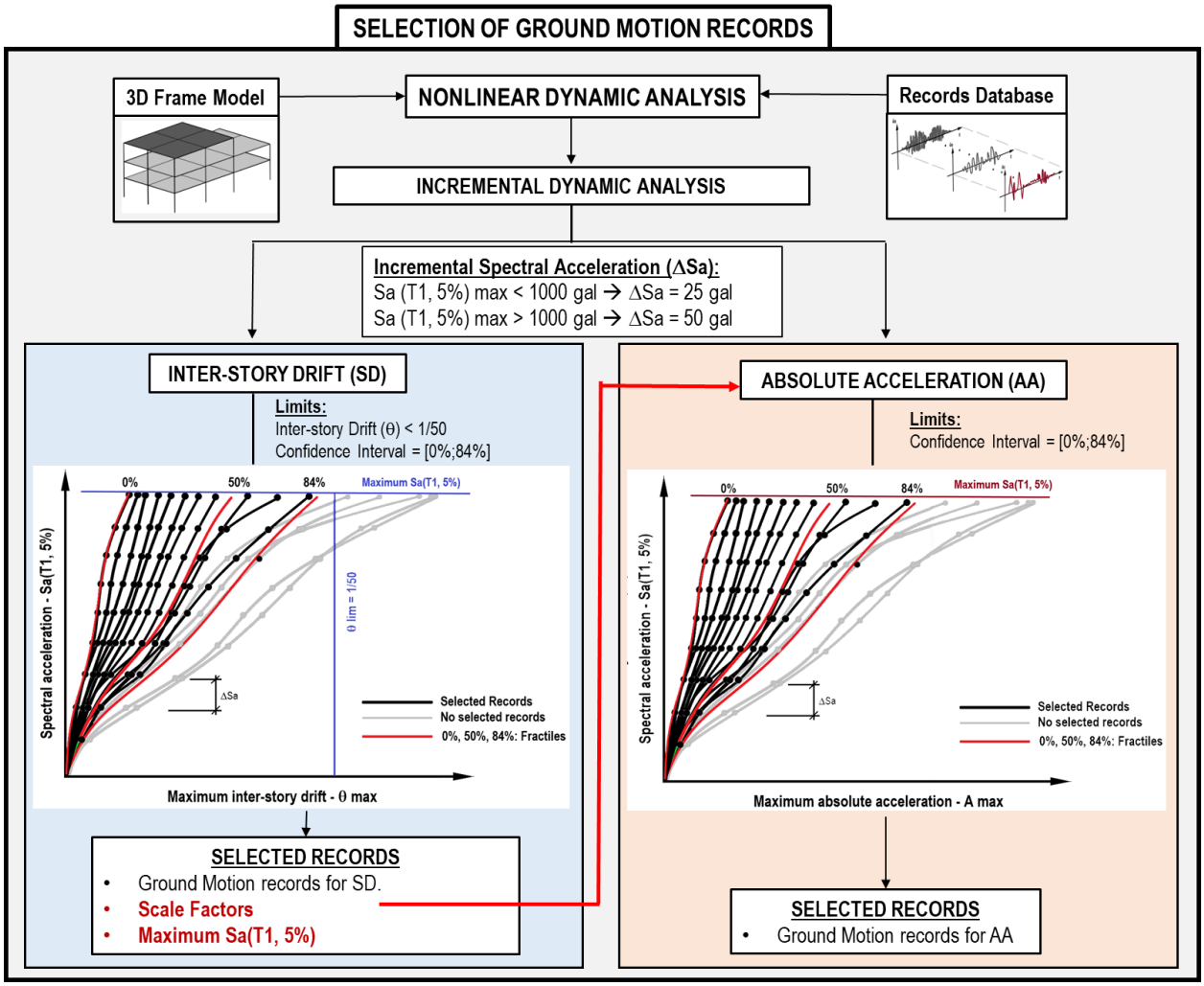

Figure 3.11. Selection of ground motion records for inter-story drift and acceleration flowchart.

Figure 3.12, Figure 3.13, Figure 3.14, and Figure 3.15 show the IDA curves for SD and AA of the database and selected records. The black dashed lines are the 0%, 50%, and 84% fractiles. Besides this, the green, yellow, orange, and red dashed lines depict the damage condition threshold limits.

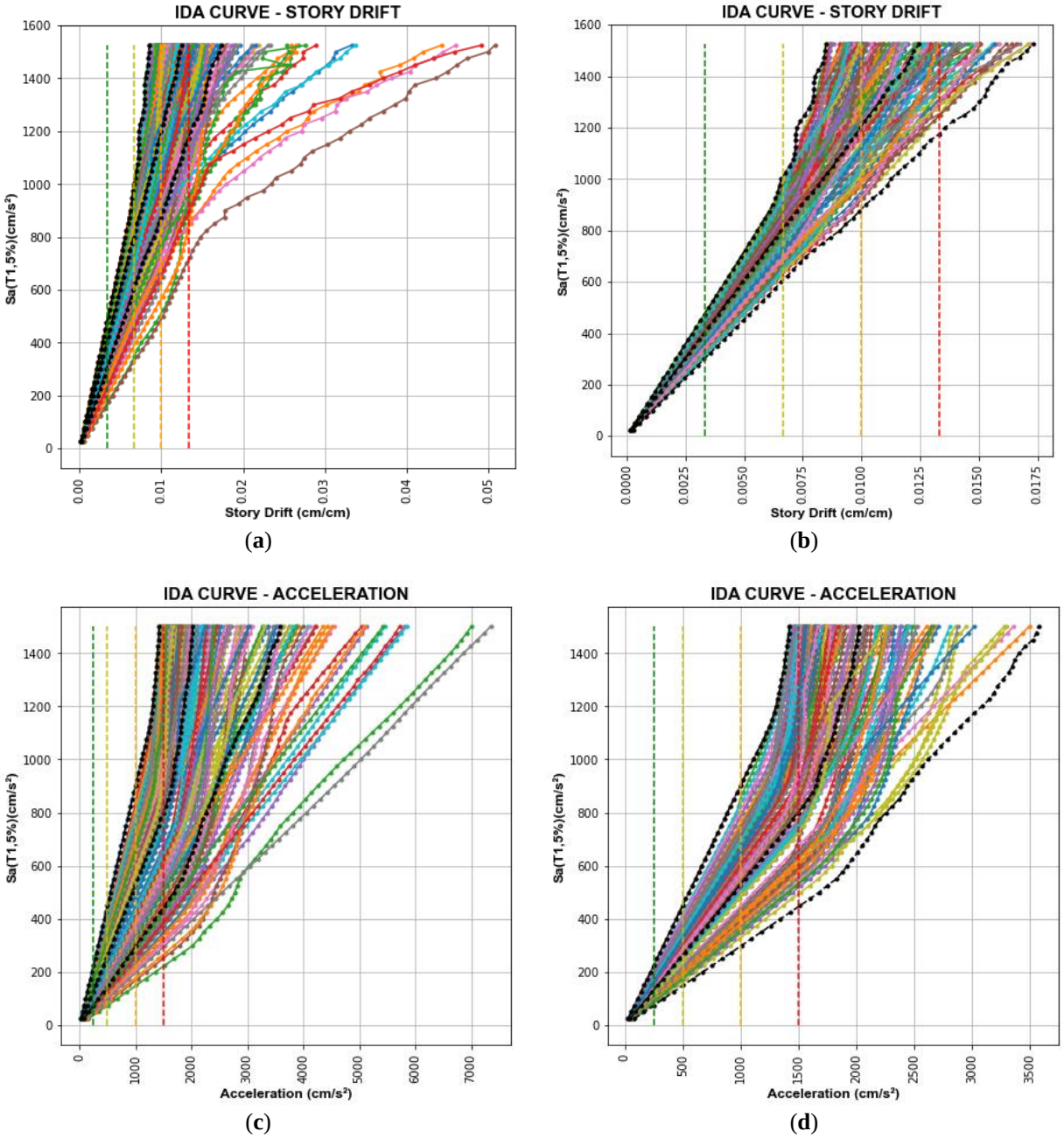

Figure 3.12. IDA Curves of Tahara City Hall building. (a) IDA curves of the database for SD; (b) IDA curves of selected records for SD; (c) IDA curves of the database for AA; (d) IDA curves of selected records for AA.

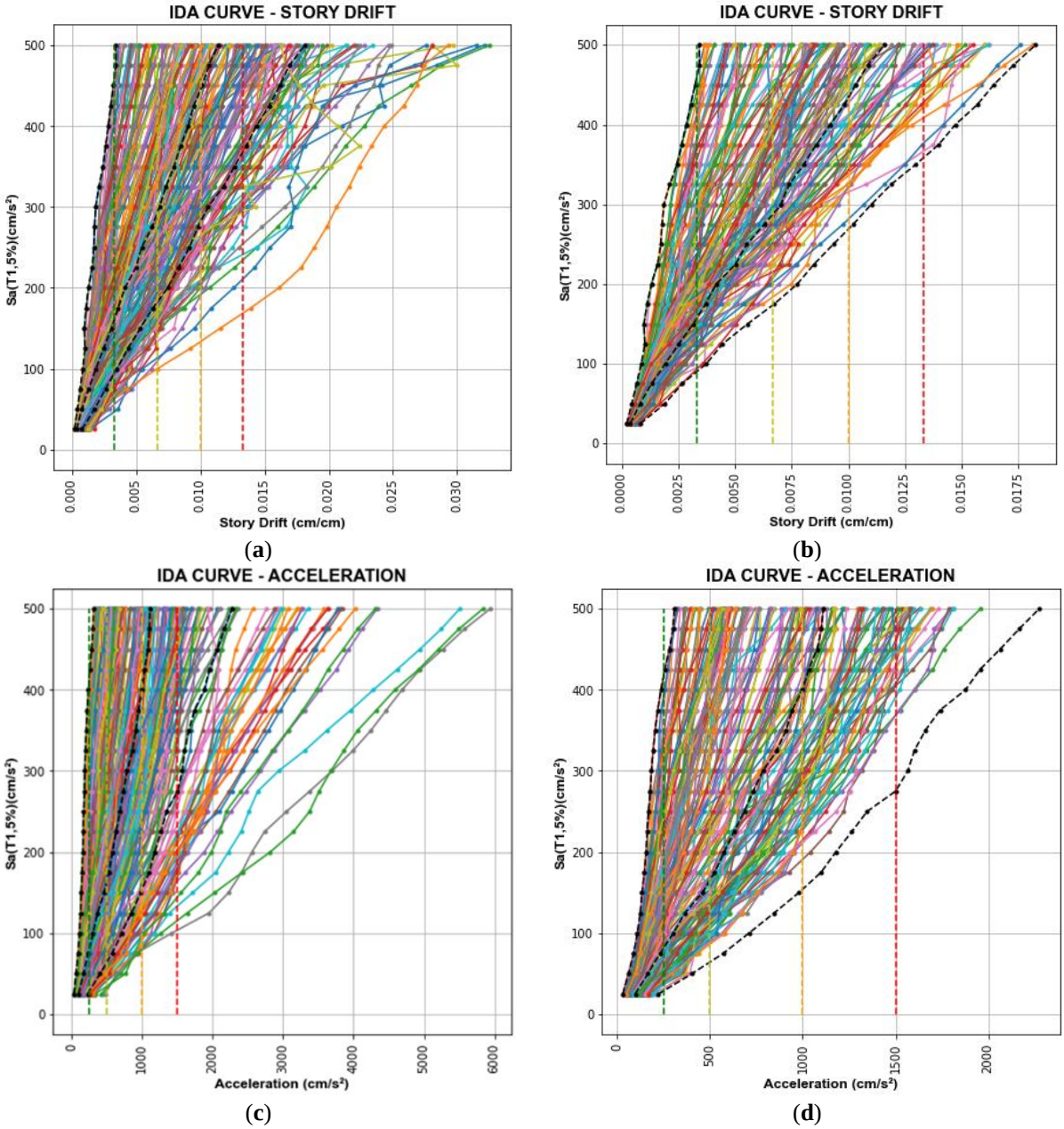

Figure 3.13. IDA Curves of Toyohashi Fire Station building. (a) IDA curves of the database for SD; (b) IDA curves of selected records for SD; (c) IDA curves of the database for AA; (d) IDA curves of selected records for AA.

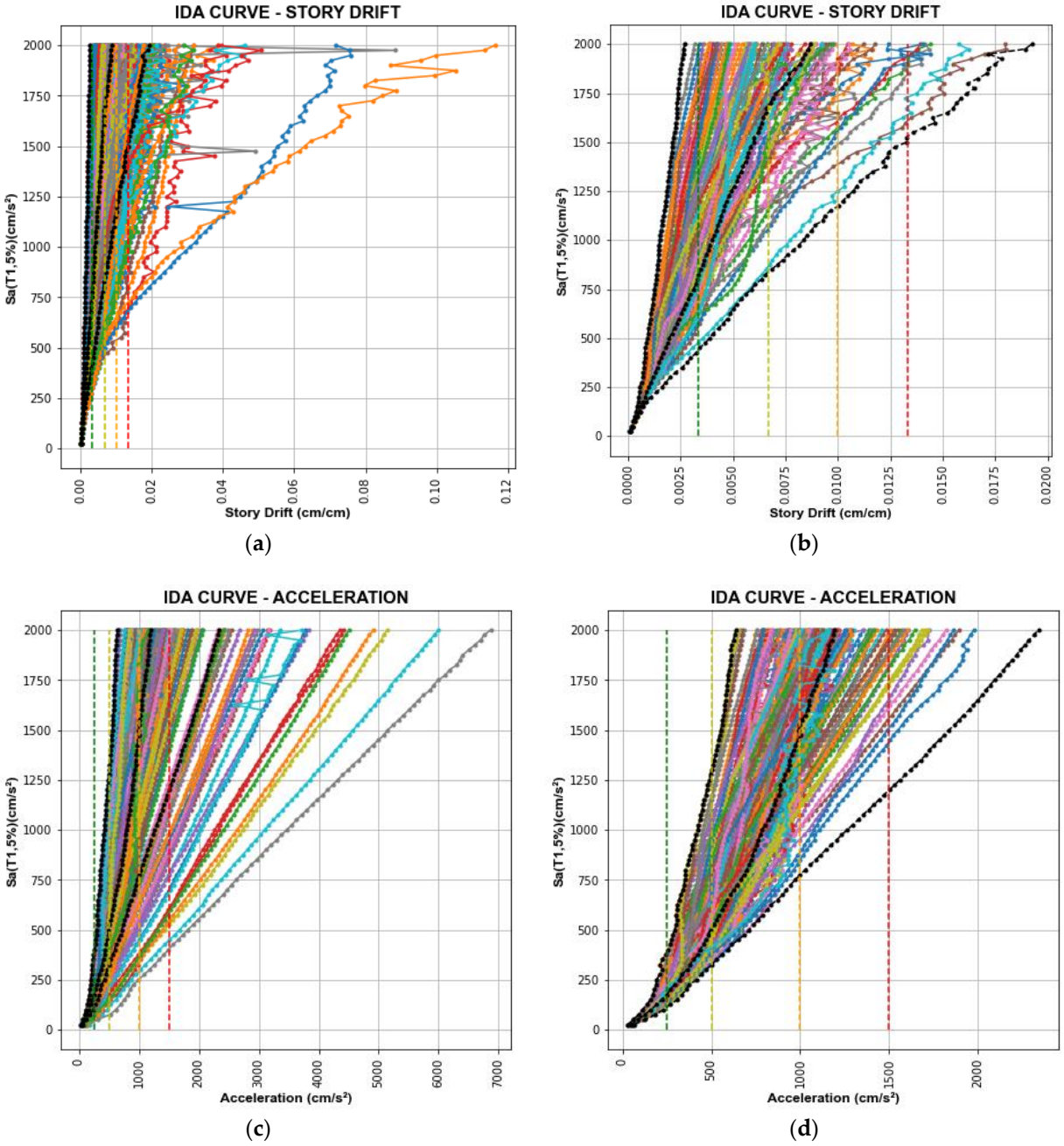

Figure 3.14. IDA Curves of RC building – X direction (a) IDA curves of the database for SD; (b) IDA curves of selected records for SD (c) IDA curves of the database for AA; (d) IDA curves of selected records for AA analyses.

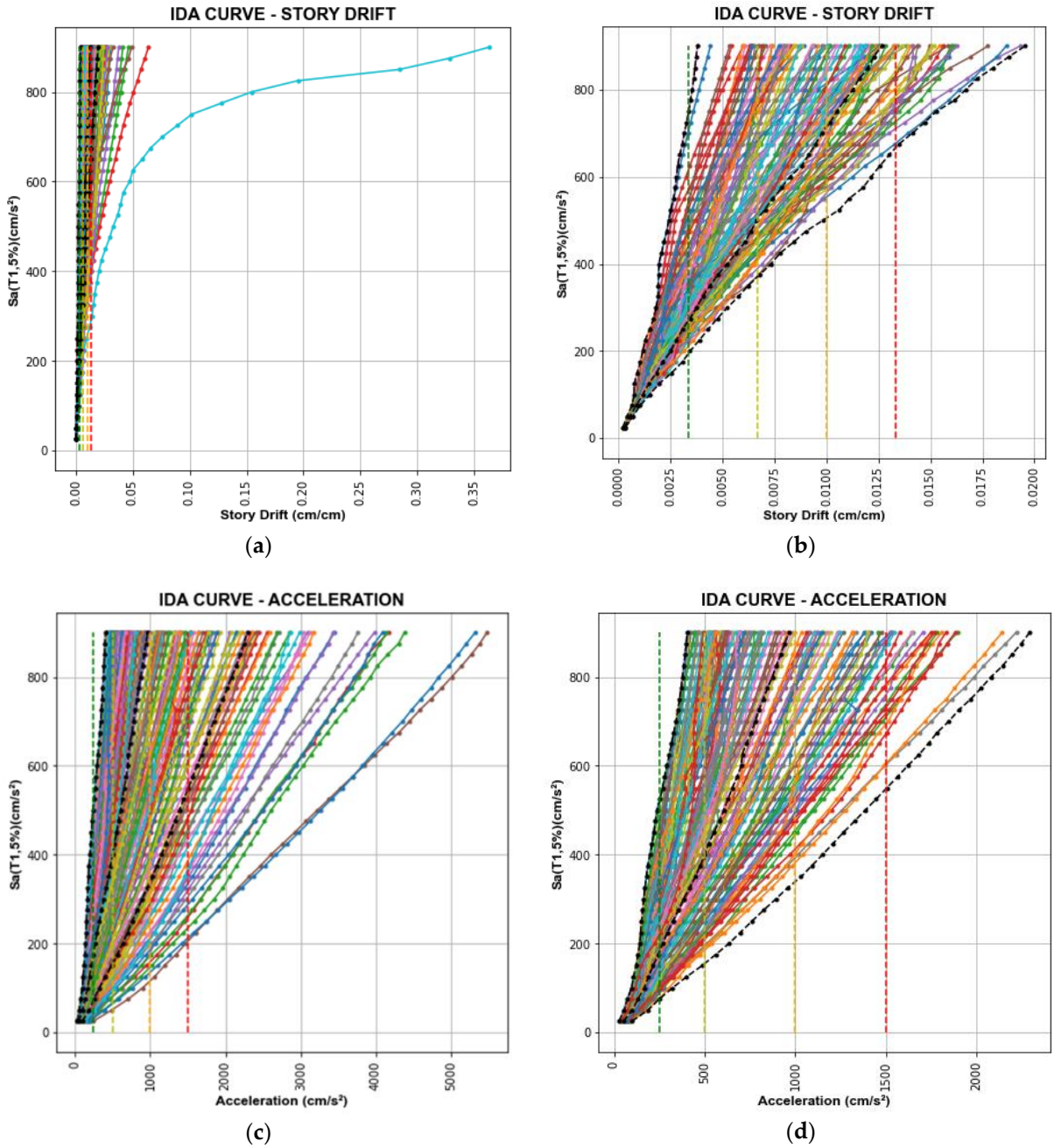

Figure 3.15. IDA Curves of RC building – Y direction (a) IDA curves of the database for SD; (b) IDA curves of selected records for SD (c) IDA curves of the database for AA; (d) IDA curves of selected records for AA.

Figure 3.16, Figure 3.17, Figure 3.18, and Figure 3.19 show the acceleration response spectra (Sa) of the selected records subdivided into training and validation records used for the CNN models for SD and AA analyses. Besides this, the validation records for the SD and AA analyses are the same in order to consider the same earthquake events. Additionally, Sa is 100 gal at the fundamental period of each target building.

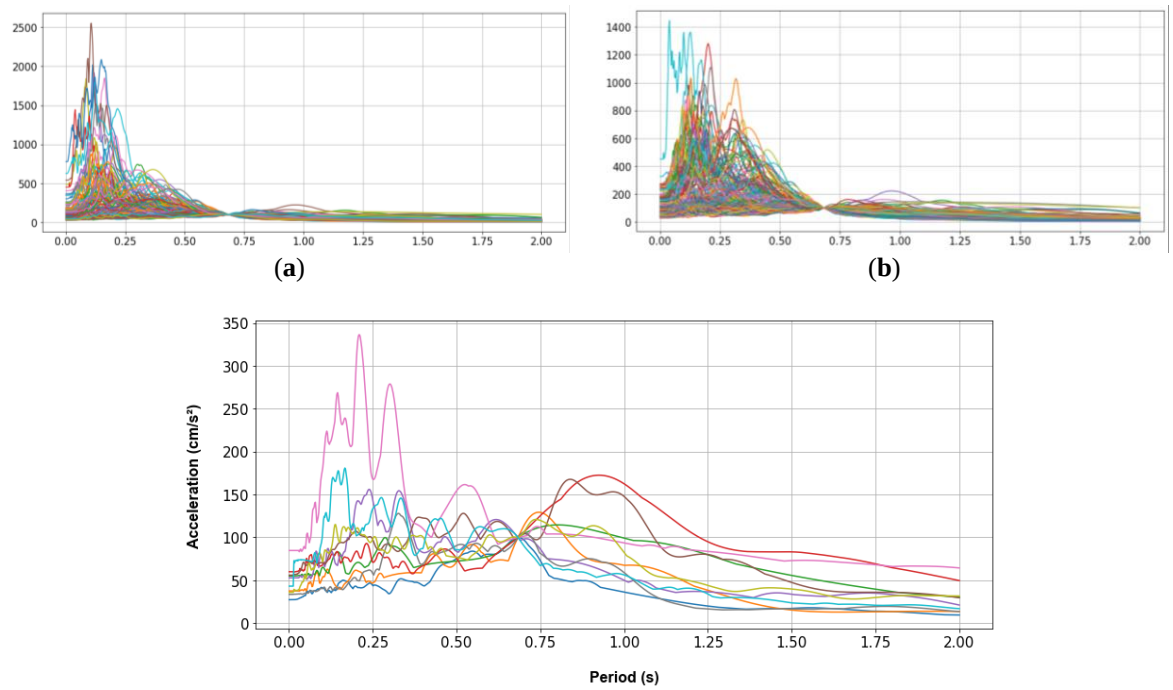

Figure 3.16. Acceleration response spectrum of Tahara City Hall building at T1 = 0.681 s and Sa(T1) = 100 gal. (a) Training records for SD; (b) Training records for AA; (c) Validation records for SD and AA analyses.

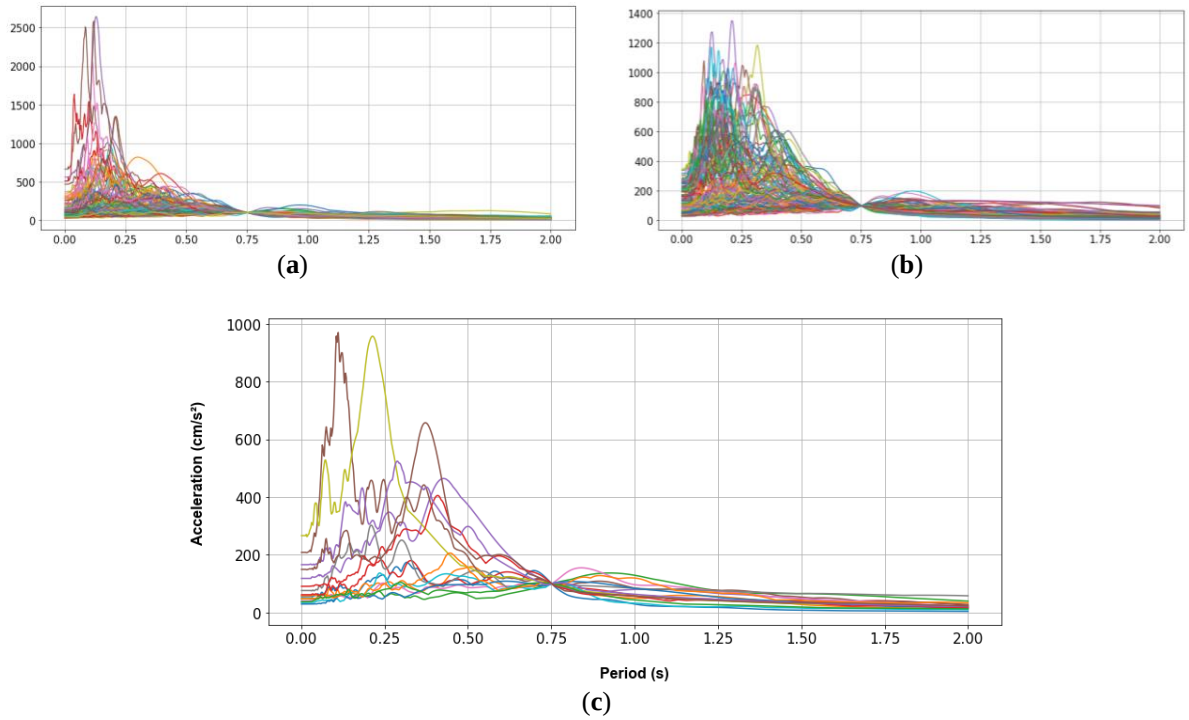

Figure 3.17. Acceleration response spectrum of Toyohashi Fire Station building at T1 = 0.748 s and Sa(T1) = 100 gal. (a) Training records for SD; (b) training records for AA; (c) Validation records for SD and AA analyses.

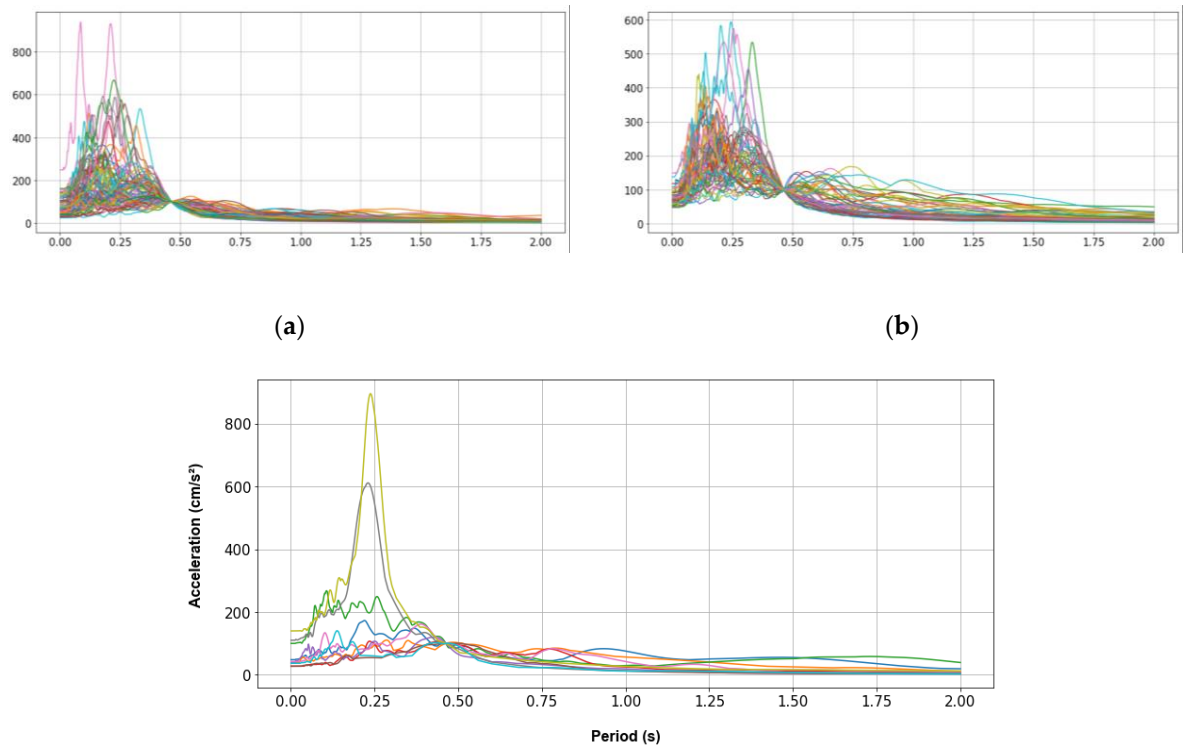

(a) (b)

(c)

Figure 3.18. Acceleration response spectrum of RC building – X direction at T_1 = 0.460 s and Sa(T_1) = 100 gal (a) Training records for SD; (b) Training records for AA (c) Validation records for SD and AA.

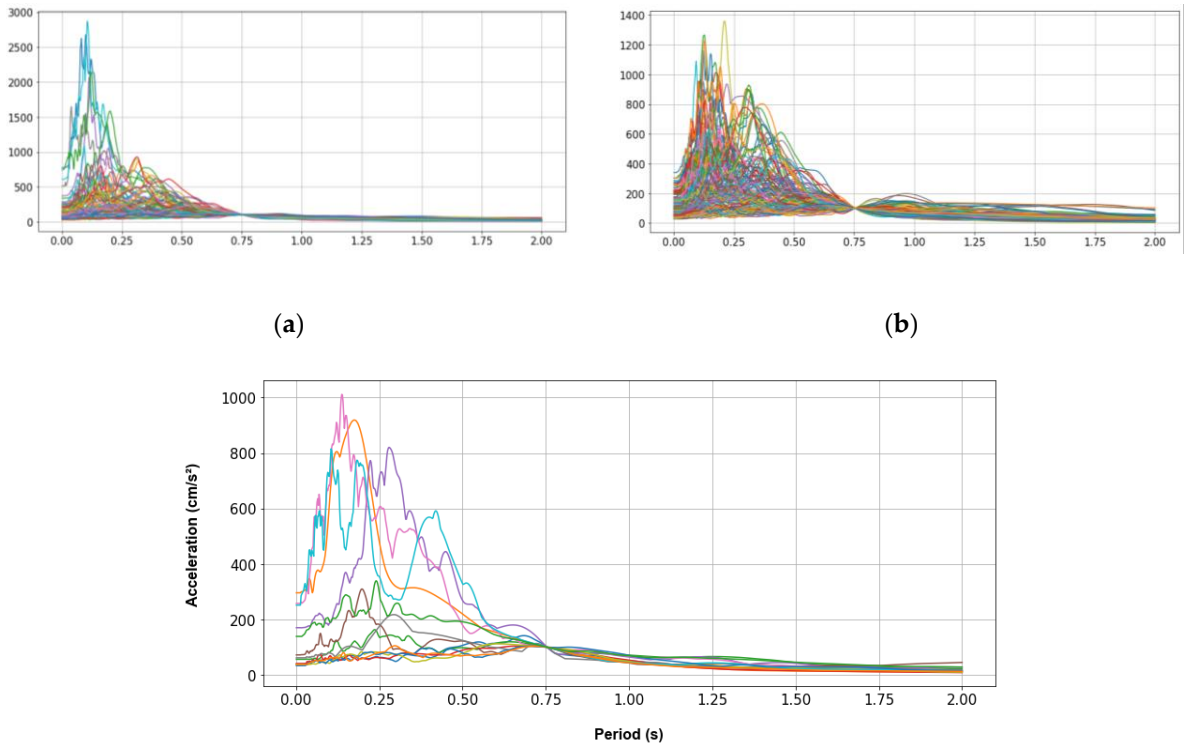

(a) (b)

(c)

Figure 3.19. Acceleration response spectrum of RC building – Y direction at T_1 = 0.751 s and Sa(T_1) = 100 gal (a) Training records for SD; (b) Training records for AA (c) Validation records for SD and AA analyses.

3.3.4.2 Selection of records for Tahara City Hall building

After selecting the records, 130 and 142 records were chosen for SD and AA, respectively, shown in Figure 3.12b and Figure 3.12d.

The selected records are split into 120 and 132 for training CNN models for SD and AA. Besides this, ten records have been used for the validation process in both analyses.

3.3.4.3 Selection of records for Toyohashi Fire Station building

After selecting the records, 115 and 144 records have been chosen for CNN models for SD and AA, respectively, shown in Figure 3.13b and Figure 3.13d.

The selected records have been split into 99 and 126 for training CNN models for SD and AA. Besides this, 16 records are used for the validation process for both analyses.

3.3.4.4 Selection of records for RC building

X – Direction:

After selecting the records, 83 and 60 records have been chosen for CNN models for SD and AA, respectively, shown in Figure 3.14b and Figure 3.14d.

The selected records have been split into 73 and 50 for training CNN models for SD and AA. Besides this, ten records are used for the validation process for both analyses.

Y – Direction:

After selecting the records, 94 and 135 records have been chosen for CNN models for SD and AA, respectively, shown in Figure 3.15b and Figure 3.15d.

The selected records have been split into 81 and 122 for training CNN models for SD and AA. Besides this, 13 records are used for the validation process for both analyses.

3.4 Machine learning methodology

3.4.1 Wavelet power spectrum as input data of CNN

The acceleration record of the upper floor is obtained from the sensor installed on the target building. Since these records are non-stationary signals, they are transformed in order to capture their characteristics in the time and frequency domains. In this study, the wavelet transform is used.

The wavelet spectrum is defined by Equation 2-5, and the square of the module is the wavelet power spectrum (WPS), defined by Equation 3-1.

$$WPS(t,f) = WS^2 \qquad \textit{Equation 3-1}$$

WS was used in Chapter 2 for the maximum absolute acceleration response on the upper floor. These results were used as images for the input data of the CNN model. However, since WPS increases the coefficients of WS exponentially, the signal's main characteristics are intensified to train the CNN model. For example, Figure 3.20 shows a random acceleration response, WS, and WPS in 2D and 3D. Notice that WPS depicts the main frequencies more evidently than WS.

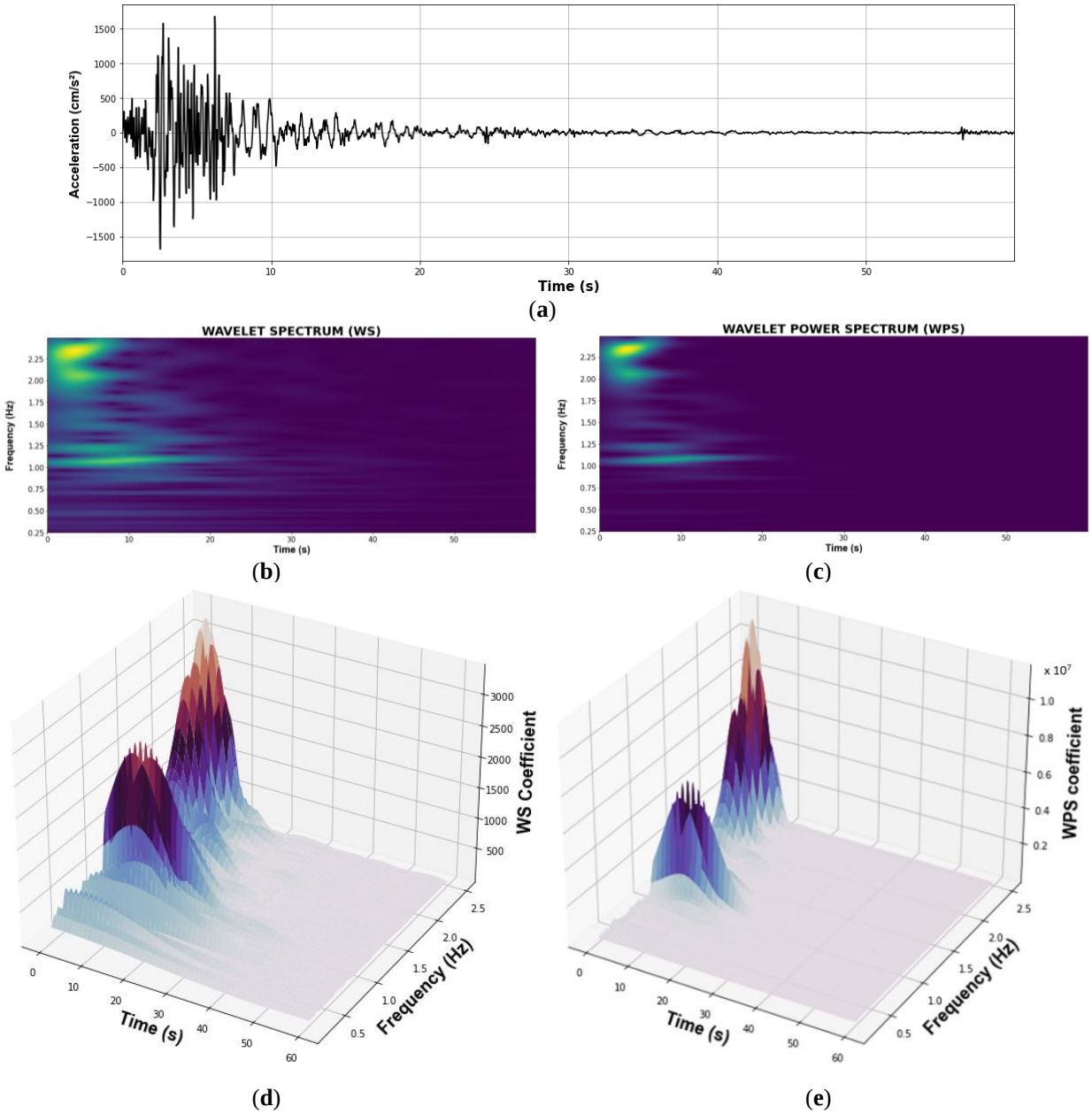

Figure 3.20. Wavelet spectrum and wavelet power spectrum. (a) Acceleration wave; (b) 2D WS; (c) 2D WPS; (d) 3D WPS; (e) 3D WPS.

3.4.2 Convolutional neural network model

In this study, CNN uses the images obtained from the WPS. In order to keep the size of the original image of the feature map, the same-padding or zero-padding method and ReLU function are used in this study. The CNN model without the max-pooling of the Chapter 2 converged more effectively. Nonetheless, the CNN model used for this study converged more efficiently using max-pooling layers because of the more significant amount of data. The number of the convolutional or max-pooling layer depends on the architecture of the CNN model (see Table 3.1). After the convolutional and max-pooling layers, the outputs are connected to a one-dimensional array, the fully connected layer. This iterative process is performed until finding the lowest Mean Squared Error (MSE) using 50 epochs. The hyperparameters used in this study are shown in Table 3.1. They were obtained after several processes of training and validation. However, methods are recommended to optimize the hyperparameters [70,71].

Table 3.1. Hyperparameters of CNN models.

Layer	Type	Hyperparameter	Tahara City Hall Building		Toyohashi Fire Station Building	
			SD	AA	SD	AA
01	Convolutional	Number of kernels	8	8	8	8
		Size of kernels	3 × 3	3 × 3	3 × 3	3 × 3
02	Pooling	Size of pooling filter	2 × 2	2 × 2	2 × 2	2 × 2
03	Convolution	Number of kernels	8	8	8	8
		Size of kernels	3 × 3	3 × 3	3 × 3	3 × 3
04	Pooling	Size of pooling filter	2 × 2	2 × 2	---	2 × 2
05	Convolution	Number of kernels	8	8	8	8
		Size of kernels	3 × 3	3 × 3	3 × 3	3 × 3
06	Pooling	Size of pooling filter	2 × 2	2 × 2	---	2 × 2
07	Convolution	Number of kernels	8	8	8	8
		Size of kernels	3 × 3	3 × 3	3 × 3	3 × 3
08	Pooling	Size of pooling filter	2 × 2	2 × 2	2 × 2	2 × 2
09	Fully connected	Output	6	6	7	7

3.4.3 Training and validation processes

As mentioned in the methodology, there are two processes used to obtain a trained CNN model, the training process (TP) and the validation process (VP).

In the TP, the CNN model is trained using the WPS of absolute acceleration on the top floor of the target building. Then, the prediction results of the CNN model are compared to the SD and AA of each floor of the target building. The IDA numerical procedure is called the data preparation process in the methodology and obtains the SD and AA. The TP provides a prepared model to make predictions; however, its accuracy should be checked in the validation process.

In the VP, new input data are obtained by the data preparation process. The new WPS is used in the trained CNN model and automatically predicts the results (SD or AA). The following results are compared to reference data:

- The usability of the building, in which the availability of the building occupancy is evaluated after an earthquake,
- The total damage condition, in which it is possible to identify the damage state of the target building,
- Story damage condition, in which it is possible to identify the damage state of each floor of the target building,
- Total comparison of the SD or AA.

In general, one of the most potent advantages of the ML method in SHM is the rapid prediction result when an earthquake occurs. In other words, even though the TP and VP take a long time to obtain the final CNN model, it is carried out before the earthquake, but the prediction is obtained automatically. Therefore, it is possible to identify the damage states of actual buildings (3D regular or irregular structural configurations) immediately after the earthquake.

3.5 Prediction and validation of the target buildings

The results of predicting the responses and damage levels of the target buildings are summarized as follows:

- Figure 3.21 and Figure 3.22 show SD and AA results of the Tahara City Hall building, respectively;
- Figure 3.23 and Figure 3.24 show SD and AA results of the Toyohashi Fire Station building, respectively;
- Figure 3.25, Figure 3.26, Figure 3.27, and Figure 3.28 show SD and AA results of the RC building, respectively;
- Figure 3.21a, Figure 3.22a, Figure 3.23a, Figure 3.24a, Figure 3.25a, Figure 3.26a, Figure 3.27a, and Figure 3.28a show the training loss using MSE, which decreases with the epochs increasing in TP;
- A confusion matrix is used to evaluate the prediction accuracy of the total and story damage condition (see Figure 3.21b,c, Figure 3.22b,c, Figure 3.23b,c, Figure 3.24b,c, Figure 3.25b,c, Figure 3.26b,c, Figure 3.27b,c, and Figure 3.28b,c). The confusion matrix represents the correct and incorrect predictions through the number of coincidences with the reference data. The rows and columns of the matrix are tagged as the predicted and the true label, respectively. Therefore, the number of well-matched predictions is located diagonally of the matrix;
- Figure 3.21d, Figure 3.22d, Figure 3.23d, Figure 3.24d, Figure 3.25d, Figure 3.26d, Figure 3.27d, and Figure 3.28d show the accuracy of the damage condition of each floor;
- e, Figure 3.22e, Figure 3.23e, Figure 3.24e, Figure 3.25e, Figure 3.26e, Figure 3.27e, and Figure 3.28e show the comparison of the prediction results using the coefficient of determination or R-squared as defined by Equation 3-2:

$$R^2 = 1 - \frac{\sum_i^N (y_{ref,i} - y_{pred,i})^2}{\sum_i^N (y_{ref,i} - \overline{y_{ref}})^2} \qquad \textit{Equation 3-2}$$

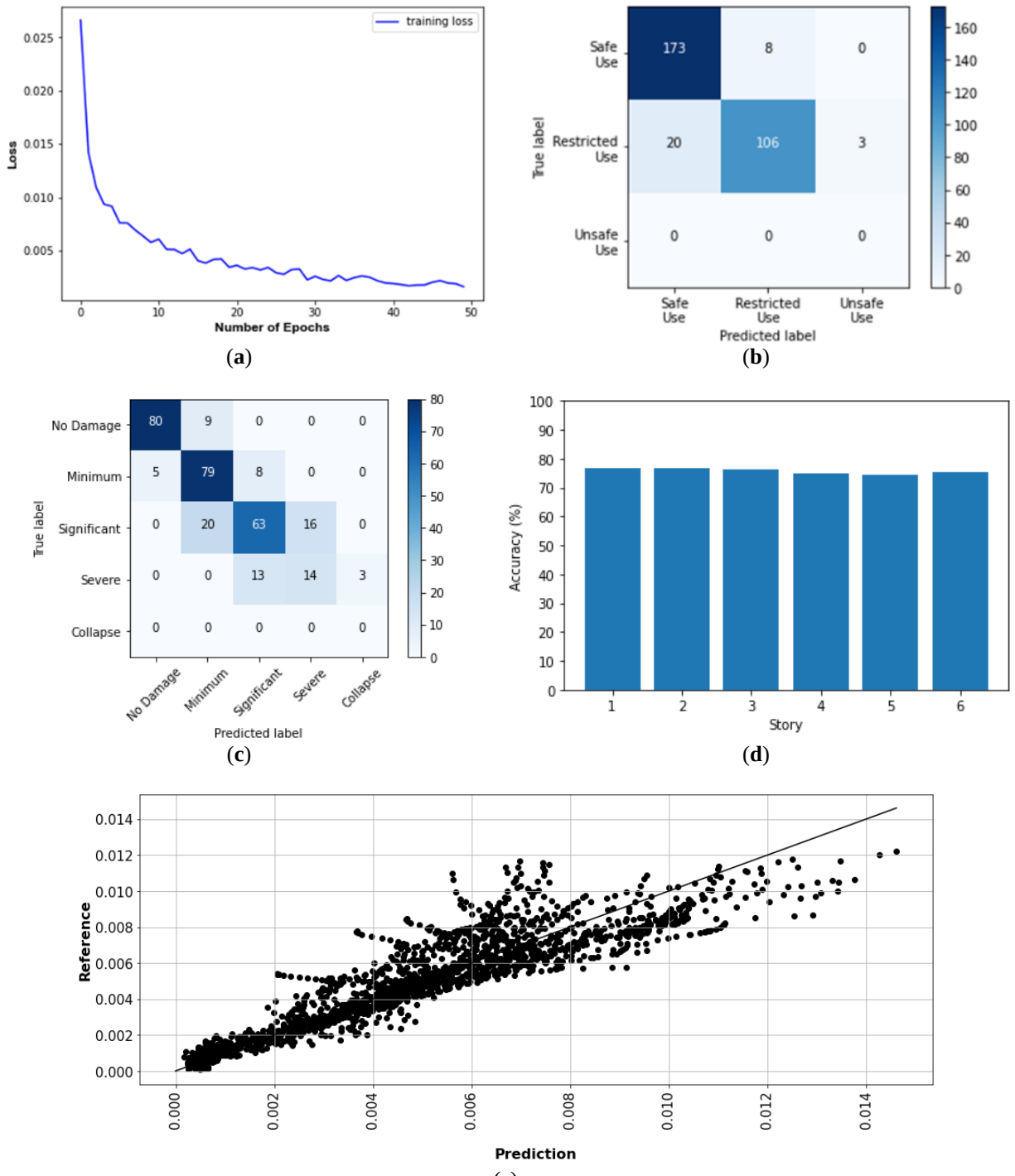

Figure 3.21. SD results of the TP and VP for Tahara City Hall building: (a) Convergence curve – Loss in the TP; (b) Confusion matrix – Usability of the building by VP; (c) Confusion matrix – Total damage condition by VP; (d) Confusion matrix – Story damage condition by VP; (e) Total comparison of SD.

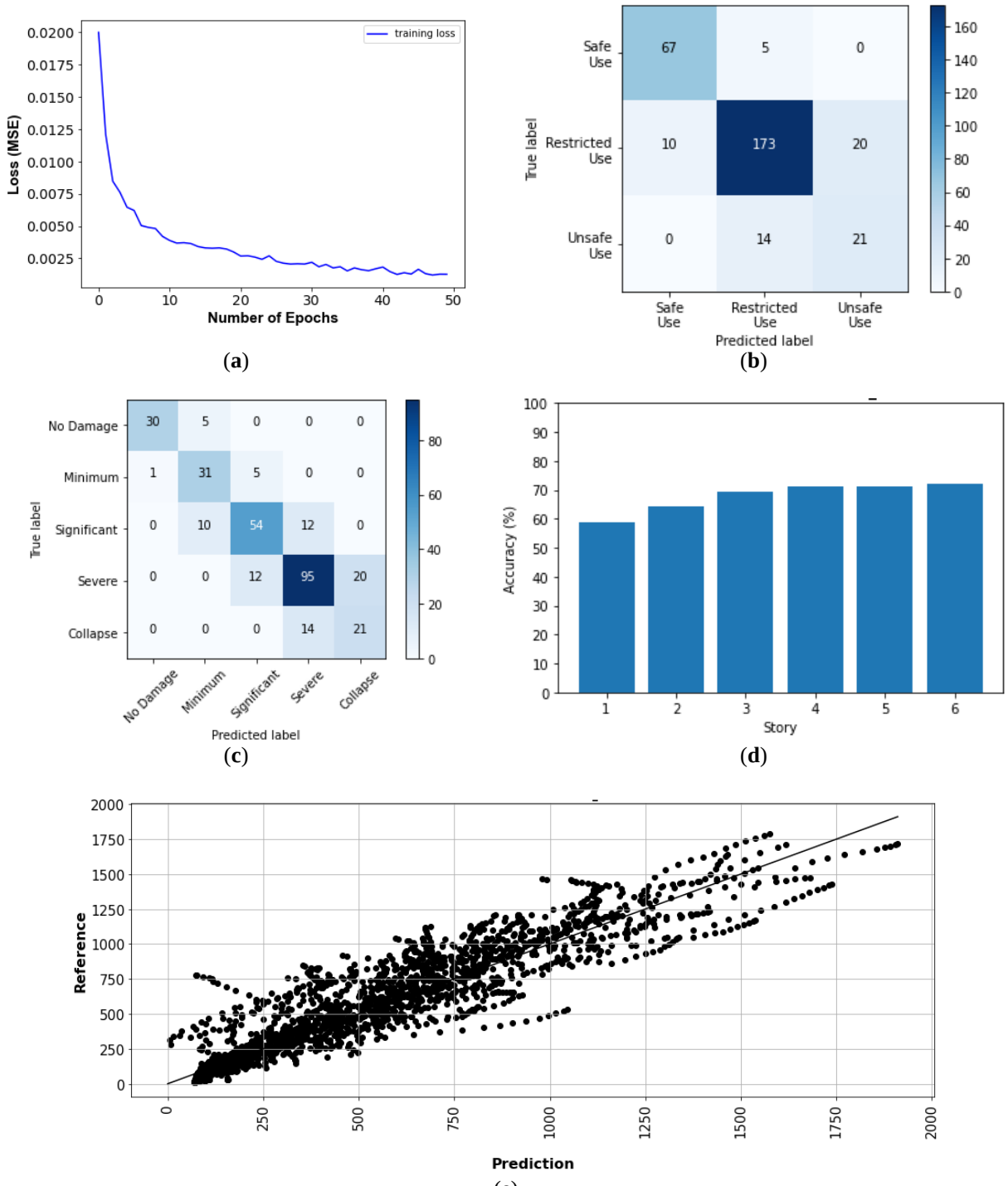

Figure 3.22. AA results of the TP and VP for Tahara City Hall building: (a) Convergence curve – Loss in the TP; (b) Confusion matrix – Usability of the building by VP; (c) Confusion matrix – Total damage condition by VP; (d) Confusion matrix – Story damage condition by VP; (e) Total comparison of AA.

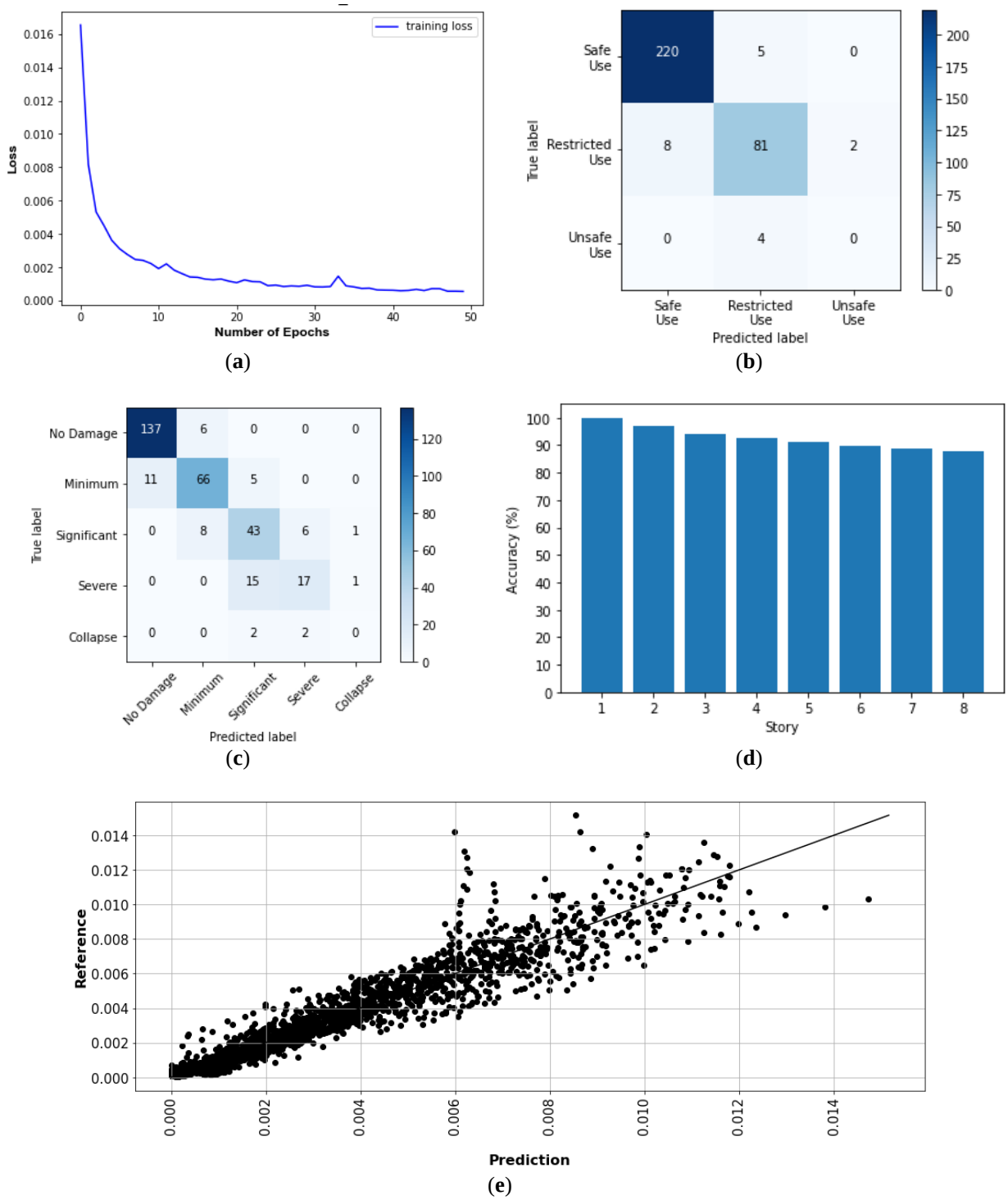

Figure 3.23. AA results of the TP and VP for Toyohashi Fire Station building: (a) Convergence curve – Loss in the TP; (b) Confusion matrix – Usability of the building by VP; (c) Confusion matrix – Total damage condition by VP; (d) Confusion matrix – Story damage condition by VP; (e) Total comparison of AA.

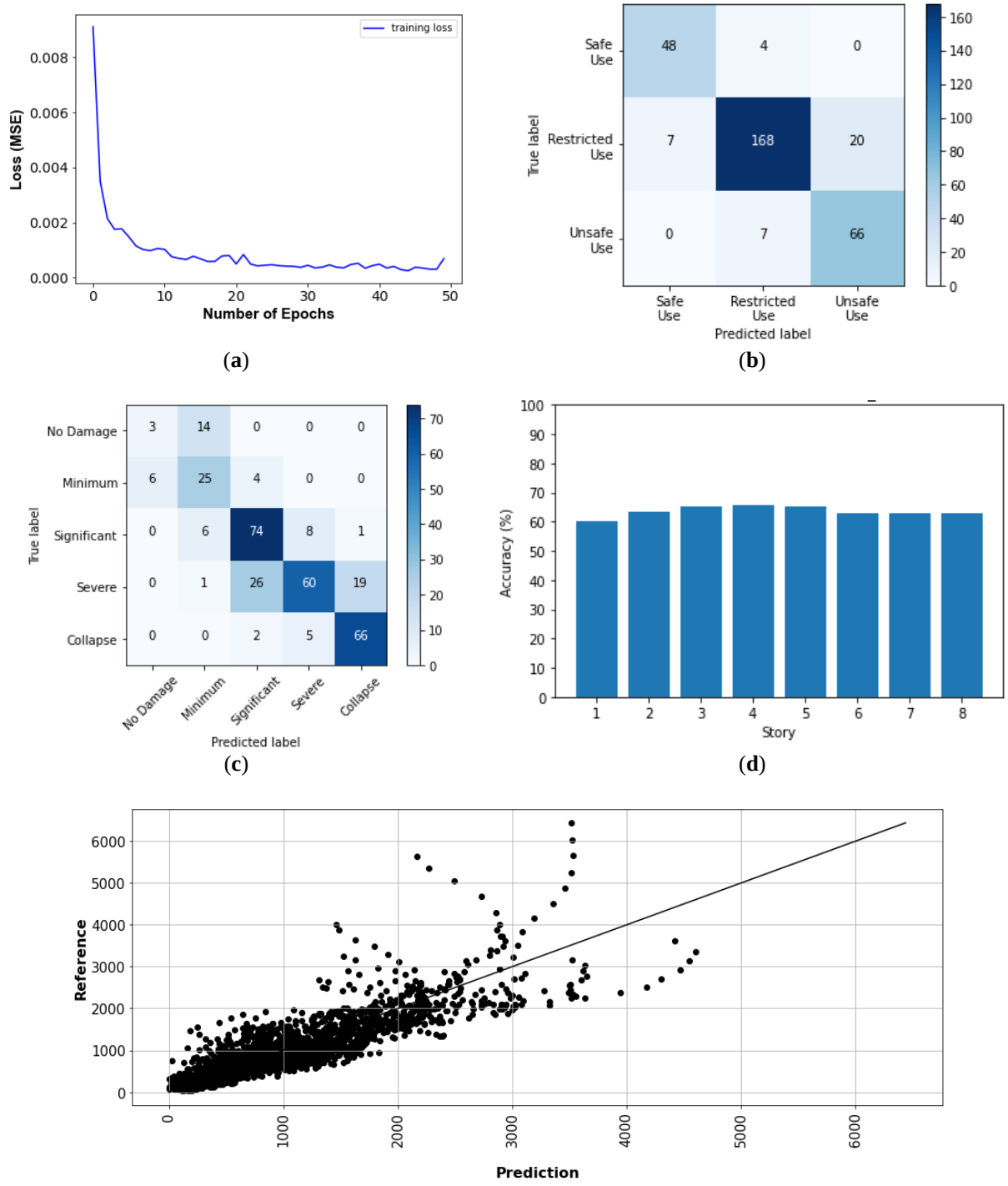

Figure 3.24. AA results of the TP and VP for Toyohashi Fire Station building: (a) Convergence curve – Loss in the TP; (b) Confusion matrix – Usability of the building by VP; (c) Confusion matrix – Total damage condition by VP; (d) Confusion matrix – Story damage condition by VP; (e) Total comparison of AA.

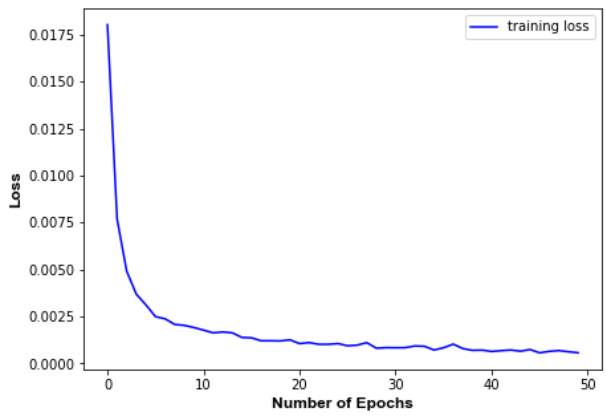

(a)

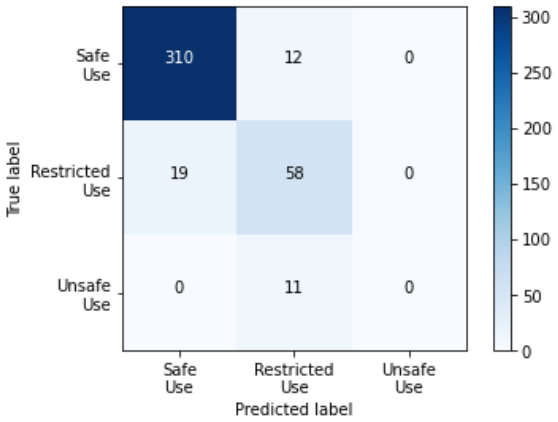

(b)

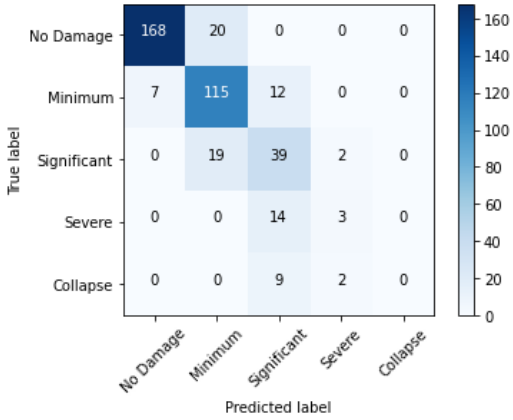

(c)

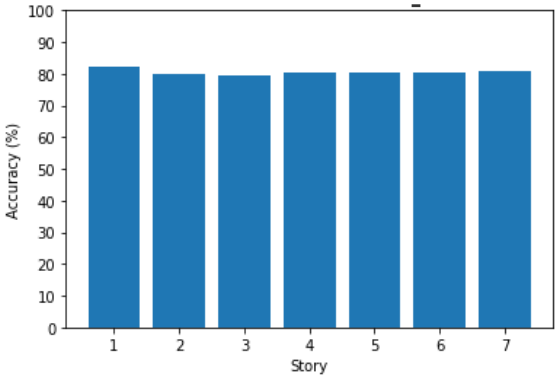

(d)

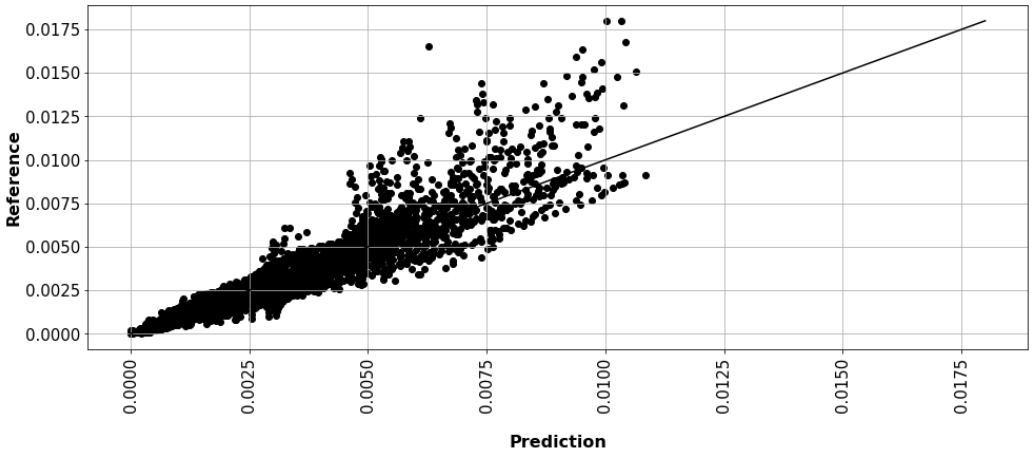

(e)

Figure 3.25. SD results of the TP and VP for RC building X-direction: (a) Convergence curve – Loss in the TP; (b) Confusion Matrix – Usability of the building by VP; (c) Confusion Matrix – Total damage condition by VP; (d) Confusion Matrix – Story damage condition by VP; (e) Total comparison of SD

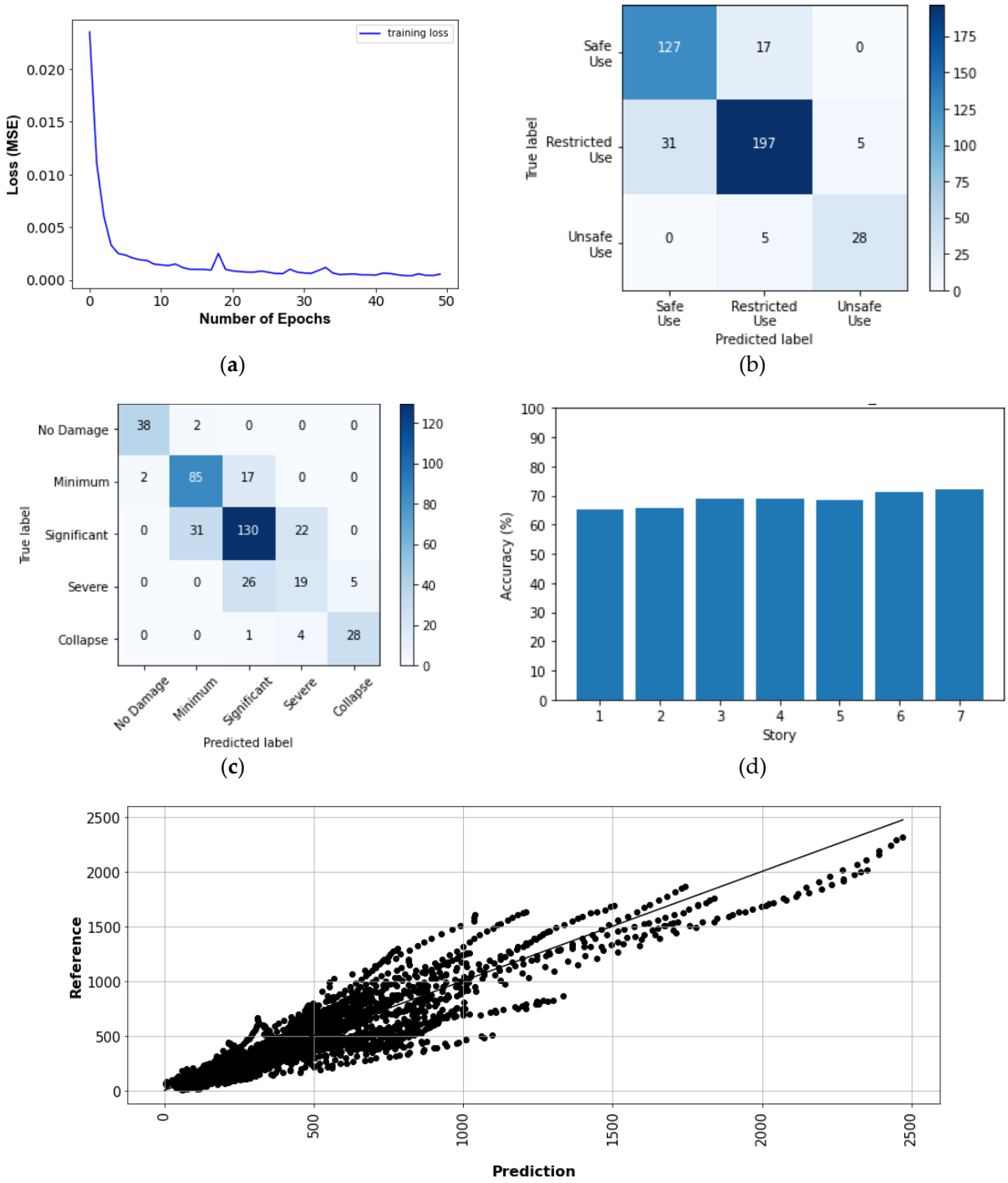

Figure 3.26. AA results of the TP and VP for RC building X-direction: (a) Convergence curve – Loss in the TP; (b) Confusion Matrix – Usability of the building by VP; (c) Confusion Matrix – Total damage condition by VP; (d) Confusion Matrix – Story damage condition by VP; (e) Total comparison of AA

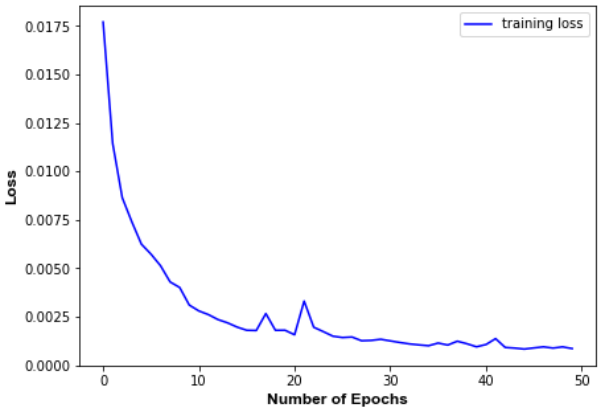

(a)

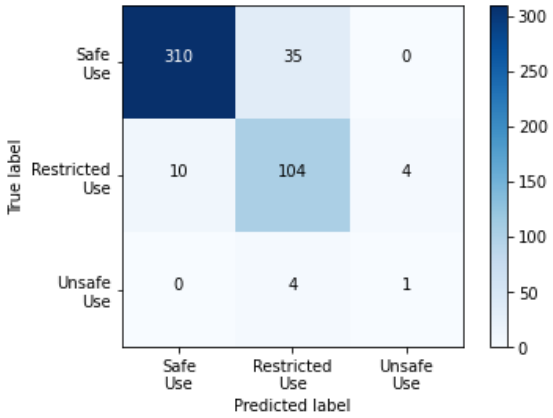

(b)

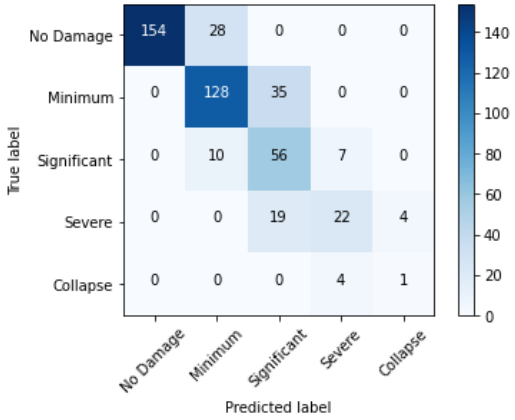

(c)

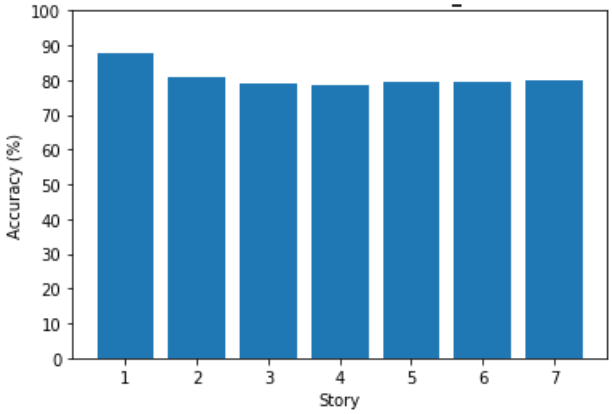

(d)

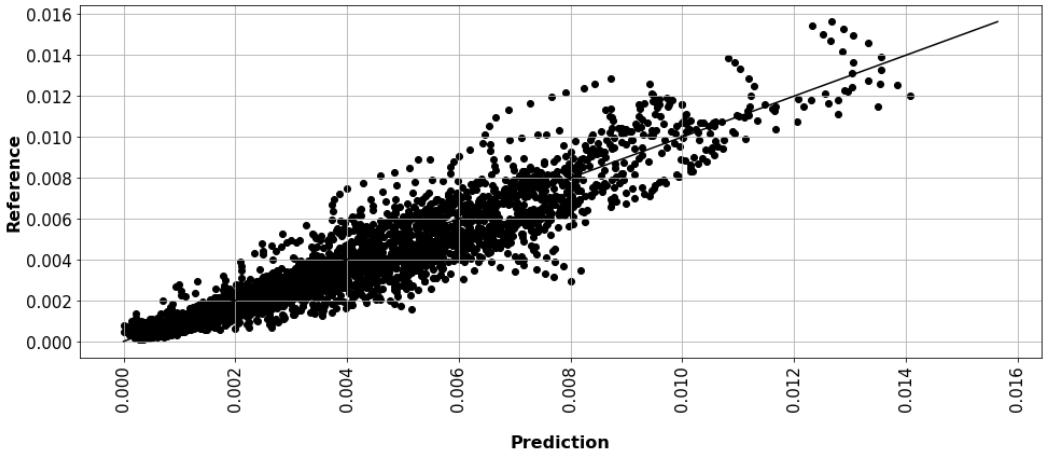

(e)

Figure 3.27. SD results of the TP and VP for RC building Y-direction: (a) Convergence curve – Loss in the TP; (b) Confusion Matrix – Usability of the building by VP; (c) Confusion Matrix – Total damage condition by VP; (d) Confusion Matrix – Story damage condition by VP; (e) Total comparison of SD

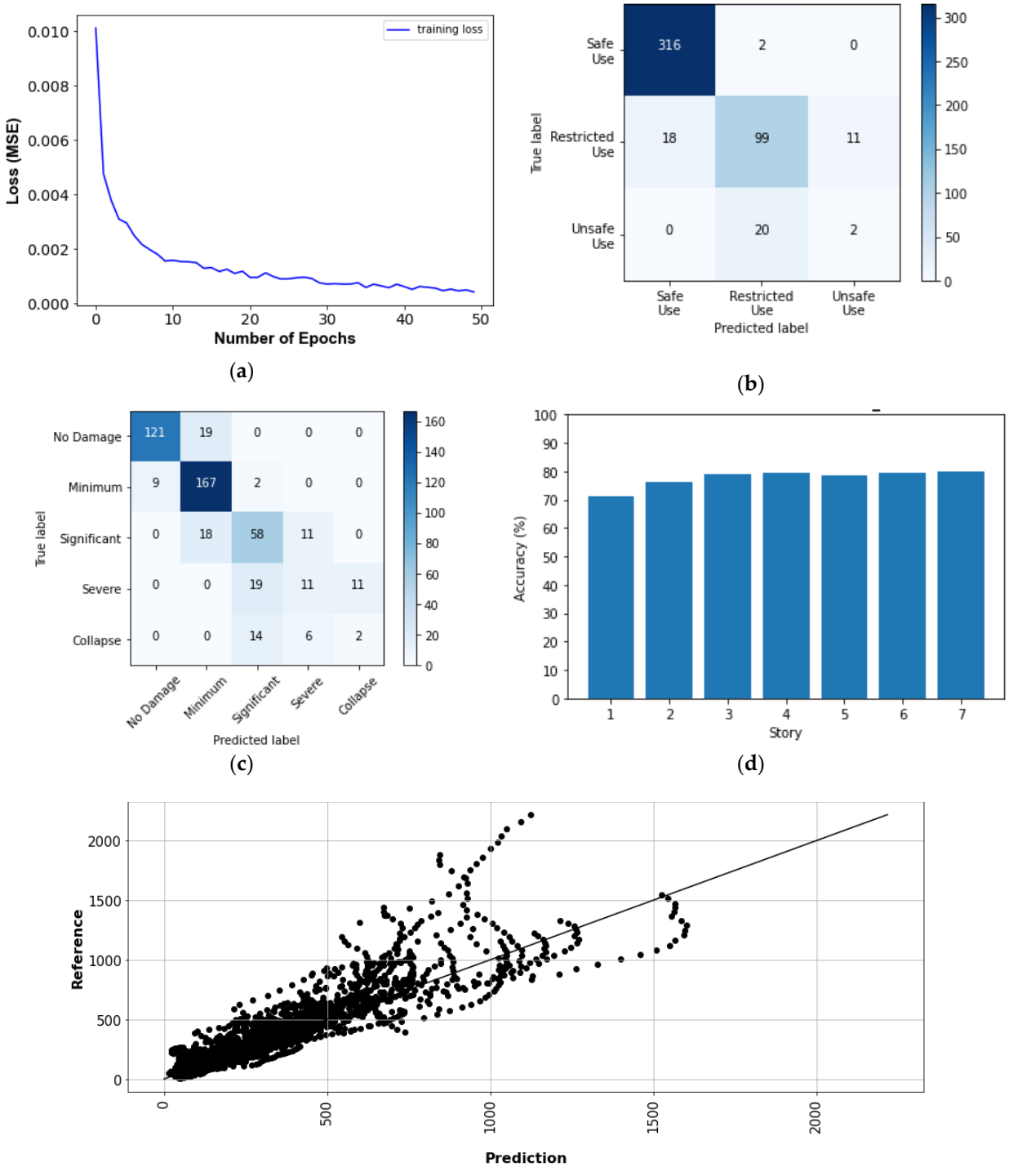

Figure 3.28. AA results of the TP and VP for RC building Y-direction: (a) Convergence curve – Loss in the TP; (b) Confusion Matrix – Usability of the building by VP; (c) Confusion Matrix – Total damage condition by VP; (d) Confusion Matrix – Story damage condition by VP; (e) Total comparison of AA.

Table 3.2 shows the evaluation accuracy of the target buildings in the VP. The results are summarized below:

- For the Tahara City Hall building, the maximum accuracy and R2 are 90.0% (usability of the building) and 0.825, respectively;
- For the Toyohashi Fire Station building, the maximum accuracy and R are 100% (damage condition of the basement) and 0.909, respectively;

- For the RC building in the X-direction, the maximum accuracy and R^2 are 89.8% (usability of the building) and 0.835, respectively;
- For the RC building in the Y-direction, the maximum accuracy and R^2 are 89.1% (usability of the building) and 0.871, respectively;
- In general, the accuracy of the estimation of SD is the highest.

Table 3.2. Evaluation accuracy of target buildings.

Accuracy evaluation		Tahara City Hall building		Toyohashi Fire Station building		RC Building			
						X - Direction		Y - Direction	
		SD	AA	SD	AA	SD	AA	SD	AA
Usability of the Building (Accuracy)		90.0%	84.2%	94.1%	88.1%	89.8%	85.9%	88.7%	89.1%
Total damage condition (Accuracy)		76.1%	74.5%	82.2%	71.2%	79.3%	73.2%	77.1%	76.7%
Story damage condition (Story accuracy)	Basement	--	--	100%	60.0%	--	--	--	--
	Story 1	76.8%	58.7%	96.9%	63.6%	82.2%	65.1%	87.6%	71.4%
	Story 2	76.9%	64.4%	94.1%	65.3%	79.8%	65.7%	81.0%	76.3%
	Story 3	76.3%	69.2%	92.4%	65.8%	79.5%	68.9%	78.9%	79.1%
	Story 4	74.8%	71.3%	91.1%	65.2%	80.3%	69.1%	78.7%	79.4%
	Story 5	74.4%	71.4%	89.9%	63.0%	80.5%	68.6%	79.3%	78.5%
	Story 6	75.3%	71.9%	88.8%	62.7%	80.5%	71.1%	79.7%	79.5%
	Story 7	--	--	87.8%	62.7%	80.8%	71.9%	80.0%	80.0%
Total comparison (R^2)		0.825	0.817	0.909	0.732	0.835	0.830	0.871	0.799

3.6 Conclusions and discussion

In this research article, a previous methodology proposed by the authors has been improved and applied to two instrumented buildings in Aichi Prefecture in Japan, called Tahara City hall and Toyohashi Fire Station. Also, it is applied to a third artificial structure called RC building in both directions. The summary of the proposed methodology is as follows:

- CNN models are trained per target building using the WPS of the absolute acceleration of the top floor record as input data to predict the SD and AA values. SD and AA are used as indicators to detect the damage state of the structures;
- A methodology to select records in order to reduce the variability of the structural responses using IDA is proposed, wherein the confidence interval between the 0% and 84% fractiles is adopted;
- The evaluation accuracy is discussed on the usability of the building, total damage condition, story damage condition, and total comparison of the damage indicator;
- The maximum accuracy and R^2 for the Tahara City Hall building are 90.0% (usability of the building) and 0.825, respectively;
- The maximum accuracy and R^2 for the Toyohashi Fire Station building are 100% (damage condition of the basement) and 0.909, respectively;
- The maximum accuracy and R^2 for the RC building in the X-direction are 89.8% (usability of the building) and 0.835, respectively.
- The maximum accuracy and R^2 for the RC building in the Y-direction are 89.1% (usability of the building) and 0.871, respectively.
- In general, the accuracy of the estimation of SD is the highest.

Finally, the improved methodology based on CNN immediately detects the structural damage condition of buildings, considering only one sensor on the top floor. Since the training and validation processes are computed before, a prediction can be obtained immediately after an earthquake. However, it is necessary to select records to improve the accuracy, and the ML model does not provide information on the feature importance (black box). Additionally, uncertainty is introduced from only one random selection of records for training and validation processes. So, selecting the training and testing records randomly several times is recommended.

Chapter 4. Machine Learning–Based Damage Detection using Intensity Measures for Three-Dimensional Buildings

4.1 Introduction

Chapter 3 proposed a methodology using only the time– and frequency–domain of the sensor response represented by the wavelet power spectrum obtains high accuracy for predicting damage conditions. However, CNN models do not reveal feature importance and require record selection for accuracy. Additionally, randomly selecting training and testing records multiple times can reduce uncertainty caused by only one selection.

This study updates and improves the damage identification method proposed in Chapter 3, as follows:

- The structural response used as a damage identifier is the story drift ratio.
- The methodology is applied to all database records (without selection).
- Seven ML methods are used and compared to CNN results.
- The input data for the ML models use Intensity Measures (IM) computed from the ground and roof sensor response.
- Several random record selections and statistical analyses are carried out in order to reduce its bias.
- The validation of the ML models is applied to two instrumented buildings in Japan.

This study was published by the author in [72]. This chapter contains sections as follows: In Section 4.2, a review of relevant literature is presented. In this study, the research methodology utilized is discussed in Section 4.3. It is validated in Section 4.4 through a case study and the Input Ground Motion utilized, and the results are shown in Section 4.5 of the target buildings. Finally, Section 4.6 presents the conclusion and discussion of the results.

4.2 Literature review

Currently, seismic instrumentation by acceleration sensors is used worldwide because it allows for characterizing the structure's performance before, during, and after an earthquake occurrence. For example, according to earthquake-resistance design standards, a minimum of 12 sensors are required for buildings with a number of stories from 6 to 10 above the ground for evaluating all structural directions [73,74]. However, researchers have developed methodologies with a sparse number of sensors to predict the performance of buildings immediately after an earthquake occurs. For instance, Xu and Mita [75] presented a method that estimates the maximum story drift ratio and time histories of the relative story displacements of buildings using one acceleration sensor on the roof level. Also, studies on optimal sensor placement for damage detection were developed by researchers [76-78].

This study presents a methodology to obtain the structural damage condition of buildings (represented by the maximum story drift ratio) and the optimum location of a sparse number of sensors using Intensity Measures (IMs) and ML methods.

The IMs represent the structural characteristic of signals based on acceleration, velocity, displacement, or a combination among them (hybrid) [79]. They are obtained from the sensor's signals and used as features for training seven ML models. In order to establish the optimum ML method and sensor's location, the accuracy and dispersion (represented by the determination coefficient and the standard deviation of the maximum story drift ratios) are compared by applying them to the Tahara City Hall and Toyohashi Fire Station buildings (target buildings). Also, the results are compared to the methodology using wavelet power spectra and the convolutional neural network method to predict the damage condition.

4.3 Research methodology

This research studies three sensor locations: Ground, Roof floor, and Rooftop sensor locations, as defined in Figure 4.1.

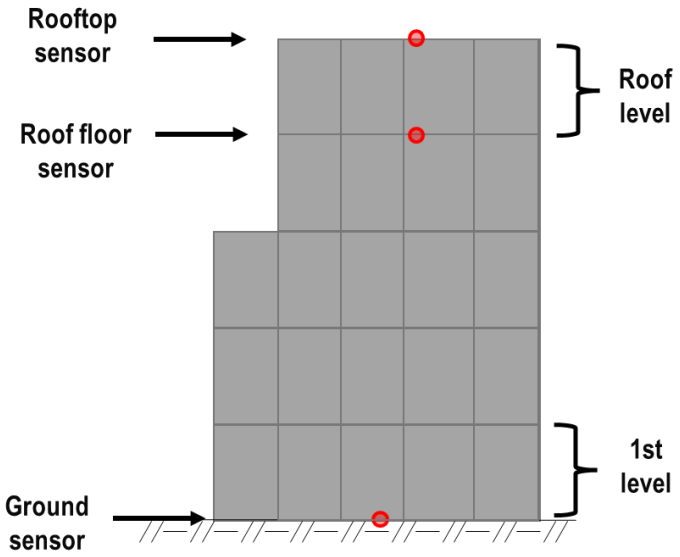

Figure 4.1. Definition of the sensor's location on the target building.

From the location of the sensors, five cases are studied for the target buildings:

Table 4.1. Sensor location cases.

Abbreviation	Case according to the sensor location usability
G	Only using the Ground sensor
RF	Only using the Roof floor sensor
Rt	Only using the Rooftop sensor
G + RF	Using the Ground and Roof floor sensor
G + Rt	Using the Ground and Rooftop sensor

The procedure to obtain the damage condition of buildings is as follows and its scheme is shown in Figure 4.2:

- Obtain the signal acceleration by the sensors.
- Obtain the Intensity Measures.
- Use the IMs as features for the ML models.
- Predict the maximum story drift ratio with the ML models.
- Classify the predicted maximum story drift ratio to obtain the damage condition of the building.

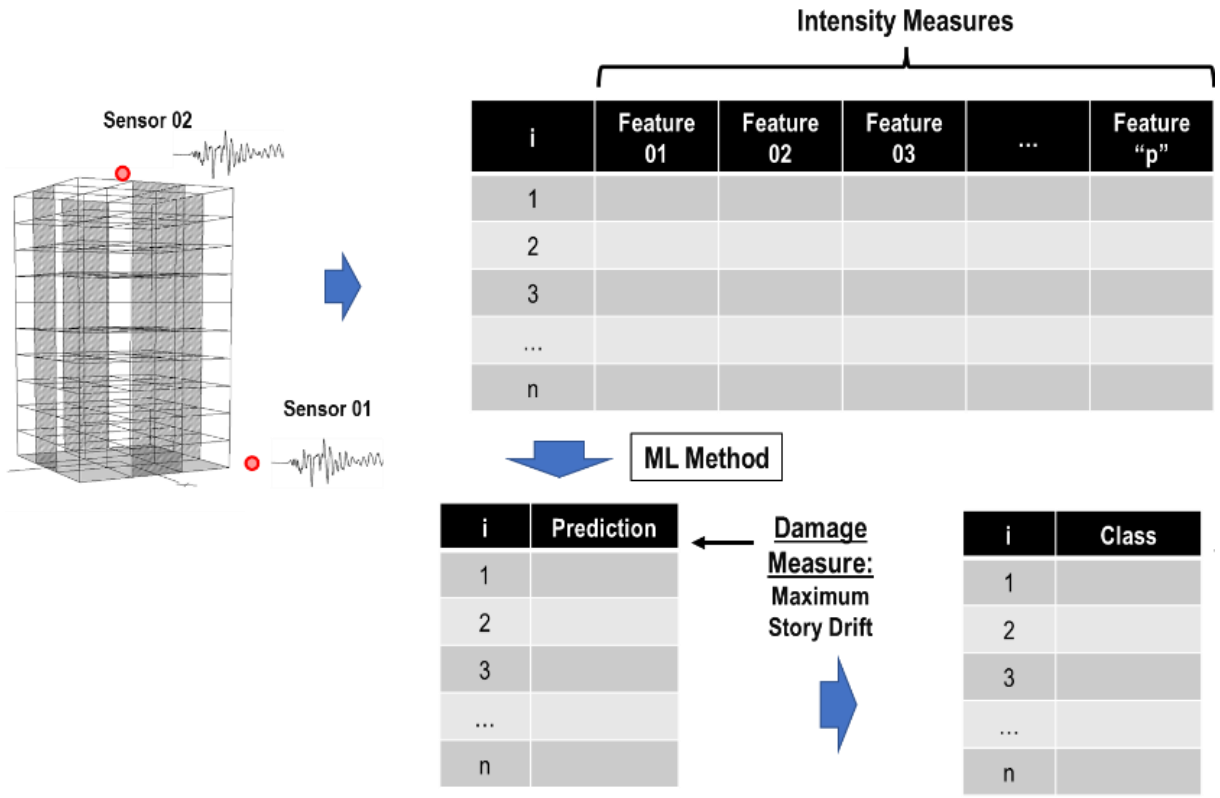

Figure 4.2. Procedure scheme of the study.

4.3.1 Intensity measures (IMs)

The IMs can be obtained based on either acceleration (A), velocity (V), displacement (D), or combining them (H: hybrid IM). They have been studied over the years to characterize the structural building responses using only the ground motion acceleration [26]. Table 4.2 shows the IMs used in this study.

Since the acceleration sensors were considered in this study, the double integration process was used to obtain the velocity and displacement signals.

Table 4.2. Intensity measures

N°	Name	Abbreviation	Based on	Definition	Reference
1	Peak Ground Acceleration	PGA	A	$PGA = \max_{0 \le t \le t_f} \lvert \ddot{u} \rvert$	[80]
2	5% damped first-mode Spectral Acceleration	Sa(T_1, 5%)	A	$S_a(T_1, 5\%) = \lvert max\ (\ddot{u}_{(T_1,5\%)} + \ddot{u}_g) \rvert$	[80,81]
3	Average Spectral Acceleration	Sa_{avg}	A	$Sa_{avg} = \left(\prod_{i=1}^{n} S_{a(T_i)} \right)^{1/n}$	[82]
4	Effective Peak Acceleration	EPA	A	$EPA = \frac{1}{2.5} * \int_{0.1}^{0.5} S_{a(T,h=5\%)} dT$	[83]
5	SR Power-law form IM	IM_{SR}	A	$IM_{SR} = S_a(T_1)^{1-\alpha} S_a\left(\sqrt{R}T_1\right)^{\alpha}$	[84]
6	CR Power-law form IM	IM_{CR}	A	$IM_{CR} = S_a(T_1)^{1-\alpha} S_a\left(\sqrt[3]{R}T_1\right)^{\alpha}$	[84]
7	Earthquake Power Index	EPI	A	$EPI = \frac{1}{t} * \int_0^t {a_{(\tau)}}^2 \, d\tau$	[85]
8	Root Mean Square Acc.	RMS	A	$RMS = \sqrt{EPI}$	[85]
9	Bojórquez & Iervolino IM	I_{Np}	A	$I_{N_P} = S_a(T_1, 5\%) \cdot \left(\frac{Sa_{avg}}{S_a(T_1, 5\%)} \right)^{\alpha}$	[86]
10	Arias Intensity	AI	A	$AI = \frac{\pi}{2g} * \int_0^t {a_{(\tau)}}^2 \, d\tau$	[69]
11	Sarma & Yang IM	A_{95}	A	$A_{95} = 0.05 \cdot \int_0^t {a_{(\tau)}}^2 \, d\tau$	[87]
12	Characteristic Intensity	I_C	A	$I_c = RMS^{1.5} \cdot t95\_t05^{0.5}$	[88]
13	Riddell & Garcia Acceleration IM	Ia	A	$I_a = a_{max} \cdot t95\_t05^{1/3}$	[89]
14	Cumulative Absolute Velocity	CAV	A	$CAV = \int_0^t \lvert a_{(\tau)} \rvert \, d\tau$	[90]
15	Standardized Cumulative Absolute Velocity	S-CAV	A	$S - CAV = \sum_{i=1}^{N} \left(H_{(PGA_i - 0.025)} \int_{i-1}^{i} \lvert a_{(t)} \rvert dt \right)$	[91]
16	Two-parameter hazard IM	TPH	A	$R_{S_a} = {S_a(T_f)}/{S_a(T_1)}$ $TPH = S_a(T_1) \cdot {R_{S_a}}^{\alpha}$	[92]
17	Peak Ground Velocity	PGV	V	$PGV = \max_{0 \le t \le t_f} \lvert v_{(t)} \rvert$	[80,93]
18	Squared Velocity	V_{sq}	V	$V_{sq} = \int_0^t {v_{(\tau)}}^2 \, d\tau$	[79]
19	Root Squared Velocity	V_{rms}	V	$V_{rms} = \sqrt{V_{sq}}$	[79]
20	Fajfar et al. IM	I_F	V	$I_F = PGV \cdot t95\_t05^{0.25}$	[94]
21	Riddell & Garcia Velocity IM	I_v	V	$I_v = PGV^{2/3} \cdot t95\_t05^{1/3}$	[89]
22	5% damped first-mode Spectral Velocity	Sv(T1, 5%)	V	$S_v(T_1, 5\%) = S_{v(T_1,h)}$	[80,81]
23	Housner Spectrum Intensity	SI_H	V	$SI_H = \int_{0.1}^{2.5} S_V \, d\tau$	[95]
24	Peak Ground Disp.	PGD	D	$PGD = \max_{0 \le t \le t_f} \lvert u_{(t)} \rvert$	[80]
25	5% damped first-mode Spectral Displacement	Sd(T1, 5%)	D	$S_d(T_1, 5\%) = S_{d(T_1,h)}$	[80,81]
26	Riddell & Garcia Velocity IM	I_d	D	$I_d = PGD \cdot t95\_t05^{1/3}$	[89]
27	Cosenza & Manfredi IM	Iz	H	$I_Z = {\left(\int_0^t {a_{(t)}}^2 \, dt \right)}/{(PGA \cdot PGV)}$	[96]

4.3.2 Machine learning methods

The following seven ML methods are used, and their parameters are calibrated after several runs (training process) in order to optimize the prediction. The optimum IMs are obtained from the feature importance level (from 0 to 1), which was obtained using the Gini importance technique [59,97] of the regression tree methods (no for Linear regression and Multilayer perception).

4.3.2.1 Linear Regression

This method assumes the output (prediction) is linearly dependent on the features. The coefficients (weights) are updated in order to minimize the prediction error obtained from the reference and predicted values [98,99].

The procedure is as follows: For "n" observations:

$$y_i = w_0 + w_1 x_1^i + w_2 x_2^i + \cdots + w_m x_m^i + \in \qquad \textit{Equation 4-1}$$

where:

- ✓ i: observation case
- ✓ y_i: dependent variable
- ✓ x_j^i: independent or explanatory variables
- ✓ w_0 : y-intercept (constant term)
- ✓ w_m: slope coefficients for each explanatory variable
- ✓ m: number of independent variables
- ✓ $\in$: the model's error term or the residuals

If $\in = 0$, then Equation 4-1 can be expressed as:

$$y_i \approx w_0 + \sum_{j=1}^{m} w_j x_j^i = \sum_{j=0}^{m} w_j x_j^i = \vec{w} \cdot \vec{x} \qquad \textit{Equation 4-2}$$

where:

$$\vec{w} = [w_0, w_1, \cdots, w_m]$$

$$\vec{x_i} = \left[1, x_1^i, x_2^i, \cdots x_m^i\right]$$

In the least-squares setting, the optimum parameter is defined as such that minimizes the sum of mean squared loss:

$$\vec{\widehat{w}} = \min_{w} \|Xw - y\|_2^2 \qquad \textit{Equation 4-3}$$

If the independent and dependent variables are expressed in matrices X and Y, respectively, then the loss function can be rewritten as:

$$\|Xw - y\|_2^2 = (X\vec{w} - Y)^T (X\vec{w} - Y) = L(D, \vec{w}) \qquad \textit{Equation 4-4}$$

As the loss is convex, the optimum solution lies at gradient zero. The gradient of the loss function is:

$$\vec{\hat{w}} = \frac{\partial L(D,\vec{w})}{\partial \vec{w}} \rightarrow 0 \qquad \textit{Equation 4-5}$$

4.3.2.2 Decision Tree

This method builds the best decision-making tree by splitting and selecting the order of the roots and leaves. The leaves are chosen when it is not possible for more optimization below those nodes [100,101]. There are two types of Decision Trees methods: classification and regression. The method scheme is shown in Figure 4.3.

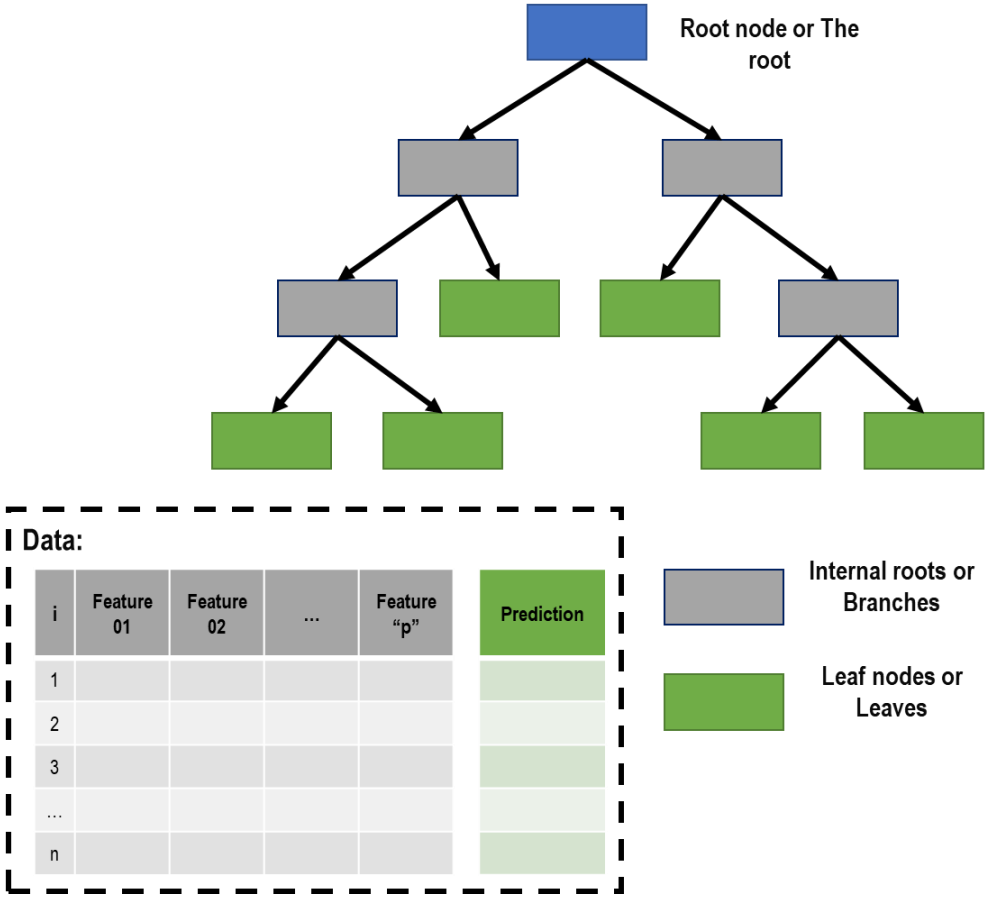

Figure 4.3. Decision Tree scheme.

Tree Impurity: The tree with less impurity will predict better than trees with more impurity. An example of tree impurity is shown in Figure 4.4.

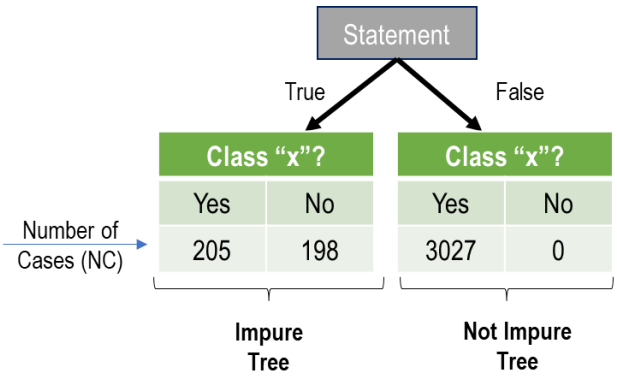

Figure 4.4. Tree impurity example.

The methods to quantify the "impurity" are the criteria to measure the quality of a split. They are Gini Impurity and Entropy. Additionally, it is possible to limit how trees grow—for example, by defining the impurity, setting the minimum number of samples required at a leaf node, or setting the maximum depth of the tree.

Gini Impurity: If Gini Impurity for a leaf = GI, it can be expressed as:

$$GI = 1 - (P[X = 'Yes'|leaf])^2 - (P[X = 'No'|leaf])^2 \qquad \textit{Equation 4-6}$$

$$Total_{GI} = w_{true} \cdot GI_{true} + w_{false} \cdot GI_{false} \qquad \textit{Equation 4-7}$$

where:

- ✓ $w_{true} = \frac{NC_{true}}{NC_{total}}$
- ✓ $w_{false} = \frac{NC_{false}}{NC_{total}}$

If a statement comes from a numerical feature, first, sorting it from the lowest to the highest value is necessary. The GI is calculated for the average of all adjacent values. The final GI is the lowest. The lowest GI is generally used to choose the best Root node and internal roots. When the GI is 0, it becomes to leaf.

Entropy: Measures the similarities and differences of a set of variables. The entropy is the highest when we have the same probability of a set of variables. On the other hand, it is the lowest when there are no differences in a set of variables. The Entropy is the Expected value of the surprise.

$$E = \sum P(X = x) \cdot x = \sum p(x) \cdot log\left(\frac{1}{p(x)}\right) \qquad \textit{Equation 4-8}$$

where:

- ✓ Probability of surprise = $P(X = x)$
- ✓ Surprise = x

Tree Splitting: The criterion to select the best split is according to the MSE_{total}. The scheme of the tree splitting is shown in Figure 4.5.

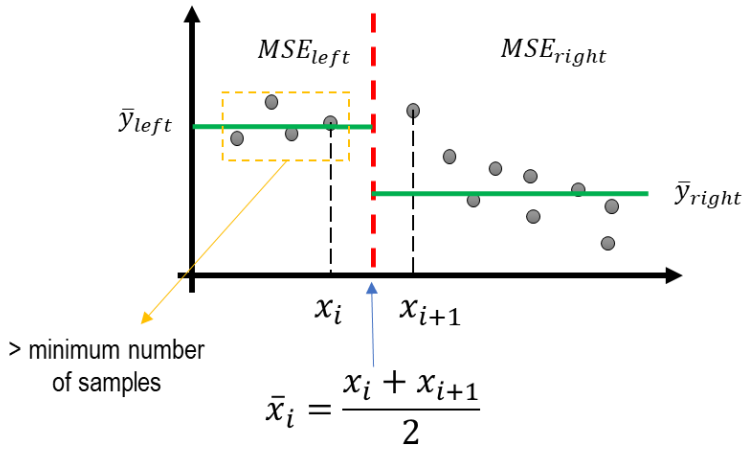

Figure 4.5. Tree splitting scheme.

The total MSE is obtained from the sum of MSE on the left and right sides.

$$MSE_{total} = MSE_{left} + MSE_{right} \qquad \textit{Equation 4-9}$$

The $\bar{x}_i$ that provides the minimum MSE_{total} is the selected split value. The data is split into two groups by finding the minor MSE threshold. MAE could replace MSE.

Cost Complexity Pruning: In order to avoid overfitting, the pruning method is carried out. The three running scheme is shown in Figure 4.6.

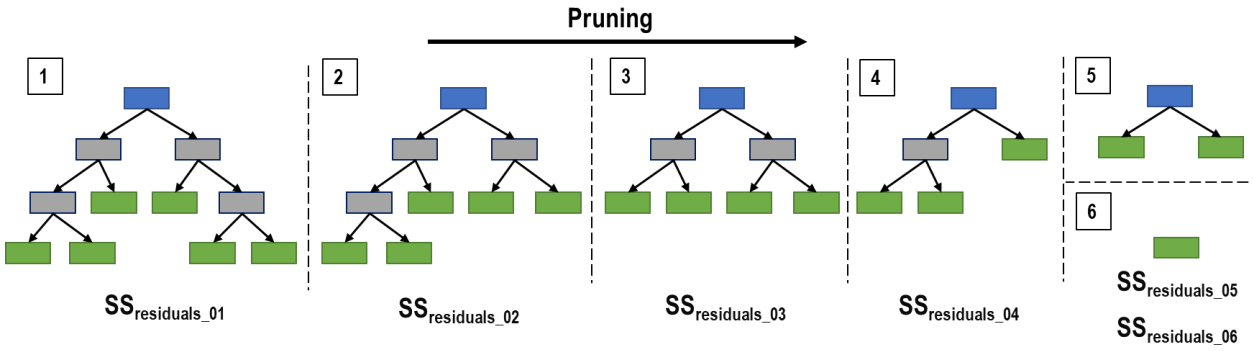

Figure 4.6. Tree pruning scheme.

The score of the tree in each case ($Tree\ Score_i$) can be expressed as:

$$Tree\ Score_i = SS_{residuals\_i} + (\alpha \cdot T_i) \qquad \textit{Equation 4-10}$$

where:

- ✓ α is a tuning parameter
- ✓ T_i is the total number of leaves
- ✓ $(\alpha \cdot T_i)$ is the tree complexity penalty

In order to obtain the best accuracy, different α is evaluated using the total data (training and test data). Later, the smallest Tree Score is obtained using de α found previously by evaluating new training and test data in order to get a newly pruned tree. This last process is repeated by shifting the training and test data. Figure 4.7 shows an example of the accuracy obtained by varying α, and Figure 4.8 shows an example of the maximum depth of the tree.

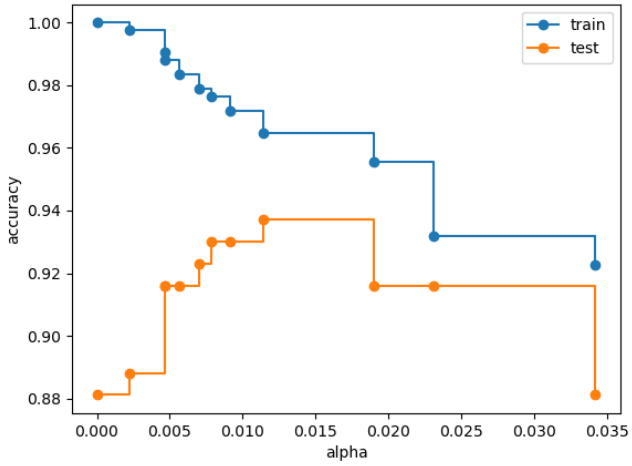

Figure 4.7. Example of accuracy vs. α for training and testing sets.

Figure 4.8. Example of the maximum depth of the tree.

Decision Tree Advantages:

- ✓ Understandable and interpretable.
- ✓ Normalization is not required.
- ✓ For classification and regression.
- ✓ White box model.

Decision Tree Disadvantages:

- ✓ Overfitting is possible but avoided by pruning, setting the minimum number of samples required at a leaf node, or setting the maximum depth of the tree.
- ✓ Decision trees can be unstable but avoided by using decision trees within an ensemble (Random Forest).
- ✓ The decision tree is not good at extrapolation because the prediction is not a continuous or smooth function.

The parameters used in this study are shown in Table 4.3.

Table 4.3. Decision Tree parameters

Parameters	Value
Function to measure the quality of a split	MSE
Maximum depth of the tree	No-limit
Minimum number of samples to split	2
Minimum number of leaf nodes	1
Maximum number of leaf nodes	No-limit

4.3.2.3 Random Forest

This method builds several decision trees (forest) from bootstrapped datasets (a new random dataset with the same size as the original one), increasing its accuracy in this way. The new data to predict is evaluated in the forest [59,102].

Bootstrapped dataset: It is a dataset that has the same size as the original. The samples are selected randomly from the original dataset. The samples can be chosen more than once. Bootstrapping the data and using the aggregate to decide is called "Bagging." The Bootstrapped datasets scheme for the random forest method is shown in Figure 4.9.

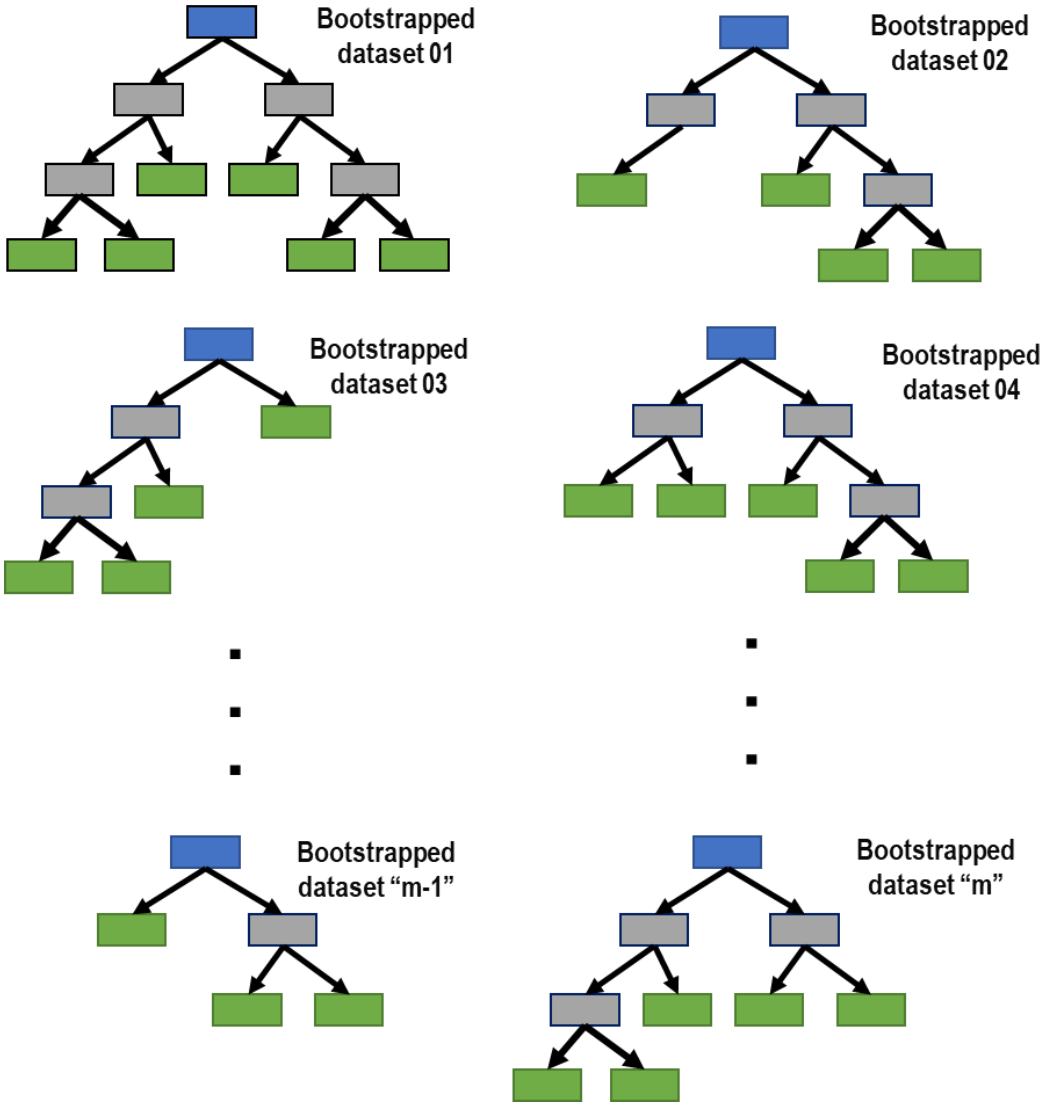

Figure 4.9. Random Forest scheme.

Accuracy: In order to measure the accuracy, the Out-Of-Bag dataset is evaluated in the random forest. The proportion of Out-Of-Bag samples incorrectly classified is the "Out-Of-Bag Error." The Out-Of-Bag dataset scheme is shown in Figure 4.10.

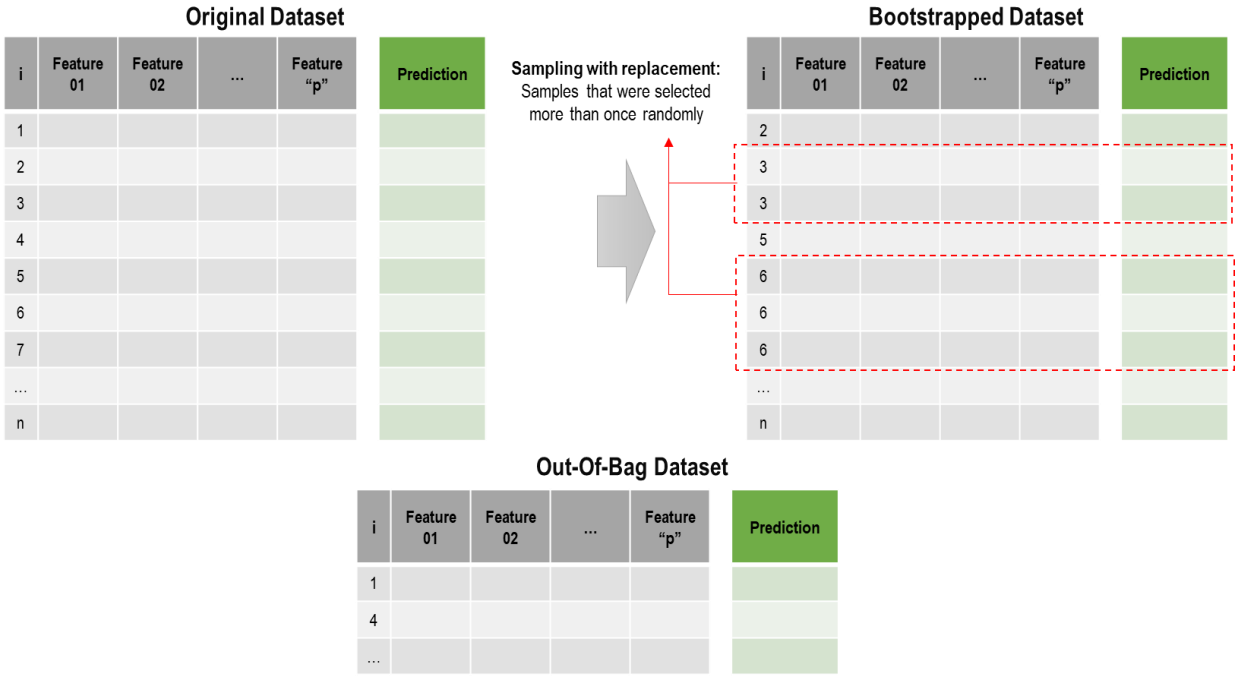

Figure 4.10. Out-Of-Bag dataset scheme.

The parameters used in this study are shown in Table 4.4.

Table 4.4. Random Forest parameters

Parameters	Value
Number of trees in the forest	100
Function to measure the quality of a split	MSE
Maximum depth of the tree	No-limit
Minimum number of samples to split	2
Minimum number of leaf nodes	1
Maximum number of leaf nodes	No-limit

4.3.2.4 Gradient Boosting (Gradient Boost)

This method makes a tree to obtain residuals instead of predictions. Then, a new predictor is built using the previous predictor (the first one predicts the same value for all and then is updated) and adds the residuals predictor (a learning rate scales it). Therefore, the new predictor is based on the previous tree's errors [59]. Figure 4.12 shows the scheme of the new predictor, and Figure 4.13 shows the scheme to obtain the residuals using the new prediction.

It starts by making a single leaf instead of a tree or stump. This leaf represents an initial guess for the samples' weights. For this continuous value, the first guess is the average value. Like AdaBoost, Gradient Boost builds fixed-sized trees based on the previous tree's errors, but unlike AdaBoost, each tree can be larger than a stump. Also, like AdaBoost, Gradient Boost scales the trees. However, Gradient Boost scales all trees by the same amount (learning rate). Then Gradient Boost builds another tree based on the previous tree's errors and then scales the tree. The scheme to obtain the residuals using the average prediction is shown in Figure 4.11.

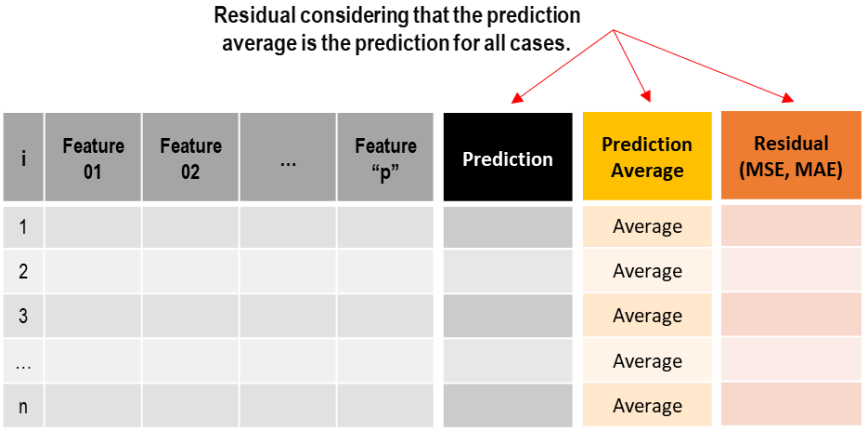

Figure 4.11. Residuals using the prediction average.

If two or more rows of data (features) predict the same residual leaf, the result taken is the average value. Make a tree considering a maximum depth (8-32) in order to predict residuals instead of predictions.

$$NewPredicted_{value} = Prediction + (learning\_rate)(residual) \qquad Equation\ 4\text{-}11$$

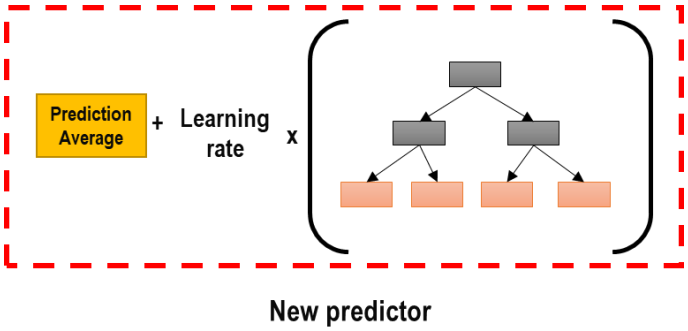

Figure 4.12. New predictor in Gradient Boost.

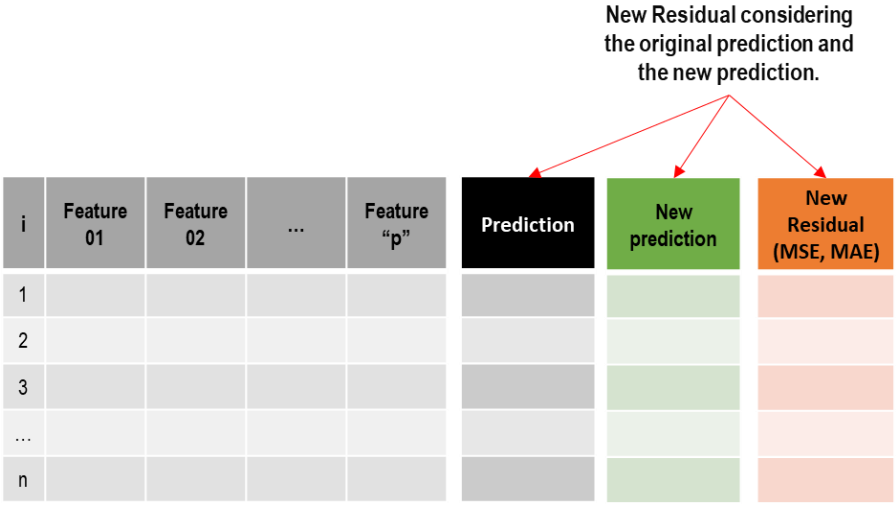

Figure 4.13. Residuals using the new prediction.

This process is repeated several times in order to reduce the residual by making trees until the maximum specified (number of estimators) or adding additional trees does not significantly reduce the size of the residuals.

The parameters used in this study are shown in Table 4.5.

Table 4.5. Gradient Boost parameters

Parameters	Value
Number of estimators	100
Learning rate	0.1
Function to measure the quality of a split	MSE
Maximum depth of the tree	No-limit
Minimum number of samples to split	2
Minimum number of leaf nodes	1
Maximum number of leaf nodes	No-limit

4.3.2.5 AdaBoost

It is a meta-estimator (an estimator which takes another estimator as a parameter, Decision Tree in this case) that begins by fitting a regressor on the original dataset and then fits additional copies of the regressor on the same dataset, but where the weights of instances are adjusted according to the error of the current prediction. As such, subsequent regressors focus more on complex cases. [59]

Stumps: AdaBoost creates a forest of stumps rather than trees. However, stumps are not great at making accurate predictions (weak learners). For this reason, it uses weights in order to vote for the final prediction. Figure 4.14 shows the scheme of a stump.

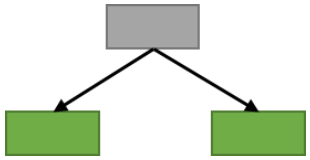

Figure 4.14. Stump scheme.

Some stumps get more influence in the classifications than others. The previous stump's error influences how the following stump is made. Figure 4.15 shows the scheme of stumps with different weights (depicted by size).

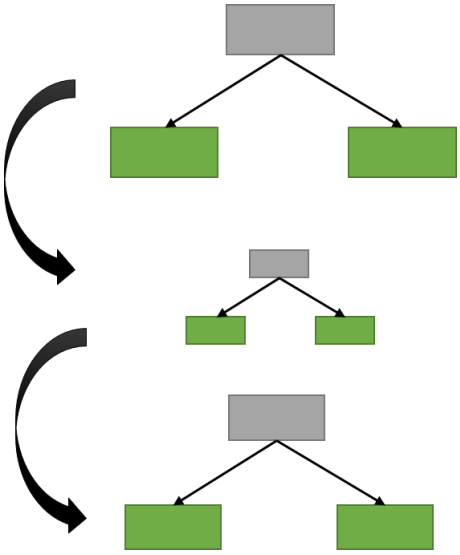

Figure 4.15. Scheme of stumps with different weights (depicted by size).

Figure 4.16 shows the methodology used in the AdaBoost method. The stump with the minimum Gini Index is the first in the forest.

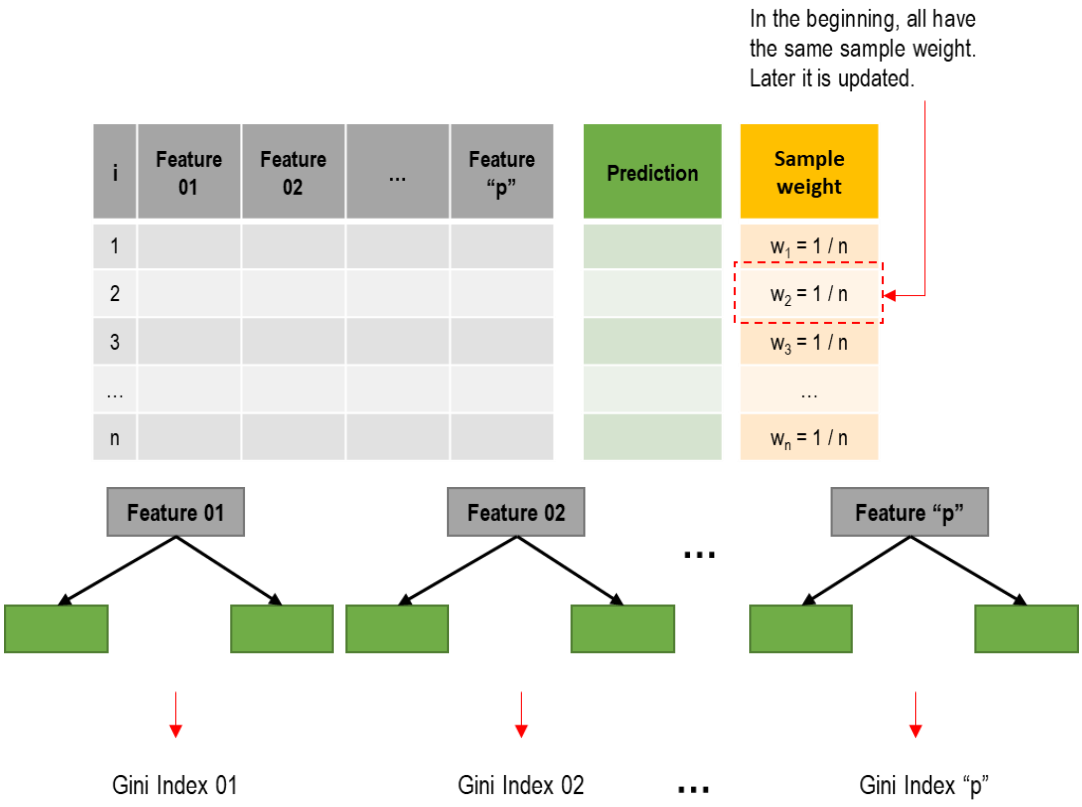

Figure 4.16. AdaBoost methodology.

Total weighted error (*TWE*): For a stump is the sum of the weights associated with the incorrectly classified samples. It will always be between 0 for a perfect stump and 1 for a non-perfect stump prediction.

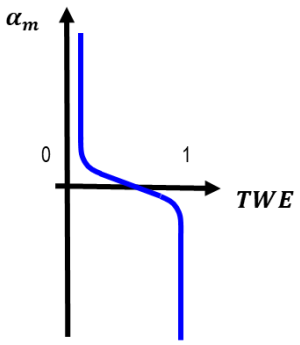

Figure 4.17. Total weighted error vs α_m

$$TWE = \sum w^{incorrect} \qquad \textit{Equation 4-12}$$

$$\alpha_m = \frac{1}{2} \cdot log\left(\frac{1 - TWE}{TWE}\right) \qquad \textit{Equation 4-13}$$

where:

α_m: Amount of say

Obtaining new sample weights:

$$w_i^* = w_{old}^{incorrect} \cdot e^{\alpha_m}$$

$$w_i^* = w_{old}^{correct} \cdot e^{-\alpha_m}$$

$$w_{new} = \frac{w_i^*}{\sum w_i^*}$$

Weighted Gini Indexes (WGI): The New sample weights are used to determine which variable should split the next stump. The WGI takes into account the misclassified samples (larger sample weight).

i	Feature 01	Feature 02	…	Feature "p"	Prediction	New Sample weight
1						w_{new-1}
2						w_{new-2}
…						…
n						w_{new-n}

Figure 4.18. New sample weight scheme.

The parameters used in this study are shown in Table 4.6.

Table 4.6. AdaBoost parameters

Parameter	Value
Number of estimators	50
Maximum depth of the tree	3
Minimum number of samples to split	2
Minimum number of leaf nodes	1
Maximum number of leaf nodes	No-limit
Loss function to update the weights	linear

4.3.2.6 Extreme Gradient Boosting (XGBoost)

This ML method is called extreme because it is built with several parts. Like Gradient Boost, the regression tree is obtained using residuals instead of predictions by the similarities and gain values method for splitting and getting the thresholds. The pruning method is used to reduce this tree. Also, this method uses the Regularization parameter to minimize the prediction's sensitivity to individual observations. Finally, it uses the original previous predictor and learning rate to obtain a new predictor [103]. The parameters used in this study are shown in Table 4.7.

Table 4.7. XGBoost parameters

Parameter	Value
Number of estimators	100
Learning rate	0.1
Function to measure the quality of a split	MSE
Maximum depth of the tree	No-limit
Minimum number of samples to split	2
Minimum number of leaf nodes	1
Maximum number of leaf nodes	No-limit

4.3.2.7 Multilayer Perceptron

It interconnects a group of units or nodes and transmits signals (information) to other "neurons" inspired by the biological neural networks that constitute animal brains. Each connection has weights that are adjusted to reduce the error. [100,104].

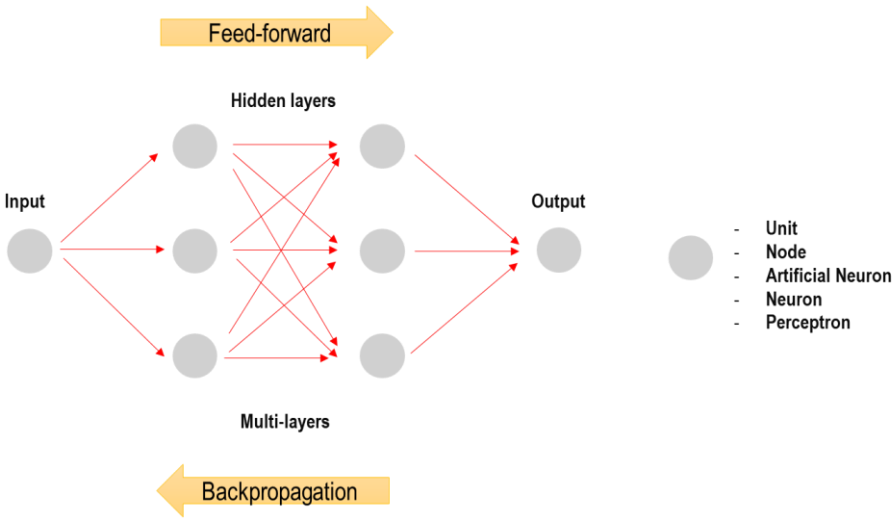

Figure 4.19. Multilayer Perceptron network scheme.

The parameters used in this study are shown in Table 4.8.

Table 4.8. Multilayer Perceptron parameters

Parameter	Value
Hidden layer size	100
Maximum number of iterations	100
Learning rate	0.001
Batch size	2
Activation function	ReLU

4.4 Case study and input ground motion

4.4.1 Target buildings

The Tahara City Hall (TCH) and Toyohashi Fire Station (TFS) buildings located in Japan are studied in this research (shown in Figure 3.2 and Figure 3.4, respectively). They are instrumented with two sensors in G and the RF locations. However, this research also evaluates the case of the sensor on the rooftop (Rt location).

4.4.2 Nonlinear structural models for the target buildings

The buildings used in this chapter are the same as modeled in section 3.3.2.

4.4.3 Ground motion records

The selection of records procedure proposed in Chapter 3 is not considered in order to include the variability of the records. For this reason, the original 183 ground motion acceleration records are used in this chapter.

4.4.4 Incremental dynamic analyses

The Incremental Dynamic Analysis (IDA) obtains the structural responses (maximum story drift ratio), increasing the ground motion intensity by a representative IM. The scale factors are selected in order to cover the elastic and inelastic behavior. Sa(T1, 5%) is used as IM for developing the incremental analysis

[105]. Also, all the records were scaled in order to obtain the same Sa(T1, 5%). The minimum, maximum and incremental steps of Sa(T1, 5%) were 25, 2000, and 25 gal, respectively. Since the TCH building has an irregular structural configuration, the incremental step of Sa(T1, 5%) over 250 gal was each 5 gal. Therefore, 65 880 and 14 640 nonlinear time-history analyses were carried out for TCH and TFS buildings.

4.4.5 Structural damage condition of buildings

The damage condition is obtained only using the story drift ratio from Chapter 2 and shown in Table 1.1.

Since the collapse state is greater than 1/75 (0.0133), results greater than 0.02 were not considered in order to increase and reduce the accuracy and dispersion of the ML models, respectively.

4.5 Prediction and validation of the target buildings

4.5.1 Training and testing process

For the training and testing process, 146 (80%) records and 37 (20%) new records were randomly selected, respectively. In order to increase the number of results for each ML model (to reduce a biased process), 50 random records selection were carried out. Therefore, 50 prediction results are obtained.

The prediction accuracy of the ML models is evaluated by the coefficient of determination (R^2) (an example result is shown in Fig. 4.20(a)). A normal distribution function of the R^2 from the 50 prediction results is assumed (see Fig. 4.20(b)). The maximum (Max.), mean, and standard deviation (σ) of the R^2 are computed to compare the effectiveness and the dispersion among the ML models and sensor locations. Besides, the importance level of the features (IMs) for predicting is obtained for each case, as shown in Fig. 4.20(c).

Table 4.9 and Table 4.10 show the ML method results for the Tahara City Hall and Toyohashi Fire Station buildings. The IMs are ordered descending from left to right (collected from the feature importance levels greater than 0.05).

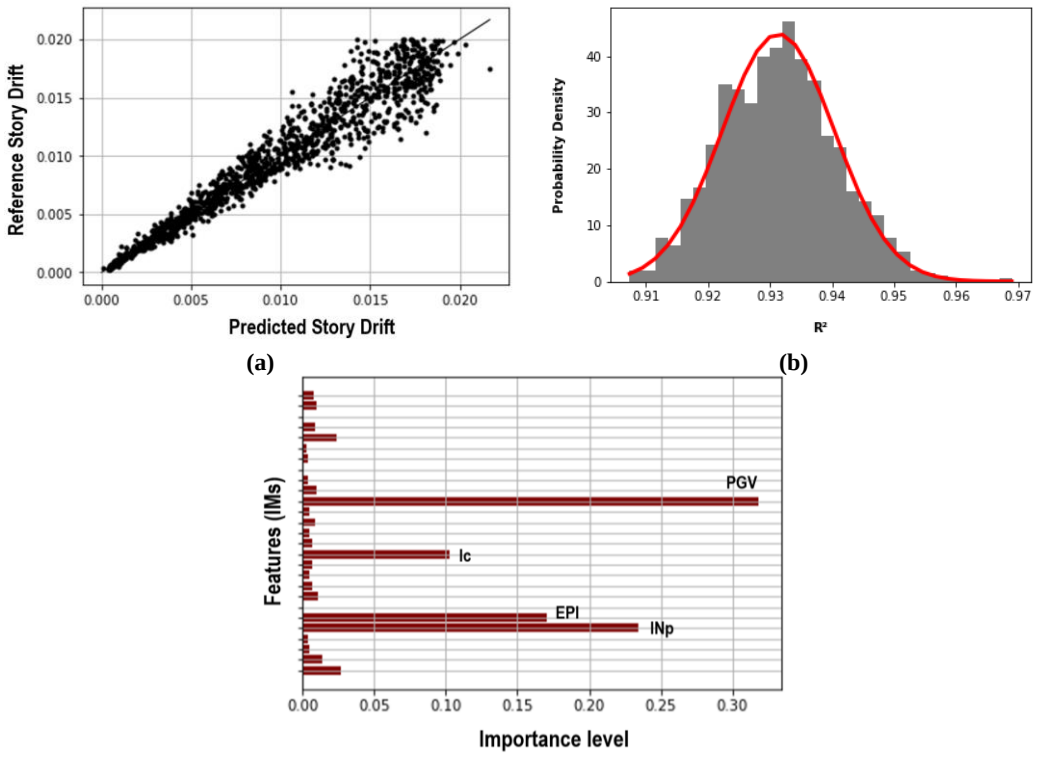

Fig. 4.20. Results example (a) Story drift prediction and reference (R^2 = 0.94). (b) Normal distribution function of the R^2 from the 50 records selection cases (mean = 0.931; σ = 0.009). (c) Importance levels of the features (IMs).

Table 4.9. Tahara City Hall building results.

Coefficient of determination (R^2) and Intensity Measures								
Sensor Location	**Linear Regression**				**Decision Tree Regressor**			
	Maximum	**Mean**	**σ**	**IM**	**Maximum**	**Mean**	**σ**	**IM**
G	**0.912**	**0.867**	0.035	---	0.847	0.76	0.038	SaT1, EPA
Rt	**0.913**	0.831	0.046	---	0.801	0.71	0.041	PGA, TPH, SIH, PGV
RF	**0.906**	0.794	0.092	---	0.82	0.751	0.034	PGA
G + Rt	0.91	0.745	0.663	---	0.857	0.8	0.034	G_SaT1, R_EPA, R_PGA
G + RF	**0.925**	0.768	0.135	---	0.824	0.765	0.039	R_PGA
Sensor Location	**Random Forest Regressor**				**Gradient Boosting Regressor**			
	Maximum	**Mean**	**σ**	**IM**	**Maximum**	**Mean**	**σ**	**IM**
G	0.905	0.849	0.027	SaT1, EPA	0.908	0.865	**0.024**	SaT1, EPA
Rt	0.876	0.817	0.032	PGA, PGV, SIH	0.897	**0.857**	**0.021**	PGA, PGV
RF	**0.906**	0.826	0.033	PGA	0.904	**0.845**	0.031	PGA
G + Rt	0.915	0.867	0.026	G_SaT1, R_EPA, R_PGA	**0.926**	**0.892**	**0.021**	G_SaT1, R_PGA, R_EPA, G_INp
G + RF	0.898	0.859	0.025	R_PGA	0.914	**0.875**	**0.02**	R_PGA, G_SaT1
Sensor Location	**AdaBoost Regressor**				**XGBoost Regressor**			
	Maximum	**Mean**	**σ**	**IM**	**Maximum**	**Mean**	**σ**	**IM**
G	0.877	0.824	0.03	SaT1, Inp, EPA	0.88	0.831	0.032	INp, SaT1, EPA
Rt	0.842	0.798	0.023	PGA, PGV, TPH, EPI, RMS, A95, SIH, Iz	0.88	0.827	0.033	PGV, PGA, EPI
RF	0.855	0.82	0.021	PGA, SaT1, EPA, TPH, PGV, A95, RMS	0.88	0.822	0.038	PGA, EPA, PGV, SIH
G + Rt	0.891	0.845	0.024	G_SaT1, R_PGA, G_INp,G_PGV	0.913	0.865	0.023	R_PGA, G_INp
G + RF	0.89	0.845	0.025	G_SaT1, R_PGA, R_SaT1	0.903	0.855	0.029	R_PGA, G_INp, G_SaT1
Sensor Location	**Multilayer Perceptron Regressor**				**Convolutional Neural Network**			
	Maximum	**Mean**	**σ**	**IM**	**Maximum**			
G	0.889	0.805	0.056	---	---			
Rt	0.866	0.78	0.057	---	0.825			
RF	0.881	0.804	0.05	---	---			
G + Rt	0.895	0.79	0.124	---	---			
G + RF	0.882	0.801	0.064	---	---			

Table 4.10. Toyohashi Fire Station building results.

Coefficient of determination (R^2) and Intensity Measures								
Sensor Location	**Linear Regression**				**Decision Tree Regressor**			
	Maximum	**Mean**	**σ**	**IM**	**Maximum**	**Mean**	**σ**	**IM**
G	**0.927**	**0.877**	0.062	---	0.832	0.777	0.031	SIH, RMS
Rt	**0.958**	**0.935**	0.013	---	0.903	0.866	0.017	PGV, RMS
RF	0.9	0.837	0.041	---	0.801	0.812	0.024	PGV, PGA, Ic
G + Rt	**0.958**	0.914	0.054	---	0.899	0.862	0.022	R_PGV, R_Ic
G + RF	**0.951**	0.84	0.126	---	0.884	0.812	0.024	R_SIH, R_PGV
Sensor Location	**Random Forest Regressor**				**Gradient Boosting Regressor**			
	Maximum	**Mean**	**σ**	**IM**	**Maximum**	**Mean**	**σ**	**IM**
G	0.916	0.877	0.018	SIH	0.915	0.873	0.022	SIH, EPA
Rt	0.949	0.927	0.018	PGV	0.951	0.931	0.009	PGV, PGA, RMS
RF	0.907	0.855	0.022	PGV, Ic	0.908	0.865	0.02	PGV, Ic, EPA, EPI, RMS, PGA
G + Rt	0.95	0.928	0.012	R_PGV	0.95	0.928	0.012	R_PGV, R_RMS, G_SaT1
G + RF	0.929	0.899	0.019	G_SIH	0.925	0.893	0.016	G_SIH, G_PGV, R_RMS
Sensor Location	**AdaBoost Regressor**				**XGBoost Regressor**			
	Maximum	**Mean**	**σ**	**IM**	**Maximum**	**Mean**	**σ**	**IM**
G	0.884	0.836	0.023	SIH, EPA, TPH, SaT1	0.916	0.864	0.027	SIH, Ic
Rt	0.922	0.901	0.012	PGV, PGA, SaT1	0.94	0.923	0.01	PGV, INp, EPI, Ic
RF	0.843	0.8	**0.02**	EPA, PGV, TPH, INp	0.899	0.85	0.027	PGV, EPI, TPH
G + Rt	0.922	0.897	0.015	R_PGV, R_PGA, R_INp	0.942	0.918	0.013	R_PGV, R_Ic, R_EPI, G_SaT1
G + RF	0.886	0.849	0.02	G_EPA, G_SaT1, G_SIH, R_SIH	0.92	0.884	0.019	G_SIH, G_PGV, R_EPI, G_SaT1
Sensor Location	**Multilayer Perceptron Regressor**				**Convolutional Neural Network**			
	Maximum	**Mean**	**σ**	**IM**	**Maximum**			
G	0.897	0.799	0.052	---	---			
Rt	0.936	0.889	0.037	---	0.909			
RF	0.876	0.756	0.198	---	---			
G + Rt	0.936	0.875	0.036	---	---			
G + RF	0.905	0.816	0.063	---	---			

For the CNN method [64], only the maximum R^2 was obtained from Rt location, which is 0.825 and 0.909 for Tahara City Hall and Toyohashi Fire Station buildings, respectively. Notice that the Gradient Boosting method provides better results than the CNN method.

4.6 Conclusions and discussion

In this research, a proposed methodology is proposed to obtain the structural damage condition of buildings and the optimum location of a sparse number of sensors using Intensity Measures and Machine Learning methods. This methodology is applied to two actual buildings, Tahara City Hall and Toyohashi Fire Station buildings, and the results are summarized as follows:

- For the Tahara City Hall building, the Gradient Boost is the ML method that gives the best maximum, mean, and σ of the R^2 results, which are 0.926, 0.892, and 0.021, respectively. They are obtained using the G + Rt sensor location. They are greater than the given by the CNN method [64].
- For the Toyohashi Fire Station building, the Gradient Boost is the ML method that gives the optimum maximum, mean, and σ of the R^2 results, which are 0.951, 0.931, and 0.009, respectively. They are obtained using the Rt sensor location. They are greater than the given by the CNN method [64].
- The optimum sensor location is when the Ground and Rooftop sensors work simultaneously or only the Rooftop sensor.
- The acceleration intensity measures are the main features for predicting the Tahara City Hall building's damage condition.
- The velocity intensity measures are the main intensity measures for Toyohashi Fire Station.

The methodology using several Intensity measures from the sensor response obtains high accuracy for predicting damage conditions of buildings' three-dimensional frame models without selecting records. The building's damage condition and feature importance are possible to detect immediately after the earthquake occurs because the ML is trained and validated beforehand. Additionally, the uncertainty is studied by randomly selecting the training and testing records, obtaining a low dispersion with high accuracy. This process helps to decide the best sensor's location and IMs for prediction. However, only new records are predicted for instrumented buildings. Then, it is recommended to propose a methodology to predict new buildings, which will be studied in the next chapter.

Chapter 5. Rapid Post-Earthquake Damage Detection of Buildings based on Machine Learning

5.1 Introduction

It is possible to predict the damage condition of buildings using information from other buildings with similar features. For example, the fundamental vibration period of buildings, which is obtained approximately using the number of stories or their height [106], is one of the most used parameters to estimate the global stiffness of a structure. Likewise, the lateral load-resisting system can be estimated from the plastic deformation mechanism of the structure. [107,108]. On the other hand, the structural acceleration, velocity, or displacement response of a building is influenced by its structural properties and earthquake input characteristics [109]. For example, intensity measures (IM) based on the earthquake ground acceleration have the greatest impact on short-period structures [79]. Therefore, it is possible to establish an archetype (parametric model) of the buildings built by their main structural characteristics and select the best and minimum set of buildings to be the reference to accurately predict the damage condition of the rest of the buildings under various intensity measures. This process is possible using ML methods which capture the main features of input data in order to predict particular output data [18,98].

This study proposes ML methods to predict the damage condition of RC resisting-moment frame buildings based on the building configurations and IMs of input earthquakes and roof sensor acceleration responses. IDA are carried out to cover the elastic and inelastic behavior of the building. The ML models are trained using a different number of stories and spans in X and Y directions to predict the damage condition of the building expressed by inter-story drift ratios. The proposed ML model can be used to detect post-earthquake damage in many other buildings without sensors, based on earthquake acceleration data observed by sensors installed on the ground or on the roof of the building. This study was published by the author in [110].

This chapter contains sections as follows: In section 5.2 presents the methodology and provides an overview of the proposed research procedure. Section 5.3 shows the information to obtain the structural responses from the design of the archetype buildings using the virtual work method, selections of records, and the IDAs presenting several intensity measures. Section 5.4 presents the ML methodology to predict the damage condition of buildings, the case study results, and their discussion. Finally, section 5.5 presents a summary of the conclusions of the research.

5.2 Research methodology

Figure 5.1 shows the procedure to obtain the structural responses used in the ML methods. An archetype of buildings is developed, designed using the virtual work method, and verified using nonlinear static analysis. On the other hand, ten records are selected using the uniform hazard spectrum and used as input ground accelerations for Incremental Dynamic Analyses. The result is 60000 structural linear and nonlinear responses.

In this study, the ML methods use IMs, the number of stories, and the number of spans in X and Y directions as input data and the maximum inter-story drift ratio as output data. Additionally, the ground motion records are split randomly to obtain the data in the training process (80% of records) and the testing process (10% of records). Likewise, the buildings are split randomly to obtain the data in the training process (10% of buildings) and the testing data (90% of buildings). In order to reduce the bias due to the random splitting, this process is carried out several times.

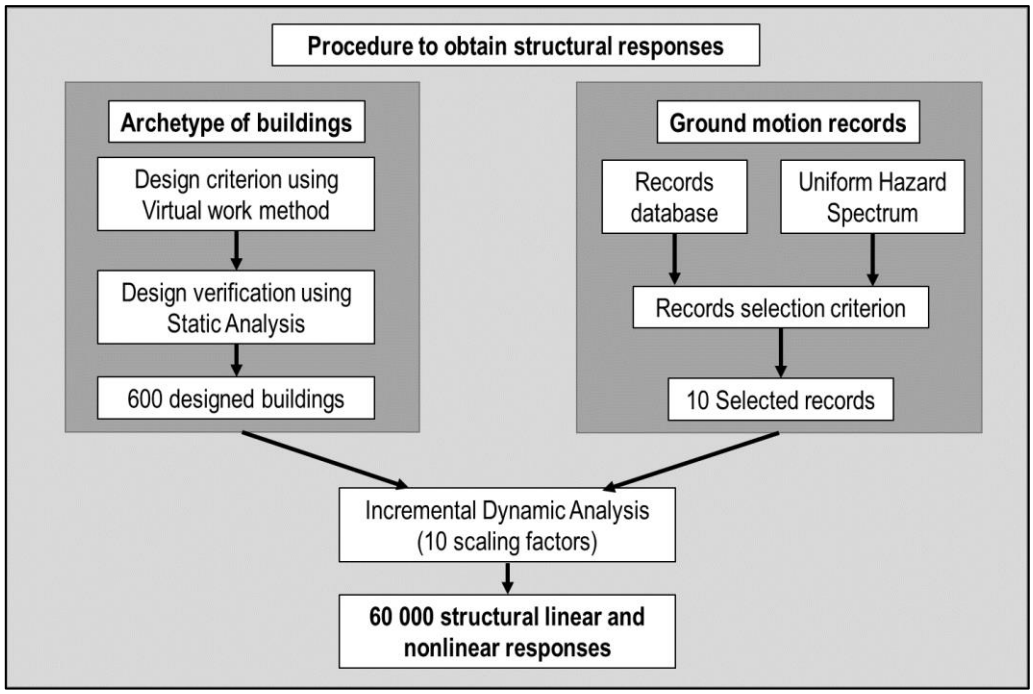

Figure 5.1. Procedure to obtain structural responses.

5.3 Structural design and input ground motions

5.3.1 Archetype of buildings

5.3.1.1 Structural distribution

RC moment-resisting frame system is used for the archetype of buildings. Figure 5.2 shows the plan and elevation view of the archetype of buildings.

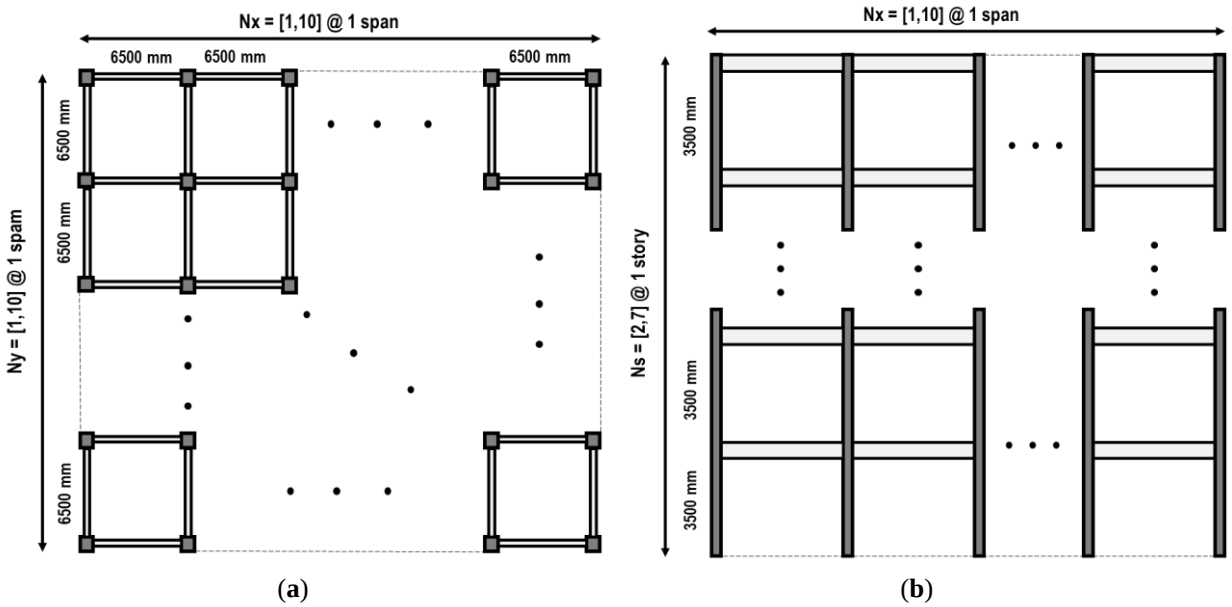

Figure 5.2. Archetype of buildings: (a) Plan view; (b) Elevation view.

Table 5.1 shows the key design variables of the archetype of buildings. Six hundred buildings are generated.

Table 5.1. The key design variables of the archetype.

Variable	Name	Values
Ns	Number of stories	2 to 7
Nx	Number of spans in the x-direction	1 to 10
Ny	Number of spans in the y-direction	1 to 10
H	Story height [mm]	3500
Lx	Span length [mm]	6500
Ly	Span length [mm]	6500
w	Story weight [kN/m²]	10

5.3.1.2 Structural design criterion

The virtual work method was used to determine the lateral strength and design the members of the buildings. According to the principle of virtual work, a plastic mechanism of the building is assumed under horizontal seismic forces, as shown in Figure 5.3. From the principle of energy conservation, the external work is equal to the internal work, as defined by Equation 5-1 [111]:

$$WE = WI \qquad \textit{Equation 5-1}$$

where WE is the external work by the external forces, and WI is the internal work by the internal force of the structural members. Using this formula, the member capacity of the building can be determined from the horizontal force corresponding to the required base shear. The following assumptions are considered in order to obtain the rebar detailing of beams and columns, as shown in Figure 5.3:

- The cross-section of columns is square.
- Only plastic hinges are at the base of the columns.
- Plastic hinges at the ends of all beams except roof beams.
- The beam and column rotations are equal to the roof drift ratio.
- The yielding moment of the columns is 1.5 times the yielding moment of the beams.

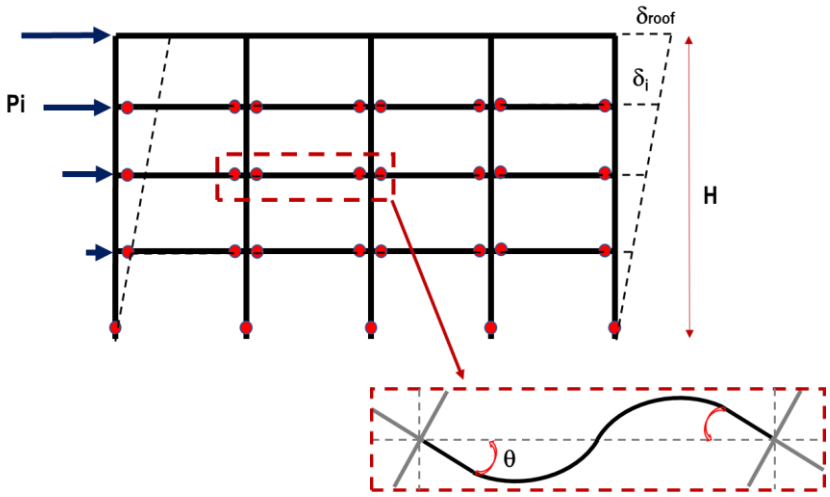

Figure 5.3. Collapse mechanism and vertical distribution load assumed.

From the assumptions, the internal and external work are defined by the Equation 5-2 and Equation 5-3:

$$WI = \sum My_{column} \cdot \theta + \sum My_{beam} \cdot \theta \qquad \textit{Equation 5-2}$$

$$WE = \sum P_i \cdot \delta_i \qquad \textit{Equation 5-3}$$

where My_{column} is the yield moment of the column, My_{beam} is the yield moment of the beam, θ is the yield rotation of the members, P_i is the external load (triangular distribution) and δ_i is the absolute displacement of the building (triangular distribution).

The base shear coefficient used in this criterion is 0.3 based on the Japanese design standard [112]. Then, the base shear force is defined by Equation 5-4:

$$V_{base} = 0.3 \cdot W_{total} = \sum P_i = \frac{n \cdot (n+1)}{2} \cdot P \qquad \textit{Equation 5-4}$$

where V_{base} is the base shear force, W_{total} is the total weight of the building, n is the number of stories of the building, and P is the external force of the first floor which is obtained from Equation 4. For this plastic mechanism and assuming a triangular deformation distribution, θ is equal to the roof drift ratio, as Equation 5-5 shows:

$$\theta = \frac{\delta_{roof}}{H} = \frac{n \cdot \delta}{H} \qquad \textit{Equation 5-5}$$

where δ_{roof} is the absolute displacement of the roof level, δ is the displacement of the first floor, and H is the total height.

The cross-section size of the columns in order to avoid the axial and shear failure is obtained by Equation 5-6:

$$B^2 \geq \frac{N}{0.3 \cdot f_c} \; and \; B \leq {}^{h_c}/_{3} \qquad \textit{Equation 5-6}$$

where B is the size of the column, N is the axial force at the column, f_c is the compressive strength of the concrete, and h_c is the clear height of the column. The cross-section height range of the beams in order to avoid shear failure is obtained by Equation (7):

$$h_b = \left\lfloor \frac{L}{12}; \frac{L}{10} \right\rfloor \; and \; b = \frac{h_b}{2} \qquad \textit{Equation 5-7}$$

where L is the length of the beam, and its width is b. The yield moment of the column is calculated by Equation (8) [113]:

$$My_{column} = \begin{cases} 0.8 \cdot a_{tc} \cdot f_{yc} \cdot B + 0.5 \cdot N \cdot B \cdot \left(1 - \dfrac{N}{B^2 \cdot f_c}\right), if \; 0 < N \leq N_b \\ \left(0.8 \cdot a_{tc} \cdot f_{yc} \cdot B + 0.12 \cdot B^3 \cdot f_c\right) \cdot \left(\dfrac{N_{max} - N}{N_{max} - N_b}\right), if \; N_b < N \leq N_{max} \end{cases} \qquad \textit{Equation 5-8}$$

where a_{tc} is the rebar area in the tension side of the column section, f_{yc} is the steel-yielding strength used for the column, N_b and N_{max} are the balance and maximum axial force, respectively, which can be approximated by Equations (9) and (10):

$$N_b = 0.4 \cdot B^2 \cdot f_c \qquad \textit{Equation 5-9}$$

$$N_{max} = B^2 \cdot \left(f_c + \frac{f_y}{1.2}\right) \qquad \textit{Equation 5-10}$$

The yield moment of the beam is calculated by Equation (11) [113]:

$$My_{beam} = 0.9 \cdot a_{tb} \cdot f_{yb} \cdot (h_b - r) \qquad \textit{Equation 5-11}$$

where a_{tb} is the rebar area in the tension side of the beam section, f_{yb} is the steel-yielding strength used for the beam, h_b is the height of the beam, and r is the minimum distance of the center of tension rebars to the external fiber of the beam.

5.3.1.3 Nonlinear structural models for the target buildings

The buildings are modeled as the section 3.3.2.

5.3.1.4 Verification of the structural design

The structural design of buildings is verified by the nonlinear static analysis (pushover), comparing the base shear force coefficient at the inter-story drift greater or equal to 1/100 with the minimum value of 0.3. Note that the member sizes, rebar distribution, and the minimum and maximum rebar ratio satisfy the recommendations of the Architectural Institute of Japan Standard [113]. Figure 5.4 shows the box plot of the base shear coefficient of 600 buildings by stories for the inter-story drift 1/150, 1/100, 1/75, and 1/50. Almost all buildings have a base shear force coefficient of more than 0.3 when the inter-story drift exceeds 1/75.

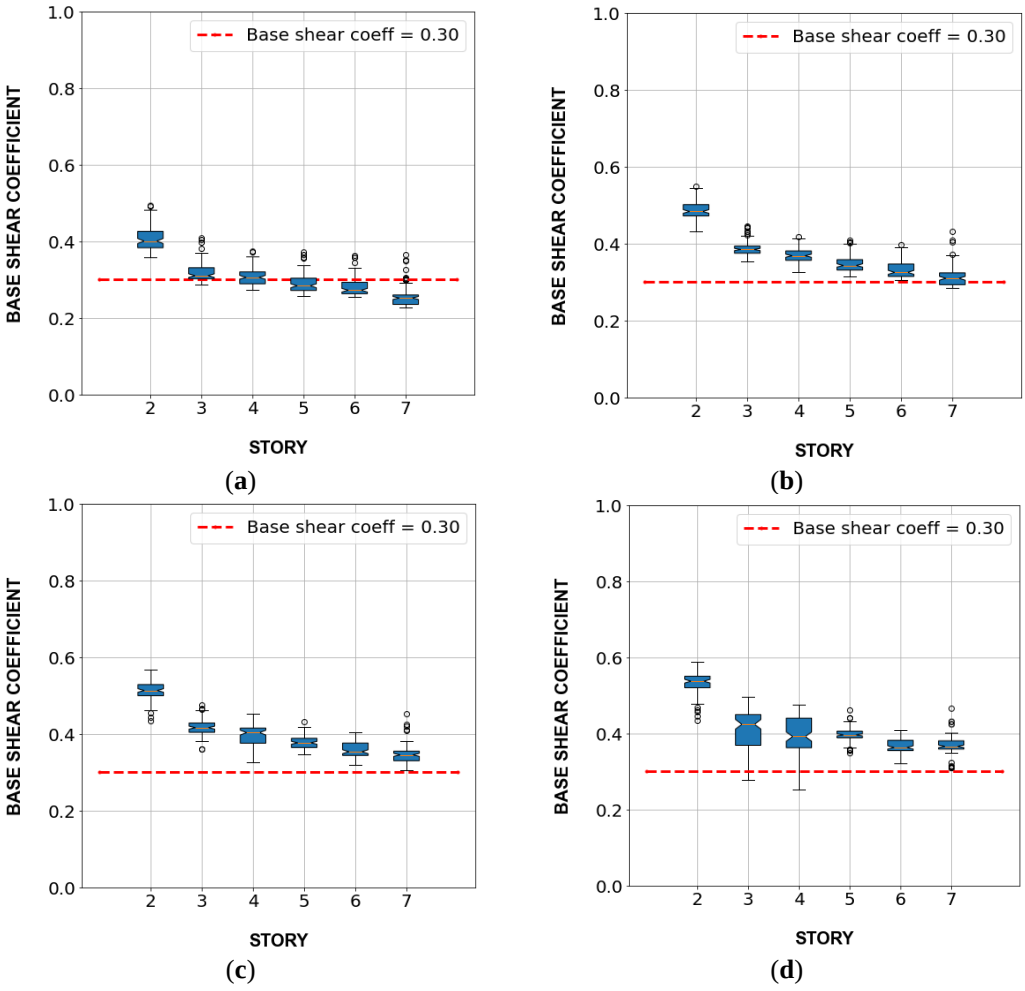

Figure 5.4. Box plot of base shear coefficient of buildings by the number of stories: (a) Inter-story drift = 1/150; (b) Inter-story drift = 1/100; (c) Inter-story drift = 1/75; (d) Inter-story drift = 1/50.

Table 2 shows the member sizes of columns and beams of each story.

Table 5.2. Member size of each number of stories.

Number of stories	2	3	4	5	6	7
Column size [mm]	500x500	600x600	700x700	800x800	900x900	900x900
Beam size ($b \times h_b$) [mm]	300x600	300x600	350x650	350x650	350x700	400x700

5.3.2 Ground motion records

5.3.2.1 Target response spectrum

The Uniform Hazard Spectrum (UHS) is a response spectrum with an equal probability of exceedance of a particular hazard in all structural periods. This paper uses Nagoya's 2500-year return period Uniform Hazard Spectrum (UHS) [112] as the target response spectrum of input earthquakes. This UHS is the acceleration response spectrum of a 5% damping ratio on reference ground (the shear wave velocity in the first 30m of soil is 292m/s), corresponding to an exceedance probability of 2% in 50 years.

5.3.2.2 Records selection criterion

Moscoso et al. [64] created a database of 183 records from the ground motion records obtained in the Center of Engineering Strong Motion Data by the USGS and the California Geological Survey [67]. It consists of records with less than 3000 samples and PGA greater than 400 gals. Also, the record data are cut off between 5% to 95% of the Aries Intensity, where the main energy is released in this time range [68].

Then, the records are further selected in order to obtain the minimum Mean Squared Error (MSE) defined by Equation (12) against the target acceleration response spectra:

$$MSE = \frac{1}{N} \cdot \sum_{i=1}^{N} (SF_1 \cdot Sa_{rec} - Sa_{target})^2, \qquad \textit{Equation 5-12}$$

where SF_1 is the scaling factor in obtaining the minimum MSE for the evaluated record, Sa_{rec} is the unscaled response spectrum of the evaluated record, and Sa_{target} is the target response spectrum.

Finally, a set of 10 ground motion records and their scaling factors are selected as shown in Table 5.3.

Table 5.3. List of selected records and the scaling factor.

Record name	Scaling factor (SF_1)
Kumamoto2016_EW	1.58
Hokkaido2018_EW	2.24
Northridge1994_360	3.55
Northridge1994_90	3.12
Petrolia1992_270	2.82
LomaPrieta1989_90	2.67
Chuetsu2004_EW	1.36
Hokkaido2003_NS	2.64
LomaPrieta1989_0	2.85
Westmorland1981_90	2.61

Figure 5.5 shows the target spectrum, the spectrum of the selected records, and the fundamental period range of studied buildings (between 0.237 and 0.609 seconds).

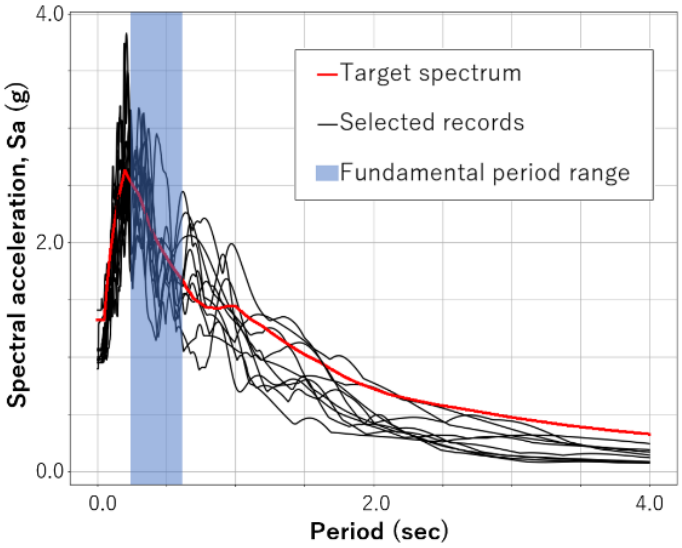

Figure 5.5. Target Spectrum, selected records, and fundamental period range of studied buildings.

5.3.3 Incremental dynamic analysis

The IDA has been used to obtain buildings' linear and nonlinear responses. IDA requires performing a series of nonlinear time-history analyses in which the scale factors of ground motions are gradually increased until the collapse capacity of the structure is reached [114]. SF_2 are applied to the records after matching to the target spectrum. SF_2 are from 0.10 to 0.30 each 0.10 and from 0.50 to 2.00 each 0.25 in this study.

The IDA curve represents the relationship between Intensity Measure (IM) and Damage Measure (DM). The IMs can be obtained based on either acceleration (A), velocity (V), displacement (D), or combining them (H: hybrid IM). In this study, 27 IMs are selected as shown in

Table 4.2. The maximum inter-story drift ratio (story drift) is selected as DM.

Ten scaling factors of input ground motions are selected for all buildings to capture the linear and nonlinear behavior. As an example, the IDA curve of the three-story (Ns) building with two spans in the x-direction (Nx) and five spans in the y-direction (Ny) is shown in Figure 5.6.

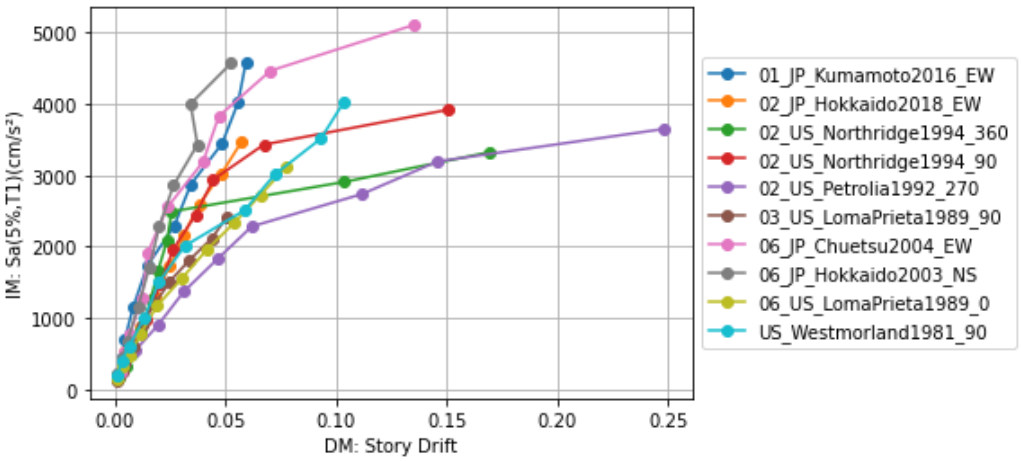

Figure 5.6. IDA curve for the building of Ns = 3, Nx = 2, and Ny = 5.

5.4 ML methodology to predict the damage condition of the building

5.4.1 Damage condition state

The scaling factors of ground motions are determined regarding the damage conditions in Table 1.1 so that the story drift could range from No Damage to Collapse condition.

5.4.2 Input and output data for the ML models

The input data are Intensity Measures (from the ground and/or roof response acceleration), the number of spans in X and Y directions (Nx and Ny), and the number of stories (Ns). The output data are the story drifts.

5.4.3 Case studies with different input data

In determining the IM from the sensor record, two cases are considered in this study. The record is obtained from the ground motion sensor in the first case, as shown in Figure 5.7.

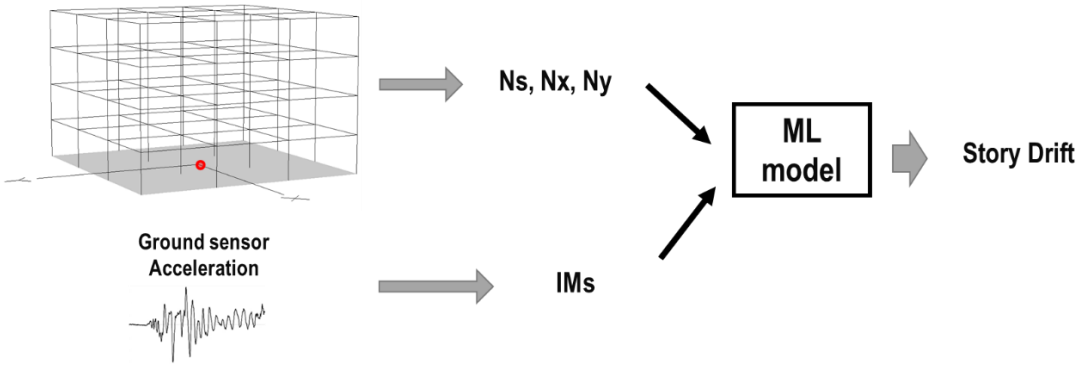

Figure 5.7. 1st case: Damage detection using only ground sensors of the buildings (red dot represents the location of the sensor).

In the second case, the records are taken from the ground and roof sensor, and IMs are calculated by both records, as shown in Figure 5.8.

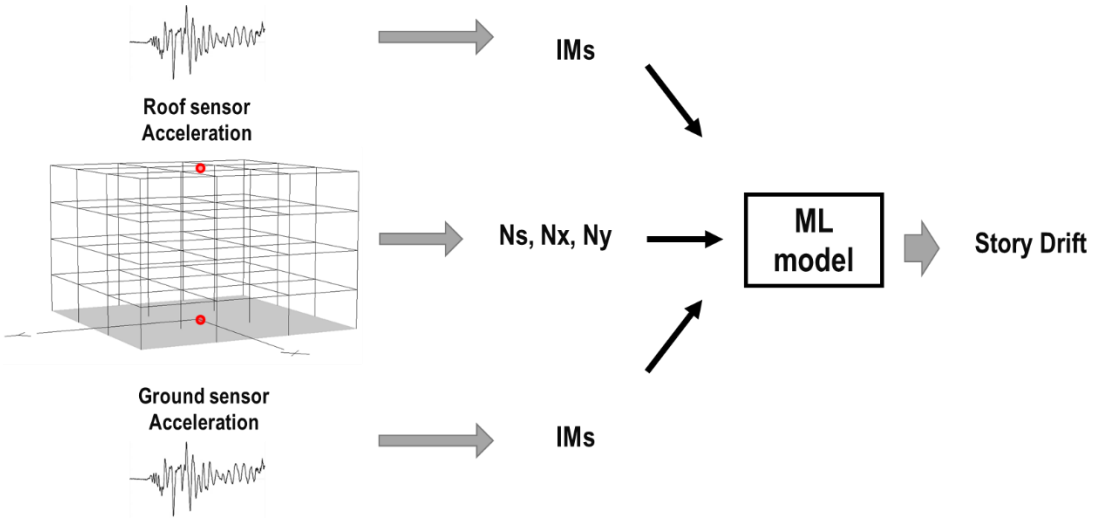

Figure 5.8. 2nd case: Damage detection using ground and roof sensors of the buildings (red dots represents the location of the sensors).

5.4.4 Random selection of records and buildings for the ML models

80% and 20% of the records are used for the training and testing processes, respectively. Random record selections are carried out ten times in order to reduce bias. The ML model is trained and tested for each set of records. The accuracy of the ML prediction is evaluated using the coefficient of determination (R^2), and its mean (R^2_mean) and standard deviation (in order to evaluate the dispersion) of R^2 values come from the ten iterations. Figure 5.9 shows the procedure of the record selections of the ML model.

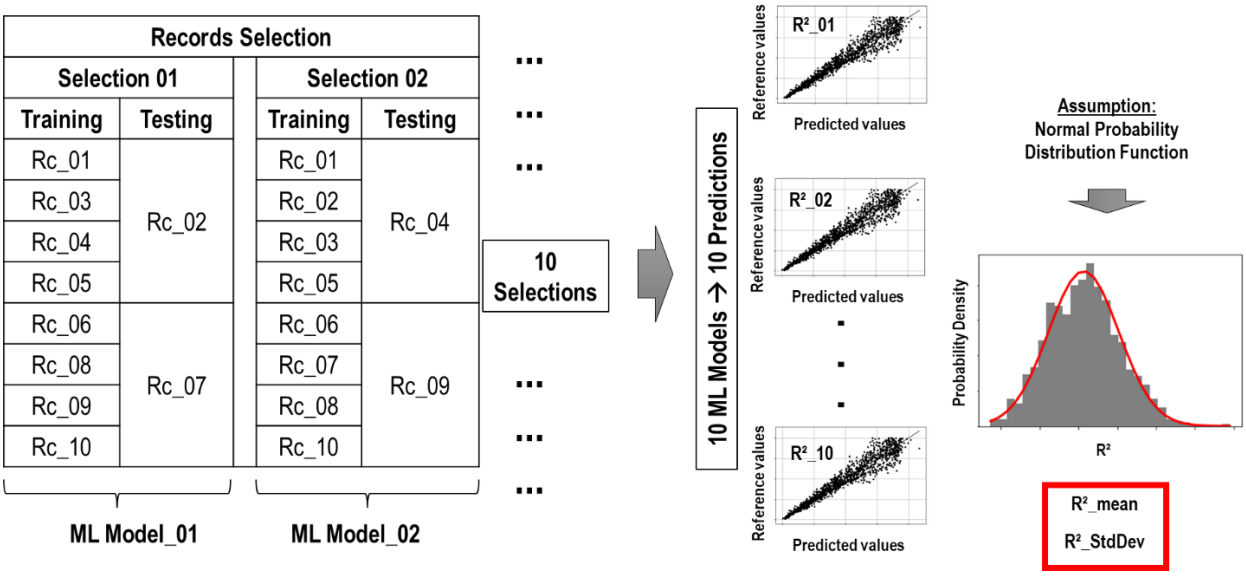

Figure 5.9. Procedure of the record selection of the ML model.

On the other hand, this study randomly selects 10% and 90% of the 600 buildings for training and testing processes, respectively, as shown in Figure 5.10.

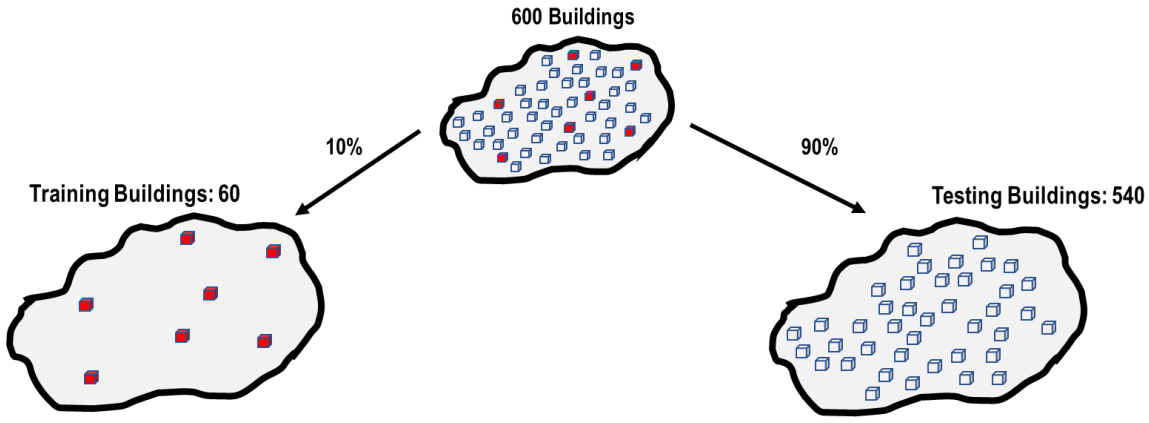

Figure 5.10. Splitting of buildings.

Random building selections are carried out 200 times to reduce bias. The ML model is trained and tested for each set of buildings. The maximum R^2_mean and its standard deviation of the iterations determine the best training buildings. Figure 5.11 shows the procedure of the building selection of the ML model.

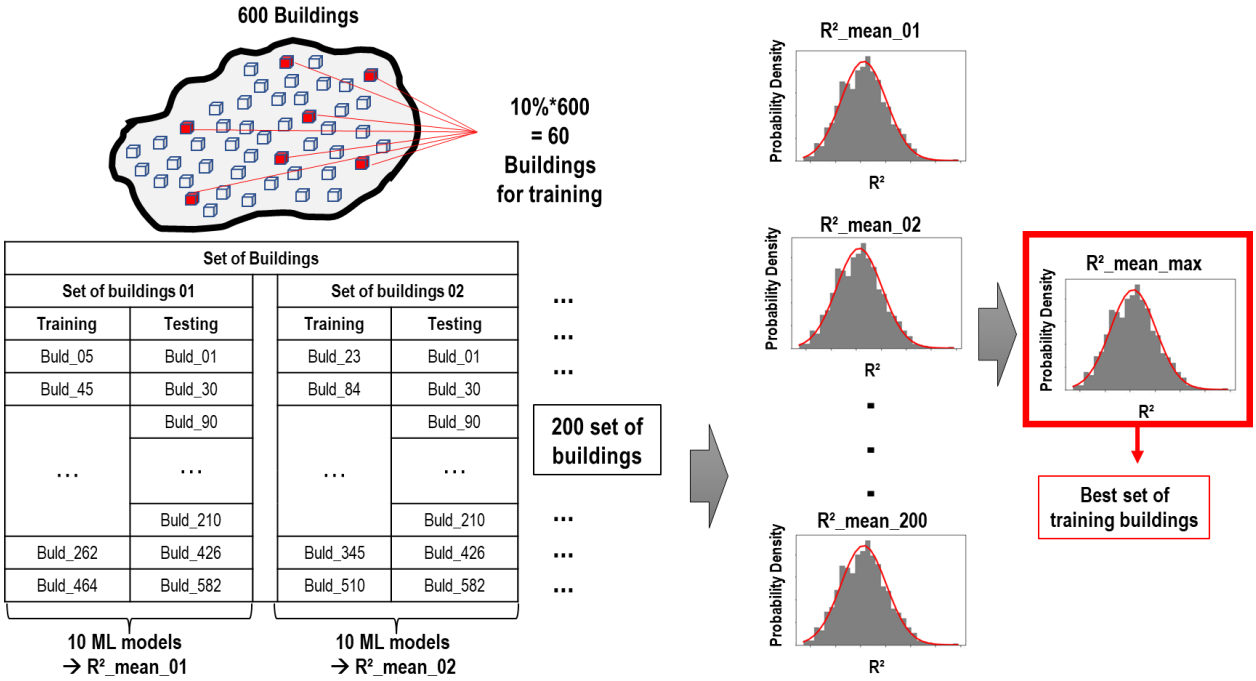

Figure 5.11. Procedure of the building selection of the ML model.

5.4.5 Machine learning methods

The ML method used are the defined in the section 4.3.2.

5.4.6 Case study results

5.4.6.1 1st case study using the ground sensor data.

Table 5.4 shows the ML results for the 1st case, where the IMs are ordered descending from left to right (collected from the feature importance levels greater than 0.05). Even though the difference between R^2 and the standard deviation for all the ML methods is generally insignificant, the main results are as follows:

- The maximum R^2 obtained by the Random Forest method is 0.942: A95, IMcr, AI, and Ic.
- The maximum R^2_mean obtained by the Gradient Boost method is 0.870: A95, AI, Ic, and IMcr.
- The minimum standard deviation obtained by the Decision Tree method is 0.047: A95 and AI.
- The IM present in all the ML methods is A95.

Figure 5.12 shows the results of the Random Forest method of the 1st case. Figure 5.12a compares the predicted and reference story drift for the maximum R^2 which is 0.942. Figure 5.12b shows the normal distribution function of the R^2 where its mean and standard deviation are 0.867 and 0.054, respectively. Figure 5.12c shows the importance levels of the features (IMs, Ns, Nx, and Ny) in which A95, IMcr, AI, and Ic have contributions greater than 0.05.

Table 5.4. The results of the 1st case study.

Coefficient of determination (R^2) and Intensity Measures							
Linear Regression				**Decision Tree**			
Maximum	**Mean**	**Standard deviation**	**Intensity Measure**	**Maximum**	**Mean**	**Standard deviation**	**Intensity Measure**
0.912	0.820	0.062	---	0.914	0.857	0.047	A95, AI
Random Forest				**Gradient Boost**			
Maximum	**Mean**	**Standard deviation**	**Intensity Measure**	**Maximum**	**Mean**	**Standard deviation**	**Intensity Measure**
0.942	0.867	0.054	A95, IMcr, AI, Ic	0.937	0.870	0.068	A95, AI, Ic, IMcr
AdaBoost				**XGBoost**			
Maximum	**Mean**	**Standard deviation**	**Intensity Measure**	**Maximum**	**Mean**	**Standard deviation**	**Intensity Measure**
0.899	0.857	0.048	SdT1, A95, IMcr, SIH, Ic, IMsr	0.919	0.818	0.089	A95, IF, Sa_Avg, EPA
Multilayer Perceptron							
Maximum	**Mean**	**Standard deviation**	**Intensity Measure**				
0.931	0.820	0.065	---				

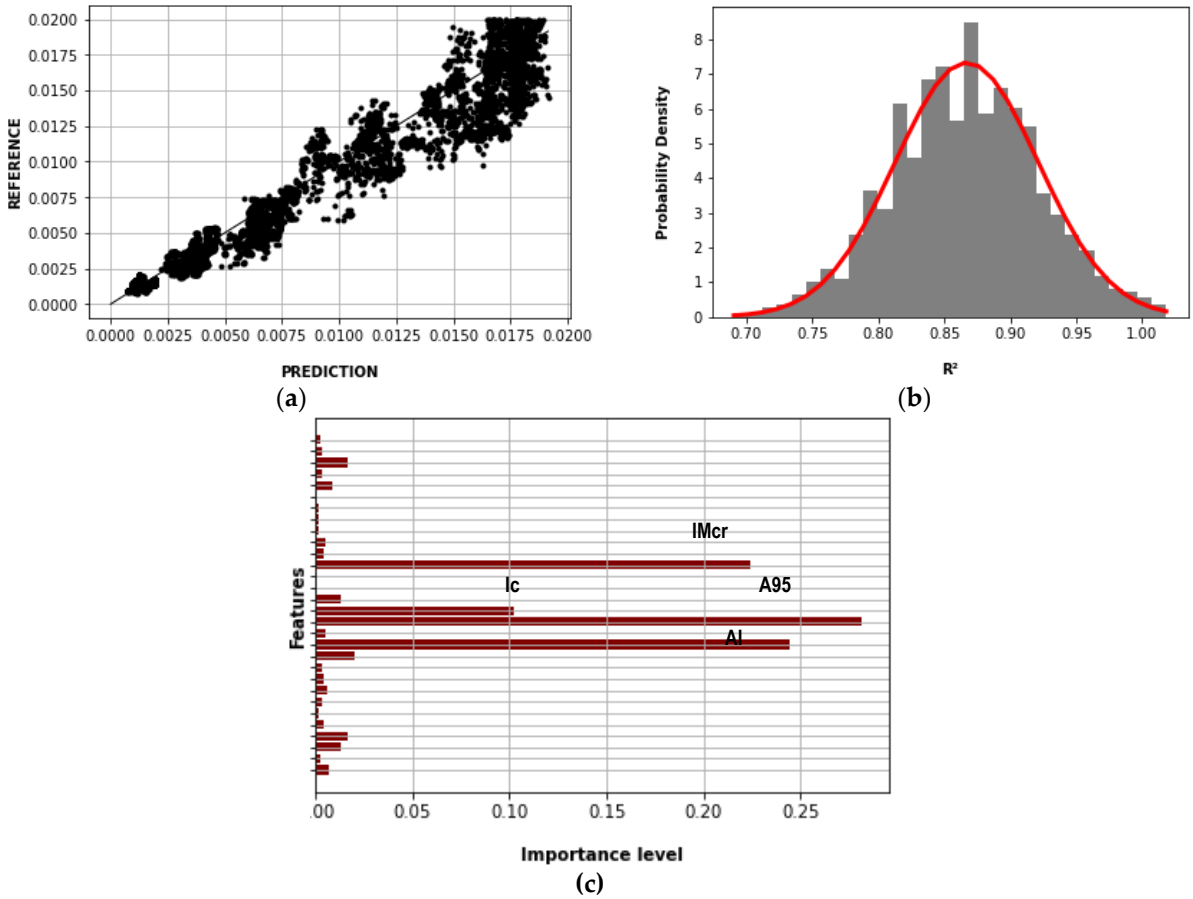

Figure 5.12. Random forest results – 1st case: (a) Story drift prediction and reference (R^2 = 0.942); (b) Normal distribution function of the R^2 (mean = 0.867; standard deviation = 0.054); (c) Importance levels of the features.

5.4.6.2 2nd case study using both the ground and roof sensor data.

Table 5.5 shows the ML results for the 2nd case, where the IMs are ordered descending from left to right (collected from the feature importance levels greater than 0.05). Even though the difference between R^2 and the standard deviation for all the ML methods is generally insignificant, the main results are as follows:

- The maximum R^2 obtained by the Gradient Boost method is 0.942: R_PGA and R_PGV.
- The maximum R^2_mean obtained by the Gradient Boost method is 0.902: R_PGA and R_PGV.
- The minimum standard deviation obtained by the Linear Regression method is 0.016.
- The IM present in all the ML methods is R_PGA.

Table 5.5. The results of the 2nd case study.

Coefficient of determination (R^2) and Intensity Measures							
Linear Regression				**Decision Tree**			
Maximum	**Mean**	**Standard deviation**	**Intensity Measure**	**Maximum**	**Mean**	**Standard deviation**	**Intensity Measure**
0.927	0.897	0.016	---	0.884	0.776	0.075	R_PGA, R_PGV
Random Forest				**Gradient Boost**			
Maximum	**Mean**	**Standard deviation**	**Intensity Measure**	**Maximum**	**Mean**	**Standard deviation**	**Intensity Measure**
0.934	0.893	0.038	R_PGA	0.942	0.902	0.037	R_PGA, R_PGV
AdaBoost				**XGBoost**			
Maximum	**Mean**	**Standard deviation**	**Intensity Measure**	**Maximum**	**Mean**	**Standard deviation**	**Intensity Measure**
0.917	0.896	0.024	R_PGA, R_SIH, R_Sa_Avg, G_Ic, G_CAV	0.93	0.862	0.038	R_PGA, R_PGV, R_IF
Multilayer Perceptron							
Maximum	**Mean**	**Standard deviation**	**Intensity Measure**				
0.930	0.881	0.054	---				

Figure 5.13 shows the results of the Gradient Boost method of the 2nd case. Figure 5.13a compares the predicted and reference story drift for the maximum R^2 which is 0.942. Figure 5.13b shows the normal distribution function of the R^2 where its mean and standard deviation are 0.909 and 0.037, respectively. Figure 5.13c shows the importance levels of the features (IMs, Ns, Nx, and Ny) in which R_PGA and R_PGV have contributions greater than 0.05.

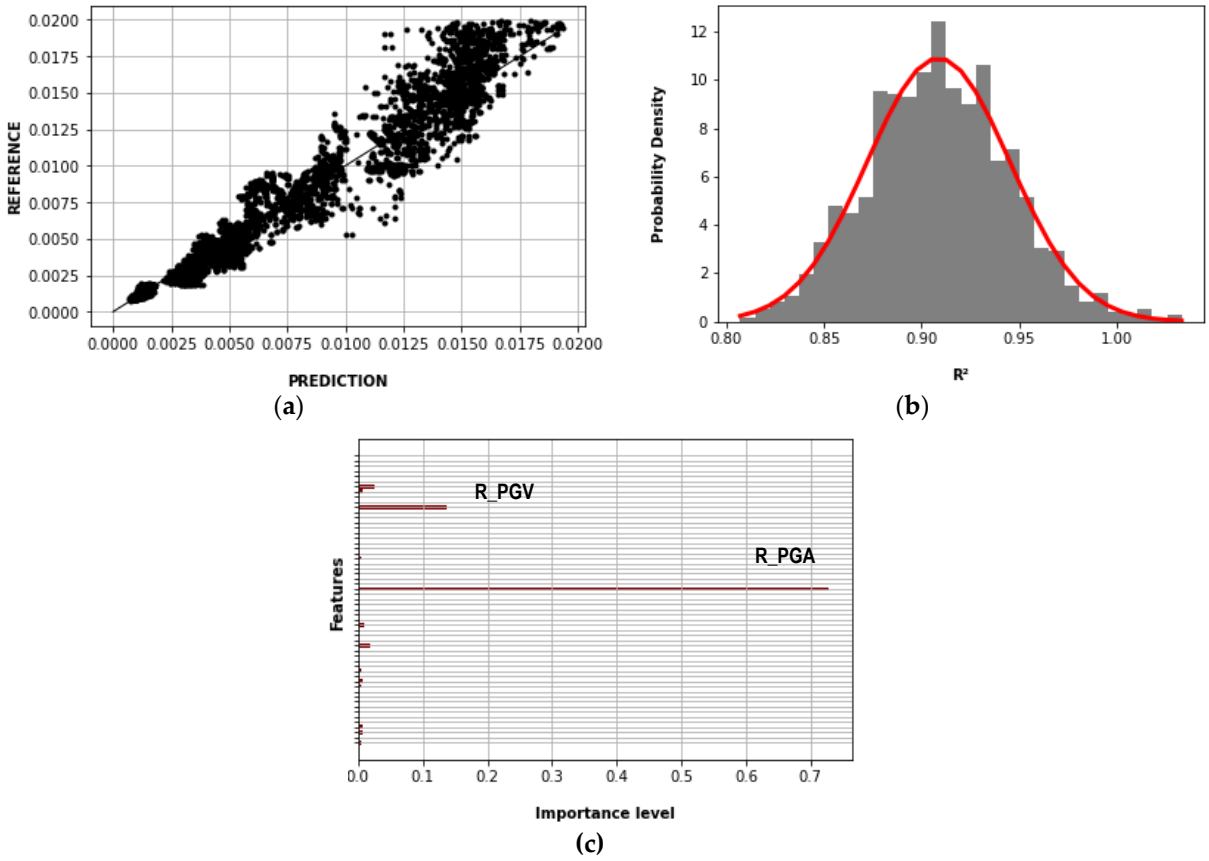

Figure 5.13. Gradient Boost results – 2nd case (a) Story drift prediction and reference (R^2 = 0.942); (b) Normal distribution function of the R^2 (mean = 0.902; standard deviation = 0.037); (c) Importance levels of the features (IMs).

5.4.6.3 Computation time

The structural analyses and the ML methodology process are carried out on a computer with 20 Intel® Xeon® W-2255 CPUs @3.70 GHz, 256Gb of RAM, and 1 NVIDIA RTX A5000 GPU card. The ML algorithms are developed using the Scikit learn library [115] under Python 3.8.3.

The number of structural models is 10000 per story, considering: ten earthquakes, ten scaling factors, ten spans in the X-direction, and ten spans in the Y-direction. Table 5.6 shows the computation time of the structural analyses per story. The consumed computation time was optimized by running 16 structural models in parallel.

Table 5.6. Computation time of the structural analyses per story.

Story	Total time (10 000 structural models per story) (h)
2	5.95
3	9.82
4	16.37
5	25.20
6	35.83
7	26.68

The number of models is 2000 per ML method, considering: 10 selections of earthquakes and 200 sets of buildings. Table 5.7 and Table 5.8 show the computation time for the 1st and 2nd cases, respectively.

Table 5.7. Computation time for 1st case.

ML method	Training time per model (s)	Testing time per model (s)	Total time (2000 models per ML method) (s)
Linear Regression	0.0011	0.0008	3.8
Decision Tree	0.0211	0.0010	44.2
Random Forest	1.3454	0.0435	2777.8
Gradient boost	0.5960	0.0047	1201.5
AdaBoost	0.2381	0.0243	524.7
XGboost	0.0929	0.0028	191.5
Multilayer Perceptron	5.3261	0.0153	10682.9

Table 5.8. Computation time for 2nd case.

ML method	Training time per model (s)	Testing time per model (s)	Total time (2000 models per ML method) (s)
Linear Regression	0.0015	0.0010	4.9
Decision Tree	0.0617	0.0015	126.3
Random Forest	3.6086	0.0439	7304.9
Gradient boost	1.8039	0.0074	3622.7
AdaBoost	0.5831	0.0479	1262.0
XGboost	0.1187	0.0029	243.2
Multilayer Perceptron	7.1770	0.0363	14426.6

5.4.6.4 Discussion of results

As shown in Figure 5.12c and Figure 5.13c, the importance levels of IMs are higher than the structural features of the buildings (Nx, Ny, and Ns). Even though the total number of buildings is 600, the number of record features comes from 27 IMs of 10 results (scaling factors) per building. Then, the results depend mainly on the records variability, establishing the model's accuracy. For this reason, it is recommended to increase the number of records in future studies to cover more earthquake features.

Although the accuracy and dispersion for both cases are similar, the main result difference comes from the influence of the building response features. Table 5.4 shows that the main IMs for the 1st case come from the ground sensors against the 2nd from the roof sensors, as shown in Table 5.5. Moreover, the main IMs for the 1st case are based on acceleration and, for the 2nd case, on acceleration and velocity. In addition, for all the ML methods except Decision Tree, the R^2_mean and the standard deviation are the highest and lowest for the 2nd case, concluding that the 2nd case provides the best high-accuracy and low-dispersion. However, the inclusion of roof sensors is not feasible easily. Therefore, it is recommended to include roof sensors to increase accuracy and decrease dispersion progressively.

For both cases, Linear Regression and Multilayer Perceptron are the fastest and slowest ML methods, as shown in Table 5.7 and Table 5.8. It is because of the complexity of their algorithms measured by the number of trainable parameters involved. Even though the training and validation could be computationally intensive, once the ML model is developed, it can automatically predict the elastic and inelastic structural responses and detect the damage condition immediately after the earthquake. For this reason, the Gradient boost (the lowest R^2_mean) is considered the most effective ML method in both cases of this study.

5.5 Conclusions

This study proposes a methodology to predict the damage condition of RC resisting-moment frame buildings using ML methods. The methodology is applied to 600 buildings, and the results are summarized as follows:

- The virtual work method is used to design RC moment-resisting frame system models considering a plastic mechanism, external load, and deformation distribution. The rebar area, distribution of rebars, and realistic member sizes of beams and columns are calibrated using the recommendations of the Japanese standard. The static nonlinear analysis is used to verify the design by comparing the base shear coefficient at the inter-story drift ratio greater or equal to 1/100 with the target value of 0.3.
- The ground motion records are selected for PGA greater than 400 gals, 5%-95% of Arias intensity time range, and its response spectrum matches the Uniform Hazard Spectrum of Nagoya – Japan (target spectrum) of the exceedance probability of 2% in 50 years;
- Incremental Dynamic Analyses are carried out of the target buildings in order to obtain the responses covering the linear and nonlinear behavior;
- Two cases are considered to obtain the Intensity Measures from the sensor records: the 1st case considers the ground sensors, and the 2nd case considers the ground and roof sensors;
- Seven Machine learning methods are used to predict the damage condition of the buildings represented by the inter-story drift ratio. The training process uses 27 Intensity measures obtained from the ground and/or roof sensor responses, the number of stories, and the number of spans in X and Y directions as input data;
- In order to reduce the bias of random selection of records and buildings for the training and testing processes, 10 and 200 selections are considered, respectively. An R^2 mean and standard deviation are obtained for each records selection to evaluate the accuracy of the ML model, and the maximum R^2 mean and its standard deviation to obtain the best training buildings.
- For the 1st case, the maximum R^2 obtained by the Random Forest method is 0.942, the maximum R^2 mean obtained by the Gradient Boost method is 0.870, and the minimum standard deviation obtained by the Decision Tree method is 0.047. The IM present in all the ML methods is A95.
- For the 2nd case, the maximum R^2 obtained by the Gradient Boost method is 0.942, the maximum R^2 mean obtained by the Gradient Boost method is 0.902, and the minimum standard deviation obtained by the Linear Regression method is 0.016. The IM present in all the ML methods is R_PGA.
- The Gradient boost is considered the most effective ML method in both cases considering that it has the lowest R^2_mean.
- Although the 2nd case presents the highest and lowest R^2_mean and standard deviation, their inclusion is not easily feasible. Then, it is recommended to include them progressively.
- It is recommended to increase the number of records in future studies to cover more earthquake features.

Finally, the methodology applied to the RC archetype accurately detects the structural damage condition of buildings for all the ML methods, where the Random Forest and the Gradient Boosting methods are the most accurate, and the main IMs are those based on acceleration.

Chapter 6. Conclusions and recommendations

This research proposed several methodologies based on machine learning in combination with structural health monitoring for rapid post-earthquake damage detection of buildings. The conclusions are as follows:

- Chapter 2 proposes a methodology based on the CNN method for detecting LMM building damage (represented by the maximum ductility, story drift ratio, and absolute acceleration) using roof sensors' structural feature images (wavelet spectra). The correlation coefficients among the predicted and the reference values confirm the high accuracy of the methodology.
- Chapter 3 proposes a methodology based on the CNN method for detecting three-dimensional frame model building damage (represented by the maximum inter-story drift ratio and absolute acceleration) by selecting ground motion records (using IDA responses and a confidence interval between the 0% and 84% fractiles) and using structural feature images (power wavelet spectra) of roof sensors to increase its accuracy. The accuracy evaluation by the usability of the buildings, the damage condition, and the total comparison (determination coefficients) confirm the high accuracy of the methodology.
- Chapter 4 proposes a methodology based on seven ML methods for detecting three-dimensional frame model building damage (represented by the maximum inter-story drift ratio) using ground and roof sensors' intensity measures (based on acceleration, velocity, and displacement). The determination coefficients among the predicted and the reference values confirm the high accuracy of the methodology.
- Chapter 5 proposes a methodology based on ML methods for detecting new three-dimensional frame building damage conditions using ground and roof sensors' intensity measures (based on acceleration, velocity, and displacement). The determination coefficients among the predicted and the reference values confirm the high accuracy of the methodology.
- The building's post-earthquake condition can be detected immediately for all the methodologies since the ML is trained and validated beforehand.
- The results will be helpful for countermeasures after an earthquake, such as evacuating buildings, resuming economic and social activities, and mitigating future damage by aftershocks.

The recommendations for future works are as follows:

- This study considers fixed ductility ratio, inter-story drift ratio, and acceleration ranges to obtain the buildings' damage condition (see Table 1.1). It is recommended to compute the actual damage state per building.
- In Chapter 2, it is recommended to use other types of Hysteretic models, such as Stiffness Degrading [116,117] and Strength and Stiffness Degrading [118], for representing the story inelastic behavior of the buildings.
- In Chapter 3 and Chapter 4, it is recommended to apply to buildings of different structural configurations, lateral force-resisting systems, and materials.
- In Chapter 5, it is recommended to increase the ML methods, earthquakes of different characteristics (without selection methodology), materials, and lateral force-resisting systems such as confined masonry buildings.

References

1. United Nations World Conference on Disaster Reduction. In Proceedings of the Report of the World Conference on Disaster Reduction, Kobe, Japan, 18-22 January 2005; pp. 1-42.
2. Deam, B.; Cousins, W. Strong-Motion Instrumentation of Buildings in New Zealand. In Proceedings of the NZSEE Conference, Online, 27-29 April 2002; Paper No. 2.3.
3. INDECI. *Emergency Report No. 53—COEN-SINADECI: Pisco, Peru*; National Institute of Civil Defense of Peru: 2007.
4. Tilio, L.; Murgante, B.; Di Trani, F.; Vona, M.; Masi, A. Resilient city and seismic risk: A Spatial Multicriteria Approach. In Proceedings of the Computational Science and Its Applications-ICCSA, Spain - Santander, 20-23 June 2011; pp. 410-422.
5. Freddi, F.; Galasso, C.; Cremen, G.; Dall'Asta, A.; Di Sarno, L.; Giaralis, A.; Gutiérrez-Urzúa, F.; Málaga-Chuquitaype, C.; Mitoulis, S.A.; Petrone, C. Innovations in earthquake risk reduction for resilience: Recent advances and challenges. *International Journal of Disaster Risk Reduction* 2021, *60*, 102267.
6. Limongelli, M.P.; Çelebi, M. *Seismic structural health monitoring: from theory to successful applications*; Springer: 2019.
7. Gkoktsi, K.; Giaralis, A. A compressive MUSIC spectral approach for identification of closely-spaced structural natural frequencies and post-earthquake damage detection. *Probabilistic Engineering Mechanics* 2020, *60*, 103030.
8. Quispe, R.; Diaz, M.; Jaramillo, J.; Inocente, I. Assessment of the structural health monitoring in Edgardo Rebagliati Martins hospital with limited number of accelerometers in lima city. *Tecnia* 2022, *32*, 76-88.
9. Schanze, E.; Leiva, G.; Gómez, M.; Lopez, A. Numerical study of the seismic response of an instrumented building with underground stories. *Applied Sciences* 2021, *11*, 3190.
10. Sivasuriyan, A.; Vijayan, D.S.; Górski, W.; Wodzyński, Ł.; Vaverková, M.D.; Koda, E. Practical implementation of structural health monitoring in multi-story buildings. *Buildings* 2021, *11*, 263.
11. Mishra, M.; Lourenço, P.B.; Ramana, G.V. Structural health monitoring of civil engineering structures by using the internet of things: A review. *Journal of Building Engineering* 2022, *48*, 103954.
12. Gordan, M.; Sabbagh-Yazdi, S.-R.; Ismail, Z.; Ghaedi, K.; Carroll, P.; McCrum, D.; Samali, B. State-of-the-art review on advancements of data mining in structural health monitoring. *Measurement* 2022, 110939.
13. Alex K. Tang, P.E.; Johnsson, J. *Pisco, Peru, Earthquake of August 15, 2007: Lifeline Performance*; The American Society of Civil Engineers: 2008.
14. Antunes, P.; Lima, H.; Varum, H.; André, P. Optical fiber sensors for static and dynamic health monitoring of civil engineering infrastructures: Abode wall case study. *Measurement* 2012, *45*, 1695-1705.
15. Roghaei, M.; Zabihollah, A. An efficient and reliable structural health monitoring system for buildings after earthquake. *APCBEE procedia* 2014, *9*, 309-316.
16. Schneider, P.J.; Schauer, B.A. HAZUS—Its development and its future. *Natural Hazards Review* 2006, *7*, 40-44.
17. JSCA. The guide to safe buildings. *Performance-Based Seismic Design* 2018.
18. Worden, K.; Manson, G. The application of machine learning to structural health monitoring. *Philosophical Transactions of the Royal Society A: Mathematical, Physical and Engineering Sciences* 2007, *365*, 515-537.
19. Burkov, A. *Machine learning engineering*; True Positive Incorporated: 2020.
20. Tang, Y.; Wang, Y.; Wu, D.; Liu, Z.; Zhang, H.; Zhu, M.; Chen, Z.; Sun, J.; Wang, X. An experimental investigation and machine learning-based prediction for seismic performance of steel tubular column filled with recycled aggregate concrete. *Reviews on Advanced Materials Science* 2022, *61*, 849-872.
21. Zhao, X.-Y.; Chen, J.-X.; Chen, G.-M.; Xu, J.-J.; Zhang, L.-W. Prediction of ultimate condition of FRP-confined recycled aggregate concrete using a hybrid boosting model enriched with tabular generative adversarial networks. *Thin-Walled Structures* 2023, *182*, 110318.

22. Cardellicchio, A.; Ruggieri, S.; Nettis, A.; Renò, V.; Uva, G. Physical interpretation of machine learning-based recognition of defects for the risk management of existing bridge heritage. *Engineering Failure Analysis* 2023, 107237.
23. Tsuchimoto, K.; Narazaki, Y.; Hoskere, V.; Spencer, B.F. Rapid postearthquake safety evaluation of buildings using sparse acceleration measurements. *Structural Health Monitoring* 2021, *20*, 1822-1840.
24. Lu, X.; Xu, Y.; Tian, Y.; Cetiner, B.; Taciroglu, E. A deep learning approach to rapid regional post-event seismic damage assessment using time-frequency distributions of ground motions. *Earthquake Engineering & Structural Dynamics* 2021, *50*, 1612-1627.
25. Goulet, J.-A.; Michel, C.; Kiureghian, A.D. Data-driven post-earthquake rapid structural safety assessment. *Earthquake Engineering & Structural Dynamics* 2015, *44*, 549-562.
26. Xu, Y.J.; Lu, X.Z.; Tian, Y.; Huang, Y.L. Real-Time Seismic Damage Prediction and Comparison of Various Ground Motion Intensity Measures Based on Machine Learning. *Journal of Earthquake Engineering* 2020, *26*, 4259-4279.
27. Moscoso Alcantara, E.A.; Bong, M.D.; Saito, T. Structural Response Prediction for Damage Identification Using Wavelet Spectra in Convolutional Neural Network. *Sensors* 2021, *21*, 6795.
28. Wang, J.-F.; Lin, C.-C.; Yen, S.-M. A story damage index of seismically-excited buildings based on modal frequency and mode shape. *Engineering Structures* 2007, *29*, 2143-2157.
29. Xu, K.; Mita, A. Estimation of maximum drift of multi-degree-of-freedom shear structures with unknown parameters using only one accelerometer. *Structural Control and Health Monitoring* 2021, *28*, e2799.
30. Warr, K. *Strengthening deep neural networks: Making AI less susceptible to adversarial trickery*; O'Reilly Media: 2019.
31. Oh, B.K.; Park, Y.; Park, H.S. Seismic response prediction method for building structures using convolutional neural network. *Structural Control and Health Monitoring* 2020, *27*, e2519.
32. Tsuchimoto, K.; Narazaki, Y.; Spencer Jr, B.F. Development and validation of a post-earthquake safety assessment system for high-rise buildings using acceleration measurements. *Mathematics* 2021, *9*, 1758.
33. Hasan, M.; Ullah, S.; Khan, M.J.; Khurshid, K. Comparative analysis of SVM, ANN and CNN for classifying vegetation species using hyperspectral thermal infrared data. *The International Archives of Photogrammetry, Remote Sensing and Spatial Information Sciences* 2019, *42*, 1861-1868.
34. Keeling, R.; Chhatwal, R.; Huber-Fliflet, N.; Zhang, J.; Wei, F.; Zhao, H.; Shi, Y.; Qin, H. Empirical comparisons of CNN with other learning algorithms for text classification in legal document review. In Proceedings of the 2019 IEEE International Conference on Big Data (Big Data), 2019; pp. 2038-2042.
35. Jiang, X.; Wang, Y.; Liu, W.; Li, S.; Liu, J. Capsnet, cnn, fcn: Comparative performance evaluation for image classification. *International Journal of Machine Learning and Computing* 2019, *9*, 840-848.
36. Huerta-Lopez, C.I.; Shin, Y.; Powers, E.J.; Roesset, J.M. Time-frequency analysis of earthquake records. In Proceedings of the 12th World Conference on Earthquake Engineering, Auckland, 2000.
37. Tao, D.; Lin, J.; Lu, Z. Time-frequency energy distribution of ground motion and its effect on the dynamic response of nonlinear structures. *Sustainability* 2019, *11*, 702.
38. Cao, H.; Friswell, M. The effect of energy concentration of earthquake ground motions on the nonlinear response of RC structures. *Soil Dynamics and Earthquake Engineering* 2009, *29*, 292-299.
39. Spanos, P.D.; Giaralis, A.; Politis, N.P.; Roesset, J.M. Numerical treatment of seismic accelerograms and of inelastic seismic structural responses using harmonic wavelets. *Computer-Aided Civil and Infrastructure Engineering* 2007, *22*, 254-264.
40. Balafas, K.; Kiremidjian, A.S. Development and validation of a novel earthquake damage estimation scheme based on the continuous wavelet transform of input and output acceleration measurements. *Earthquake Engineering & Structural Dynamics* 2015, *44*, 501-522.
41. Young Noh, H.; Krishnan Nair, K.; Lignos, D.G.; Kiremidjian, A.S. Use of wavelet-based damage-sensitive features for structural damage diagnosis using strong motion data. *Journal of Structural Engineering* 2011, *137*, 1215-1228.

42. Xu, C.; Guan, J.; Bao, M.; Lu, J.; Ye, W. Pattern recognition based on time-frequency analysis and convolutional neural networks for vibrational events in φ-OTDR. *Optical Engineering* 2018, *57*, 016103.
43. Dokht, R.M.; Kao, H.; Visser, R.; Smith, B. Seismic event and phase detection using time–frequency representation and convolutional neural networks. *Seismological Research Letters* 2019, *90*, 481-490.
44. Mousavi, S.M.; Zhu, W.; Sheng, Y.; Beroza, G.C. CRED: A deep residual network of convolutional and recurrent units for earthquake signal detection. *Scientific reports* 2019, *9*, 1-14.
45. Ghahremani, B.; Bitaraf, M.; Ghorbani-Tanha, A.K.; Fallahi, R. Structural damage identification based on fast S-transform and convolutional neural networks. In Proceedings of the Structures, 2021; pp. 1199-1209.
46. Zhang, R.; Liu, Y.; Sun, H. Physics-guided convolutional neural network (PhyCNN) for data-driven seismic response modeling. *Engineering Structures* 2020, *215*, 110704.
47. Teng, S.; Chen, G.; Liu, Z.; Cheng, L.; Sun, X. Multi-sensor and decision-level fusion-based structural damage detection using a one-dimensional convolutional neural network. *Sensors* 2021, *21*, 3950.
48. Park, H.S.; An, J.H.; Park, Y.J.; Oh, B.K. Convolutional neural network-based safety evaluation method for structures with dynamic responses. *Expert Systems with Applications* 2020, *158*, 113634.
49. Oh, B.K.; Glisic, B.; Kim, Y.; Park, H.S. Convolutional neural network-based wind-induced response estimation model for tall buildings. *Computer-Aided Civil and Infrastructure Engineering* 2019, *34*, 843-858.
50. Liu, T.; Xu, H.; Ragulskis, M.; Cao, M.; Ostachowicz, W. A data-driven damage identification framework based on transmissibility function datasets and one-dimensional convolutional neural networks: Verification on a structural health monitoring benchmark structure. *Sensors* 2020, *20*, 1059.
51. Liao, W.; Chen, X.; Lu, X.; Huang, Y.; Tian, Y. Deep transfer learning and time-frequency characteristics-based identification method for structural seismic response. *Frontiers in Built Environment* 2021, *7*, 627058.
52. Saito, T. Structural Earthquake Response Analysis (STERA 3D). Available online: http://www.rc.ace.tut.ac.jp/saito/software-e.html (accessed on 22 November 2021).
53. Farge, M. Wavelet transforms and their applications to turbulence. *Annual review of fluid mechanics* 1992, *24*, 395-458.
54. Torrence, C.; Compo, G.P. A practical guide to wavelet analysis. *Bulletin of the American Meteorological society* 1998, *79*, 61-78.
55. Mueller, J.P.; Massaron, L. *Deep learning for dummies*; John Wiley & Sons: 2019.
56. Goodfellow, I.; Bengio, Y.; Courville, A. *Deep learning*; MIT press: 2016.
57. Namatēvs, I. Deep convolutional neural networks: Structure, feature extraction and training. *Information Technology and Management Science* 2017, *20*, 40-47.
58. Albawi, S.; Mohammed, T.A.; Al-Zawi, S. Understanding of a convolutional neural network. In Proceedings of the 2017 international conference on engineering and technology (ICET), 2017; pp. 1-6.
59. Géron, A. *Hands-on machine learning with Scikit-Learn, Keras, and TensorFlow*, 3rd ed.; O'Reilly Media: 2022.
60. Kingma, D.P.; Ba, J. Adam: A method for stochastic optimization. In Proceedings of the International Conference on Learning Representations (ICLR), San Diego, CA, USA, 5-8 May 2015.
61. Wang, H.; Zhang, Y.-M.; Mao, J.-X. Sparse Gaussian process regression for multi-step ahead forecasting of wind gusts combining numerical weather predictions and on-site measurements. *Journal of Wind Engineering and Industrial Aerodynamics* 2022, *220*, 104873.
62. Celebi, M. *Seismic instrumentation of buildings (with emphasis on federal buildings)*; United States Geological Survey: 2002.
63. Yoon, T.; Song, Y.; Song, J.; Cheong, M.; Cheong, S. Dynamic Inelastic Analysis of hi-rise buildings using lumped model. In Proceedings of the 13th World Conference on Earthquake Engineering, Vancouver, BC, Canada, 1–6 August 2004.

64. Moscoso Alcantara, E.A.; Saito, T. Convolutional Neural Network-Based Rapid Post-Earthquake Structural Damage Detection: Case Study. *Sensors* 2022, *22*, 6426.
65. Zhang, Y.-M.; Wang, H.; Bai, Y.; Mao, J.-X.; Xu, Y.-C. Bayesian dynamic regression for reconstructing missing data in structural health monitoring. *Structural Health Monitoring* 2022, 2097-2115.
66. Kullaa, J. Eliminating environmental or operational influences in structural health monitoring using the missing data analysis. *Journal of Intelligent Material Systems and Structures* 2009, *20*, 1381-1390.
67. Center for Engineering Strong Motion Data (CESMD). Available online: https://www.strongmotioncenter.org/ (accessed on 1 March 2021).
68. Husid, R. Características de terremotos. Análisis general. *Revista IDIEM* 1969, *8*, 21-42.
69. Arias, A. A measure of earthquake intensity. *Seismic Design for Nuclear Power Plants* 1970, 438-483.
70. Zhang, Y.-M.; Wang, H.; Mao, J.-X.; Xu, Z.-D.; Zhang, Y.-F. Probabilistic framework with bayesian optimization for predicting typhoon-induced dynamic responses of a long-span bridge. *Journal of Structural Engineering* 2021, *147*, 04020297.
71. Aszemi, N.M.; Dominic, P. Hyperparameter optimization in convolutional neural network using genetic algorithms. *International Journal of Advanced Computer Science and Applications* 2019, *10*.
72. Moscoso Alcantara, E.A.; Saito, T. Structural Damage Condition of Buildings with a Sparse Number of Sensors Using Machine Learning: Case Study. In Proceedings of the International Symposium of the International Federation for Structural Concrete, 2023; pp. 128-140.
73. LATBSDC. An alternative procedure for seismic analysis and design of tall buildings located in the los angeles region. 2020.
74. PEER. Guidelines for performance-based seismic design of tall buildings. 2010.
75. Xu, K.; Mita, A. Estimation of Maximum Drift of MDOF Shear Structures Using Only One Accelerometer. *Structural Health Monitoring* 2021, *18*, 113–120.
76. Capellari, G.; Chatzi, E.; Mariani, S. An optimal sensor placement method for SHM based on Bayesian experimental design and Polynomial Chaos Expansion. In Proceedings of the European congress on computational methods in applied sciences and engineering, Crete Island, Greece, 5–10 June 2016; pp. 6272-6282.
77. Zhang, J.; Maes, K.; De Roeck, G.; Reynders, E.; Papadimitriou, C.; Lombaert, G. Optimal sensor placement for multi-setup modal analysis of structures. *Journal of Sound and Vibration* 2017, *401*, 214-232.
78. Tan, Y.; Zhang, L. Computational methodologies for optimal sensor placement in structural health monitoring: A review. *Structural Health Monitoring* 2020, *19*, 1287-1308.
79. Buratti, N. A comparison of the performances of various ground–motion intensity measures. In Proceedings of the 15th world conference on earthquake engineering, Lisbon, Portugal, 2012; pp. 24-28.
80. Douglas, J. Earthquake ground motion estimation using strong-motion records: a review of equations for the estimation of peak ground acceleration and response spectral ordinates. *Earth-Science Reviews* 2003, *61*, 43-104.
81. Chopra, A.K. Elastic response spectrum: a historical note. *Earthquake engineering & structural dynamics* 2007, *36*, 3-12.
82. Baker, J.W.; Allin Cornell, C. Spectral shape, epsilon and record selection. *Earthquake Engineering & Structural Dynamics* 2006, *35*, 1077-1095.
83. Newmark, N.M.; Hall, W.J. *Earthquake Spectra and Design*; Earthquake Engineering Research Institute: 1982.
84. Mehanny, S.S. A broad-range power-law form scalar-based seismic intensity measure. *Engineering Structures* 2009, *31*, 1354-1368.
85. Housner, G. Measures of severity of earthquake ground shaking. In Proceedings of the US National Conference on Earthquake Engineering, Arbor, Michigan, June, 1975; pp. 25–33.
86. Bojórquez, E.; Iervolino, I. Spectral shape proxies and nonlinear structural response. *Soil Dynamics and Earthquake Engineering* 2011, *31*, 996-1008.

87. Sarma, S.; Yang, K. An evaluation of strong motion records and a new parameter A95. *Earthquake engineering & structural dynamics* 1987, *15*, 119-132.
88. Park, Y.-J.; Ang, A.H.-S.; Wen, Y.K. Seismic damage analysis of reinforced concrete buildings. *Journal of Structural Engineering* 1985, *111*, 740-757.
89. Riddell, R.; Garcia, J.E. Hysteretic energy spectrum and damage control. *Earthquake engineering & structural dynamics* 2001, *30*, 1791-1816.
90. Reed, J.W.; Kassawara, R.P. A criterion for determining exceedance of the operating basis earthquake. *Nuclear Engineering and Design* 1990, *123*, 387-396.
91. Campbell, K.W.; Bozorgnia, Y. Prediction equations for the standardized version of cumulative absolute velocity as adapted for use in the shutdown of US nuclear power plants. *Nuclear Engineering and Design* 2011, *241*, 2558-2569.
92. Cordova, P.P.; Deierlein, G.G.; Mehanny, S.S.; Cornell, C.A. Development of a two-parameter seismic intensity measure and probabilistic assessment procedure. In Proceedings of the Second US-Japan Workshop on Performance-Based Earthquake Engineering Methodology for Reinforced Concrete Building Structures, Hokkaido, Japan, 11–13 September 2000; pp. 187-206.
93. Bommer, J.J.; Alarcon, J.E. The prediction and use of peak ground velocity. *Journal of Earthquake Engineering* 2006, *10*, 1-31.
94. Fajfar, P.; Vidic, T.; Fischinger, M. A measure of earthquake motion capacity to damage medium-period structures. *Soil Dynamics and Earthquake Engineering* 1990, *9*, 236-242.
95. Housner, G.W. *Intensity of ground motion during strong earthquakes*; Pasadena, CA, USA, 1952.
96. Cosenza, E.; Manfredi, G. A seismic design method including damage effect. In Proceedings of the 11th European Conference on Earthquake Engineering, 1998; pp. 6-11.
97. Bishop, C.M.; Nasrabadi, N.M. *Pattern recognition and machine learning*; Springer: 2006.
98. Shalev-Shwartz, S.; Ben-David, S. *Understanding machine learning: From theory to algorithms*; Cambridge University Press: 2014.
99. Su, X.; Yan, X.; Tsai, C.L. Linear regression. *Wiley Interdisciplinary Reviews: Computational Statistics* 2012, *4*, 275-294.
100. Daumé, H. *A course in machine learning*; TODO: 2017.
101. Myles, A.J.; Feudale, R.N.; Liu, Y.; Woody, N.A.; Brown, S.D. An introduction to decision tree modeling. *Journal of Chemometrics: A Journal of the Chemometrics Society* 2004, *18*, 275-285.
102. Biau, G.; Scornet, E. A random forest guided tour. *Test* 2016, *25*, 197-227.
103. Chen, T.; He, T.; Benesty, M.; Khotilovich, V.; Tang, Y.; Cho, H.; Chen, K. Xgboost: extreme gradient boosting. *R package version 0.4-2* 2015, *1*, 1-4.
104. Noriega, L. Multilayer perceptron tutorial. *School of Computing. Staffordshire University* 2005, *4*, 5.
105. Shome, N. *Probabilistic seismic demand analysis of nonlinear structures*; Stanford University: 1999.
106. Satake, N.; Yokota, H. Evaluation of vibration properties of high-rise steel buildings using data of vibration tests and earthquake observations. *Journal of wind engineering and industrial aerodynamics* 1996, *59*, 265-282.
107. Subramanian, K.; Velayutham, M. Seismic performance of lateral load resisting systems. *Structural engineering and mechanics: An international journal* 2014, *51*, 487-502.
108. Baikerikar, A.; Kanagali, K. Study of lateral load resisting systems of variable heights in all soil types of high seismic zone. *International Journal of Research in Engineering and Technology* 2014, *3*, 2319-1163.
109. Wilson, J.; Lam, N. Earthquake design of buildings in Australia using velocity and displacement principles. *Australian Journal of Structural Engineering* 2006, *6*, 103-118.
110. Moscoso Alcantara, E.A.; Saito, T. Machine Learning-Based Rapid Post-Earthquake Damage Detection of RC Resisting-Moment Frame Buildings. *Sensors* 2023, *23*, 4694.
111. Shibata, A. *Dynamic Analysis of Earthquake Resistant Structures*; Tohoku University Press: Sendai, Japan, 2010.
112. AIJ. Recommendations for Loads on Buildings. 2015.
113. AIJ. Structural Calculation of Reinforced Concrete Structures (in Japanese). 2018.

114. Shafei, B.; Zareian, F.; Lignos, D.G. A simplified method for collapse capacity assessment of moment-resisting frame and shear wall structural systems. *Engineering Structures* 2011, *33*, 1107-1116.
115. Pedregosa, F.; Varoquaux, G.; Gramfort, A.; Michel, V.; Thirion, B.; Grisel, O.; Blondel, M.; Prettenhofer, P.; Weiss, R.; Dubourg, V. Scikit-learn: Machine learning in Python. *the Journal of machine Learning research* 2011, *12*, 2825-2830.
116. Clough, R. Effect of stiffness degradation of earthquake duktility requirements. In Proceedings of the Japan Earthquake Engineering Symposium, 1966; pp. 227-232.
117. Mahin, S.A.; Lin, J. *Construction of inelastic response spectra for single-degree-of-freedom systems*; 1983.
118. Kunnath, S.K.; Reinhorn, A.M.; Lobo, R. *IDARC Version 3.0: A program for the inelastic damage analysis of reinforced concrete structures*; National Center for Earthquake Engineering Research: Buffalo, NY, 1992.

Publication List

List of Papers with Referee's Review:

1. Moscoso Alcantara, Edisson Alberto, Michelle Diana Bong, and Taiki Saito. "Structural Response Prediction for Damage Identification Using Wavelet Spectra in Convolutional Neural Network," Sensors, Vol. 21(20), 6795 (23 pages) [Published, October 2021]

2. Moscoso Alcantara, Edisson Alberto, and Taiki Saito. "Convolutional Neural Network-Based Rapid Post-Earthquake Structural Damage Detection: Case Study," Sensors, Vol. 22(17), 6426 (22 pages) [Published, August 2022]

3. Moscoso Alcantara, Edisson Alberto, and Taiki Saito. "Machine Learning-Based Rapid Post-Earthquake Damage Detection of RC Resisting-Moment Frame Buildings," Sensors, Vol. 23(10), 4694 (22 pages) [Published, May 2023]

List of Papers at International Conference with Referee's Review:

1. Moscoso Alcantara, Edisson Alberto, Michelle Diana Bong, and Taiki Saito, "Structural Damage Identification Using Machine Learning: A Case Study," The 2nd International Symposium on Civil, environmental, and Infrastructure Engineering, ISCEIE22, Yogyakarta, Indonesia, August 10th and 11th, 2022.

2. Moscoso Alcantara, Edisson Alberto, and Taiki Saito, "Structural damage condition of buildings with a sparse number of sensors using Machine learning: Case Study," Building for the future: Durable, Sustainable, Resilient, fib Symposium 2023, Istanbul, Turkey, June 5th to 7th, 2023.

Appendix A: IDA and WS per story results (Chapter 2)

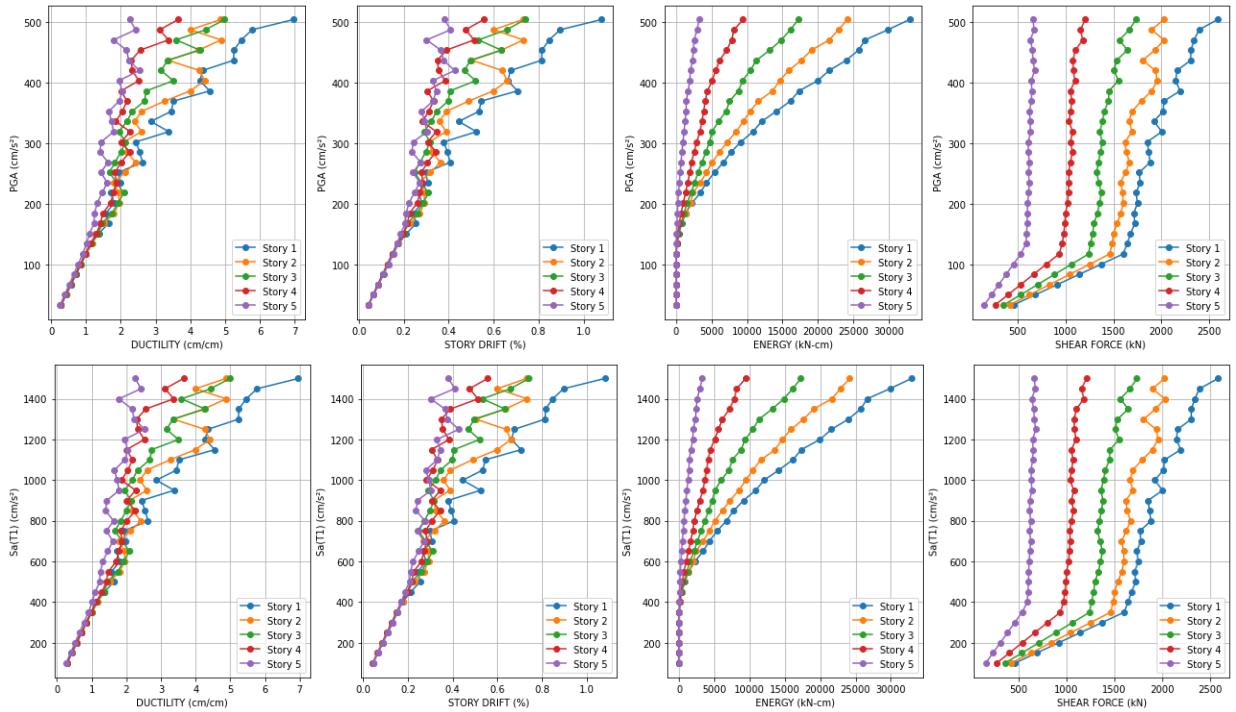

Fig.Appx. 1. IDA per story results – Record: El Centro 1940-EW

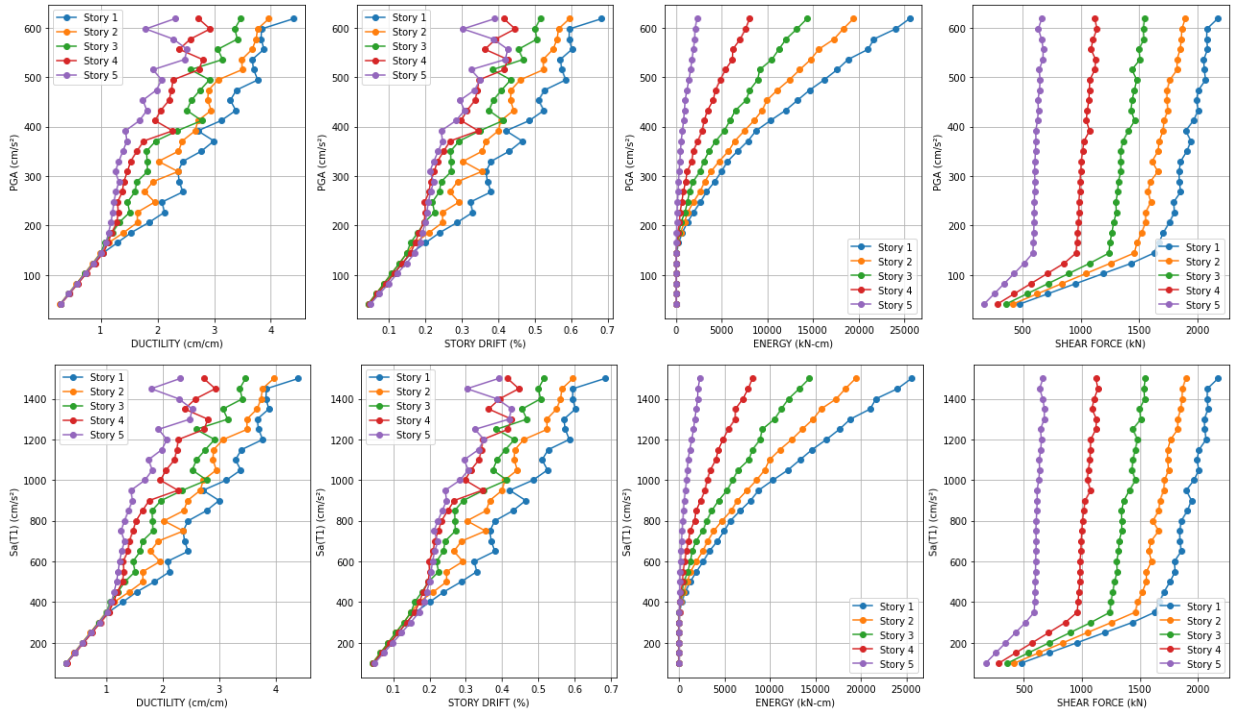

Fig.Appx. 2. IDA per story results – Record: El Centro 1940-NS

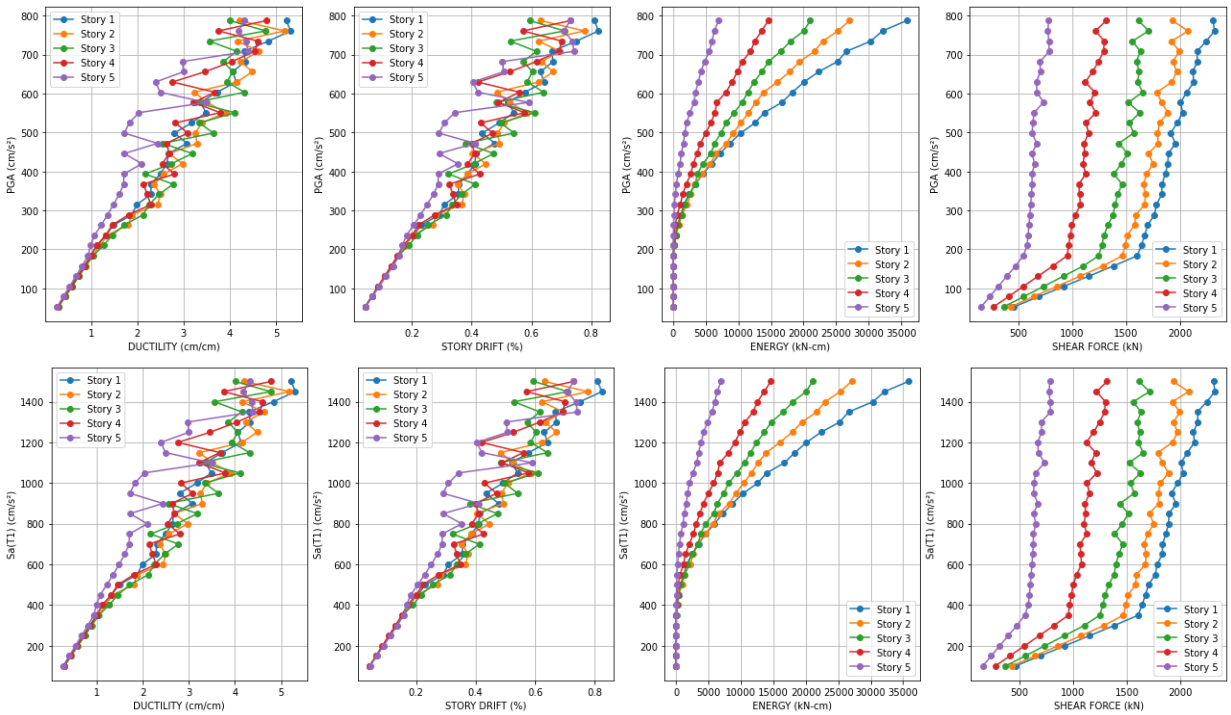

Fig.Appx. 3. IDA per story results – Record: Taft 1952-EW

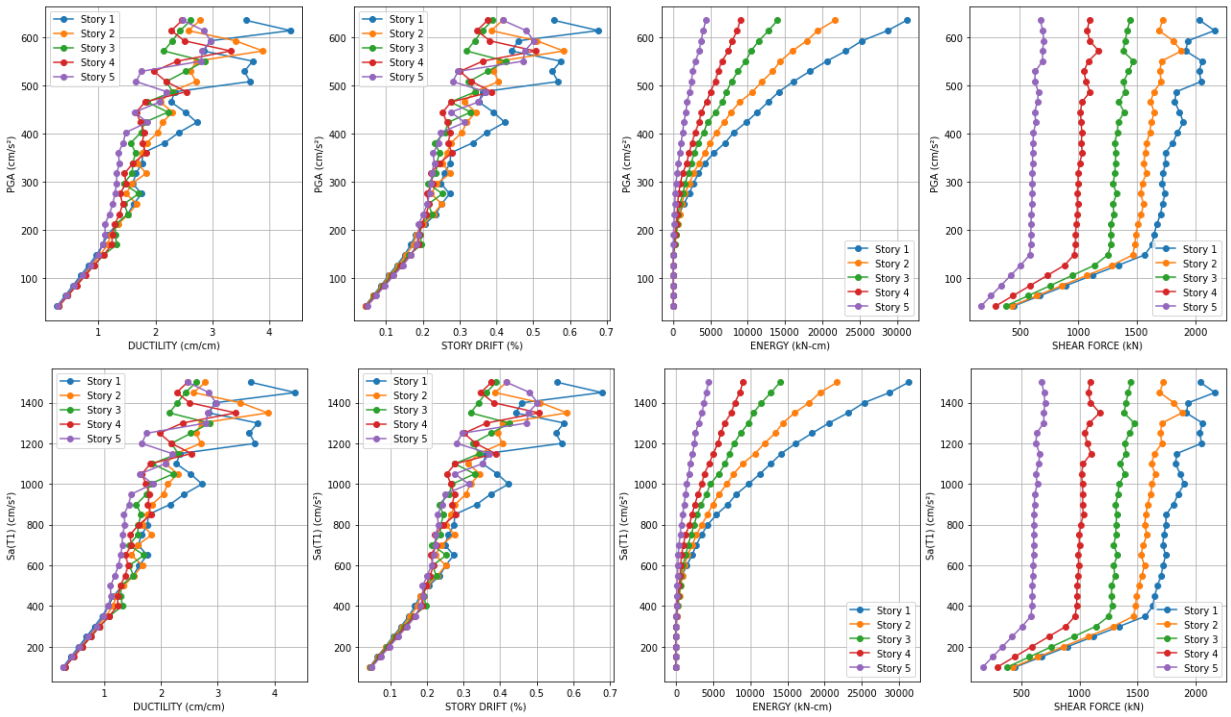

Fig.Appx. 4. IDA per story results – Record: Taft 1952-NS

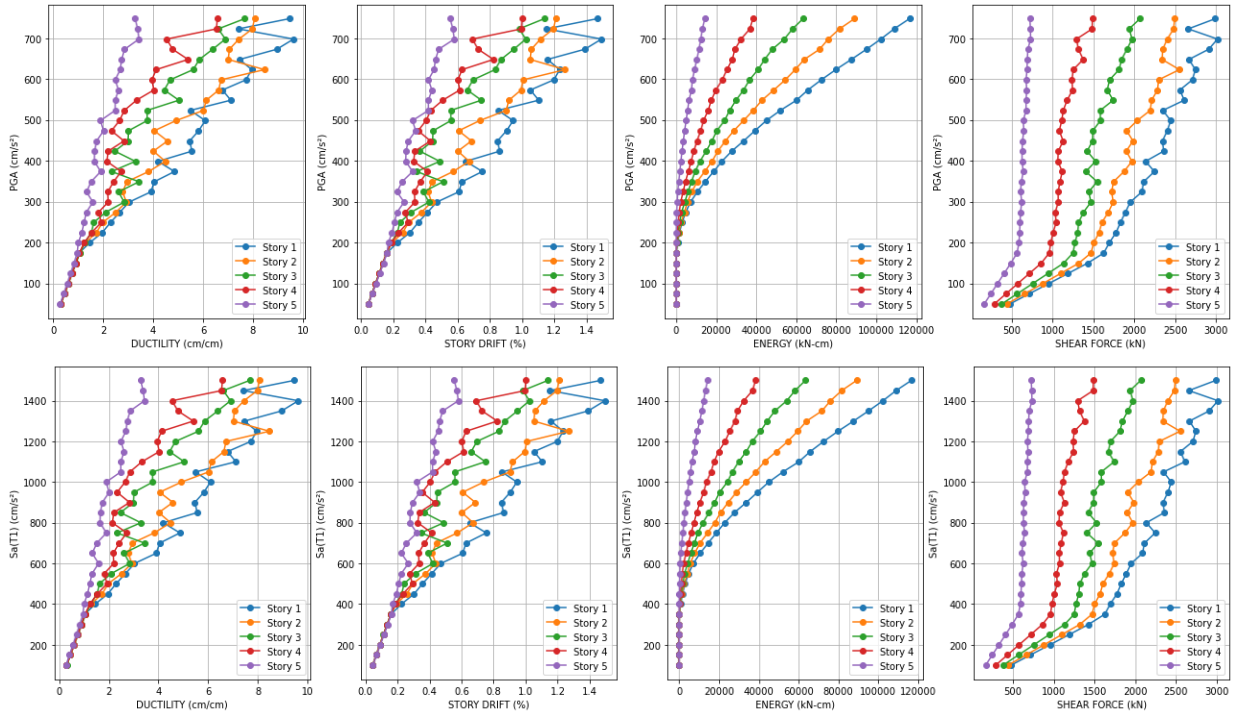

Fig.Appx. 5. IDA per story results – Record: Tohoku 1978-EW

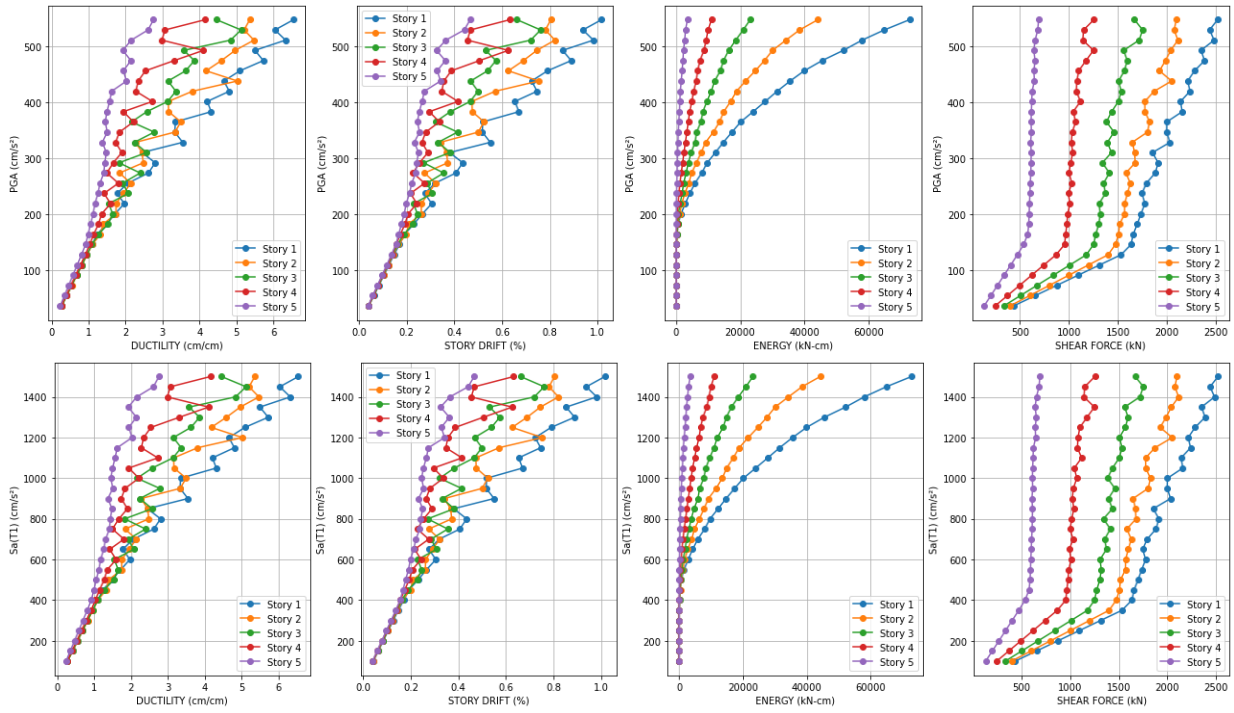

Fig.Appx. 6. IDA per story results – Record: Tohoku 1978-NS

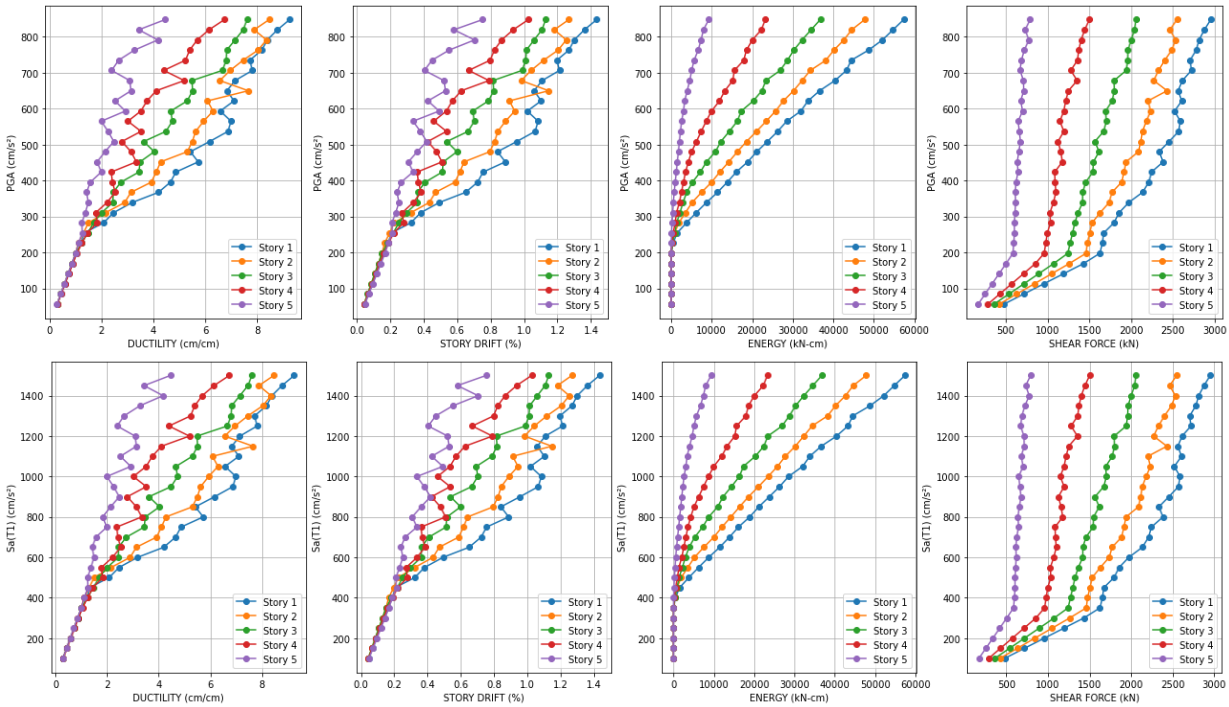

Fig.Appx. 7. IDA per story results – Record: Kobe 1995-EW

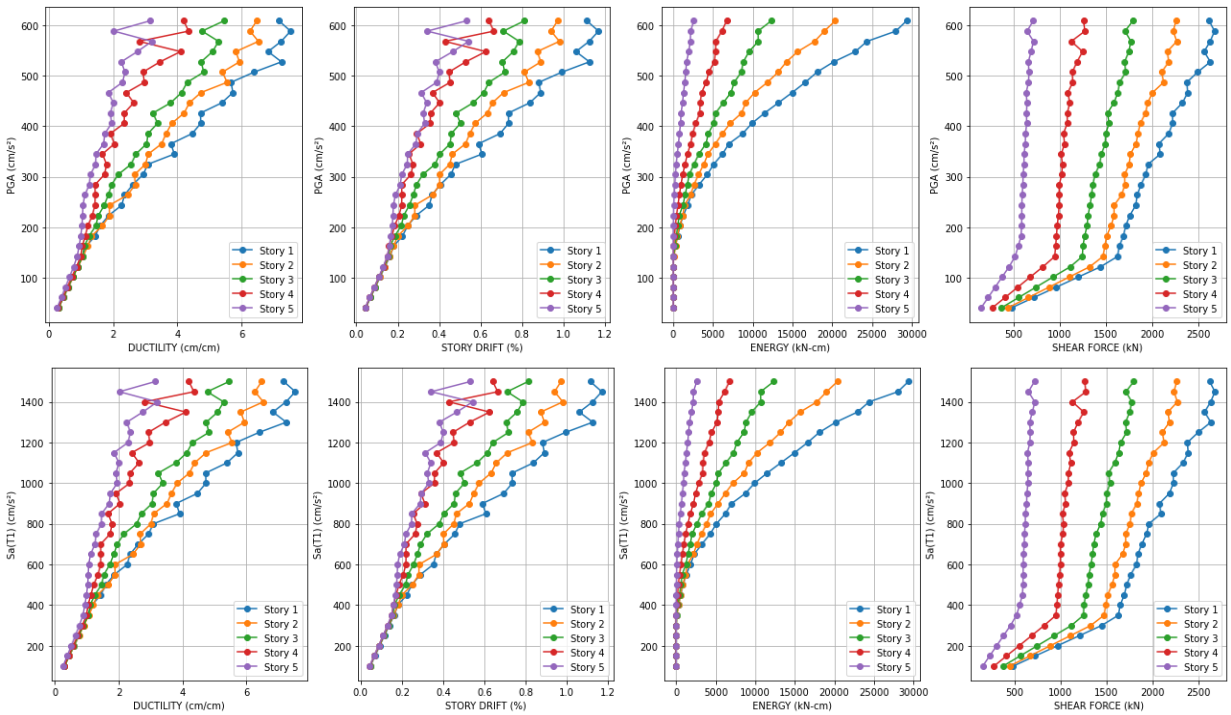

Fig.Appx. 8. IDA per story results – Record: Kobe 1995-NS

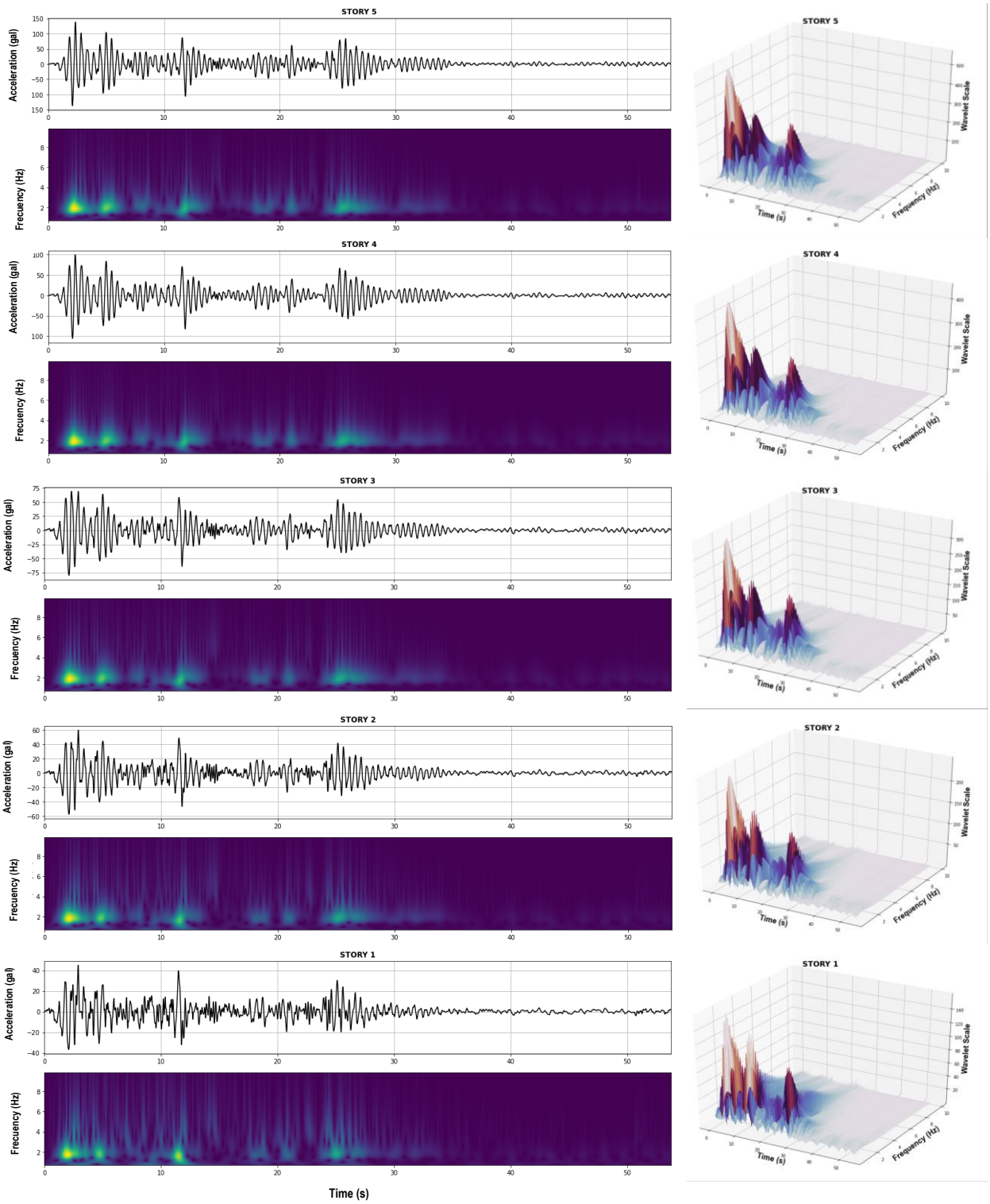

Fig.Appx. 9. WS per story results – Elastic behavior – Record: El Centro 1940-EW

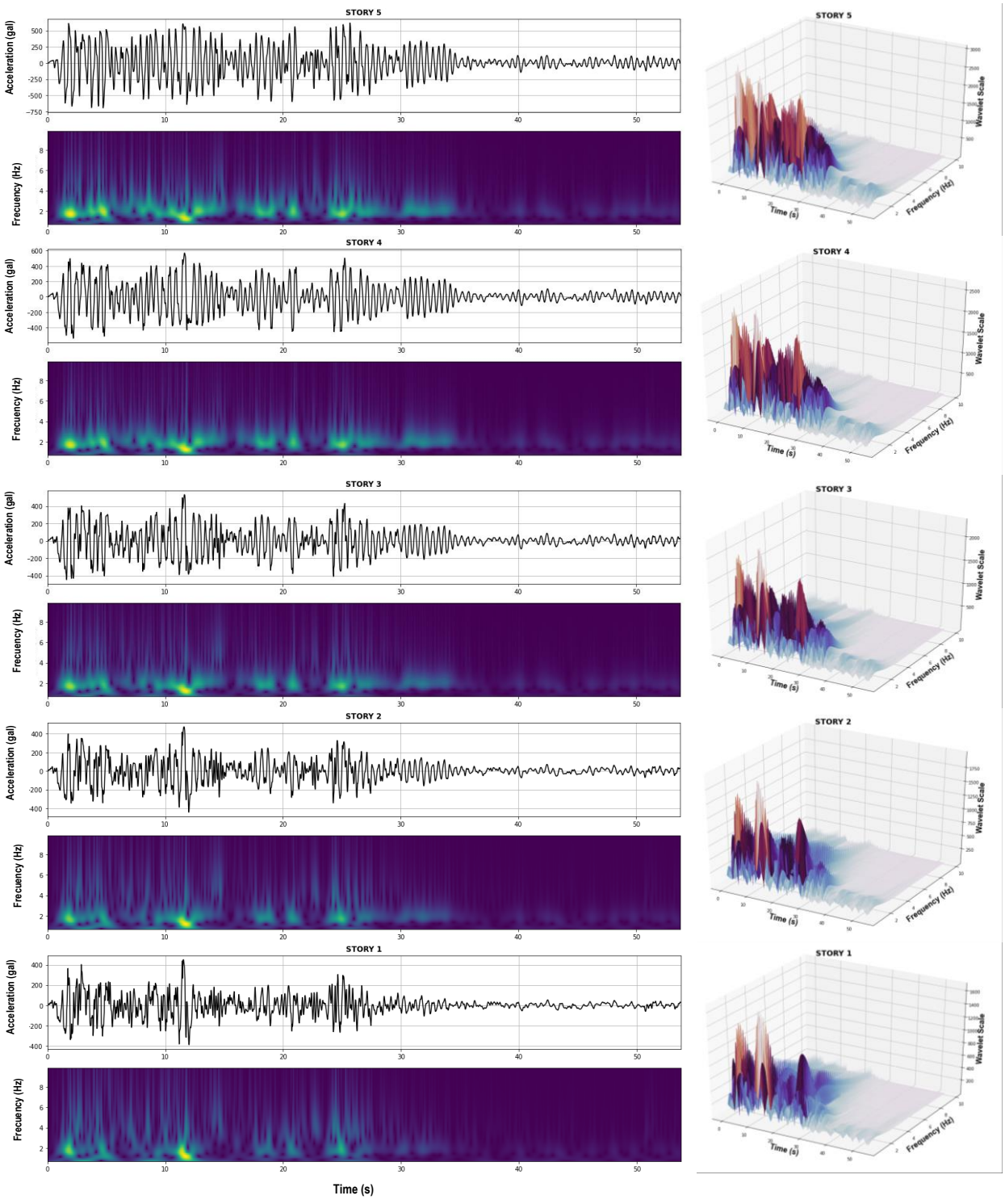

Fig.Appx. 10. WS per story results – Inelastic behavior – Record: El Centro 1940-EW

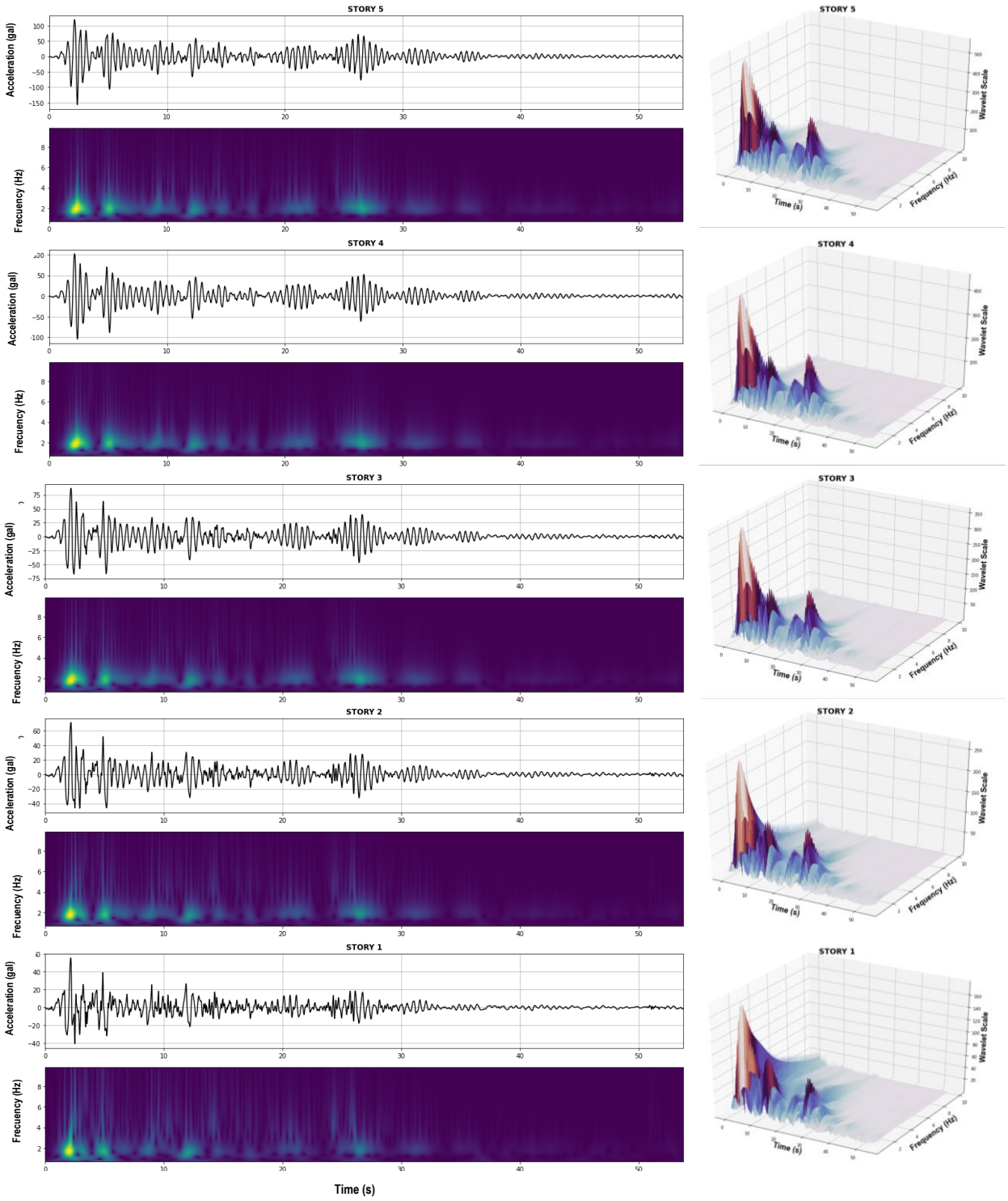

Fig.Appx. 11. WS per story results – Elastic behavior – Record: El Centro 1940-NS

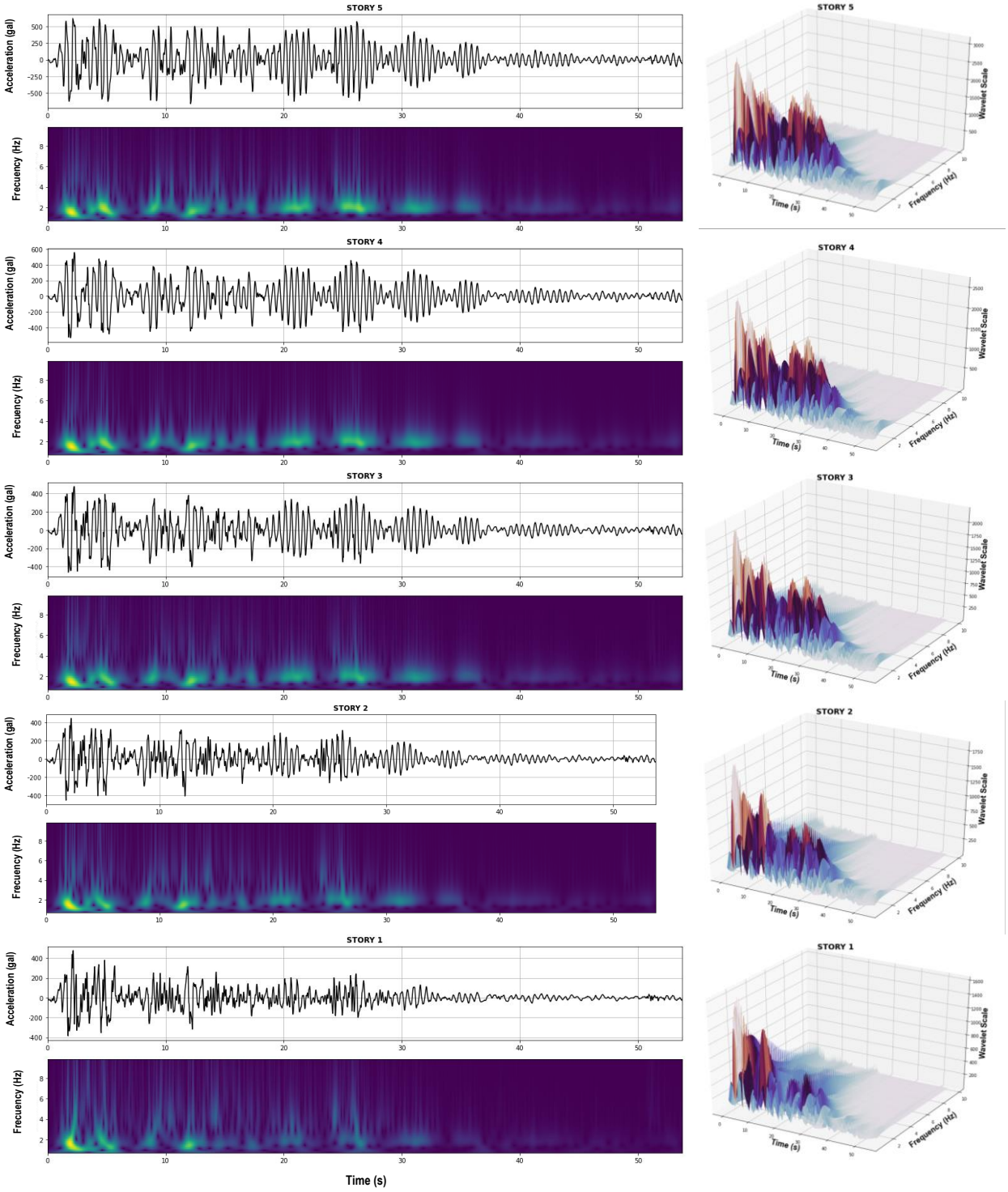

Fig.Appx. 12. WS per story results – Inelastic behavior – Record: El Centro 1940-NS

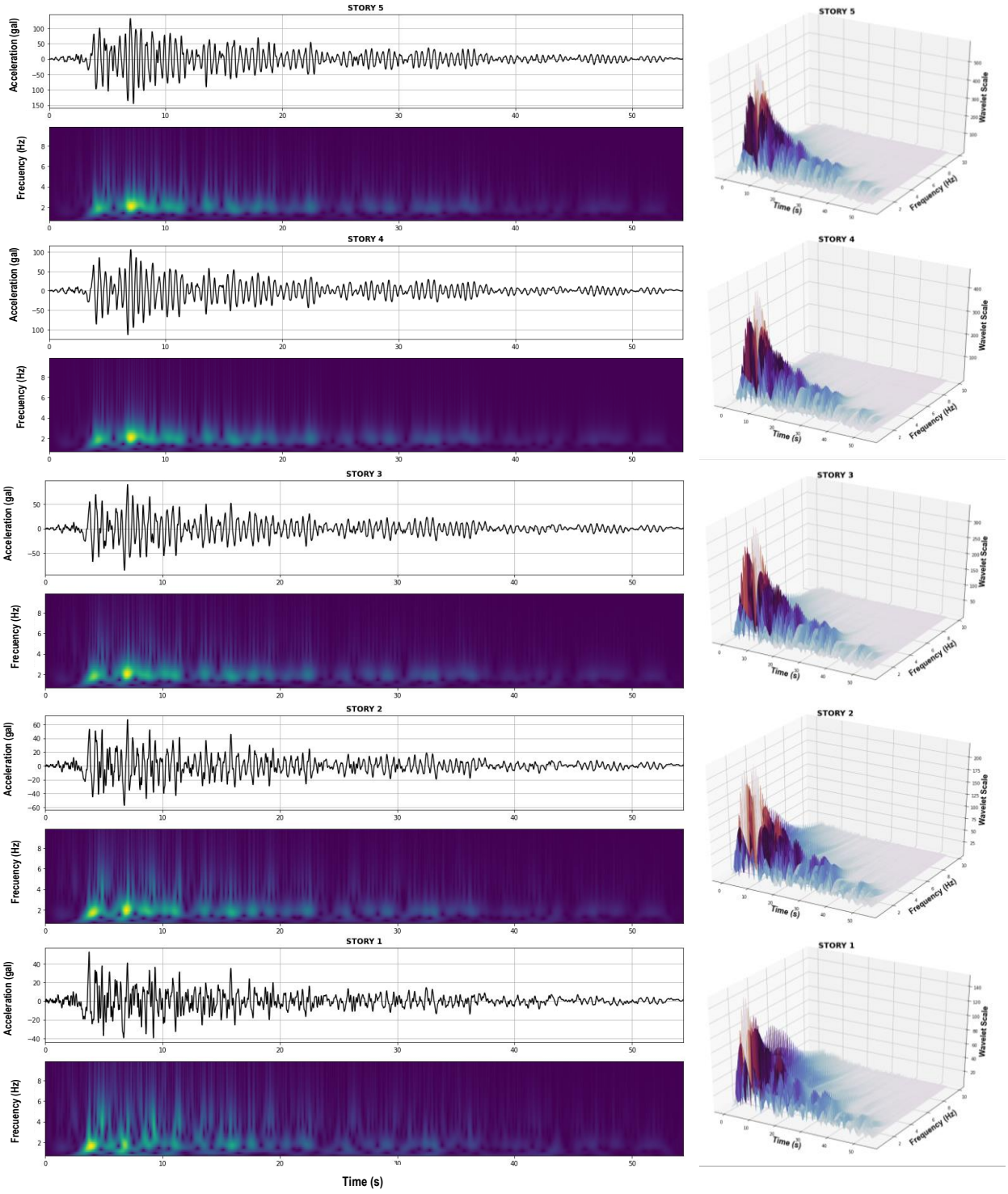

Fig.Appx. 13. WS per story results – Elastic behavior – Record: Taft 1952-EW

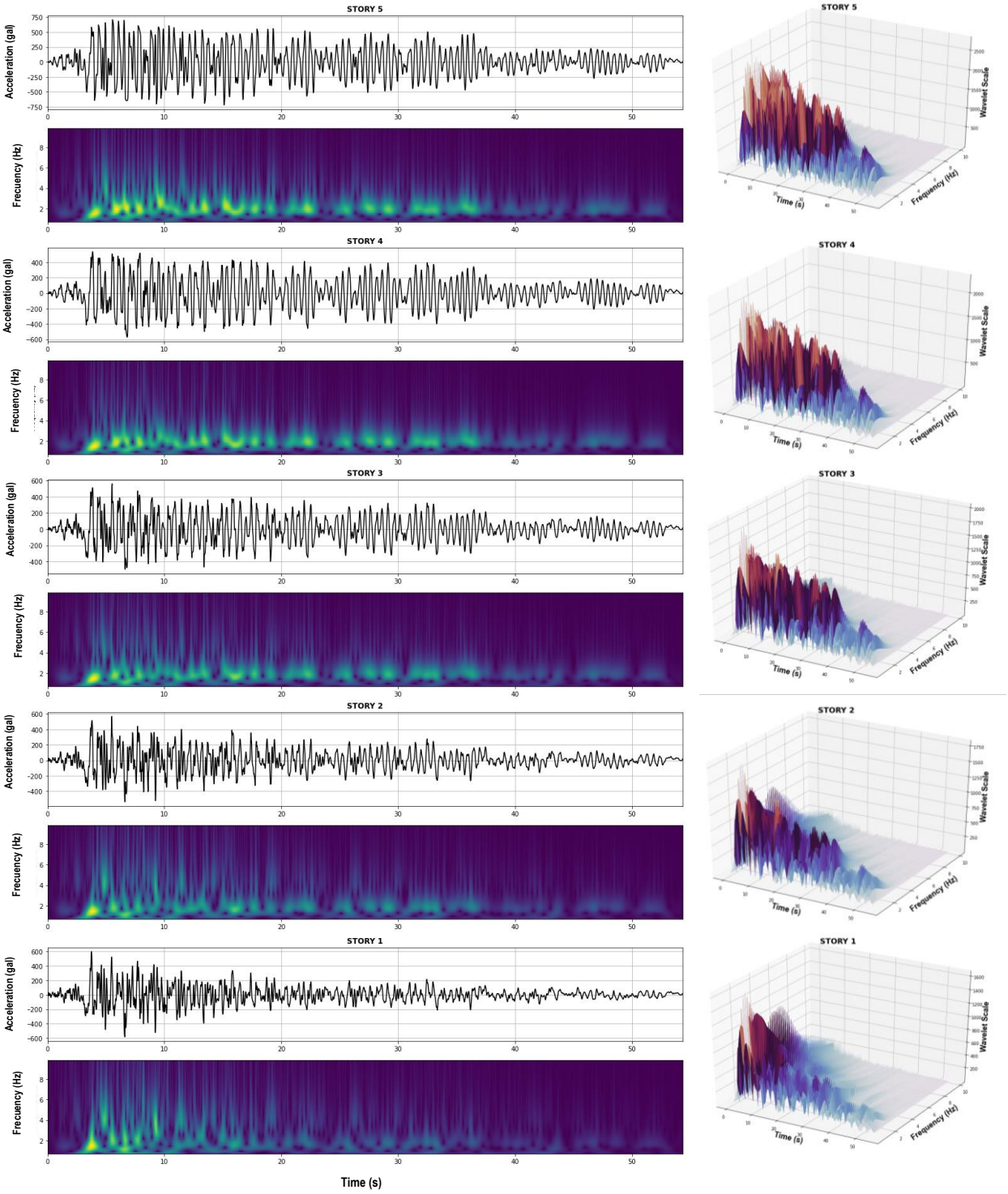

Fig.Appx. 14. WS per story results – Inelastic behavior – Record: Taft 1952-EW

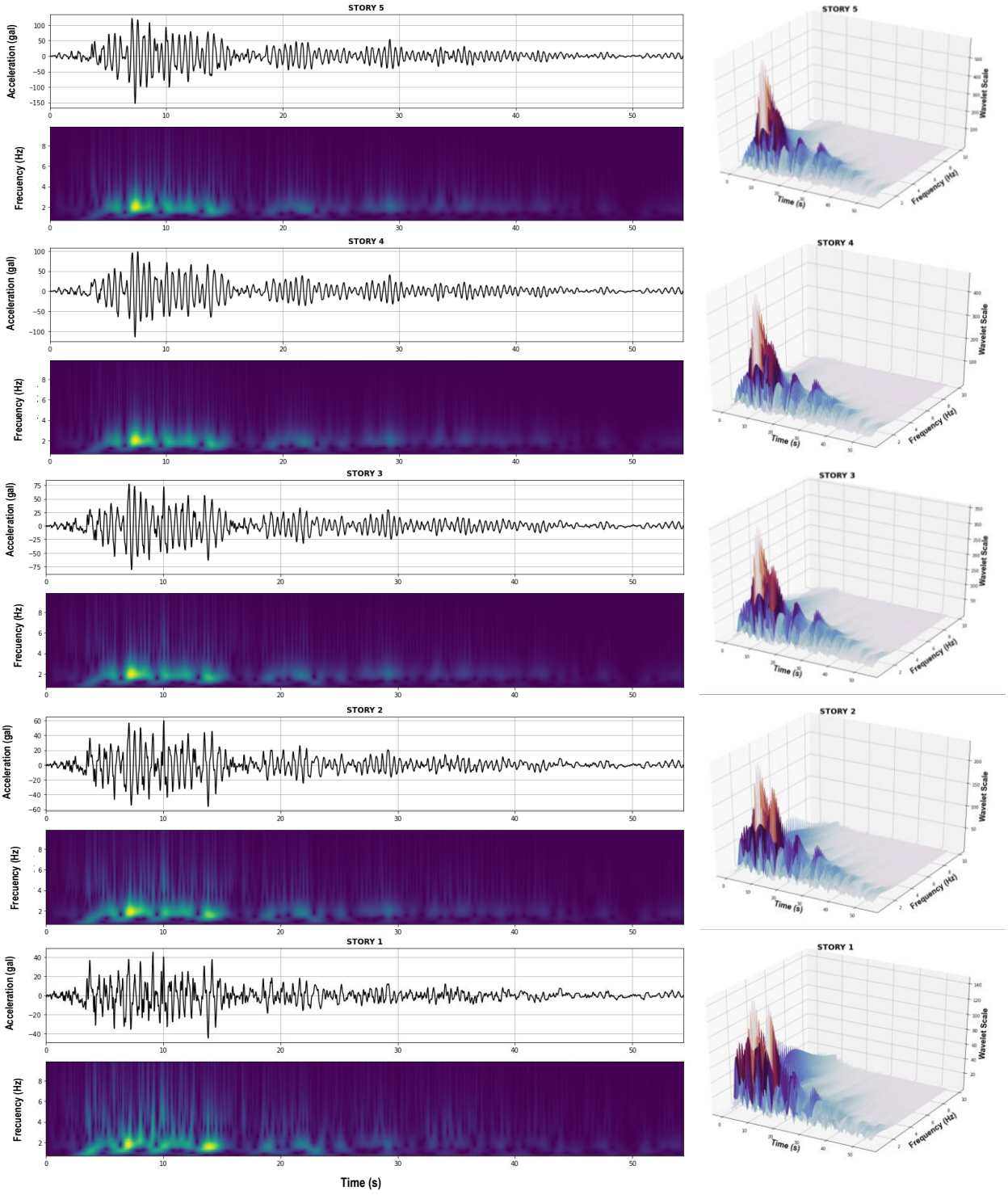

Fig.Appx. 15. WS per story results – Elastic behavior – Record: Taft 1952-NS

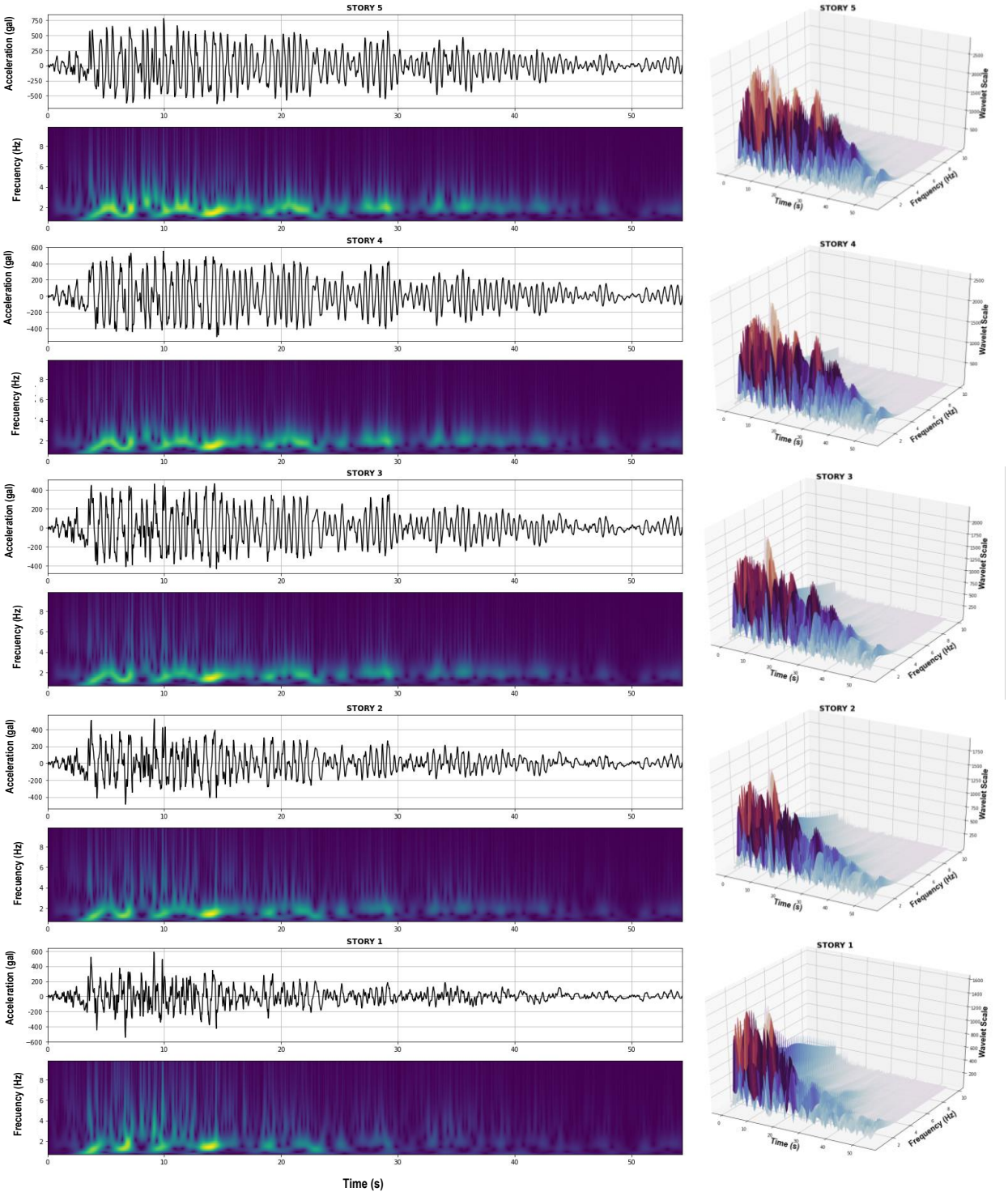

Fig.Appx. 16. WS per story results – Inelastic behavior – Record: Taft 1952-NS

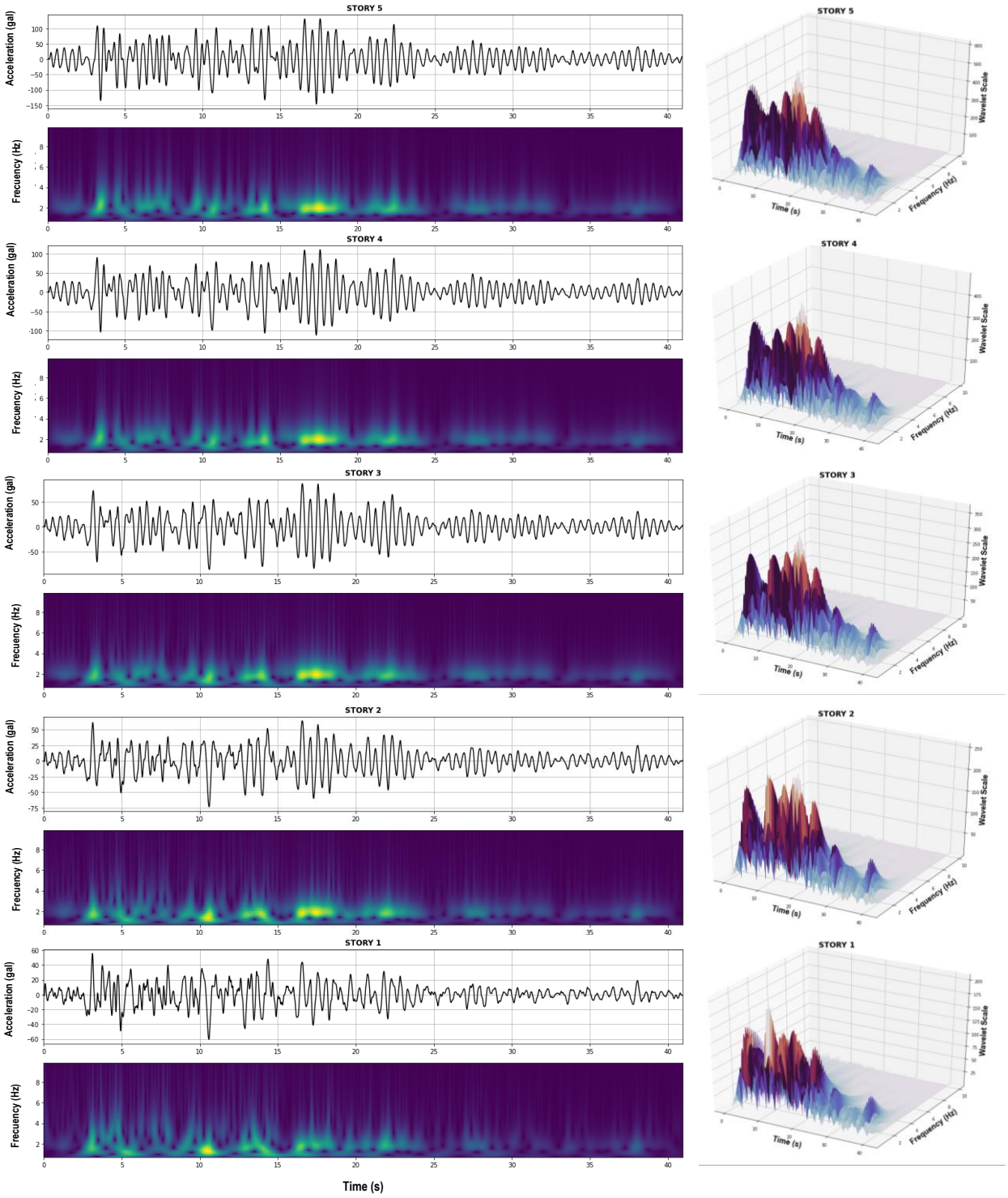

Fig.Appx. 17. WS per story results – Elastic behavior – Record: Tohoku 1978-EW

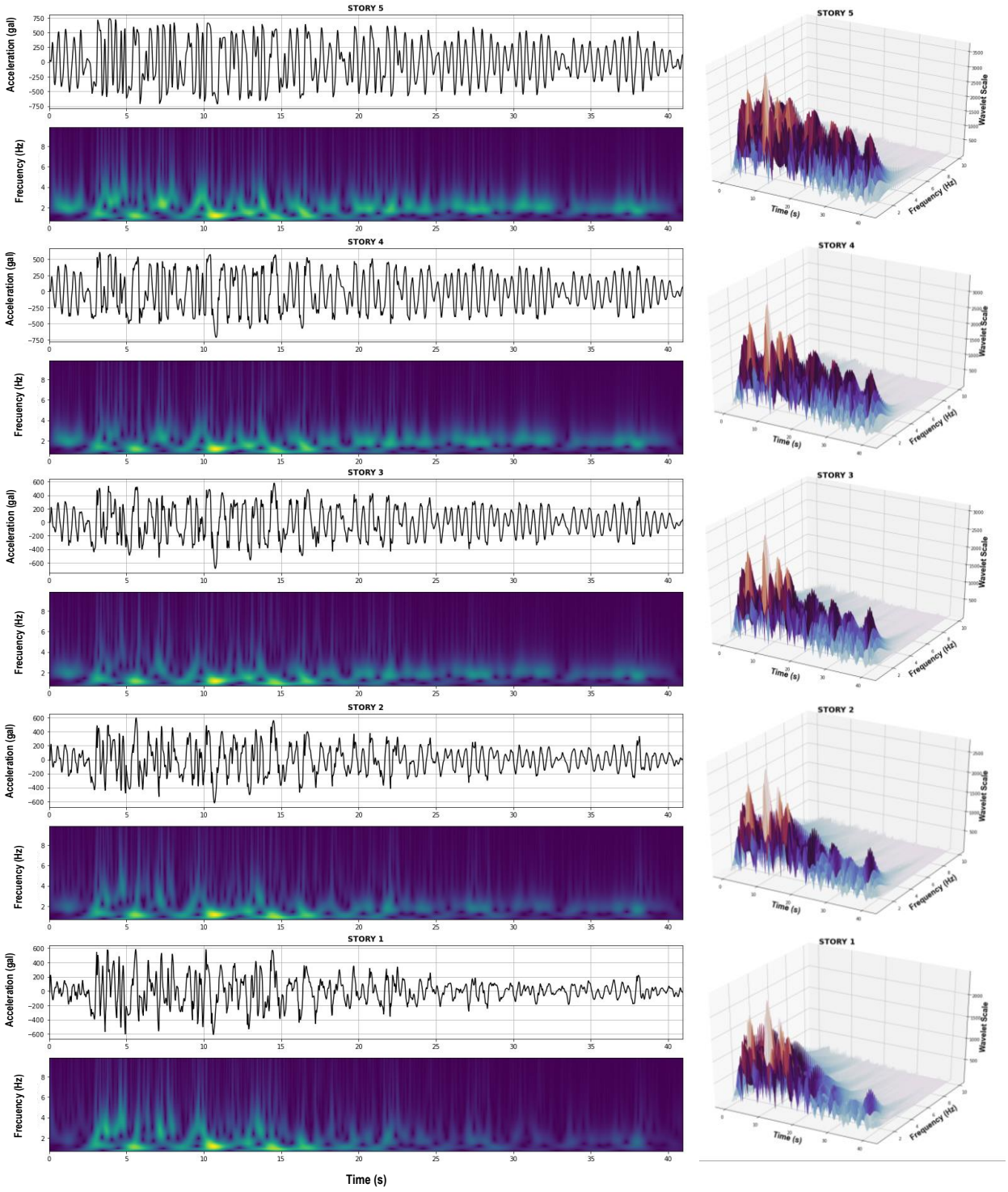

Fig.Appx. 18. WS per story results – Inelastic behavior – Record: Tohoku 1978-EW

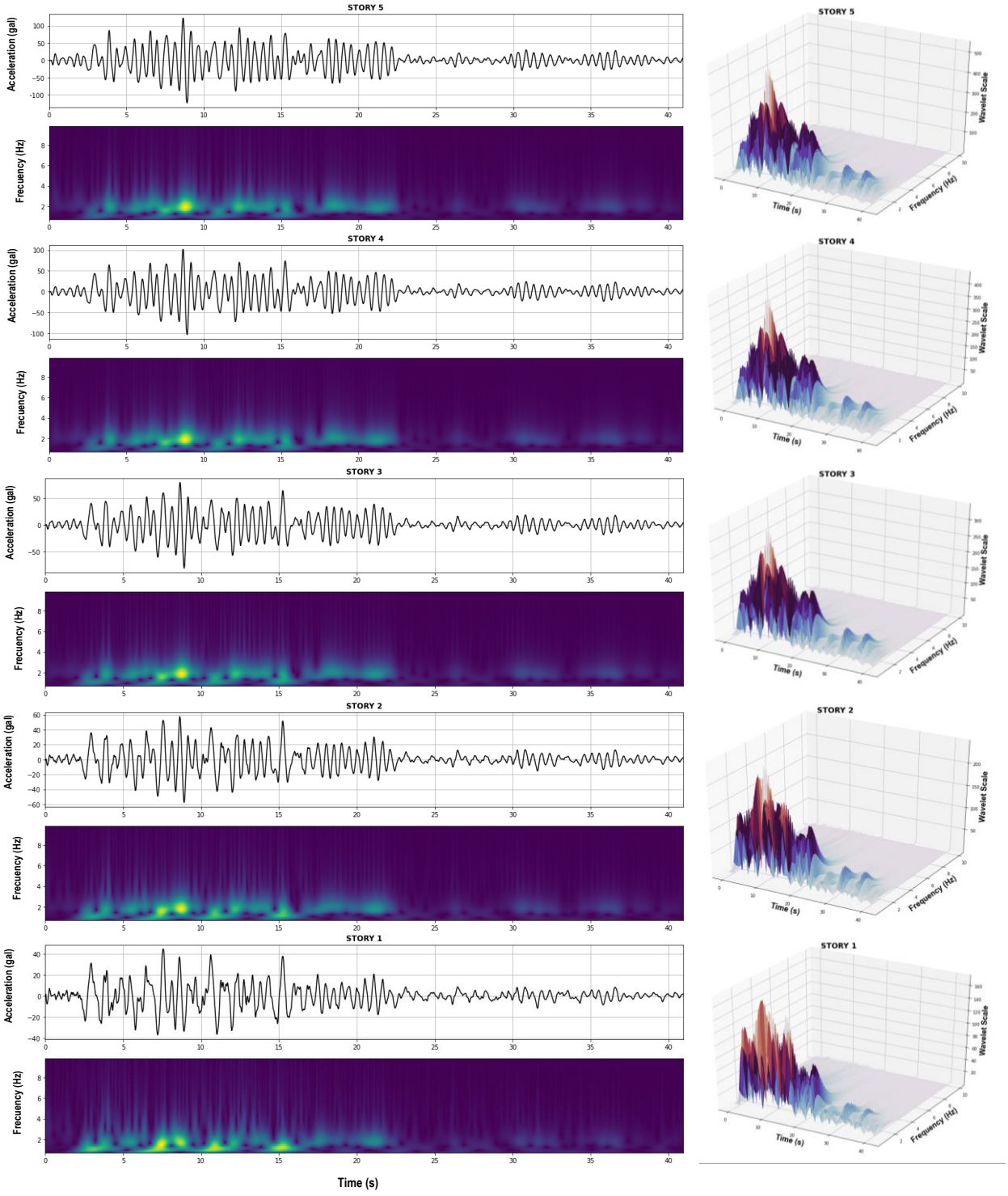

Fig.Appx. 19. WS per story results – Elastic behavior – Record: Tohoku 1978-NS

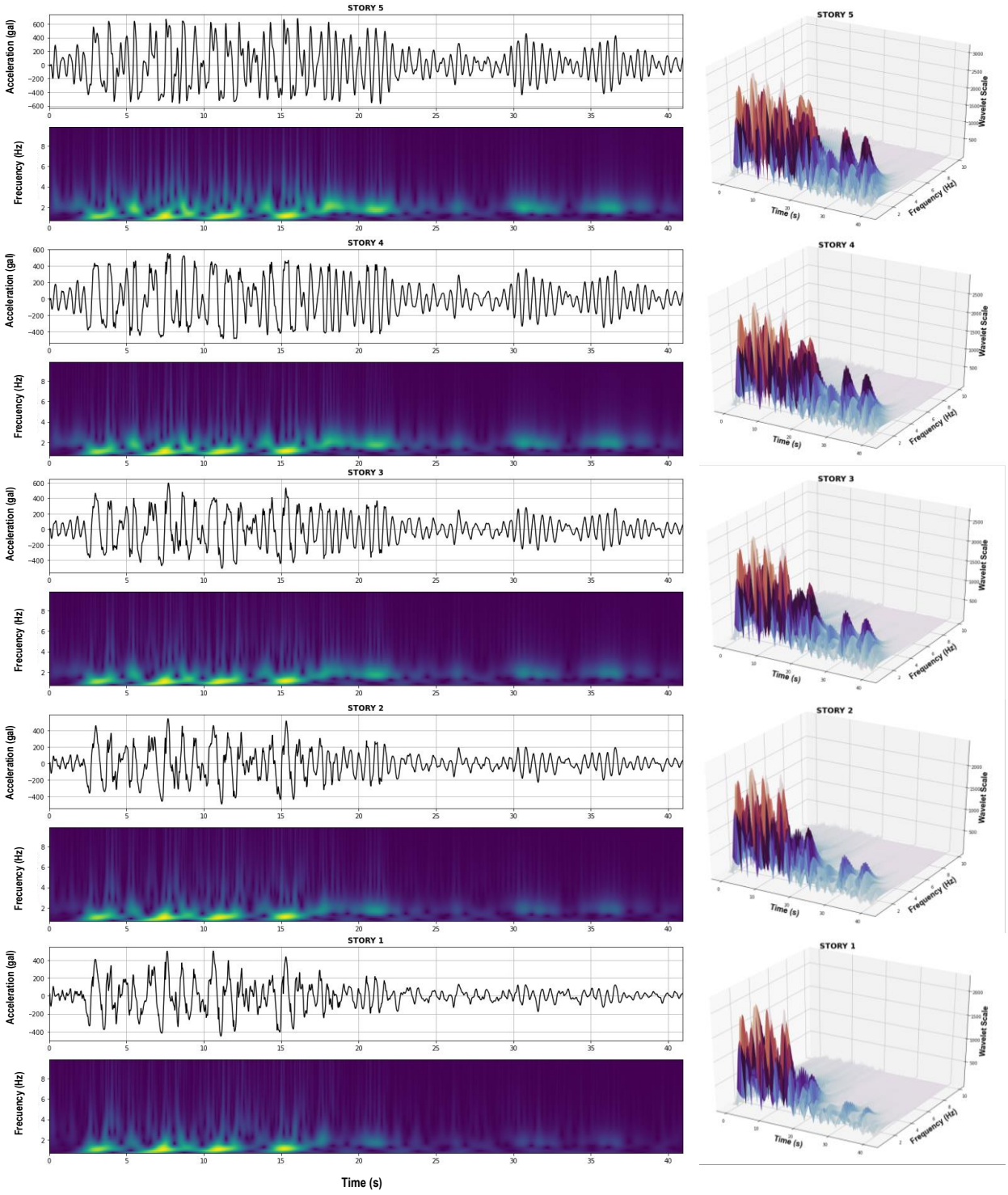

Fig.Appx. 20. WS per story results – Inelastic behavior – Record: Tohoku 1978-NS

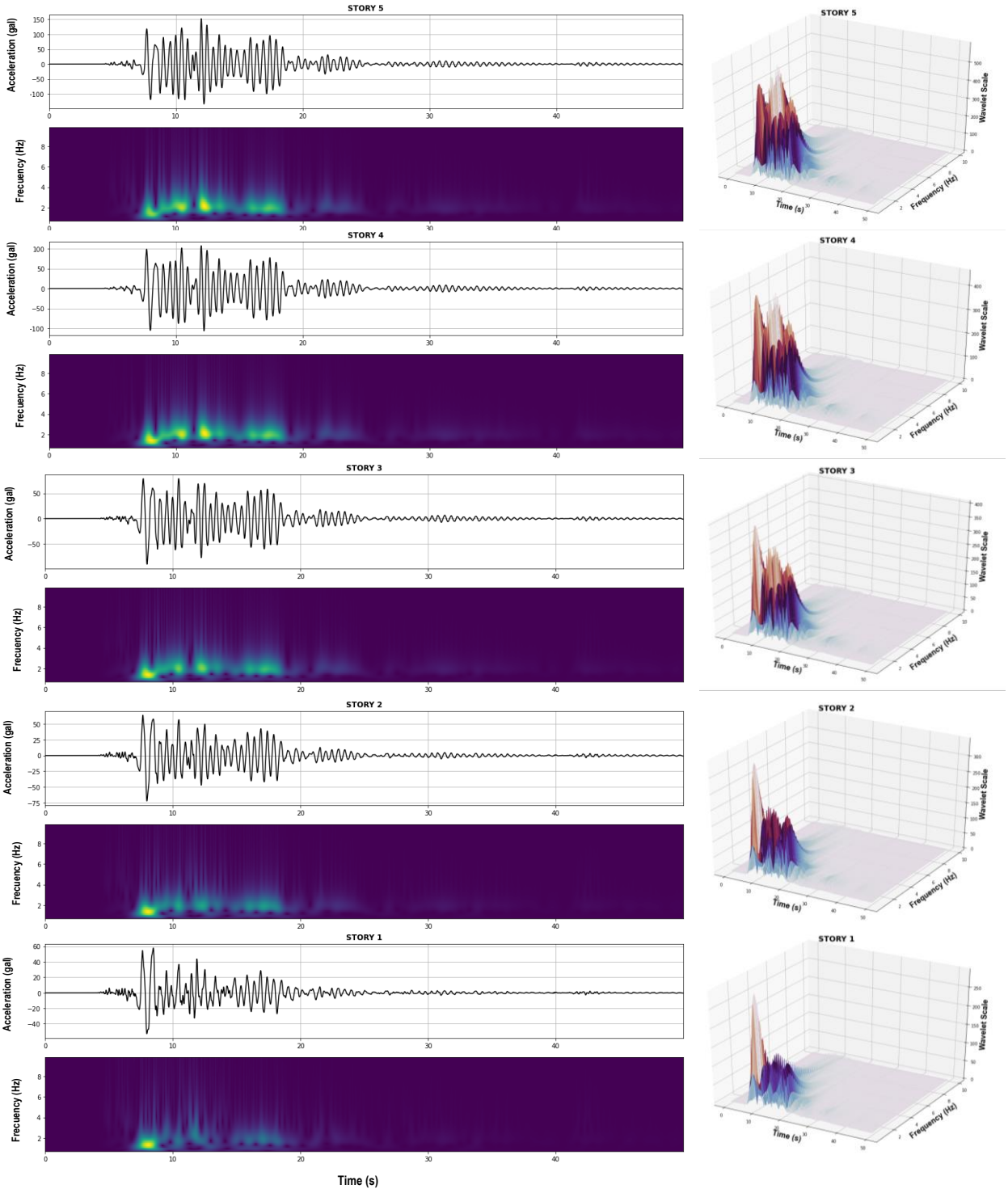

Fig.Appx. 21. WS per story results – Elastic behavior – Record: Kobe 1995-EW

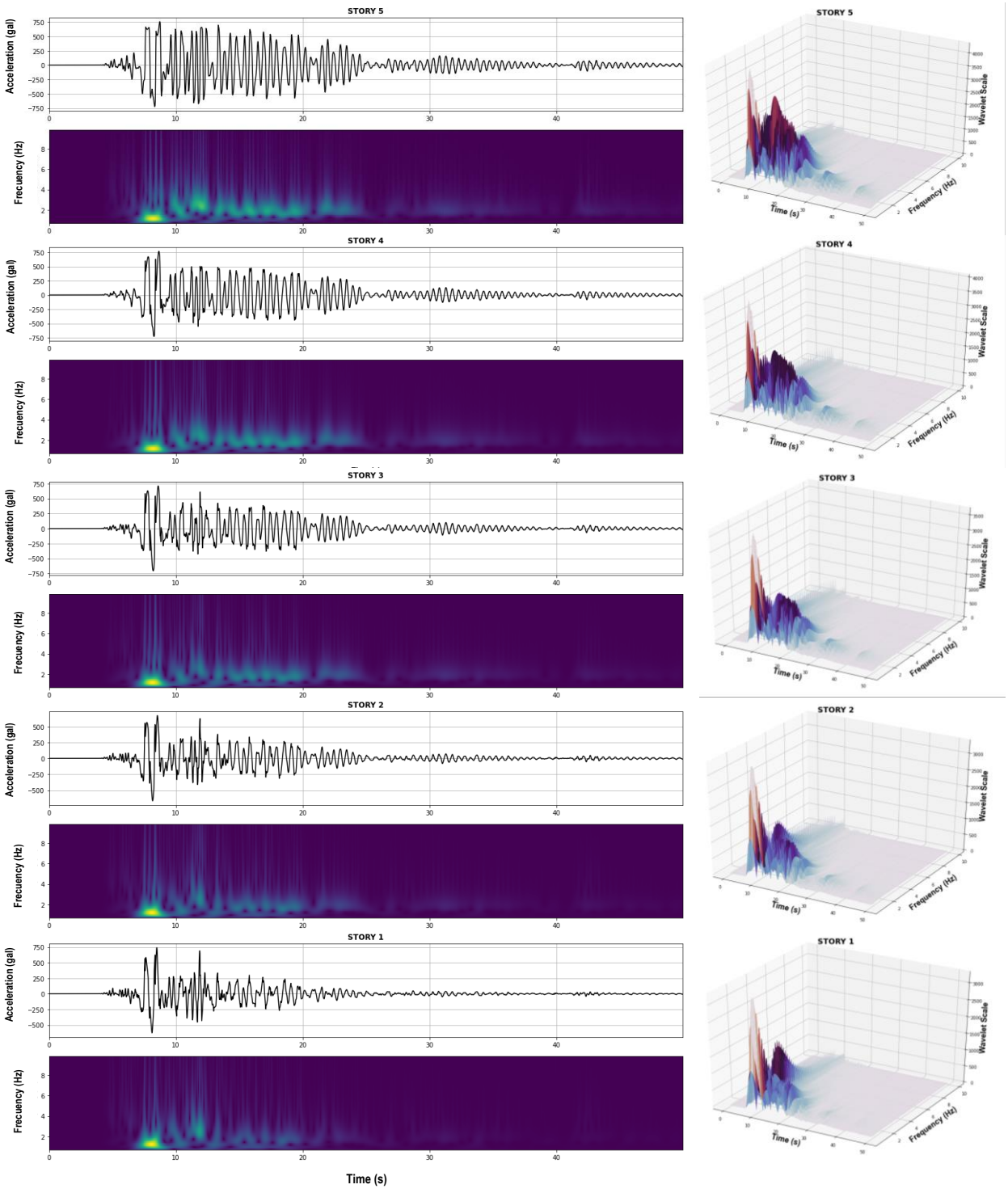

Fig.Appx. 22. WS per story results – Inelastic behavior – Record: Kobe 1995-EW

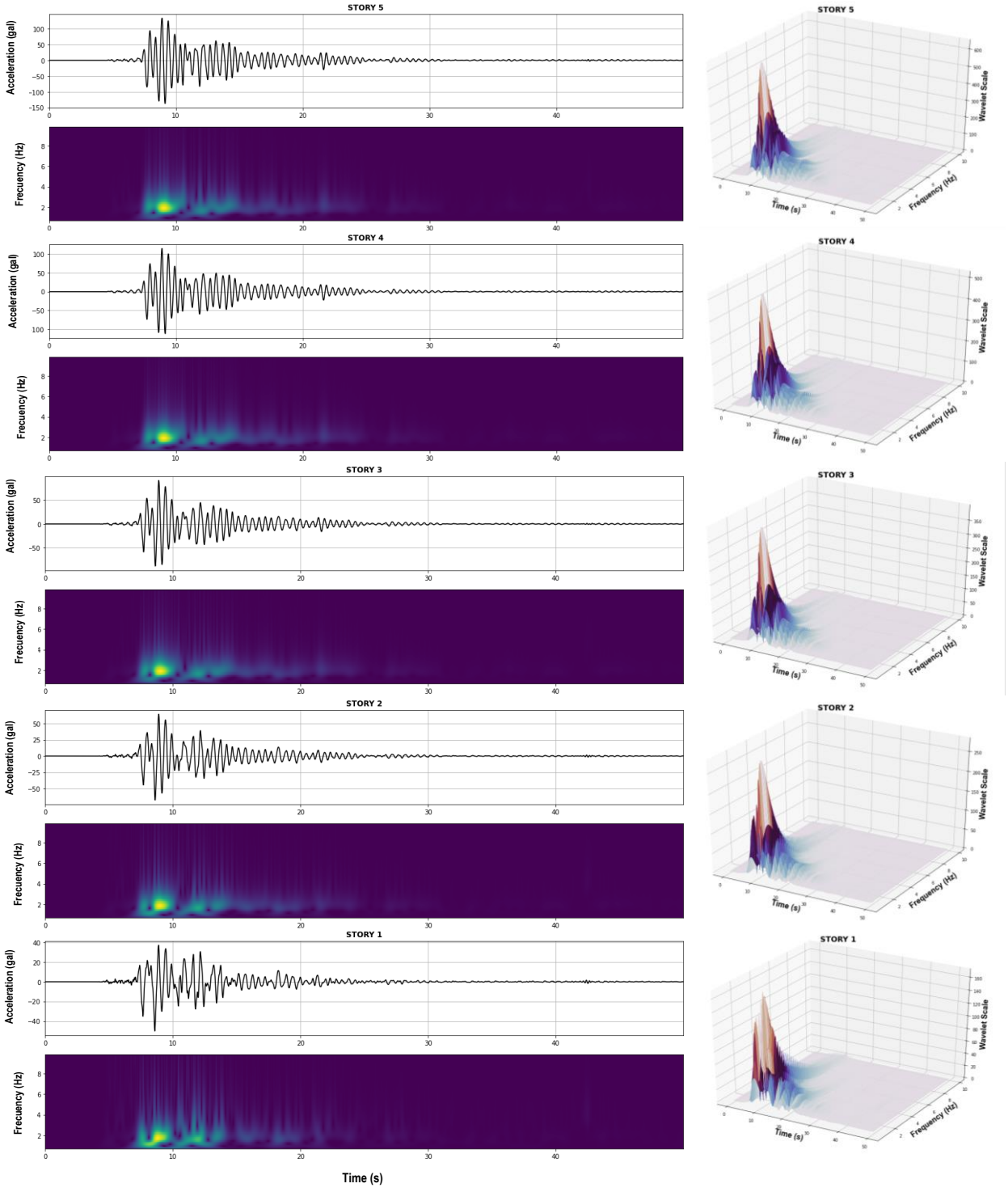

Fig.Appx. 23. WS per story results – Elastic behavior – Record: Kobe 1995-NS

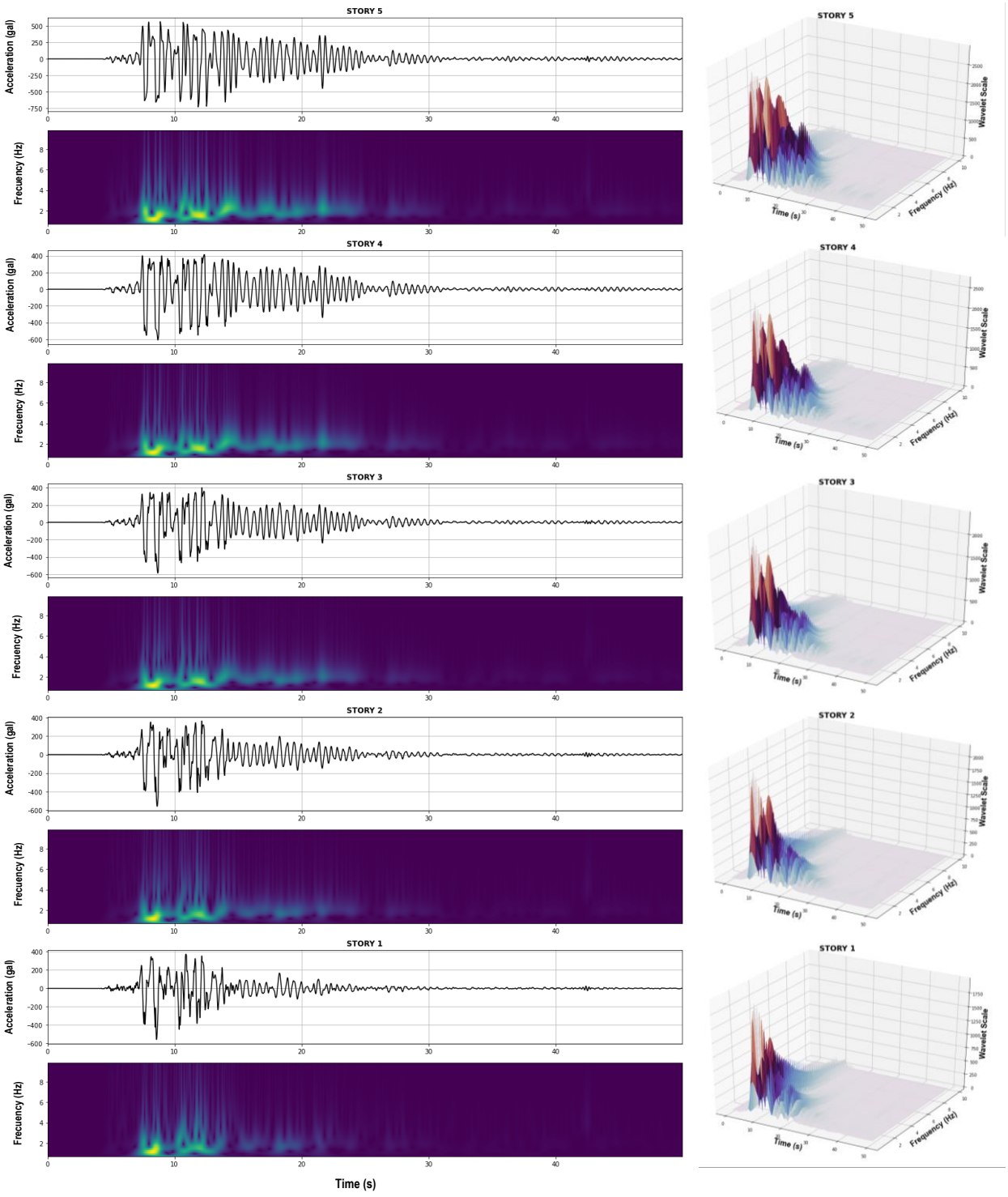

Fig.Appx. 24. WS per story results – Inelastic behavior – Record: Kobe 1995-NS

Appendix B: Prediction per record results for TCH, TFS, and RC buidlings (Chapter 3)

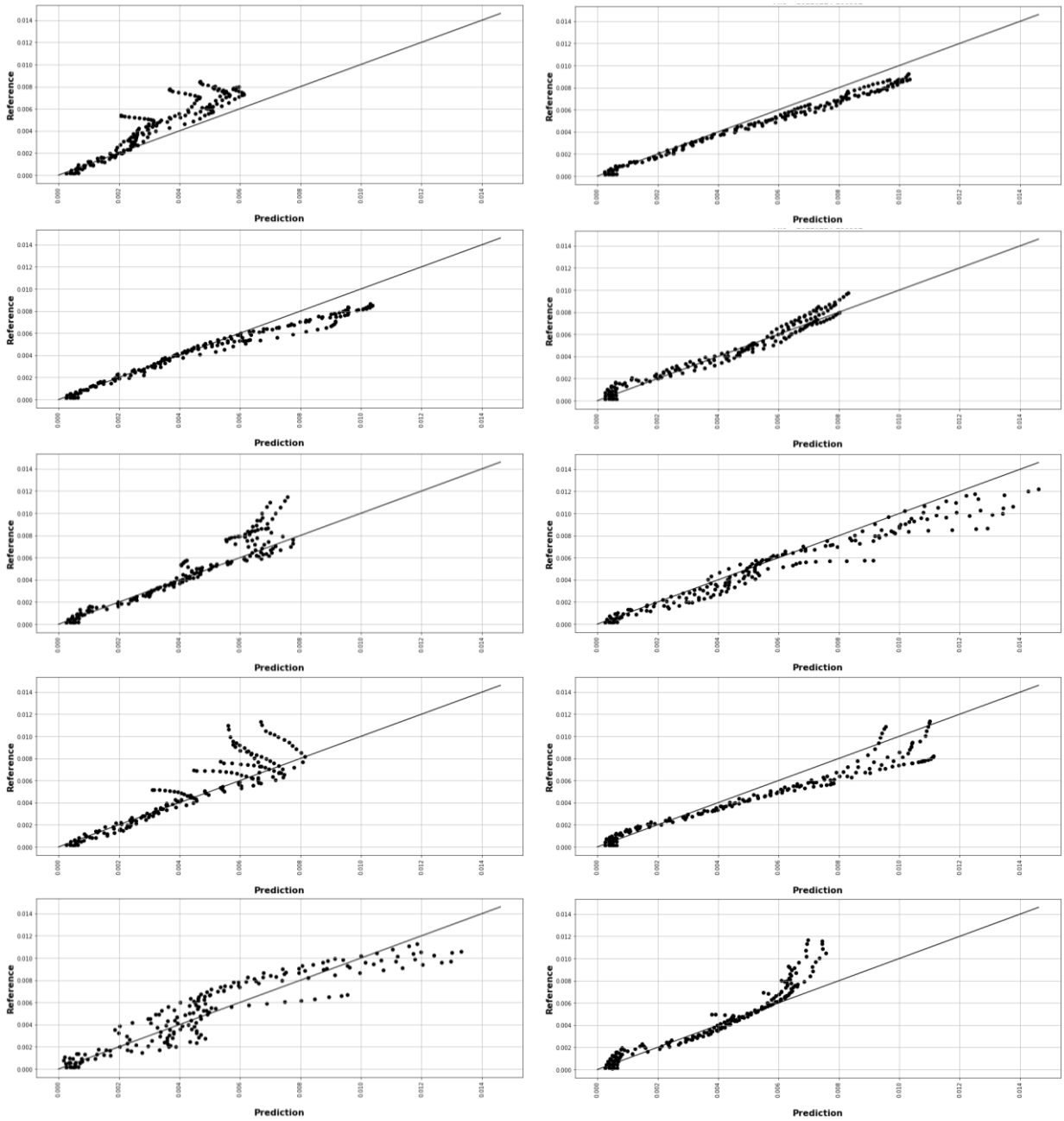

Fig.Appx. 25. Tahara City Hall Building – Story Drift ratio results – Records from left-to-right and top-to-bottom: 01_JP_Chuetsu2004_EW, 02_US_Northrigde1994_360, 05_JP_Miyagi2011_NS, 01_US_PetroliaAft1992_360, 03_TX_ChiChi1999_360, 06_TW_ChiChi1999_360, 02_JP_Fukushima2011_EW, 03_US_LomaPrieta1989_90, 08_TW_ChiChi1999_90, 02_JP_Noto2007_EW.

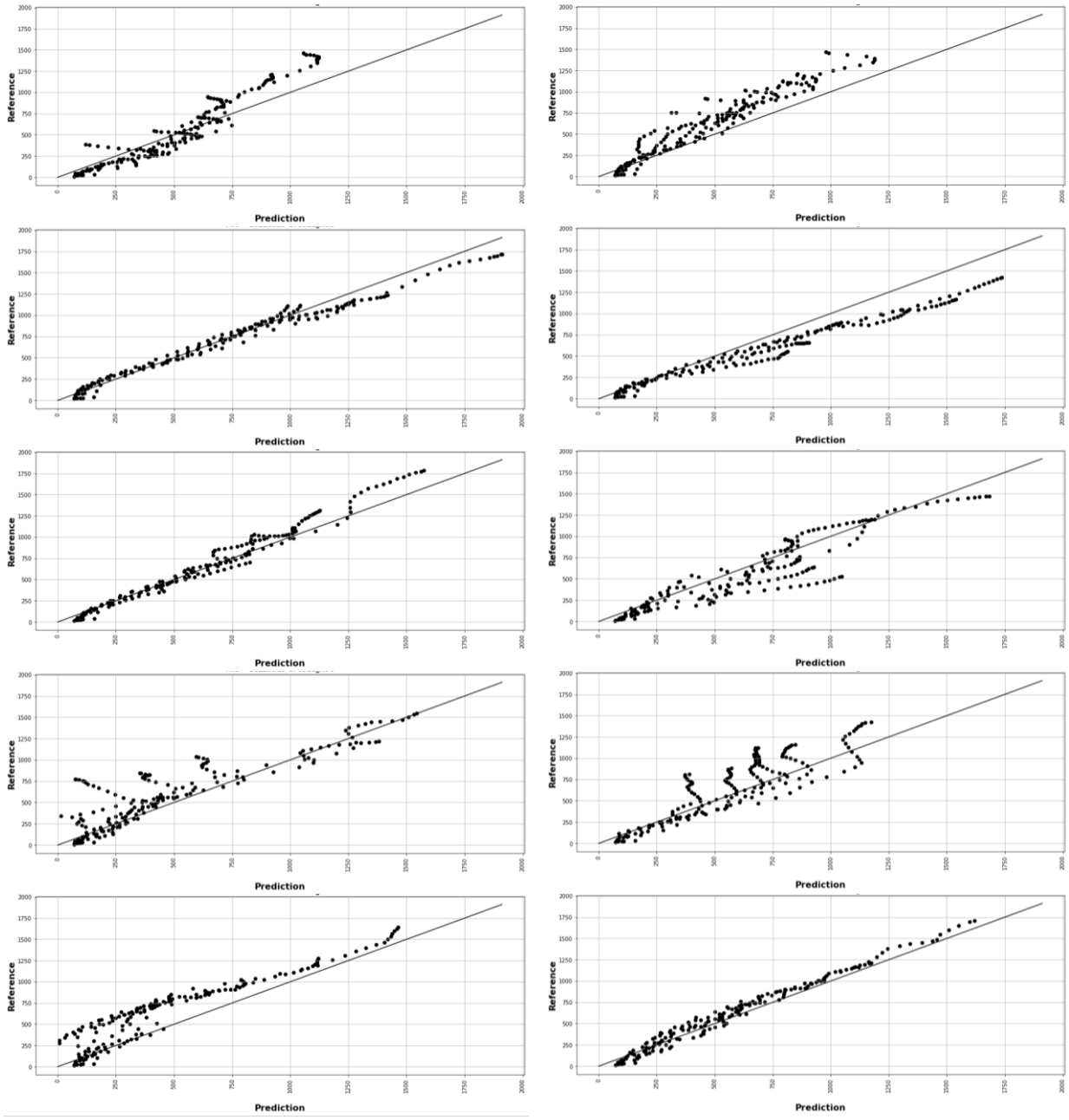

Fig.Appx. 26. Tahara City Hall Building – Acceleration results – Records from left-to-right and top-to-bottom: 01_JP_Chuetsu2004_EW, 02_JP_Noto2007_EW, 03_US_LomaPrieta1989_90, 01_US_PetroliaAft1992_360, 02_US_Northrigde1994_360, 05_JP_Miyagi2011_NS, 06_TW_ChiChi1999_360, 02_JP_Fukushima2011_EW, 03_TX_ChiChi1999_360, 08_TW_ChiChi1999_90,.

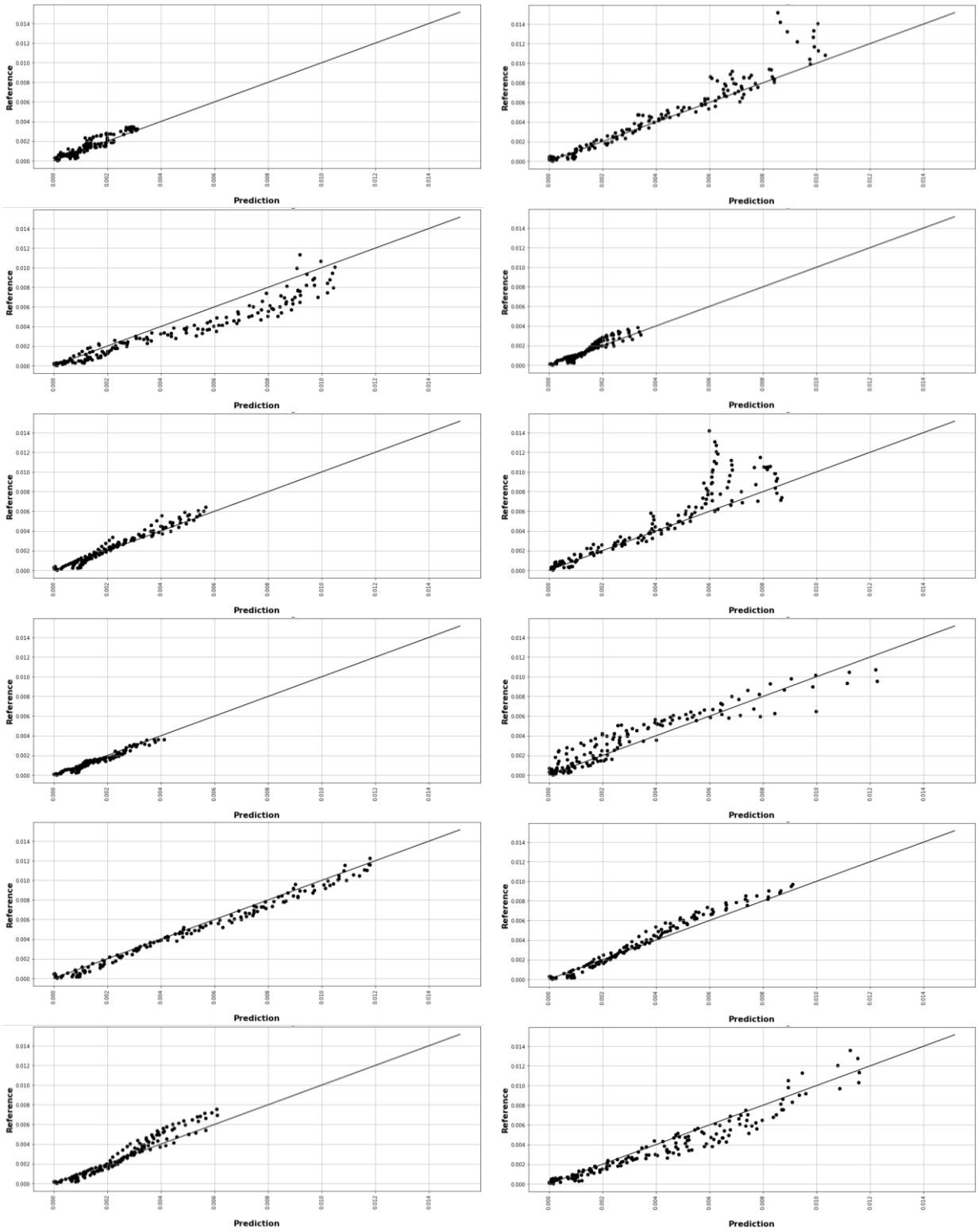

Fig.Appx. 27. Toyohashi Fire Station Building – Story Drift ratio results – Records from left-to-right and top-to-bottom: 01_JP_Miyagi2011_NS, 02_US_Petrolia1992_360, 04_JP_Chuetsu2004_NS, 07_JP_Kumamoto2016_NS, 01_US_PetroliaAft1992_90, 03_JP_Fukushima2021_NS, 04_JP_Hokkaido2018_NS, 10_JP_Fukushima2021_NS, 02_JP_Noto2007_EW, 03_TX_ChiChi1999_90, 05_JP_Hokkaido2018_NS, JP_2019FEB21_EW.

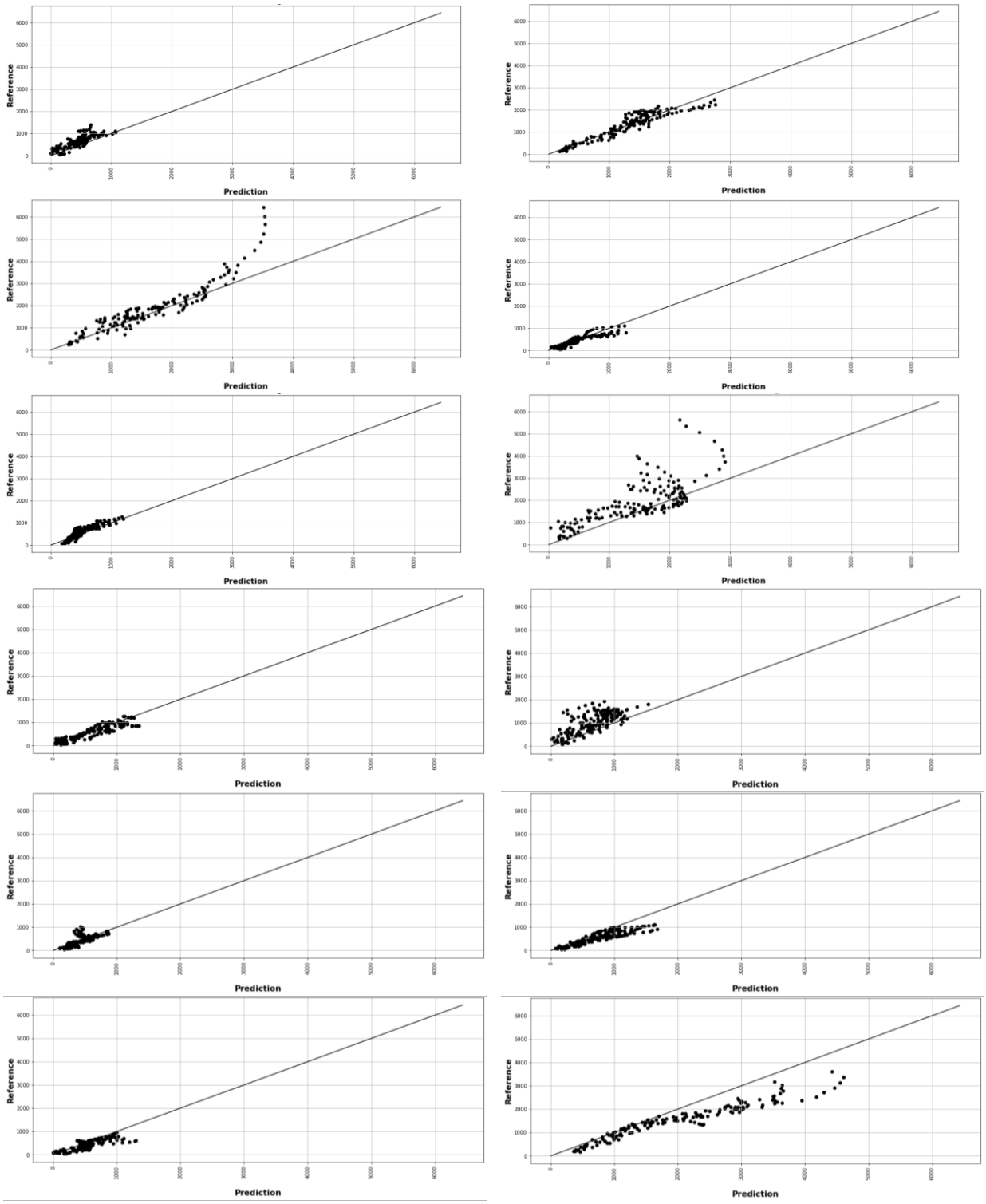

Fig.Appx. 28. Toyohashi Fire Station Building – Acceleration results – Records from left-to-right and top-to-bottom: 01_JP_Miyagi2011_NS, 02_US_Petrolia1992_360, 04_JP_Chuetsu2004_NS, 07_JP_Kumamoto2016_NS, 01_US_PetroliaAft1992_90, 03_JP_Fukushima2021_NS, 04_JP_Hokkaido2018_NS, 10_JP_Fukushima2021_NS, 02_JP_Noto2007_EW, 03_TX_ChiChi1999_90, 05_JP_Hokkaido2018_NS, JP_2019FEB21_EW.

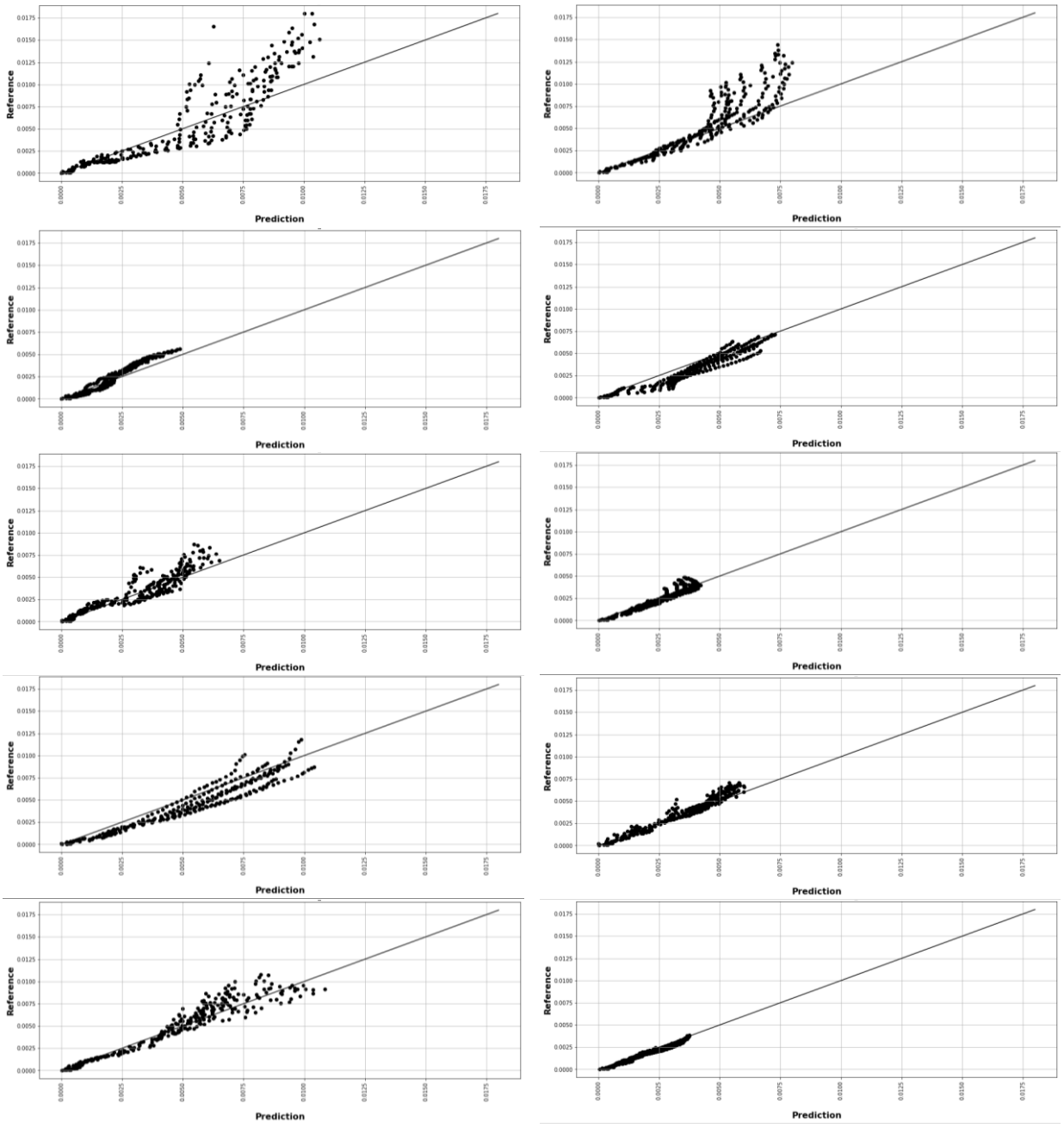

Fig.Appx. 29. RC Building – X-Direction – Story Drift ratio results – Records from left-to-right and top-to-bottom: 01_JP_Kumamoto2016_EW, 01_TX_ChiChi1999_360, 04_JP_Kumamoto2016_EW, JP_1996DEC21_EW, 04_JP_Fukushima2021_EW, 07_JP_Hokkaido2018_NS, JP_1996DEC21_NS, 04_JP_Hokkaido2018_NS, 09_TX_ChiChi1999_90, US_SierraMadre1991_90.

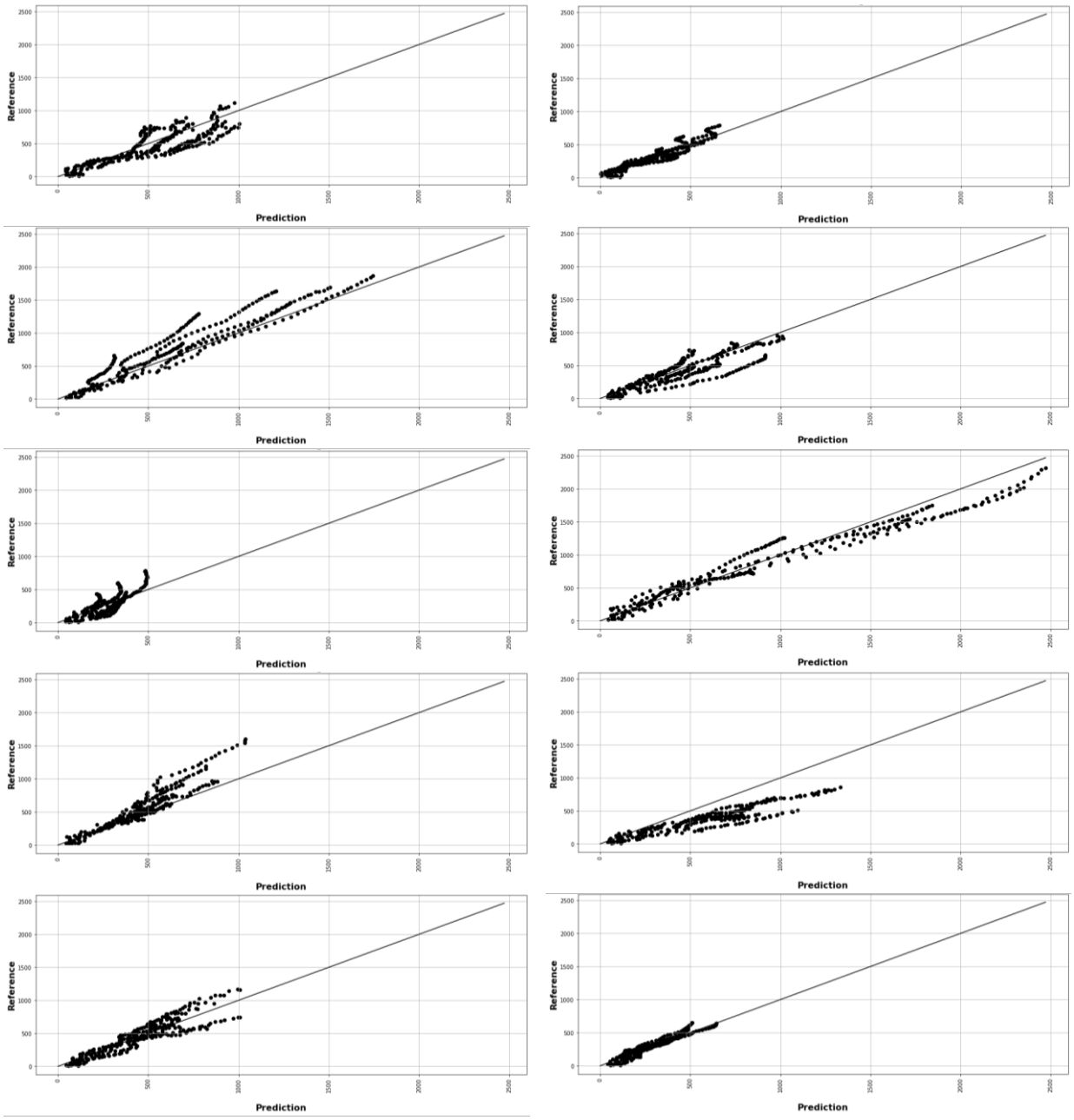

Fig.Appx. 30. RC Building – X-Direction – Acceleration results – Records from left-to-right and top-to-bottom: 01_JP_Kumamoto2016_EW, 04_JP_Kumamoto2016_EW, JP_1996DEC21_EW, 01_TX_ChiChi1999_360, 07_JP_Hokkaido2018_NS, JP_1996DEC21_NS, 04_JP_Fukushima2021_EW, 04_JP_Hokkaido2018_NS, 09_TX_ChiChi1999_90, US_SierraMadre1991_90.

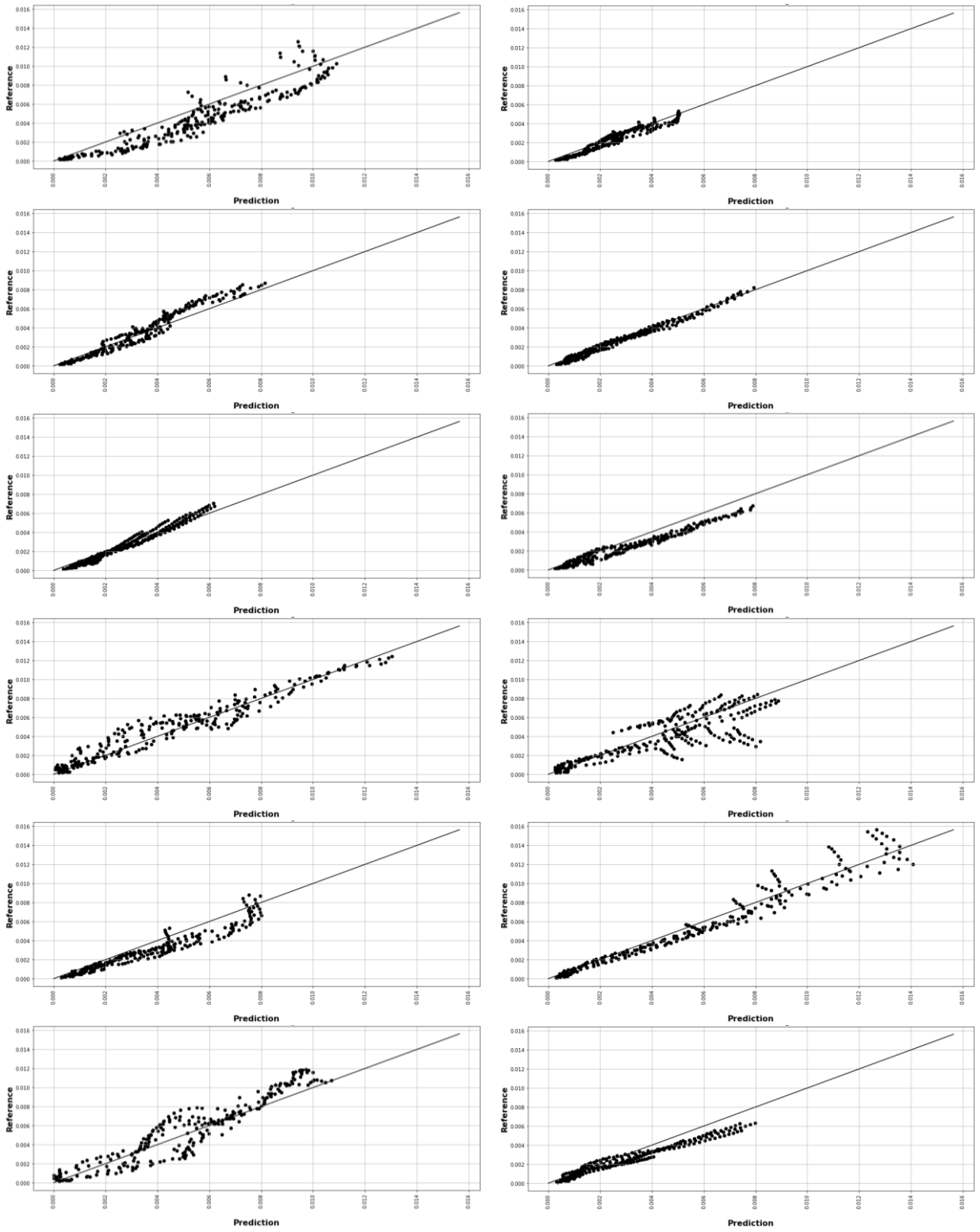

Fig.Appx. 31. RC Building – Y-Direction – Story Drift ratio results – Records from left-to-right and top-to-bottom: 10_TX_ChiChi1999_90, 07_JP_Kumamoto2016_NS, 06_TX_ChiChi1999_90, 04_US_LomaPrieta1989_90, 04_US_LomaPrieta1989_0, 01_JP_Chuetsu2004_EW, 03_JP_Miyagi2011_EW, 02_US_Anza2005_360, 03_JP_Kumamoto2016_NS, 02_US_Petrolia1992_270, 03_JP_Hokkaido2018_NS, 02_US_PetroliaAft1992_90.

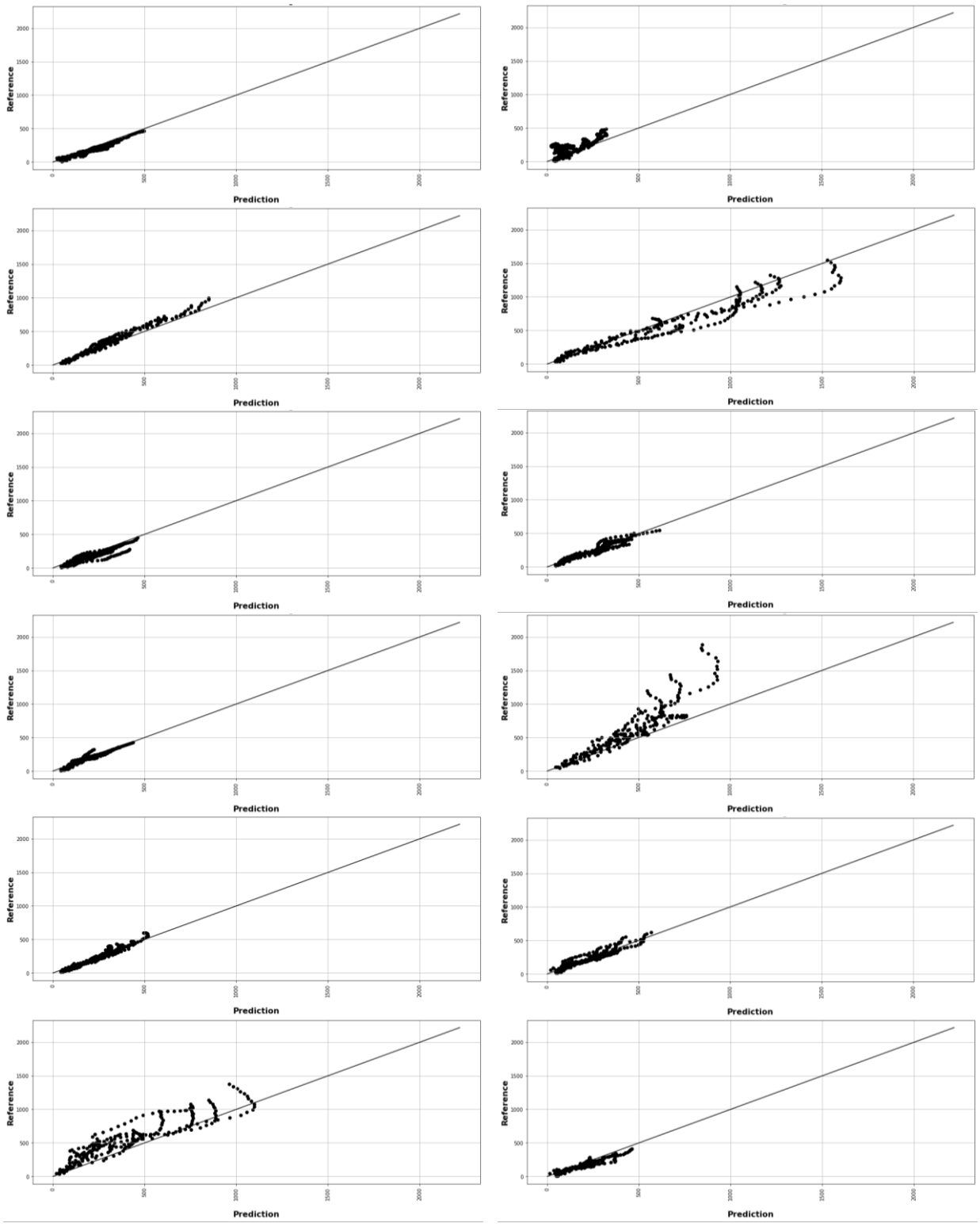

Fig.Appx. 32. RC Building – Y-Direction – Acceleration results – Records from left-to-right and top-to-bottom: 07_JP_Kumamoto2016_NS, 06_TX_ChiChi1999_90, 10_TX_ChiChi1999_90, 05_JP_Totori2000_EW, 04_US_LomaPrieta1989_90, 04_US_LomaPrieta1989_0, 02_US_PetroliaAft1992_90, 03_JP_Miyagi2011_EW, 02_US_Petrolia1992_270, 03_JP_Kumamoto2016_NS, 03_JP_Hokkaido2018_NS, 01_JP_Chuetsu2004_EW.

Appendix C: ML methods results (Chapter 4)

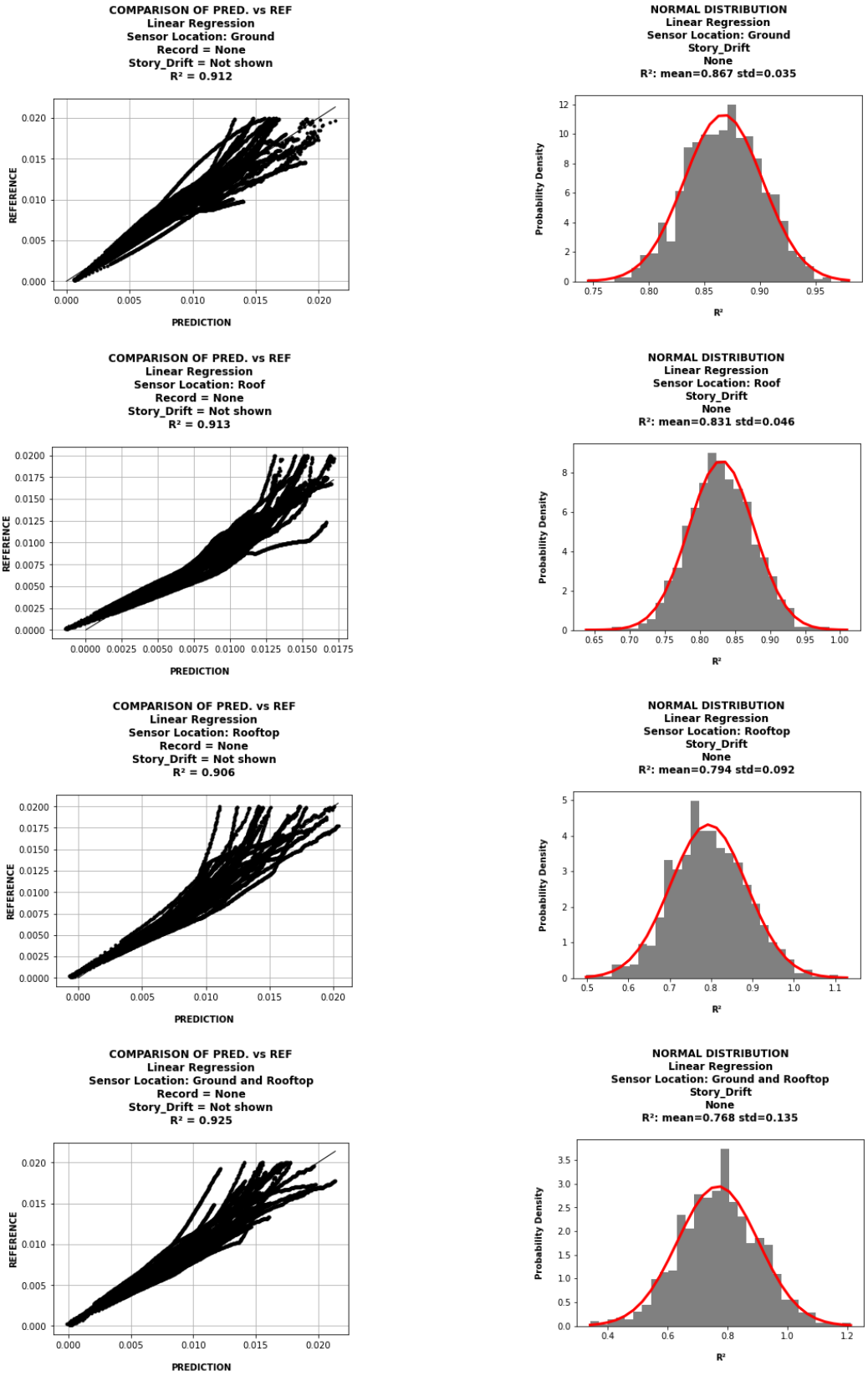

Fig.Appx. 33. Tahara City Hall building – Linear Regression

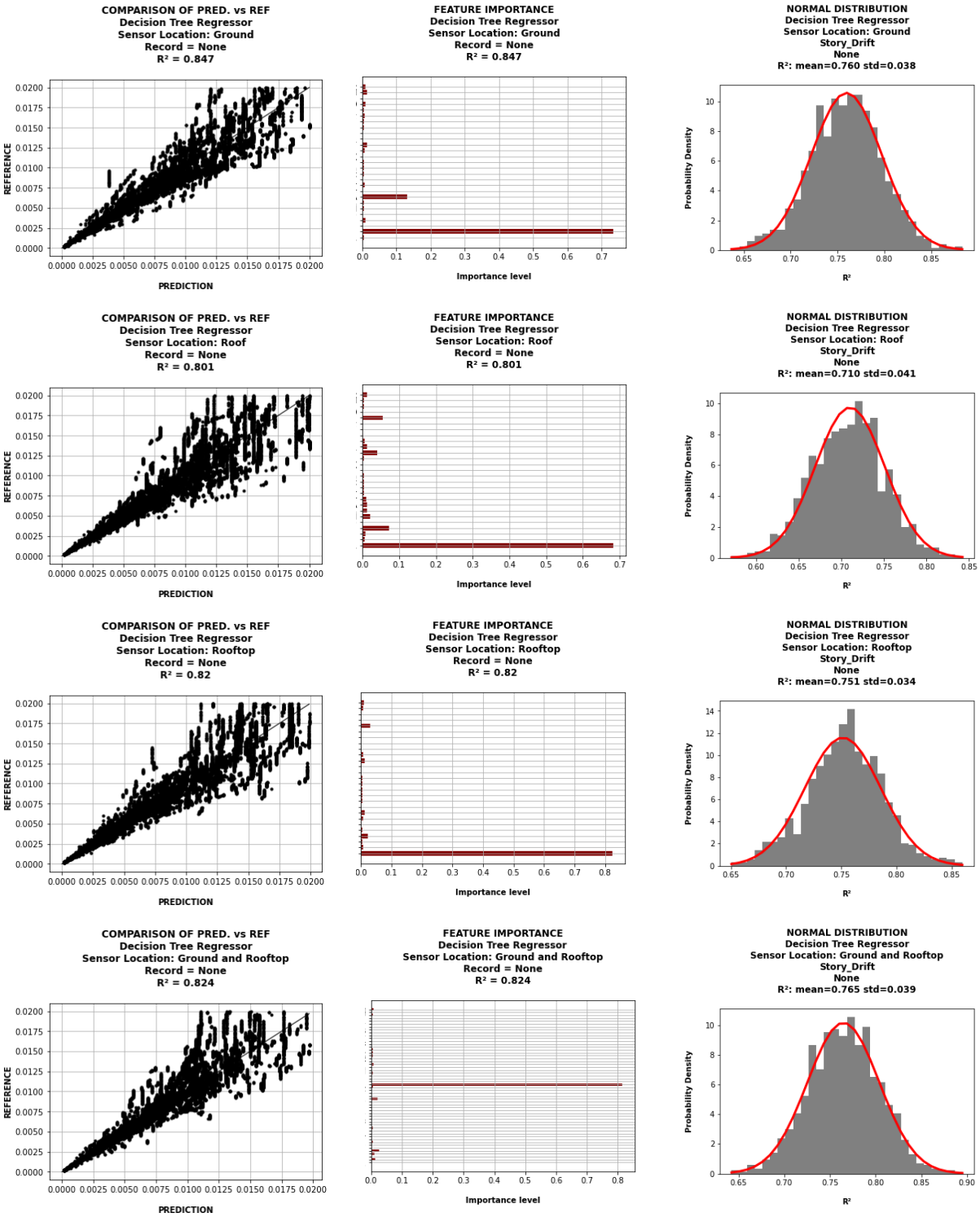

Fig.Appx. 34. Tahara City Hall building – Decision Tree

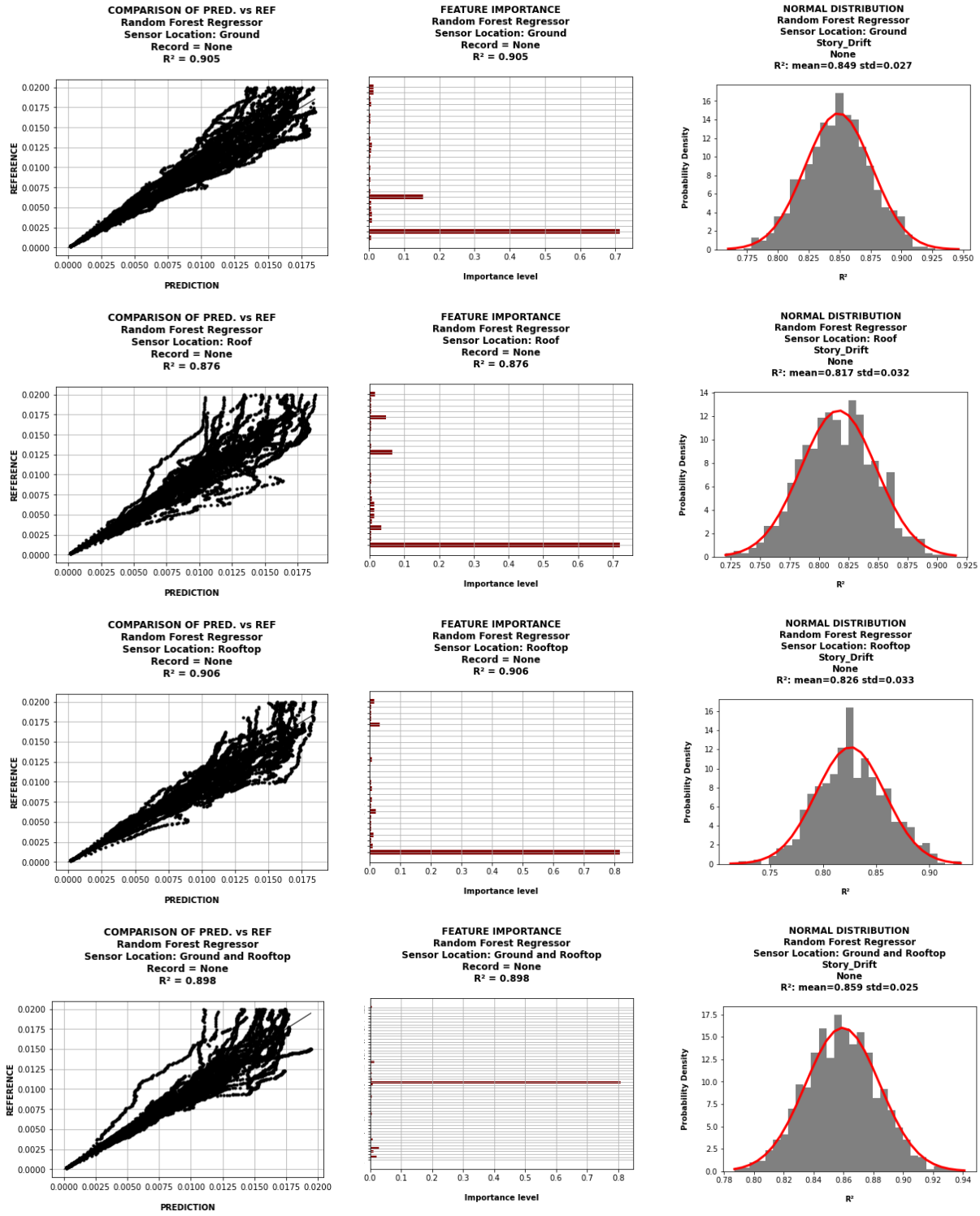

Fig.Appx. 35. Tahara City Hall building – Random Forest

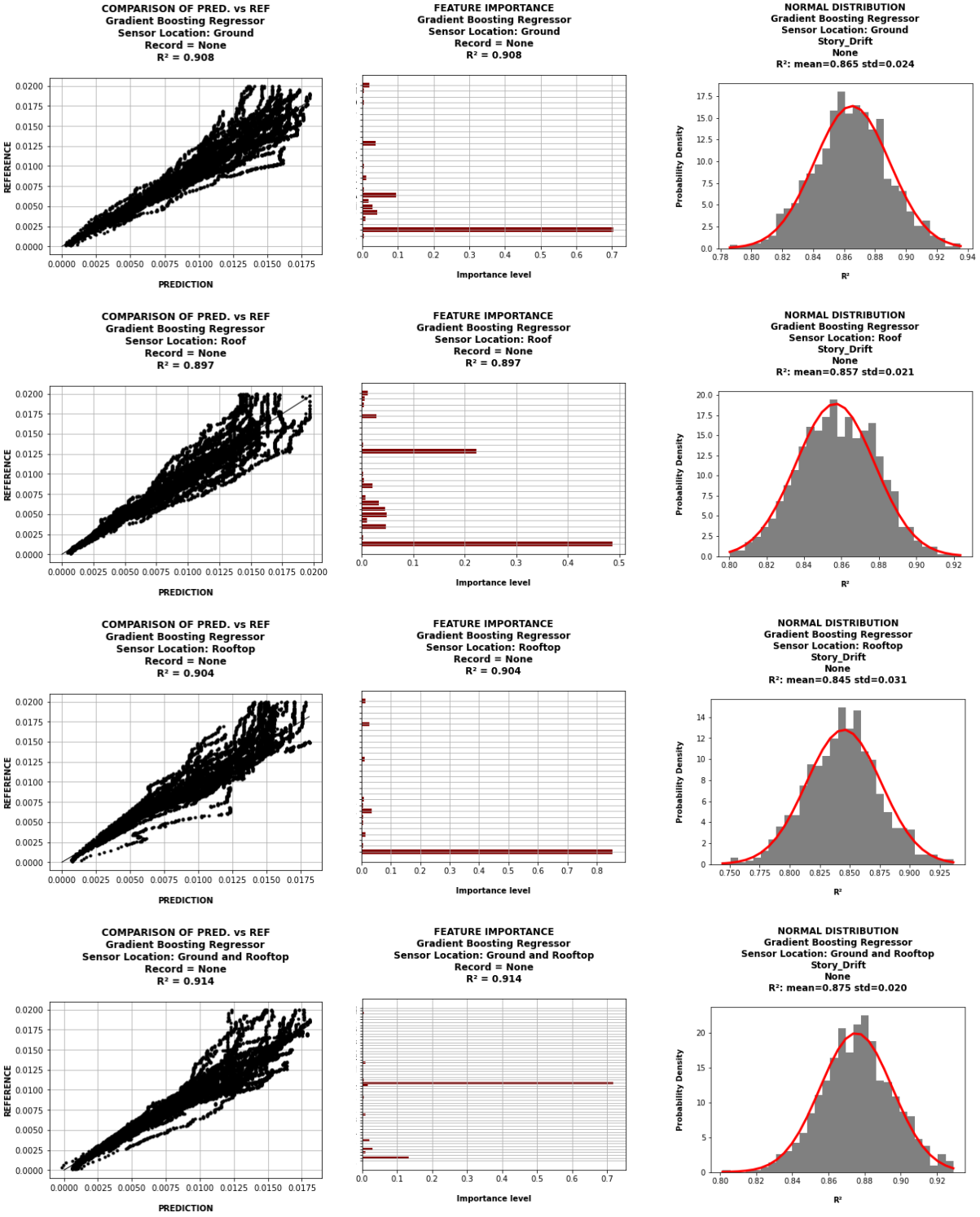

Fig.Appx. 36. Tahara City Hall building – Gradient Boost

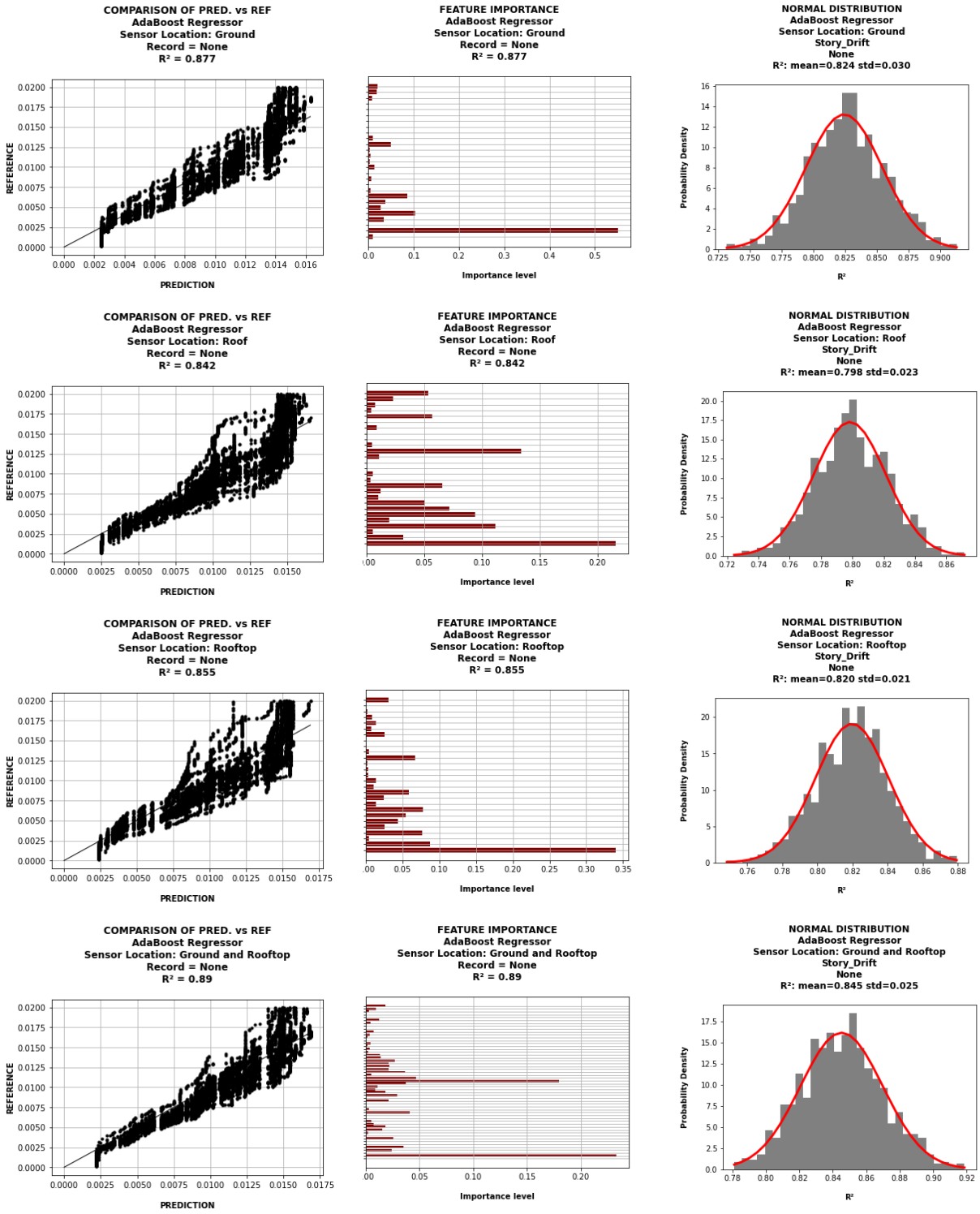

Fig.Appx. 37. Tahara City Hall building – AdaBoost

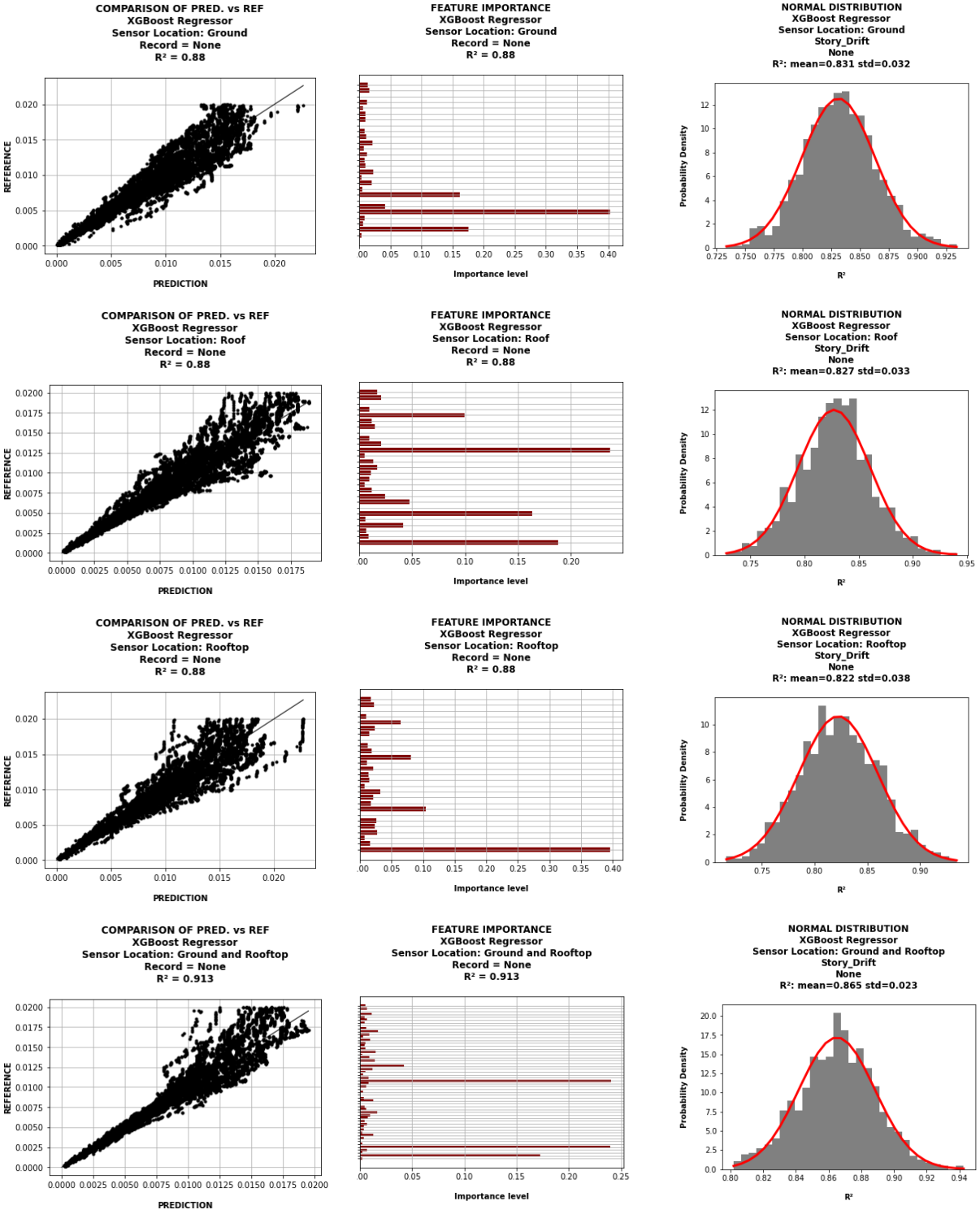

Fig.Appx. 38. Tahara City Hall building – XGBoost

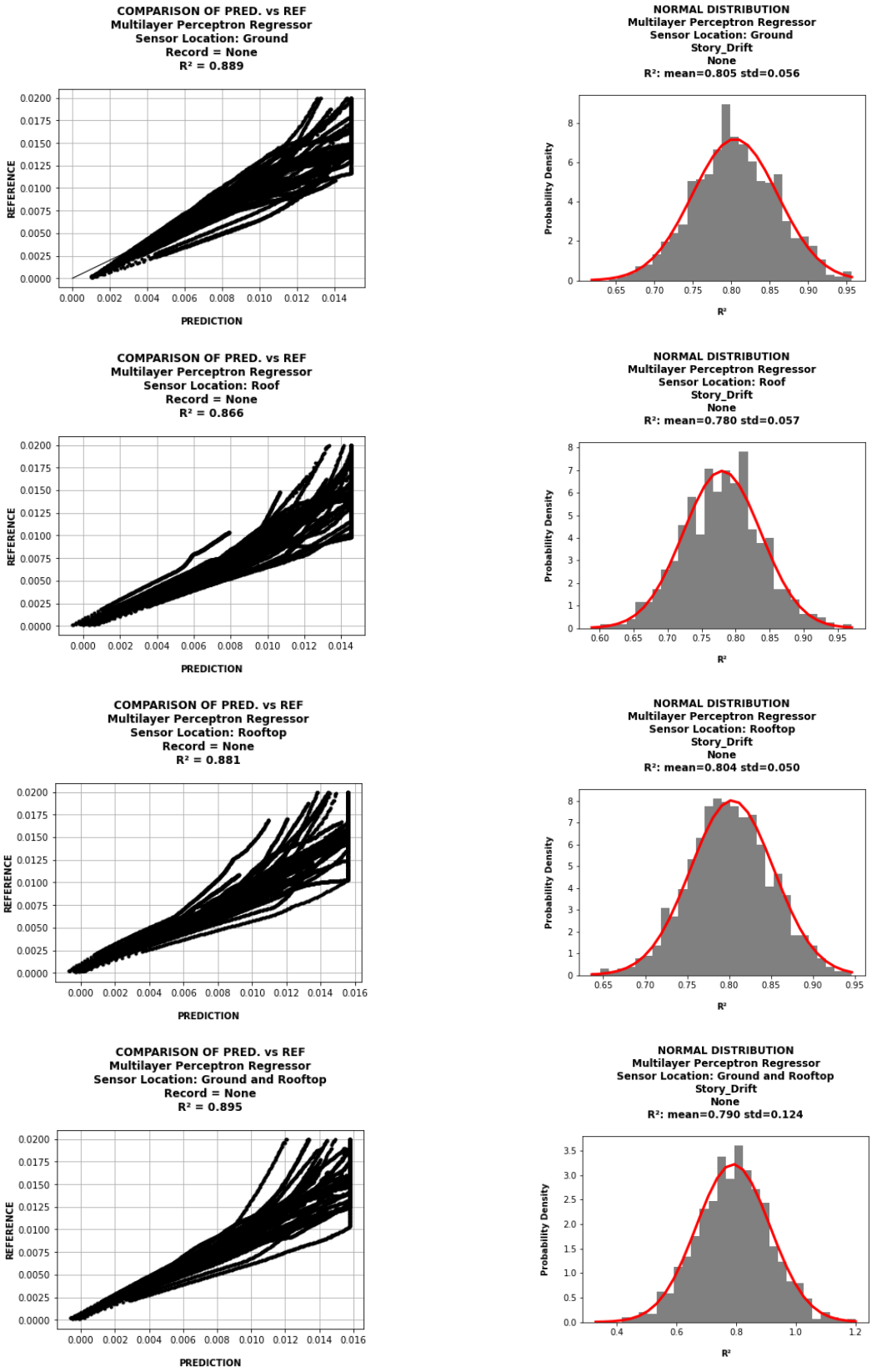

Fig.Appx. 39. Tahara City Hall building – Multilayer Perceptron

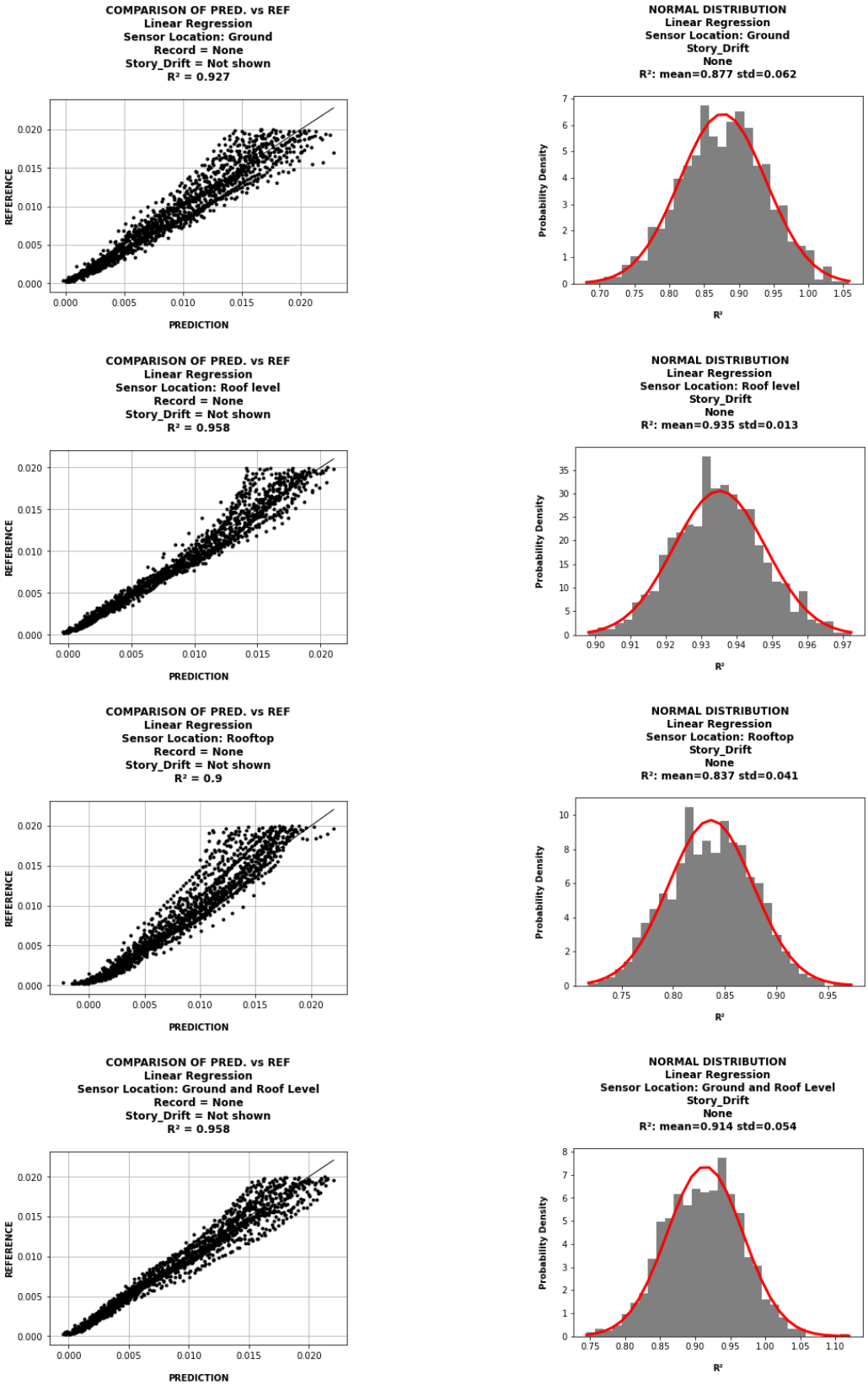

Fig.Appx. 40. Toyohashi Fire Station building – Linear Regression

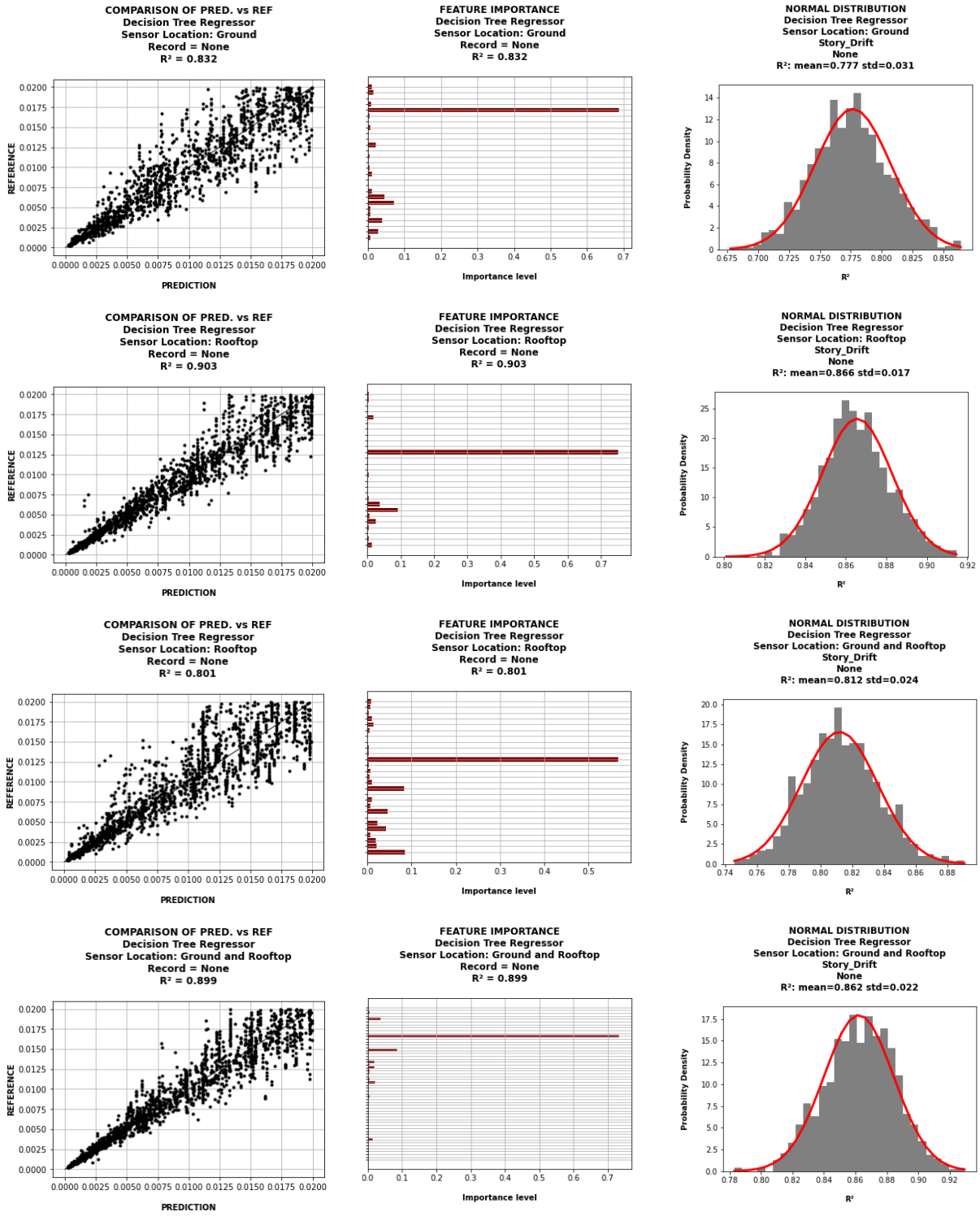

Fig.Appx. 41. Toyohashi Fire Station building – Decision Tree

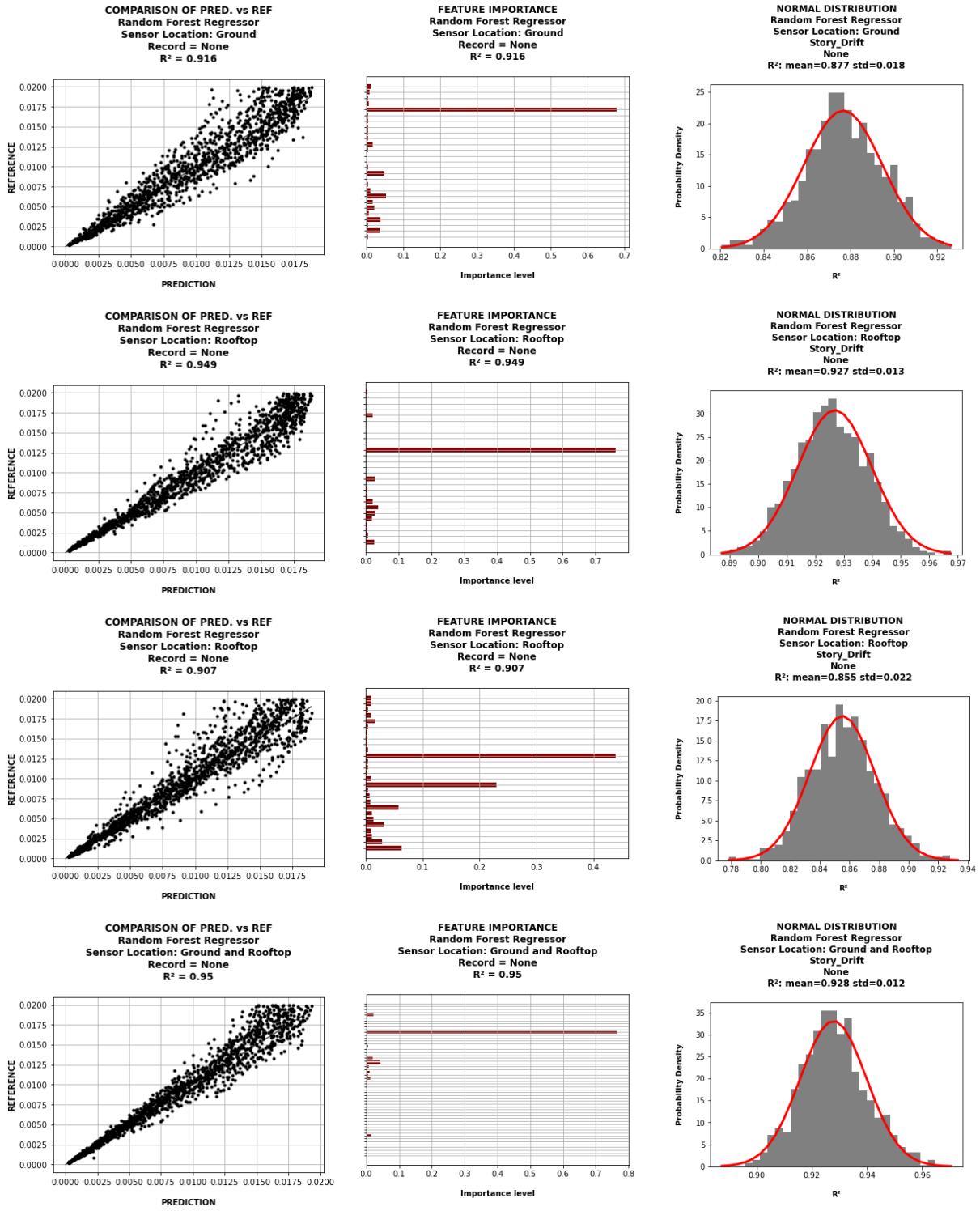

Fig.Appx. 42. Toyohashi Fire Station building – Random Forest

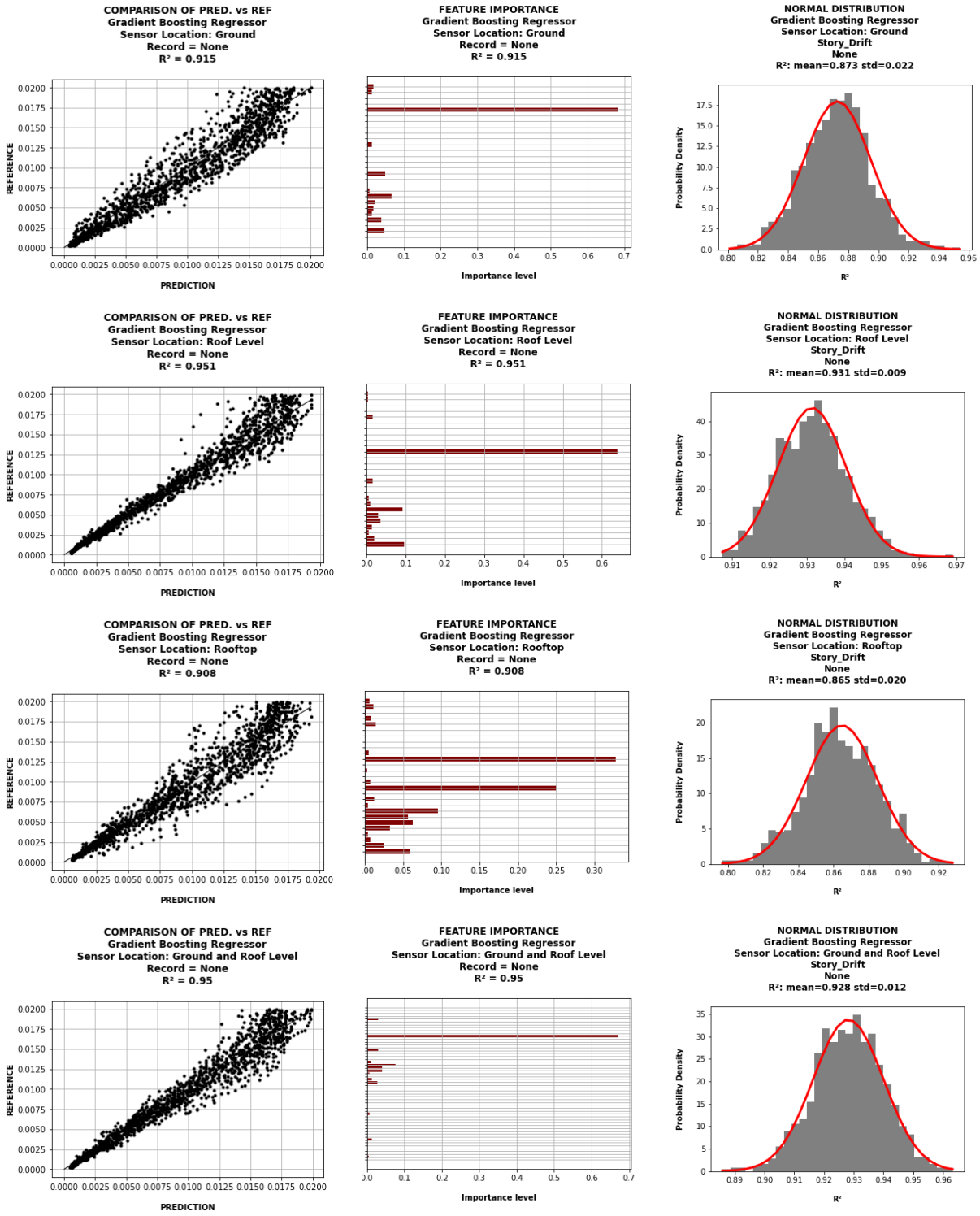

Fig.Appx. 43. Toyohashi Fire Station building – Gradient Boost

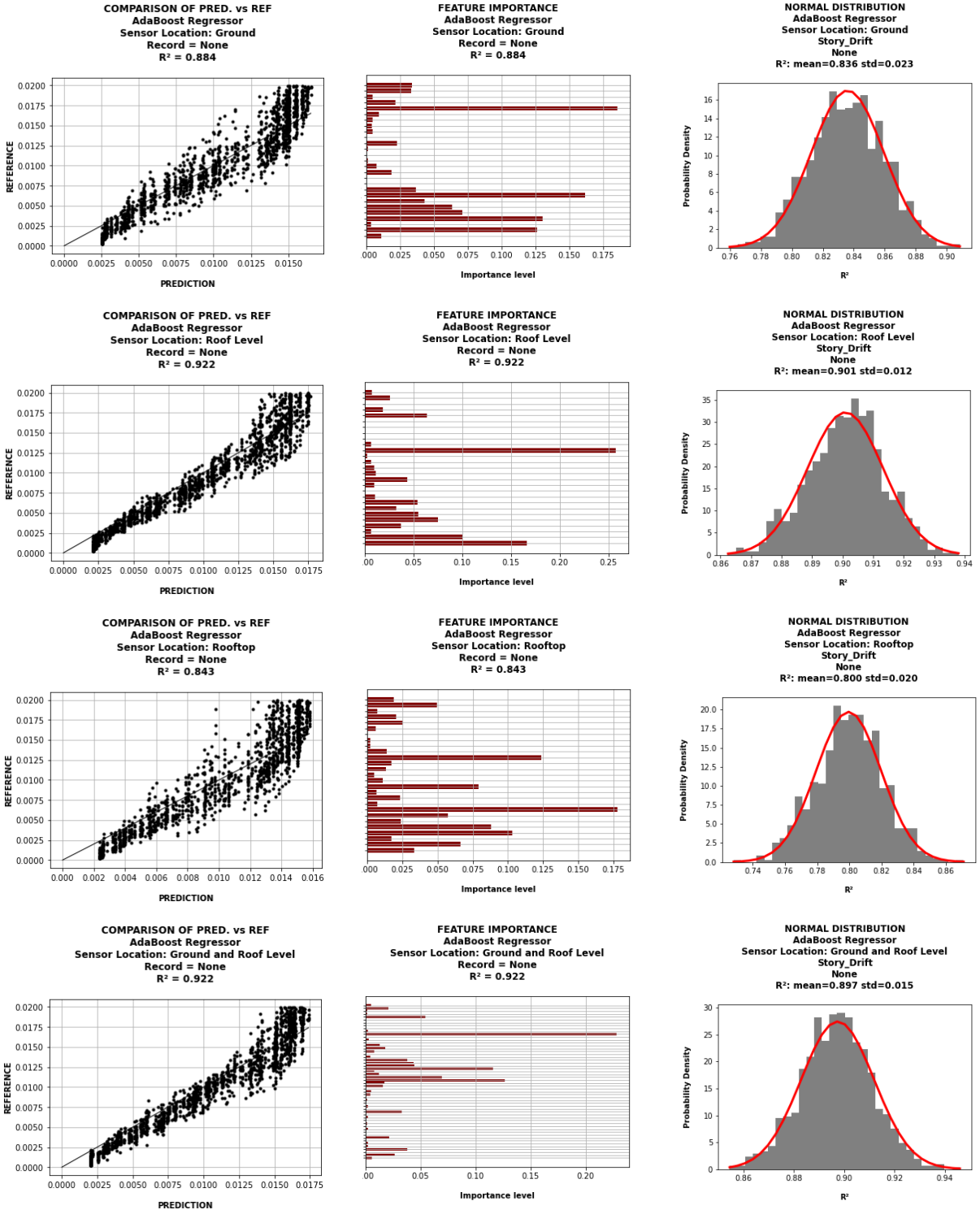

Fig.Appx. 44. Toyohashi Fire Station building – AdaBoost

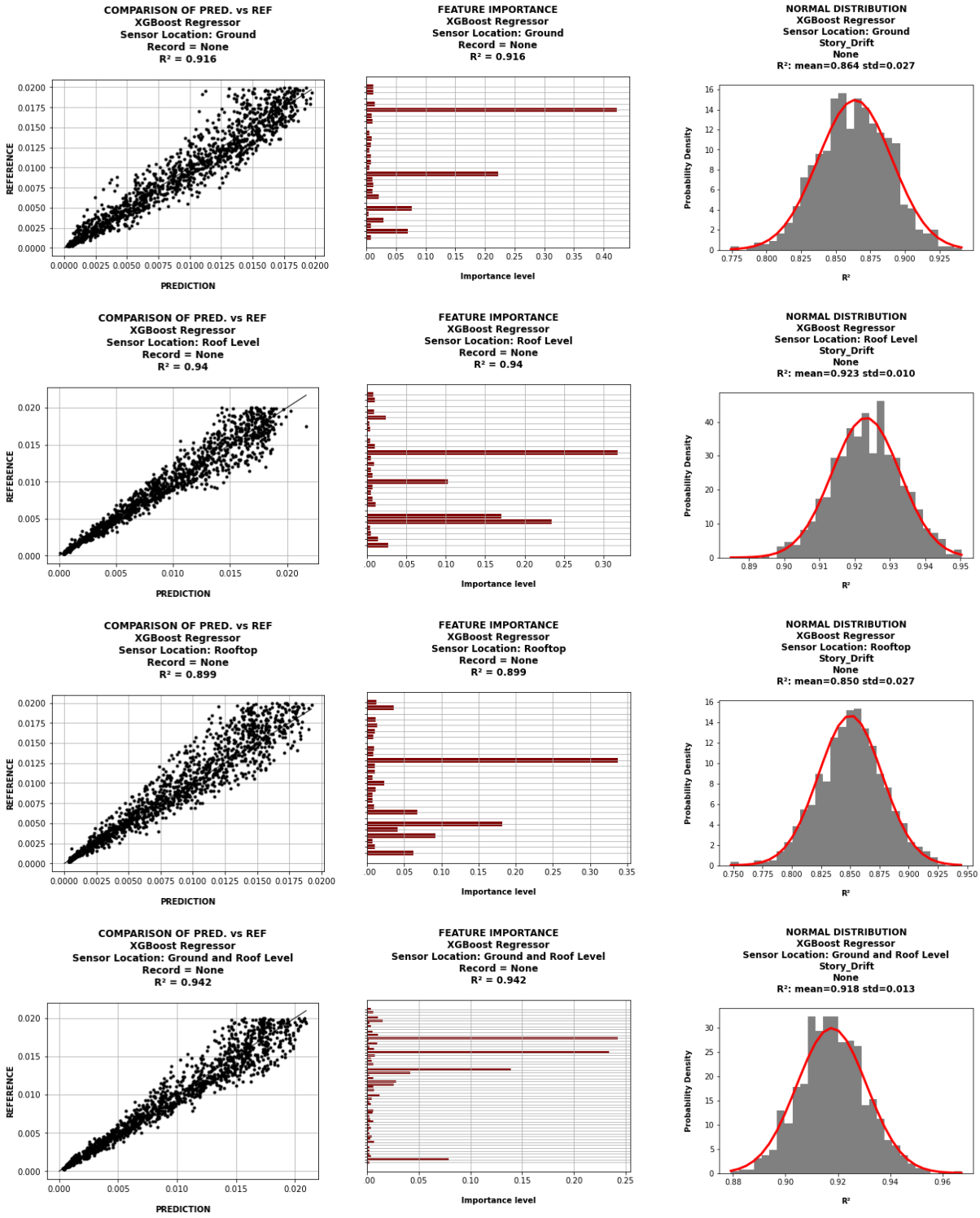

Fig.Appx. 45. Toyohashi Fire Station building – XGBoost

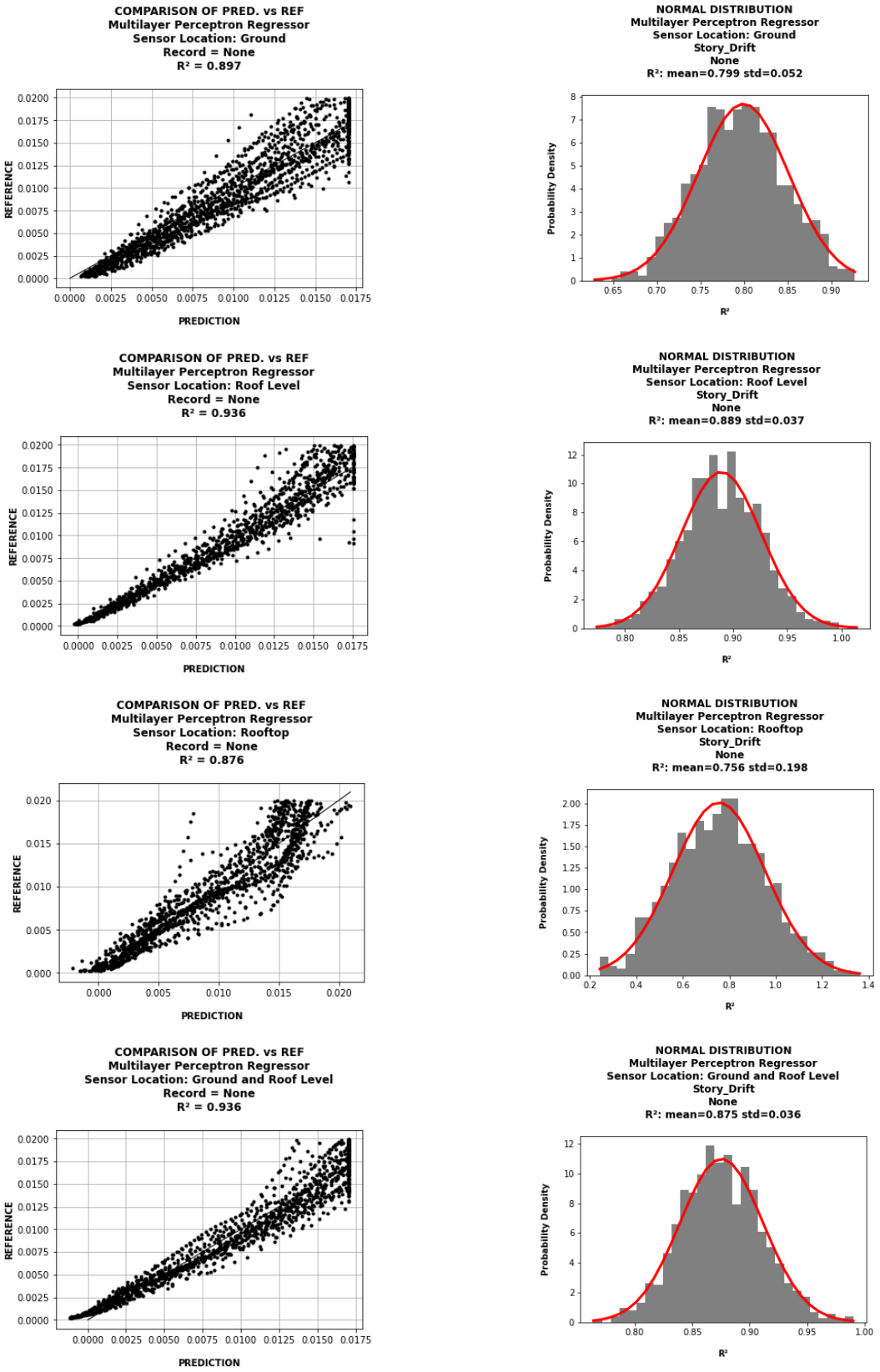

Fig.Appx. 46. Toyohashi Fire Station building – Multilayer Perceptron

Appendix D: ML methods results (Chapter 5)

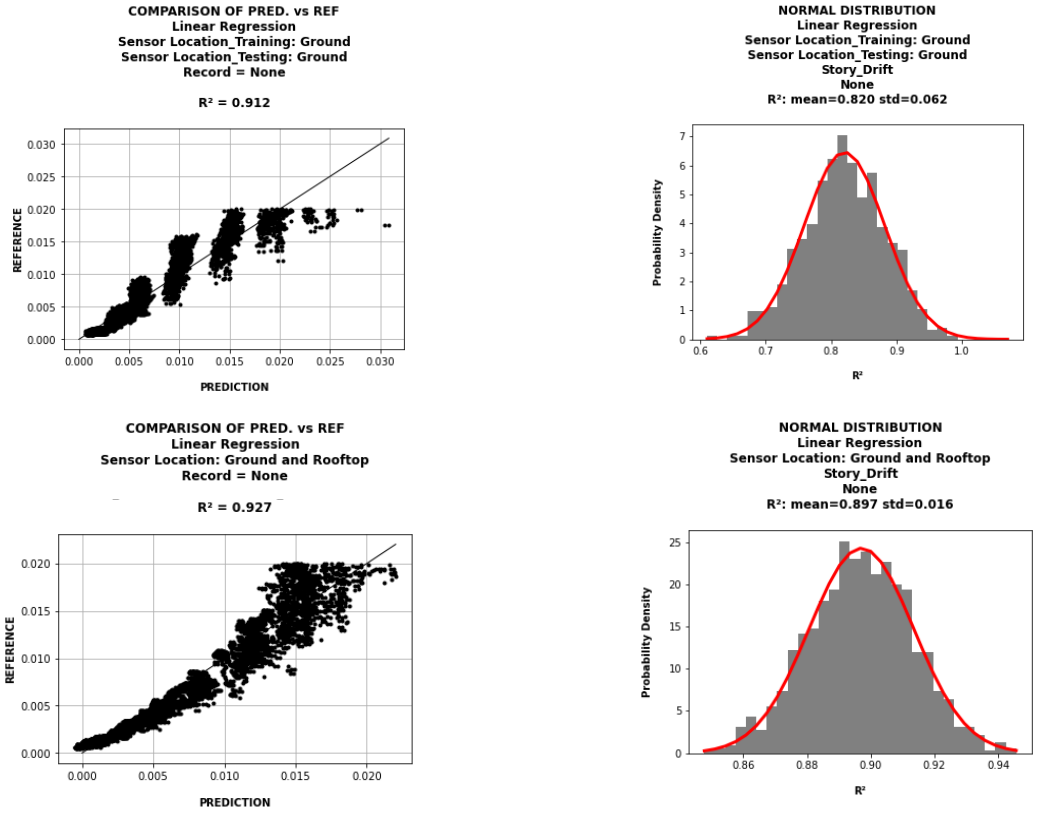

Fig.Appx. 47. Linear Regression.

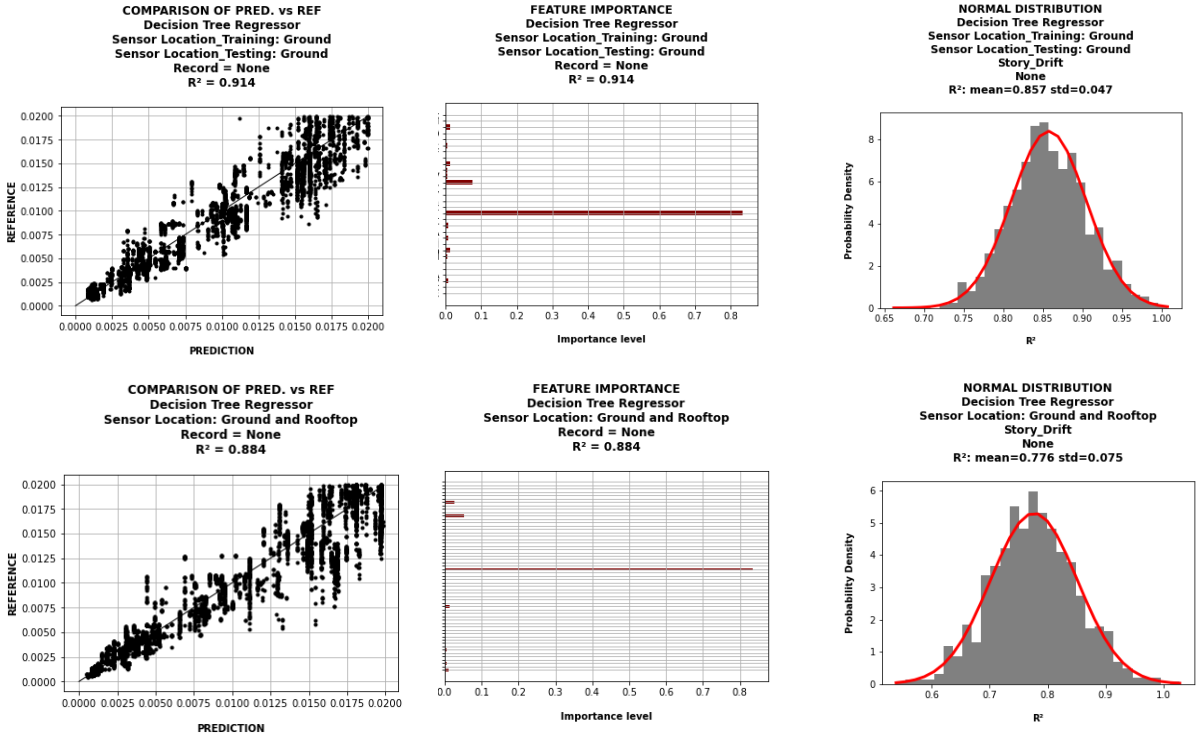

Fig.Appx. 48. Decision Tree.

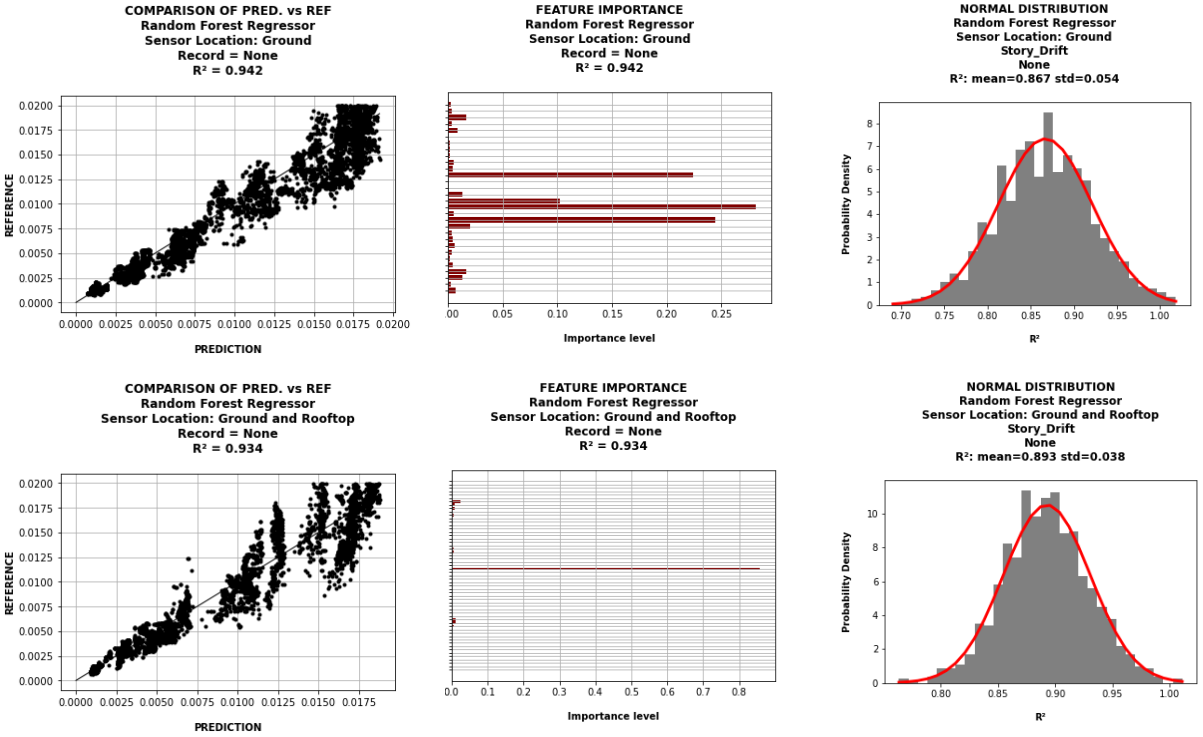

Fig.Appx. 49. Random Forest.

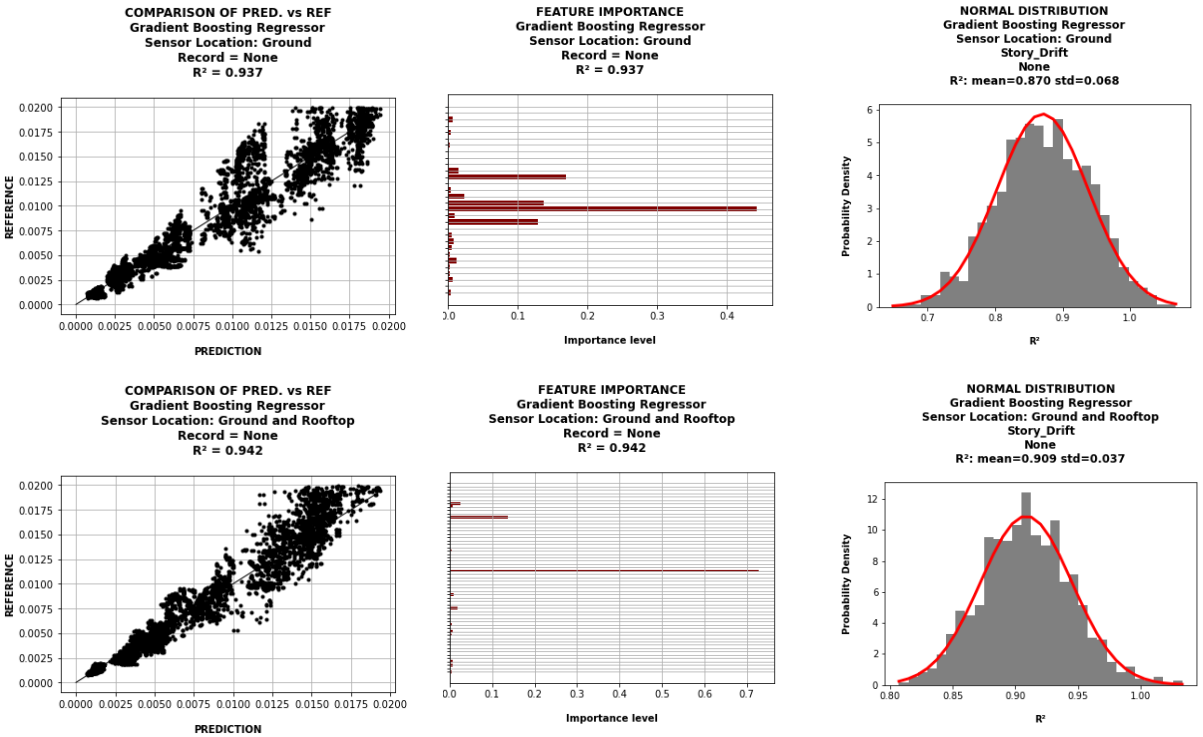

Fig.Appx. 50. Gradient Boost.

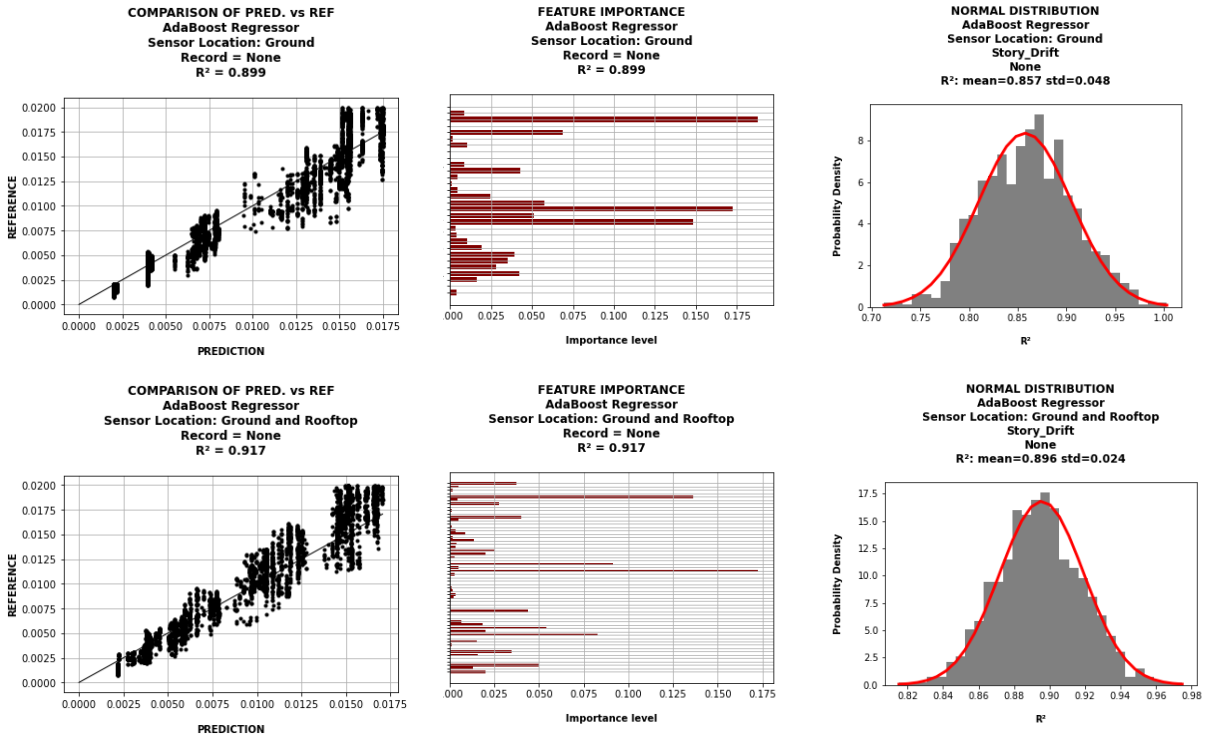

Fig.Appx. 51. AdaBoost.

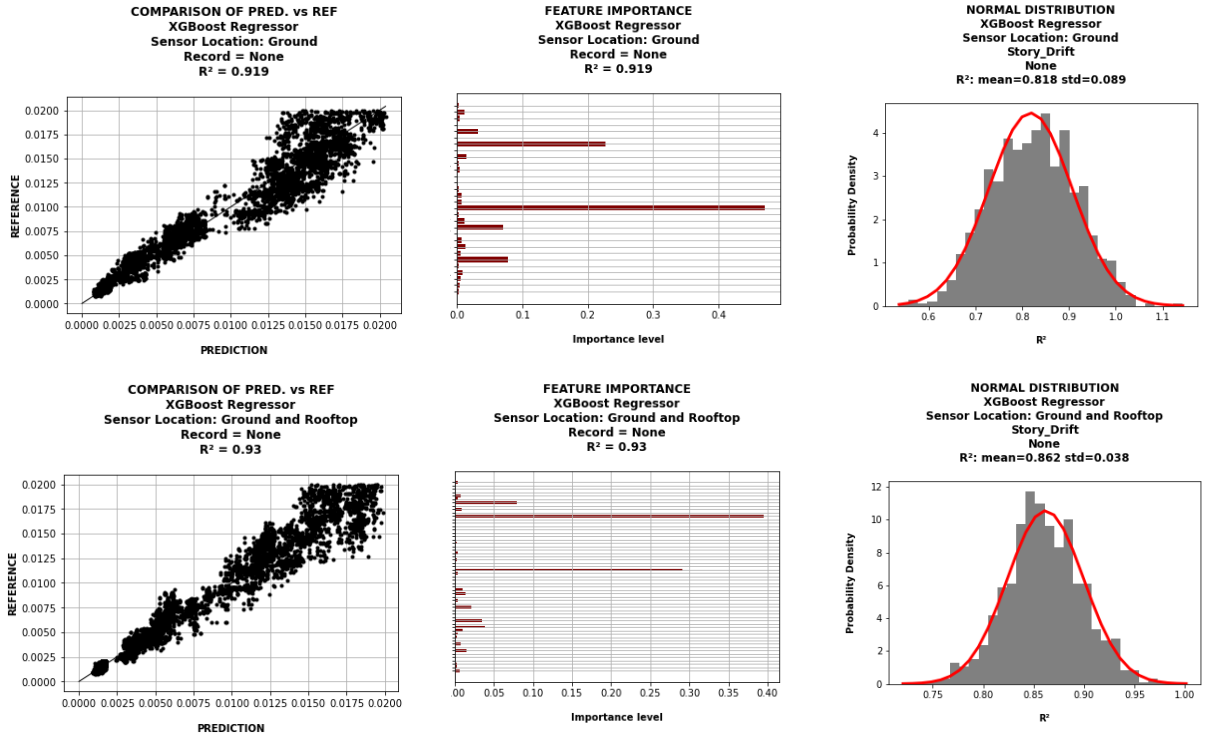

Fig.Appx. 52. XGBoost.

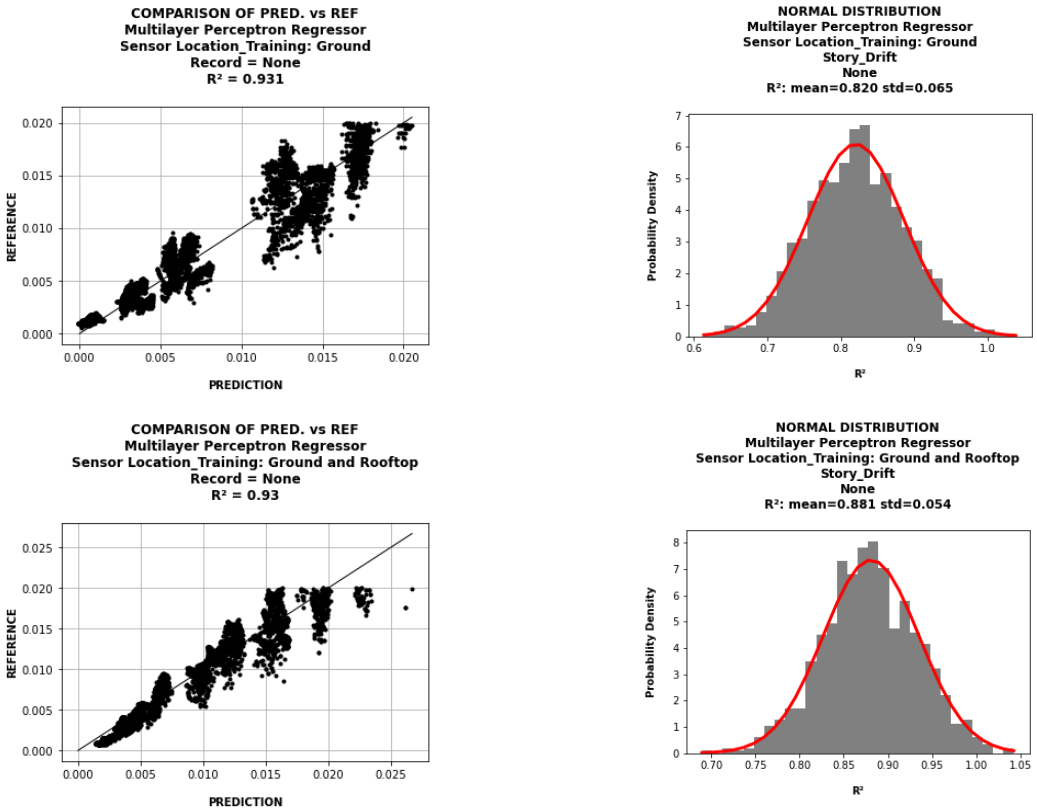

Fig.Appx. 53. Multilayer Perceptron.

Appendix E: Arias Intensity and Husid plot

Arias's Intensity (I_A) is proportional to the released energy of each record. Husid plot uses a Normalized Arias Intensity (concerning its maximum value) in the Y-Y axis ($H_{(t)}$). It is recommended to cut off between 5% to 95% Normalized Arias Intensity of records considering that in this time range is the primary energy released.

$$I_A = \frac{\pi}{2g}\int_0^{T_d} a^2 dt$$

$$H_{(t)} = \frac{\int_0^t a^2 dt}{\int_0^{T_d} a^2 dt}$$

where:

- ✓ a: Acceleration
- ✓ T_d: Total time of record

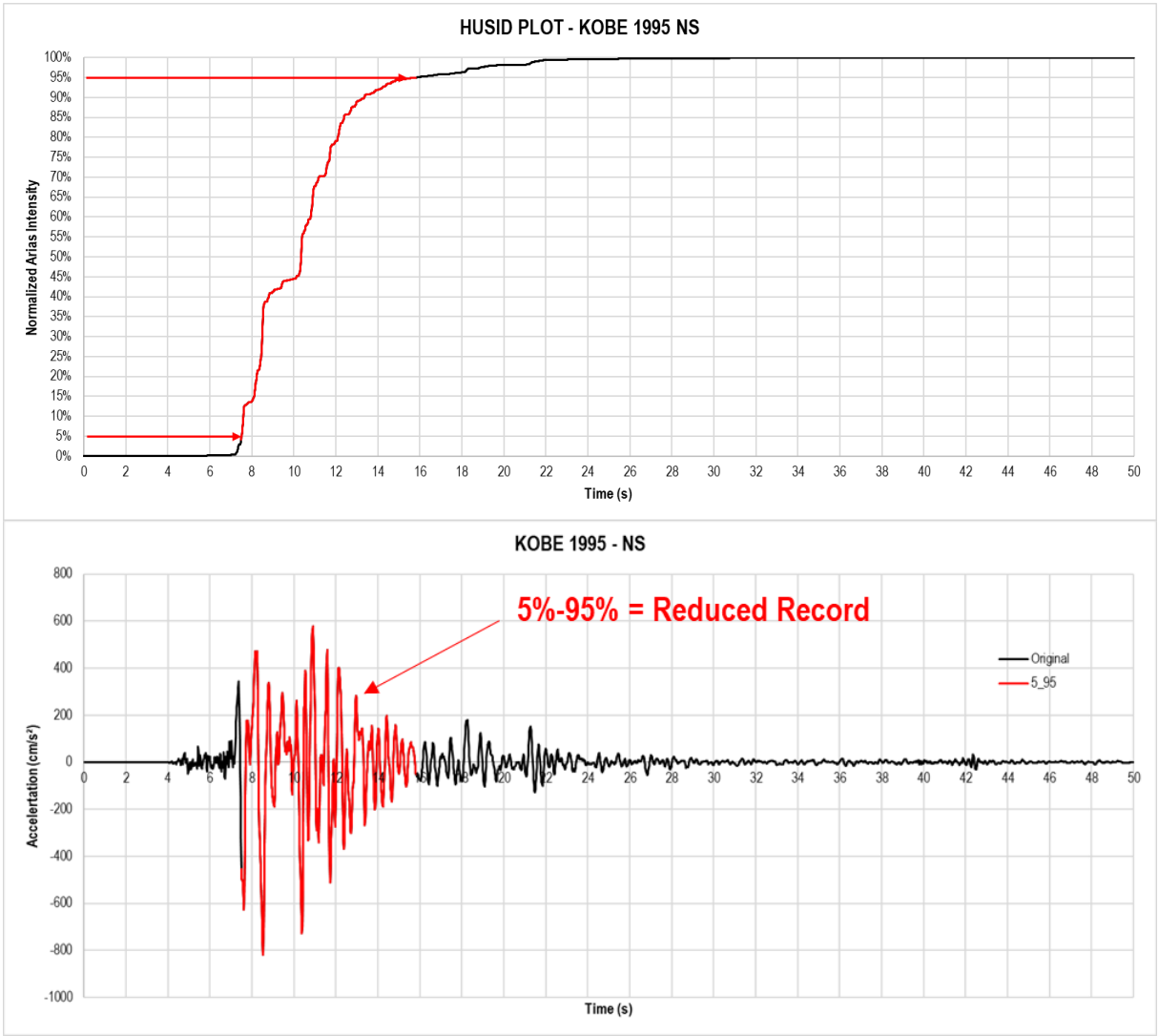

Fig.Appx. 54. Example of reduction of the number of samples by using Arias Intensity